DTU Library

Icing Problems of Wind Turbine Blades in Cold Climates

Hudecz, Adriána

Publication date:
2014

Document Version
Publisher's PDF, also known as Version of record

[Link back to DTU Orbit](#)

Icing Problems of Wind Turbine Blades in Cold Climates

Adriána Hudecz

DTU Vindenergi
Institut for Vindenergi

Resumen (maks 2000 char.):
Due to the ambitious targets on increasing the use of renewable energy sources and also the lack of conventional sites, non-conventional sites, e.g. cold climate (CC) sites are getting more attractive to wind turbine installations. Deployment of wind energy in CC areas grows rapidly. The installed wind power capacity at the end of 2012 was around 69GW, which corresponds to approximately 24% of the total (globally) installed capacity. Operation of wind turbines is challenging at CC sites. Wind turbines at these sites may be exposed to icing conditions or temperatures outside the design limits of standard wind turbines. Cold climate plays a major role in power production and safety hazards of a wind turbine. Icing is a key parameter in project development for cold climate operation. These conditions can be found in sub-arctic or arctic regions, like in the Nordic countries in Europe, in Canada and at high altitude mountains (e.g. Alps).
During the PhD work, the risk of icing events and the effect of ice accretion on wind turbine blades were studied. A small demonstration of how to identify icing event was performed using meteorological data collected in Nanortalik, in South-Greenland. A larger part of the PhD work contains experimental and numerical investigations of the impacts of ice accretion on an airfoil section with different angles of attack. The experimental study was carried out in the Collaborative Climatic Wind Tunnel located at FORCE Technology to investigate how ice accumulates for moderate low temperatures on the blade and how the aerodynamic forces are changing during the process of ice build-up. In the first part of the numerical analysis, the resulted ice profiles of the wind tunnel tests were compared to profiles simulated with using the 2-D ice accretion code whereas in the second part, computational fluid dynamics was used to numerically analyze the impacts of ice accretion on the flow behavior and the aerodynamic characteristics of the airfoil. The PhD study delivered new insights into the research in the field of wind energy in cold climate and gave suggestions for further investigations and improvements.

Technical University of Denmark

Doctoral Thesis

Icing Problems of Wind Turbine Blades in Cold Climates

Author:
Adriána Hudecz

Supervisor:
Martin Otto Laver Hansen

Co-Supervisors:
Lorenzo Battisti & Arne Villumsen

A thesis submitted in fulfilment of the requirements
for the degree of Doctor of Philosophy in engineering

in the

Fluid Mechanics Section
Department of Wind Energy

November 18, 2013

Preface

This thesis was prepared at the Department of Wind Energy, Technical University of Denmark during the period from 15th of November 2010 to 14th of November 2013 in partial fulfilment of the requirements for acquiring the degree of doctor of philosophy in engineering. The PhD study was carried out under the supervision of associate professor Martin O. L. Hansen and was co-supervised by associate professor Lorenzo Battisti from Trento University, Italy and professor Arne Villumsen former head of section of Arctic Technology Center, Technical University of Denmark.

The overall objective of the conducted research was to study the impacts of ice accretion on wind turbine blades through experimental and numerical work along with the environmental conditions, which are favourable for ice formation on structures. Some of the work presented in this thesis was previously disseminated in the following papers and conferences (a copy of the first three journal/conference papers can be found in Appendix E):

- Hudecz, A., Hansen, M. O. L., Dillingh, J. and Turkia, V. (2013). *Numerical Investigation of the Effects of Ice Accretion on a Wind Turbine Blade.* Wind Energy. (Submitted)

- Hudecz, A., Koss, H. H. and Hansen, M. O. L. (2013). *Icing Wind Tunnel Tests of a Wind Turbine Blade.* Wind Energy. (Submitted)

- Hudecz, A., Koss, H. H. and Hansen, M. O. L. (2013). *Ice Accretion on Wind Turbine Blades.* In XV. International Workshop on Atmospheric Icing on Structures, St-Johns, Newfoundland, September 8 to 11, 2013. (Oral presentation)

- Hudecz, A., Hansen, M. O. L. (2013). *Experimental Investigation of Ice Accretion on Wind Turbine Blades.* In WinterWind 2013, International Wind Energy Conference, 12-13. February 2013, Östersund, Sweden (Electronic poster presentation)

- Hudecz, A., Hansen, M. O. L., Koss, H. H. (2012). *Wind Tunnel Tests on Ice Accretion on Wind Turbine Blades.* In WinterWind 2012, International Wind Energy Conference, 7-8. February 2012, Skelleftea, Sweden (Electronic poster presentation)

These papers and posters together describe the core of the work. The dissertation comprises an overall introduction explaining the most fundamental issues and findings of wind energy in cold climates along with three research topics detailed in three separate chapters. Each chapter can be considered as an individual unit, however they cohere in some level. Each of them starts with a detailed introduction to the specific field and a thorough literature study of the recent findings. Some of the results of Chapter 3 and 4 are used in a demonstration of the transformation method presented by Seifert and Richert [1997] in Chapter 5.

Abstract

In cold climate areas, where the temperature is below $0\ ^oC$ and the environment is humid for larger periods of the year, icing represents a significant threat to the performance and durability of wind turbines. It is highly important to have a clear view of the icing process and the environmental conditions, which influence the ice accretion in order to act properly. The PhD study covers relevant issues of icing of wind turbine blades in these areas. The work itself can be divided into two fundamentally different parts. The first part compares different techniques, which can identify icing events based on environmental and meteorological parameters such as temperature, relative humidity and wind speed measurements. A small demonstration was performed with data collected in Nanortalik, in South-Greenland. Based on the results, icing occurs during periods with low wind speed, high relative humidity and subzero or close to freezing point temperatures, during night or foggy/cloudy and thus darker days. Icing might be relevant problem for the operation of wind turbines in the area, therefore when the decision is made to install wind turbines in a specific location, a detailed and dedicated risk analysis has to be carried out.

The other, larger part is the consists of experimental and numerical investigations of the process of ice accretion on wind turbine blades along with its impact on the aerodynamics. The experimental study was performed on a NACA 64-618 airfoil profile at the Collaborative Climatic Wind Tunnel located at FORCE Technology. The aerodynamic forces acting on the blade during ice accretion for different angles of attack at various air temperatures were measured along with the mass of ice and the final ice shape. For all three types of ice accretion, glaze, mixed and rime ice, the lift coefficient decreased dramatically right after ice started to build up on the airfoil due to the immediate change of the surface roughness. With increasing angle of attack the degradation of the instantaneous lift coefficient increases as well. Both the reduction of the lift coefficient and the accumulation of the ice mass are nearly linear processes. It was also seen that the shape and rate of ice is highly dependent on the angle of attack. The largest ice accretion and thus the largest lift degradation was seen for mixed ice tests. The results of the experimental investigation demonstrated that the type of the ice accretion has significant impact on the degree of the reduction of the lift coefficient and ice accumulation has strong negative influence on the flow field around the airfoil.

At the end of each simulation, the shape of the ice profile was documented by contour tracing that was then used during the numerical study. First, the collected profiles and the settings of the wind tunnel were validated by results of a numerical ice accretion model, TURBICE from VTT, Technical Research Centre of Finland. The wind tunnel parameter value, the median volume diameter, was found to be underestimated. However, after correcting the input parameters for LWC and MVD, the rime ice profiles were in good agreement with the results of the numerical modelling. Then, CFD simulations

with Ansys Fluent were carried out to numerically analyse the impact of ice accretion on the flow behaviour and on the aerodynamic characteristics of the airfoil. The trend of the reduction of lift coefficients agrees quite well with the wind tunnel test results, although based on the measured and the numerical lift coefficients of the clean airfoil, the presence of the wind tunnel walls had significant influence on the measurements requiring a correction. A significant change in the flow pattern was observed for all cases and the most significant flow disturbance was caused by mixed ice accretion. It was also shown that the lift coefficient is highly dependent on the angle of attack on which the profiles were collected. Furthermore, it can be concluded that even one hour of ice accretion can significantly reduce the lift coefficient of an airfoil and the angle of attack at which the ice builds up on the surface is highly important.

The final lift curves of rime ice accretion from both experimental and numerical investigation were used in a demonstration of the transformation model of Seifert and Richert [1997]. It was found that the transformed lift curve fits much better to the one from the CFD analysis and the method could be further developed into a very useful aerodynamic coefficient transformation model.

Acknowledgement

The last three years have been a great adventure for me. I learnt a lot about ice and how to survive cold, dark and of course windy places, aka. wind tunnels. I met a lot of very helpful and great people along the way. I am indeed indebted to them for making this three years an unforgettable experience and for ensuring that my PhD work follows the path it was supposed to.

First of all, I am very grateful for all the support and advice of my supervisor, Martin Hansen. Without your guidance and feedback, this PhD work would not have been achievable. Thank you for all the help and assistance. I would also like to thank my co-supervisors, Lorenzo Battisti and Arne Villumsen for their support, and especially to Arne for encouraging me to start a PhD.

I also have to say a huge thank you to Holger Koss, who was a great help during the wind tunnel tests, I am very grateful for our fruitful discussions and all of your feedback and comments. I owe huge thanks to Kasper Jakobsen for all the advice he gave me. It was a great experience to go to Greenland together, especially when you managed to lose me in the middle of nowhere between Assaqutaq and Sisimiut. Nice try, but you could not get rid of me:)

I am very thankful to LM Wind Power for lending me my beloved NACA 64-618 profile, which was the star of my PhD. Special thanks to Force Technology for letting me to use their unique facility. Thanks to Klaus, our helpful technician, who managed to follow my rather messy instructions (presented in Danish) and produced the rig, so it was possible to actually place the airfoil in the tunnel. I am very grateful to VTT and the people there, Jeroen Dillingh, Ville Lehtomäki, Ville Turkia, Saara Huttunen, Thomas Wallenius, Petteri Antikainen and Saygin Ayabakan, who helped me with TURBICE and welcomed and accommodated me during my stay in Espoo. It was a great experience to be among so many people who are also dealing with ice on wind turbines a a daily basis. Thank you all for the great discussions, ideas and comments not only during my visit but also before and since then.

I also have to thank my dear colleagues here at ARTEK for the four years I spent with them, and for the cakes, the laugh and the fun we had. Special thanks to Sandra and Sonia for being such good friends. I will miss our talks and lunches together. I am also thankful to Neil Davis for the discussions and feedback and also for taking the time to read my thesis before submission. Thanks for the great comments.

Last but not least, I would like to thank my family for their constant love, encourage-

ment and support. Nagyon szeretlek titeket! I am the most thankful to my beloved (and extremely patient) Ati, who encouraged me and was at my side all the way, occasionally got frozen in the wind tunnel and was (and still is) the source of energy and love.

I have met so many people during this three years, who helped a lot and were inspiration, that I could probably fill up a few more pages with acknowledgement. So for all of you:

Köszönöm! Thank you! Tusind tak! Kiitos! Danke schön! Grazie!

Contents

Abbreviations

AOA Angle of Attack

CBH Cloud Base Height

CC Cold Climate

CWT Climatic Wind Tunnel

IC Icing Climate

LTC Low Temperature Climate

LWC Cold Liquid Water Content

MVD Median Volume Diameter

Nomenclature

α Angle of attack $[^o]$

α_1 Collision efficiency

α_2 Collection efficiency

α_3 Accretion efficiency

A_i Number of indication per hour

ar Aspect ratio

B Force transducer cross talk-matrix

β Prandtl-Glauert compressibility parameter

c Chord length

C_D Drag coefficient

C_L Lift coefficient

δ_0 Lift interference parameter associated with stream direction

δ_1 Lift interference parameter associated with streamline curvature

$\triangle C_D$ Incremental correction of liftdrag coefficient

$\triangle C_L$ Incremental correction of lift coefficient

e_0 Water vapour pressure at freezing point [hPa]

$e_{w,i}^s$ Saturated water vapour pressure [hPa]

ϵ_B Blockage factor

Exc Excitation factor

G Ratio of corrected to uncorrected kinetic pressures

GFx Power amlifier's gain

g Gravitational constant $[m/s^2]$

h Height of the tunnel

K_s Sand grain roughness

$L_{v,s}$ Latent heat of sublimation $[Jkg^{-1}]$

m weight $[kg]$

M_∞ Mach number of undisturbed tunnel-stream

A Cross sectional area

F_y Normal force [N]

Ω_s **and** Ω_w Blockage factor rations

$\triangle P$ Pressure measured by the Pitot tube during wind tunnel testing [mb]

P_{atm} Atmospheric pressure of the day [mb]

E_s Vapour pressure [mb]

ρ Air density $[kg/m^3]$

R_v Gas constant for water vapour $[K^{-1}kg^{-1}]$

RH Relative humidity [%]

$RH_{w,i}$ Relative humidity based on the water pressure and the saturated water pressure

R_i Ice rate $[g/mh]$

Re Reynolds number

T Air temperature

T_0 Freezing point temperature in [K]

T_d Dew point in [K]

T_i Indication time during measurement period

T_{tot} Length of measurement period

t_a Ice accretion time [min]

U Wind speed $[m/s]$

V Particle velocity relative to the airfoil

w Mass concentration of the water droplets in air

Chapter 1

Introduction

Due to the ambitious targets on increasing the use of renewable energy sources and the lack of conventional sites, non-conventional sites, e.g. cold climate (CC) sites are getting more attractive to wind turbine installations. Deployment of wind energy in CC areas is growing rapidly. The installed wind power capacity at the end of 2012 was around 69GW, which corresponds to approximately 24 % of the total (globally) installed capacity (Navigant Research [2012]).

In cold climate areas, structures such as wires, electrical cables, meteorological masts, and wind turbines are exposed to severe conditions. At sites with temperatures below 0^oC and a humid environment for larger periods of the year, icing represents an important threat to the durability and performance of the structures. These conditions can be found in sub-arctic or arctic regions, for example in the Nordic countries in Europe, Canada, Greenland, and in high altitude mountains, e.g. in the Alps. Special case is the aerodynamic degradation of aircraft and helicopters during flight (Tammelin et al. [1998], Baring-Gould et al. [2011]).

The performance of an iced wind turbine degrades rapidly as ice accumulates. Ice can cause decreased performance of the turbine and excess vibration problems from uneven blade icing or irregular shedding of ice from the blades. It can add significant mass to the blades, causing changes in natural frequencies and increase of fatigue loads. It can also cause inefficient control hardware, such as anemometers and wind direction sensors during both wind assessment and turbine operation. It can also increase the noise level and the risk of fatigue on wind turbine foundation. There is also a high risk of ice throw, see an example in Figure 1.1c, which can be dangerous for the maintenance personnel and the nearby structures (Battisti et al. [2006], Laakso et al. [2009], Baring-Gould et al. [2011]).

Aside from the many challenges and issues, which have to be faced in relation to wind energy projects, there are technical benefits at these sites as well. Wind speed rises with approximately 0.1 m/s per 100 m of altitude in the first 1000 m. It was also shown that in these sites, the available wind power can increase by more than 10 % because of the higher air density at lower temperatures (Fortin et al. [2005]).

(a) Wind turbine operating in cloud (MPR Photo /Mark Steil).

(b) Wind turbine operating at high altitude (from $http://www.cbc.ca/$).

(c) Ice shedding from a wind turbine (photo credit: Andrea Vignaroli).

Figure 1.1: *Examples of wind turbines operating in cold climate areas.*

In Figure 1.1, three typical cold climate related scenarios are shown. In Figure 1.1a, a wind turbine is standing in foggy, in-cloud environment, Figure 1.1b shows a wind turbine at a hill side during winter time whereas in Figure 1.1c, ice sheds off the iced rotor blade. During the scenarios shown in Figure 1.1a and b, ice formation on structures is very likely.

1.1 Cold Climate

In the context of wind energy, the term *cold climate* refers to conditions favourable for the formation of atmospheric icing, or temperatures lower than the operational limits of standard wind turbines. As conditions can vary significantly from site to site, it is challenging to describe a typical cold climate site. According to the Germanischer Lloyd Wind Energy GmbH [2009],a cold climate site can be describe as the following:

"If minimum temperatures of below -20ºC have been observed during long term measure-

ments (preferably ten years or more) on an average of more than nine days a year or a yearly mean temperature of less than 0 °C, the site is defined as a cold climate site. The nine-day criteria are fulfilled, if the temperature at the site remains below -20ºC for one hour or more on the respective days. In this case, it has to be counted on special requirements for the wind turbine and the wind turbine shall be designed for cold climate conditions.”

While it is possible, active icing rarely occurs below that low temperature. At some sites, there might be low temperatures, but almost no atmospheric icing events and at other sites, the annual average temperature might be mild but heavy icing of the turbines occurs on a regular basis. Based on many years of experience with operation of wind turbines in such sites, a definition was drawn up by IEA Wind, Task 19 Wind Energy in Cold Climates saying that cold climate sites are areas where there are periods with temperature below the operational limits of standard wind turbine, defined as Low Temperature Climate (LTC) or icing events occur, as Icing Climate (IC) (Baring-Gould et al. [2011]). A graphical illustration of the definitions can be seen in Figure 1.2. Based on these definitions, the description of cold climate given by Germanischer Lloyd Wind Energy GmbH [2009] corresponds to LTC.
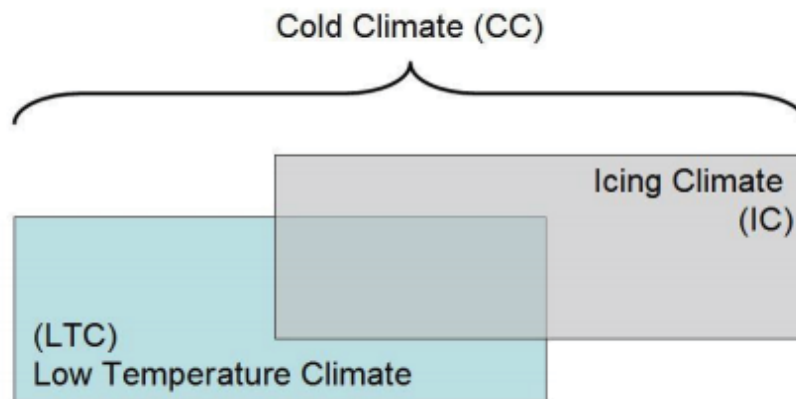
Figure 1.2: *Definition of cold climate along with low temperature climate and icing climate (Baring-Gould et al. [2011]).*

In LTC, extremely low temperatures can occur, which are often caused by clear sky radiation associated with high pressure zones and sometimes high altitude during winter time. In such sites, the operation and maintenance of wind turbines can be seriously affected by the low temperatures. IC is associated with atmospheric icing, which can have detrimental effects not only on wind turbines, but also on the meteorological instruments, such as anemometers and wind vanes (Baring-Gould et al. [2011]).

Typically, there are two types of atmospheric icing, which affect wind turbine operation, in-cloud icing (rime, glaze and mixed ice) and precipitation icing (e.g. freezing rain and wet snow) (ISO 12494 [2001], Tammelin et al. [2005]). In-cloud icing occurs when the air temperature is subzero and the cloud base is less than the site elevation. The physical and mechanical characteristics of the accreted ice depend on different meteorological and

atmospheric parameters, such as the air liquid water content (LWC), median volume diameter (MVD), air temperature, relative humidity, wind speed, atmospheric pressure and air density. It can either form rime ice or glaze ice or the mixture of these two types, further referred as mixed ice, on the surface of the wind turbine blades, see examples in Figure 1.3.

Rime ice

In case of rime ice, the water droplets freeze completely when they impact the surface. It is white, opaque, and relatively streamlined accretion formed by supercooled fog or cloud droplets. Rime ice is likely formed in strati-form clouds. The droplet size is 30 μm. It is typical at low temperatures, $-4\ ^oC$ to $-12\ ^oC$. In soft rime icing, the density of the accretion is 100-600 kg/m^3 and it has a feathery appearance. Hard rime ice's density is 600-900 kg/m^3 and the accretion has a comb-like appearance (Bose [1992], ISO 12494 [2001]).

Glaze ice

A combination of warmer temperatures than in case of rime ice accretion, higher wind speed and/or high water content, makes glaze ice accumulate on the surface. In glaze icing, not all of the water droplets, which impinge the surface, freeze immediately, hence some ran off following the streamlines towards the trailing edge where they might freeze. Glaze ice forms likely in cumuli-form clouds, and typically at relatively high air temperature, between 0 ^oC and -4 ^oC. The droplet size is 0-100 μm. It normally has a smooth, transparent, and glassy surface and high density, close to 900 kg/m^3. Glaze ice is more difficult to remove due to its inherent physical properties and higher adhesion pressure (Bose [1992], ISO 12494 [2001]).

Mixed ice

Mixed ice is the mixture of glaze and rime ice. It can form in an icing environment when the temperature is decreasing. Ice particles become embedded in glaze ice forming rough deposits (Advisory Circular [1996]), therefore it has the classic glaze characteristics in the vicinity of the stagnation line and rough, rime-like ice on both side of the stagnation zone (Addy [2000]).

1.2   The process of icing

Ice can accumulate on surfaces due to the supercooled water droplet content of the air. The icing process itself can be divided into three parts; collision, collection and accretion of water particles. The incoming water can either freeze on the surface, rush aft, evaporate, shed or stand depending on the local thermal and fluid dynamic conditions. The ice accretion is a time dependent mechanism and the rate of ice mass can be described as (Makkonen [2000]):

$$\frac{dM}{dt} = \alpha_1 \alpha_2 \alpha_3 wVA \tag{1.1}$$

Where w is the mass concentration of the water droplets in the air. V is the particle velocity relative to the airfoil and A is the cross-sectional area. α_1, α_2 and α_3 represent

(a) Rime ice accretion on a wind turbine (Tam- (b) Glaze ice accretion on a wind turbine ($http :$
melin et al. [1998]). $//www.fundysolar.com/$).

Figure 1.3: *Examples of wind turbines operating in cold climate areas.*

the collision, collection and accretion efficiencies, respectively. These three correction
factors, which have a value between 0 and 1, may reduce the rate of ice mass from its
maximum. α_1 represents the ratio of the flux density of the particles, which actually hit
the airfoil, to the maximum flux density. It is always smaller than 1, since the very small
particles tend to be carried away by the flow and thus they do not impinge. As the air
speed and the droplet size increases, α_1 increases as well. α_2 is the ratio of the flux density
of the collided particles that stick to the surface to the flux density of the particles that
impinge. E.g. since dry snow tends to bounce off the surface, $\alpha_2 \simeq 0$ (Makkonen [2000]).
α_3 represent the ratio of the rate of icing to the flux density of the stuck particles. All
the impinged water droplets freeze on the surface in case of rime ice, thus for that type
of ice, $\alpha_3 = 1$.

Depending on the MVD, LWC, wind speed and air temperature, glaze, rime or mixed
ice can form on the structures. Icing usually occurs, between 0 and -20^oC, because
below this temperature, the liquid water droplets tend to freeze and form snow in the
cloud. Figure 1.4 shows the distribution of observed icing cases as a function of the air

temperature (from Battisti [2008]).
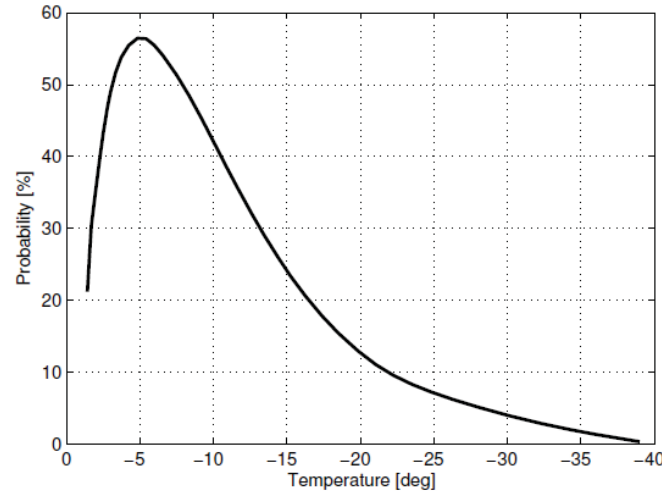
Figure 1.4: *Probability of ice formation as a function of air temperature. As temperature decreases the probability decreases as well because more and more liquid water droplets freeze as temperature drops (figure from in Battisti [2008]).*

The air speed not only influences the ice type (see Figure 1.5 from ISO 12494 [2001]) but also its amount. The collision efficiency is dependent on the wind speed. Although, MVD and LWC are the two most important parameters in modelling the icing process, neither of them can be measured accurately currently. MVD has a direct effect on the collision efficiency, since the larger droplets are less affected by the local aerodynamic forces and therefore more likely hit the object than the small ones (Gent et al. [2000]). It is also seen that larger droplets most likely form glaze ice (ISO 12494 [2001]). For higher LWC, the latent heat is larger as well, therefore not all the water droplets can freeze on impact and hence glaze ice forms. As temperature drops, the LWC decreases as well, which leads to rime ice formation (Gent et al. [2000]).
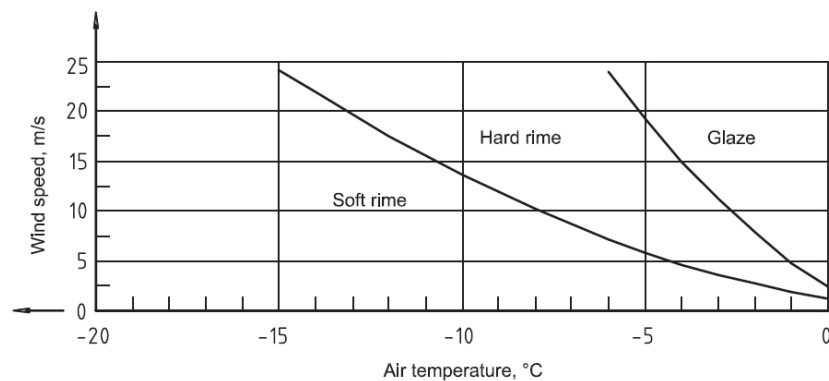
Figure 1.5: *Type of accreted ice as a function of wind speed and air temperature (ISO 12494 [2001]).*

1.3 Anti-icing and de-icing systems

Depending on the accretion time, the severity of icing and the wind resources, one could either do nothing and just accept the possible power losses or act and use ice protection systems. Ice protection can be either anti-icing or de-icing. Anti-icing system prevents any ice accumulation on the airfoil, whereas de-icing system is used to remove ice, which has accumulated. Both systems can be either passive or active (Parent and Ilinca [2010]). Passive solutions, such as hydrophobic coatings or blade painting change the physical properties of the airfoil's surface. Whereas active solutions use special systems, e.g. blade heating to remove or prevent icing.

Both Kraj and Bibeau [2006] and Fortin and Perron [2009] concluded that a combination of passive anti-icing, e.g. icephobic surface coating together with active thermal de-icing would likely provide solution. However currently, there are not any reliable surface coating available on the market.

1.4 Scope of the work

In order to describe whether icing is relevant at a specific site and thus estimate the possibilities of icing of wind turbines, it is important to understand the physical process of how ice accumulates on the blades and how environmental variables, such as humidity, temperature, wind speed, droplet size and liquid water content, influence the ice type formation on the blades. As it was shown in several studies (e.g. Bragg et al. [2005]), ice accretion has immediate effect on the operation of wind turbines. It is crucial to know how the aerodynamic properties react to the changes in the early phase of icing. Hence, it is possible to get information on its severity and the need of mitigation techniques.

The PhD study was carried out between 15. November 2010. and 14. November 2013. at Department of Wind Energy, Technical University of Denmark. As part of another ongoing wind resource investigation project, it was possible to install ice rate sensors in Greenland to study icing potential. The aim was to study the meteorological and climatic conditions based on collected data, such as air temperature, relative humidity or wind speed, when the ice sensor indicated icing. There are also direct and indirect methods using the collected meteorological information to identify icing periods, which could be compared to the periods shown by the ice rate sensors. This part of the work attempted to study icing risk in South Greenland by employing different techniques.

Experimental and numerical investigation of ice accretion on a NACA 64-618 profile made up a large part of the work. Wind tunnel tests were performed to investigate how ice accumulates for moderately low temperatures on an airfoil and how the aerodynamic forces are changing during the process of ice build-up. The tests were performed at the Collaborative Climatic Wind Tunnel located at FORCE Technology, in Kgs. Lyngby, Denmark. The aerodynamic forces acting on the blade during ice accretion for different angles of attack at various air temperatures were measured along with the mass of ice and the final ice shape. The collected ice shapes were further numerically analysed. First, they were validated by comparing the results to the output of the numerical ice modelling program, TURBICE from VTT, Technical Research Centre of Finland. Then simulations

with Ansys Fluent were conducted to analyse the impact of ice accretion on the flow behaviour and the aerodynamic characteristics of the iced airfoil at different wind speeds.

The paper of Seifert and Richert [1997] is very often cited. This paper contains very promising iced lift curve transformation method, which is tested during the PhD study and the results are compared to the outcome of the experimental and numerical investigation.

Chapter 2

Risk of icing in South-Greenland for wind energy

Remote locations all over the world are facing similar issues when it comes to power sources. The scattered cities and villages and also the isolated research stations (e.g. Summit Station in Greenland or McMurdo Station in the Antarctica) do not have direct connection to central infrastructure, such as pipelines and electricity grids. Historically, diesel and other fossil fuel based generators provided the only feasible solution in the past. However, increasing fuel costs and the worldwide ambitions to reduce the use of these energy sources led to a greater reliance on local and sustainable forms of energy (IEA-RETD [2012]).

Greenland's many small village communities with their own local electrical grids and the large geographical distances mean that the cost of energy production varies widely. In larger cities, such as Nuuk or Qaqortoq with a relatively high consumption and access to hydro-power, the cost of energy is lower, whereas in small, remote villages, it can be extremely high.

The electrical grid system of Greenland is built of small and isolated grids where almost each single town or village is responsible for its own power supply. They usually are not connected to each other due to the great distance, hence there is no central grid. This structure results in high cost of backup capacity, energy storage and fuel transport (Villumsen et al. [2009]). Energy storage in the small isolated villages is a large challenge, because the consumption usually is much lower than e.g. the energy production of a modern wind turbine.

In the recent years, to fulfill the renewable energy usage targets and to reduce the dependency of diesel fuel, the possibilities of implementing wind turbines into the already existing energy system have been investigated. Since the yearly mean temperature in Greenland is approximately $-1^{o}C$, it can be considered as cold climate site according to the definitions of Germanischer Lloyd Wind Energy GmbH [2009]. Icing is worthy of investigation to determine the threat to structures and wind turbines. Therefore as a part of the project ice rate sensors were installed in two locations in South Greenland to learn more about the relevance of icing events.

2.1   Introduction to risk of icing in Greenland

Since most parts of Greenland can be classified as cold climate locations, icing potential should be investigated before installing wind turbines. However, there have been no reports of detrimental icing of power lines or other structures in the inhabited areas. In Figure 2.1, a 6 kW Proven wind turbine can be seen, which was installed at Summit Station, in the middle of the icecap in Greenland. The severity of the rime icing was unexpected[1]. It accreted during very light wind periods, when the turbine was not operation and therefore could not shed of the particles.

Figure 2.1: *Iced 6kW Proven turbine at Summit Station,*
in Greenland. This level of icing reduces power output by
80 % or greater. (Dahl [2009])

Historically, the towns are located in sheltered places in Greenland, i.e. wind speed is quite moderate. If wind energy were introduced into the local power system, the turbine(s) would probably be located at elevated sites, where the wind resources are more favourable. These sites are not as sheltered, therefore the structures will likely have to withstand harsher environmental conditions, especially during winter.

An example of a small vertical axis wind turbine can be seen in Figure 2.2. The photo was taken at one of the relay stations of TELE Greenland by one of the employees. TELE Greenland took the initiative to implement renewable power sources to their diesel fuel based systems in order to reduce the rapidly increasing costs. Solar panels were installed at most of their stations and the possibility of installation of smaller wind turbines were also investigated. Despite the expectations, these turbines were not functional during

---

[1]Tracy Dahl, e-mail correspondence 11. January 2013

winter due to the massive amount of ice, which accreted on them, as it is seen in Figure 2.2.

Figure 2.2: *A small vertical axis wind turbine located at one of the relay stations in Greenland (photo credit: TELE Greenland).*

These examples indicate that icing is a real treat to wind turbines in Greenland, and therefore thorough investigation of the icing potential is needed as an additional feature to the wind resource studies. In 2003, Nordic Energy Research, ECON (Denmark) and Institute for Energy Technology (Norway) started a project on establishment of community-based renewable energy and hydrogen (RE/H_2) systems in the West Nordic Region. As a part of this project, wind energy monitoring was carried in Nanortalik, South Greenland. For this purpose a 50 m tall meteorological mast was erected in the town (Ulleberg and Moerkved [2008]). The station was collecting data for four years, and it was reported that only 2 % of data was missing due to icing (Aakervik [2011]). An icing event was indicated, when 5 or more consecutive wind direction measurements in a 10 minutes period were identical and the temperature was below 3 ^oC Laakso et al. [2009]. This means, that the wind vanes were iced as a block and they were not able to move.

In 2011, Arctic Technology Center at Technical University of Denmark took over the operation of the station and expanded the investigated area by installing another meteorological mast at a top of a nearby mountain (see locations in Figure 2.3). Both stations were upgraded the following year. The installation included e.g. different wind speed and direction sensors, humidity and temperature sensors and a dedicated ice rate sensor.

Figure 2.3: *Location of the stations in South-Greenland. One of the stations is located at sea level on the island of Nanortalik whereas the other one is on the top of a hill approximately 900 m above sea level on the nearby island, Sermersooq.*

However, it is difficult to detect icing and its severity. There are different direct and indirect techniques to identify icing events (Carlsson [2009]). Direct techniques are e.g. cameras and ice detectors. Indirect technique is to investigate the climatic and meteorological variables collected from the studied sites, such as wind speed and direction, temperature, relative humidity, air temperature and if available dew point and cloud base height. Using these parameters, it is possible to estimate the existence of icing (Fikke et al. [2006]). Figure 2.4 shows clear difference between the two different types of icing event, i.e. meteorological and instrumental icing. Meteorological icing is a period when meteorological conditions favour ice build-up, whereas during instrumental icing, instrument and structures are covered by ice and icing has detrimental effect on their functioning (Baring-Gould et al. [2011]).
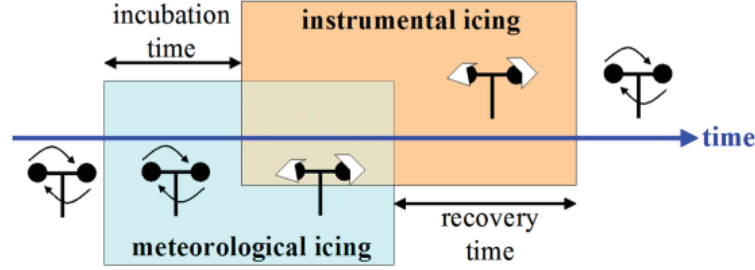
Figure 2.4: *Different stages during the icing of meteorological instruments or other structures (Cattin [2012]).*

2.2 Techniques to identify icing

Relative humidity and temperature

Temperature itself cannot identify icing events, however it shows the potential of occurrence. Although, combining temperature and relative humidity measurement is a well established method, as theoretically icing takes place when relative humidity of water vapour is around 100% (Laakso et al. [2009]). When the temperature is subzero and the humidity is high, above 95 %, it is very likely that ice builds up on the surfaces (Parent and Ilinca [2010]).

Cloud base height and temperature

As wind turbines are getting taller and they reach the clouds more often (see an example in Figure 1.1 a) and since it is shown that in-cloud icing is one of the most common type of icing (Tammelin et al. [1998]), cloud base height (CBH) is a very important parameter. It is possible to measure cloud base height directly with ceilometer. Usually, this information can be retrieved from a nearby airport. If it is not available, there is an empirical method to calculate it based on dew point. Similarly to the cloud base height, it is possible to measure dew point directly or to derive it from relative humidity and temperature (T_d, see eq. 2.1). When the height of the cloud base is lower than 100 m and temperature is subzero, it is very likely that icing occurs.

$$T_d = \frac{1}{\dfrac{1}{T_0} - \dfrac{R_v}{L_{v,s}} ln(\dfrac{e^s_{w,i} RH_{w,i}}{100 e_0})} \tag{2.1}$$

Where T_0 is the temperature in K at freezing point (273.16 K), R_v is the gas constant for water vapour (461.51 $K^{-1}kg^{-1}$), $L_{v,s}$ is the latent heat of sublimation ($2.83 x 10^6 Jkg^{-1}$), $RH_{w,i}$ is the relative humidity based on the water pressure and the saturated water pressure, e_0 is the water vapour pressure at freezing point (6.1078 hPa) and $e^s_{w,i}$ is the saturated water vapour pressure:

$$e^s_{w,i} = e_0 e^{\frac{L_{v,s}}{R_v}(\frac{1}{T_0} - \frac{1}{T})} \tag{2.2}$$

The cloud base height can be found as (Carlsson [2009]):

$$CBH = 125(T - T_d) \tag{2.3}$$

Where T is the air temperature at the ground.

Wind speed monitored by heated and unheated anemometers

Comparing the results of an unheated and heated anemometer is a very simple but rough estimation of icing. It is not possible to estimate the amount of ice, which builds up on the sensors with this technique. If the output of the two sensors is different, it can be assumed that ice accreted on the unheated one. The unheated anemometer could either show lower wind speed than the heated one or be completely frozen and give values close to zero (Ilinca [2011]). There is not any standard on the difference between the two outputs, but the literature suggests values from 5 % to 20 % (Parent and Ilinca [2010]). An estimate of the standard maximum error between the two anemometers can be found by investigating the differences in the data from summer period when icing is unlikely to occur.

Frozen anemometer

If there are not any heated anemometers installed on the meteorological station, icing events could be identified by low temperature and very slow or stand still anemometers. This is, however, an underestimation of the icing potential, since ice build-up does not necessary stop the instruments completely.

Wind vanes

It is thorough to install both heated and unheated wind vanes not only to identify the icing periods but also to be able to monitor the wind direction during icing event when the unheated instruments might be malfunctioning. If there are big differences in the wind direction measured by the two sensors, it might be due to icing. If there is only unheated wind vane installed on the meteorological mast, it can be assumed that the equipment is iced, when five or more consecutive wind direction measurements in a 10 minute series are identical and the temperature is subzero [Aakervik, 2011]. This method only provides an information about the period when significant amount of ice sticks on the surface and the wind vanes are not able to turn. This gives underestimation of the icing period because even a very small amount of ice has large effect on the performance of the sensors [Laakso et al., 2009]. However, if the STD is zero for longer period due to low wind speed, this method could, in the contrary, overestimate the icing event.

Cameras

In the last couple of years, the quality of the images has improved significantly hence cameras can capture icing events quite well on stand still structures [Cattin, 2012]. If the camera is installed on a meteorological mast and pointing towards one of the instruments, it can give a good solution to capturing icing periods.

In case of monitoring icing of wind turbine blades, the cameras can be placed either on the spinner of the rotor or on the nacelle. In case of the first method, the camera captures the same blade and rotates along with it and hence it is exposed to harsh weather conditions. Due to the flat angle of view, it could be difficult or even impossible to see the tip of

the blade. In case of placing the camera on the nacelle, the blade is captured by motion detection when it appears in the image. The camera is less exposed, but it is neither the same blade on the images nor possible to see the whole blade either. During nights and foggy periods, when icing is more likely, the quality of images decreases dramatically. Another disadvantage of using digital cameras is the lack of automatic processing.

Ice detectors

Currently there are several types of ice detectors on the market (see Homola et al. [2006]), but none of them are reliable for heavy icing conditions. Changes of some properties, such as mass, reflective properties or electrical/thermal conductivity (Ilinca [2011]) can be detected by sensors.

In Nanortalik, an optical ice detector, a HoloOptics T44 ice rate sensor, which emits infra-red light towards a reflective surface, was installed in 2011. It interprets variations between emitted light and light received by the photo sensor (HoloOptics manual). The main parts of the HoloOptics T44 are four arms and a probe. The arms contain an IR emitter and a modular detector. The probe has a reflective surface that can reflect the radiation emitted by the arms back to the detectors as long as there is no ice accretion on it (HoloOptics manual). The presence of icing is indicated when an approximately 0.01-0.03 mm thick ice layer covers the 85-95 % of the probe surface. In that case, internal heating turns on and de-ices the sensor. The sensor monitors the number of indications and also the time necessary for de-icing, which could give good information about the ice rate, R_i (g/mh). Based on the number of indications:

$$R_i = 0.76e^{0.027*Ai} \tag{2.4}$$

Where A_i is the number of indications per hour. And based on the indication time:

$$R_i = 0.94 * e^{7.6*T_i/T_{tot}} \tag{2.5}$$

Where T_i is the indication time during the measurement period and T_{tot} is the measurement period length (recommended to be 3600 s).

2.3 Sites and installations

The two sites where the meteorological masts were installed are shown in Figure 2.3. Two data collecting periods can be distinguished at the test site in Nanortalik. In the first period, the data was collected with the old set-up as a part of the 'Vest-Nordensamarbejde' project, whereas in the second period, the data was collected with the new set-up, which was installed in summer of 2012. However, in 2011 when the 'Vest-Nordensamarbejde' project ended and DTU overtook the operation of the mast, a HoloOptics ice rate sensor and a relative humidity sensor were added to the old set-up as an additional feature. Before that, the humidity data was provided by the nearby heliport's station. This station also provides 10 minutes data series and due to the relatively flat landscape and the short distance between the two locations, no corrections are necessary. The installed instruments are listed in Table 2.1 for both set-ups.

Table 2.1: *Set-up of the meteorological mast installed in Nanortalik, South Greenland.*

Old set-up		
Type	Brand	H (m)
Anemometer	NRG 40	48.8
Anemometer	Risoe P2546A	48.8
Anemometer	NRG 40	30
Anemometer	NRG 40	10
Anemometer	NRG HAE IceFree 3	43.8
Wind vane	NRG HVE IceFree 3	40.8
Wind vane	NRG 200P	41.4
Air temp.	NRG 110S	3
Humidity	RH5X	3
Ice rate sensor	HoloOptics T44	4

New set-up		
Type	Brand	H (m)
Sonic anemometer	Metek Usonic 3D Heated	50
Anemometer	Risoe P2546A	49
Wind vane	NRG 200P	49
Anemometer	Risoe P2546A	30
Anemometer	Risoe P2546A	10
Wind vane	NRG 200P	10
Pyranometer	Hekseflux LP02-05	5
Ice rate sensor	HoloOptics T44	5
Air temp.	NRG 110S	3
Air temp.	Vaisala HMP155	3
Humidity	Vaisala HMP155	3
Humidity	NRG RH-X5	3
Potential temp.		48.5-5m

The top of a mountain in the nearby island, Sermersooq was chosen based on information on possible icing events from the local telecommunication company, TELE Greenland that has a relay station located there and hence it was possible to get assistance from them during both installation and operation. There were also two different set-ups installed at this test site. In the first year a smaller, 4 m tall mast was erected with the purpose to see whether icing was a real treat there. The connection to the station was lost in February 2012 and it turned out that the set-up was destroyed during a winter storm, see photos of the set-up after installation and after winter in Figure 2.5 a and Figure 2.5 b, respectively. In the summer of 2012, a tower with an extension to 10 m was installed with extra guy wires added for security, but this setup also could not withstand the harsh winter.

Table 2.2: *Set-up of the meteorological mast installed at Sermersooq, South Greenland.*

Old set-up			New set-up		
Type	Brand	H (m)	Type	Brand	H (m)
Anemometer	NRG 40	4	Anemometer	NRG 40	10
Anemometer	Risoe P2546A	4	Anemometer	Risoe P2546A	10
Wind vane	NRG 200P	4	Wind vane	NRG 200P	10
Wind vane	NRG 200P	4	Wind vane	NRG 200P	10
Air temp.	NRG 110S	2	Air temp.	NRG 110S	3
Humidity	RH5X	2	Humidity	RH5X	3
Ice rate sensor	HoloOptics T44	3.5			

(a) Photo of the first set-up was taken in summer 2011.

(b) Photo of the first, destroyed set-up in spring 2012 (photo credit: TELE Greenland).

Figure 2.5: *Photos of the first set-up at Sermersooq, in South Greenland.*

As it can be seen from Table 2.1 and Table 2.2, ice rate sensor was installed at both sites, but unfortunately all of them got destroyed probably due to voltage fluctuation and thus overheating or lightning (see Figure 2.6). This instrument was chosen due to the way it indicates icing and the fact that it can also give information about the severity of the icing events (HoloOptics manual). In 2012, when the met mast in Nanortalik was upgraded, a new and more robust version of HoloOptics T44 was installed, but despite of the high expectations, this instrument did not survive the winter either. Therefore a final conclusion based on the direct technique to identify icing events could not be drawn.

(a) Photo of the HoloOptics ice rate sensor after installation in summer 2011.

(b) Photo of one of the arms and the connector of HoloOptics ice rate sensor in summer 2012.

Figure 2.6: *Photos of HoloOptics ice rate sensor installed in South Greenland in summer 2011.*

2.4 Data analysis

A demonstration of the previously described techniques are given in this section. The analyses are based on the first winter of data collection from the meteorological station with the old set-up from 2007-2008. Although, investigation of the wind resources were already performed as part of the Vest-Norden project (Aakervik [2011]), very small consideration of the influence of ice on the data was taken. Since the raw data was available, a detailed analysis was possible under the scope of the PhD work. The first year data was studied because the instruments were not changed or updated during the measurement campaign, which could have led to their malfunctioning and wrong measurements. The ice rate sensor was installed in a later point, therefore those data will be separately discussed.

2.4.1 Icing in winter of 2007-2008

The studied ice period started on 1. October 2007 and finished on 31. April 2008. During the summer months icing is unlikely and therefore these months are neglected. The earlier described, five different methods are used here. Numbers of daily icing hours during each months are plotted in Figure A.1-A.6 in Appendix A.

Relative humidity and temperature

Icing is very likely to occur at low air temperature and high humidity. The threshold of relative humidity was set to $RH \geq 95\%$ and of air temperature $T \leq 0^oC$. This method

implied 112 hours of icing in 16 days throughout the investigated 7 months. See plot of the daily icing hours for each month in Figure A.2.

Cloud base height and temperature

In-cloud icing is one of the main reasons for reduction of power production of wind turbines (Tammelin et al. [1998]). Low laying clouds accompanied by low air temperature cause high risk of icing. The threshold of cloud base height was 100 m, which gave 188 hours of possible icing in 29 days. A plot of the daily icing hours for each winter month during the investigated 7 months can be seen in Figure A.2.

Heated and unheated anemometer

This station was equipped with both heated and unheated anemometers, which gave a rare opportunity to compare their output. A standard, $\triangle U = 0.7m/s$ offset was found between the measurements taken by the two different anemometers. If the difference was significantly higher than this offset, icing was likely to happen. The threshold was set to $\triangle U = 1.4m/s$, in order to neglect the small differences caused by the measurement errors or other unexpected issues. There were no conditions set for temperature, because as it was also shown in Figure 2.4, instrumental icing also exists during recovery time, and hence it is possible that the air temperature is above zero and icing is still effecting the measurements in this period. In total, 446 icing hours in 56 days fulfilled this requirement, see Figure A.3.

Frozen anemometer

If an unheated anemometer is frozen and stops, it cannot measure the wind speed. However this scenario rarely happens. With this method, it is not possible to identify the incubation and recovery period, but only the events, when the anemometer was not moving. The unheated anemometer was frozen for 27 hours, in 5 days during the investigated 7 months see Figure A.4.

Wind vane and temperature

As it was explained earlier, the standard deviation of the wind vane measurements could also indicate icing. Due to the error filtering of the data some of the recordings had to be removed and therefore some compromises had to be made. Parent and Ilinca [2010] suggested that the combination of six consecutive 10 minute measurements of zero standard deviation (STD) and subzero temperature implies to the presence of ice on the vanes. In this study, these requirements were changed. A limit of two measurements of zero STD in 30 minutes would raise a flag and minimum six of these indications per day would be considered as icing day. This criteria gave 108 days when icing event might have occurred based on the unheated vane (see Figure A.5) and 17 days based on the heated one (see Figure A.6).

Example - April 2008.

In Figure 2.7, the 10 minute wind speed data for April 2008 is plotted for both heated and unheated anemometers. The earlier mentioned offset is visible on this plot. It can

also be noticed that in the beginning of the month the unheated anemometer was not measuring, i.e. it was probably frozen.
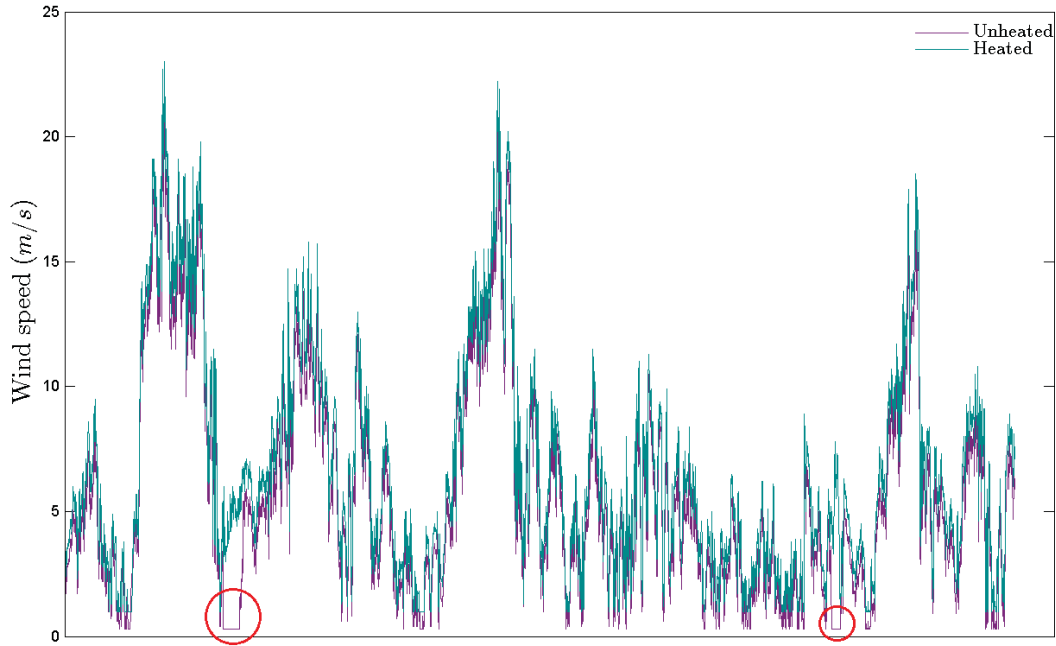

Figure 2.7: *Wind speed based on 10 minutes measurements in April 2008. There are two periods marked with red circles when the unheated anemometer was not taking measurements.*

The suspected period in the beginning of April 2008 is plotted in Figure 2.8. In this figure, 10 minutes wind speed measurements taken by both heated and unheated anemometers along with the air temperature is shown for $5 - 7^{th}$ April 2008. It can be seen that there was quite high wind and relatively warm temperature on the 5th April, but as the wind speed and the temperature decreased on the evening and night of 6th April, it is very likely that ice accumulated on the anemometers, which led to the standstill of the unheated one. Based on these curves, it is possible to clearly identify two stages of icing, which were introduced in the previous section in Figure 2.4, the instrumental icing and the recovery time. The relative humidity and temperature method also suggested icing during this period. The instrumental icing lasted very likely for 17 hours because for that long the difference between the heated and unheated anemometers were above the limit. As it can be seen in Figure 2.9, the relative humidity was high during this period, and when it is combined with subzero temperature, it is favourable for icing. The cloud base height - temperature method suggested 12 hours of icing period on the very same day. Also the heated wind vane standard deviation indicated heavy icing, in total 140, 10-min measurements of zero STD (see A.6).
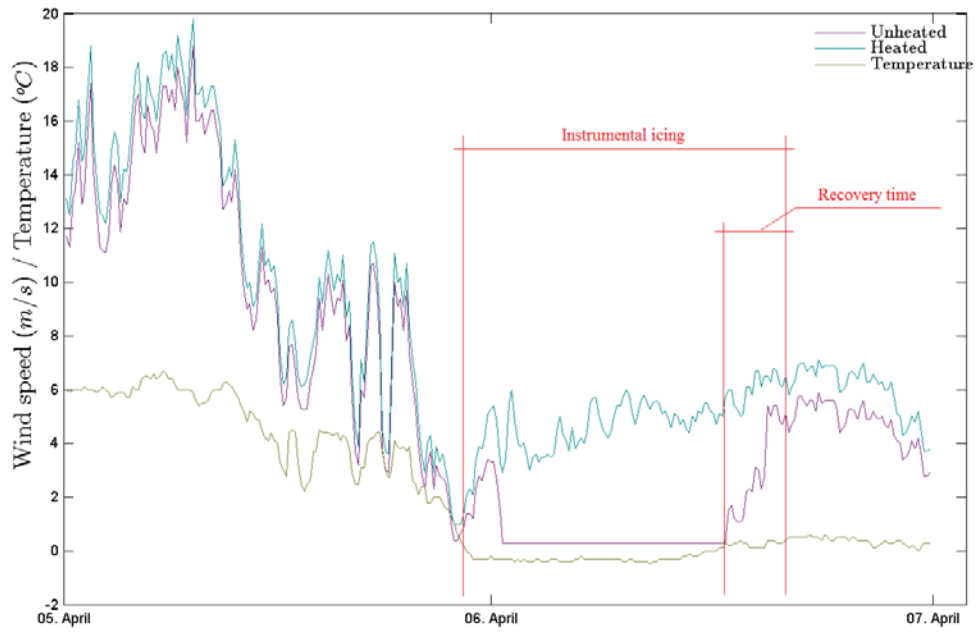
Figure 2.8: *Wind speed based on 10-min measurements along with the air temperature in 5-7th April 2008. Two ice stages are also identified, the instrumental icing and the recovery time.*
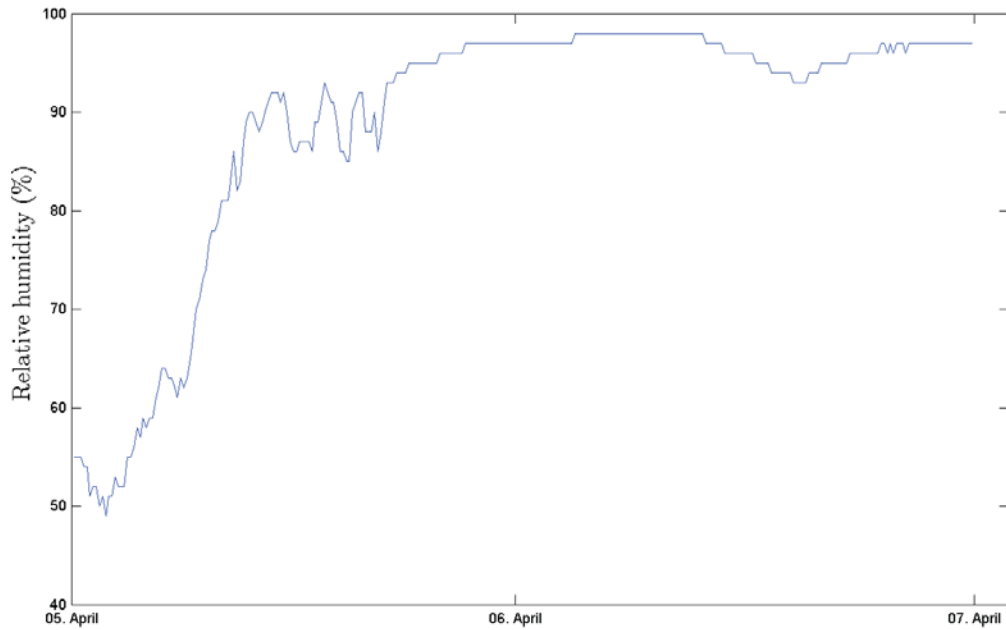
Figure 2.9: *Relative humidity 10-min measurements on 5-7th April 2008.*

2.4.2 Example - Ice sensor

As it was mentioned earlier, there were several attempts to include a dedicated ice sensor, namely HoloOptics ice rate sensor, in the set-up of the meteorological station. However after a few of days of successful measurements, they tend to break. Unfortunately due

to the remote locations, it was not possible to investigate them right after these events therefore it was impossible to find out what had happened exactly.

In the period from 25th November to 28th November 2012, the ice rate sensor indicated icing event several times for longer periods, 9 hours during the evening and night of 25th and 26th and 12 hours during the night of 28. In Table 2.3, the calculated hourly ice rates are summarized for both periods. The ice rate was calculated based on the number of indications per hour using eq. 2.4.

Table 2.3: *Ice rate during possible icing event based on indications of HoloOptics ice rate sensor along with the number of hourly indications.*

| Date	Time (h)	Number of indications	Ice rate (g/mh)
	18:00-18:50	3	0.82
	19:00-19:50	6	0.89
	20:00-20:50	17	1.20
25.11.2012	21:00-21:50	35	1.96
	22:00-22:50	3	0.82
	23:00-23:50	3	0.82
	0:00-0:50	0	0.76
26.11.2012	1:00-1:50	7	0.92
	2:00-2:50	4	0.85
	1:00-1:50	5	0.87
	2:00-2:50	19	1.27
	3:00-3:50	15	1.14
	4:00-4:50	31	1.76
	5:00-5:50	28	1.62
28.11.2012	6:00-6:50	9	0.97
	7:00-7:50	1	0.78
	8:00-8:50	2	0.80
	9:00-9:50	1	0.78
	10:00-10:50	12	1.05
	11:00-11:50	2	0.80
	12:00-12:50	1	0.78

It can be seen in Table 2.3 that more severe icing was indicated during the night of 28th November, therefore 10-min measurements of wind speed, relative humidity and temperature were plotted in Figure 2.10 to see the environmental conditions. It can be noticed that the wind speed was relatively low during the night hours whereas the relative humidity was high. The combination of these two conditions with low temperature makes the environment favourable for ice formation. The highest ice rates ($R_i = 1.76g/mh$ and $R_i = 1.62g/mh$) are found in the early morning hours between 4 and 6 am, when the wind speed was the lowest and the humidity was the highest. It can be also noted that as soon as the wind speed increased, the humidity started to drop and finally the ice accretion stopped.
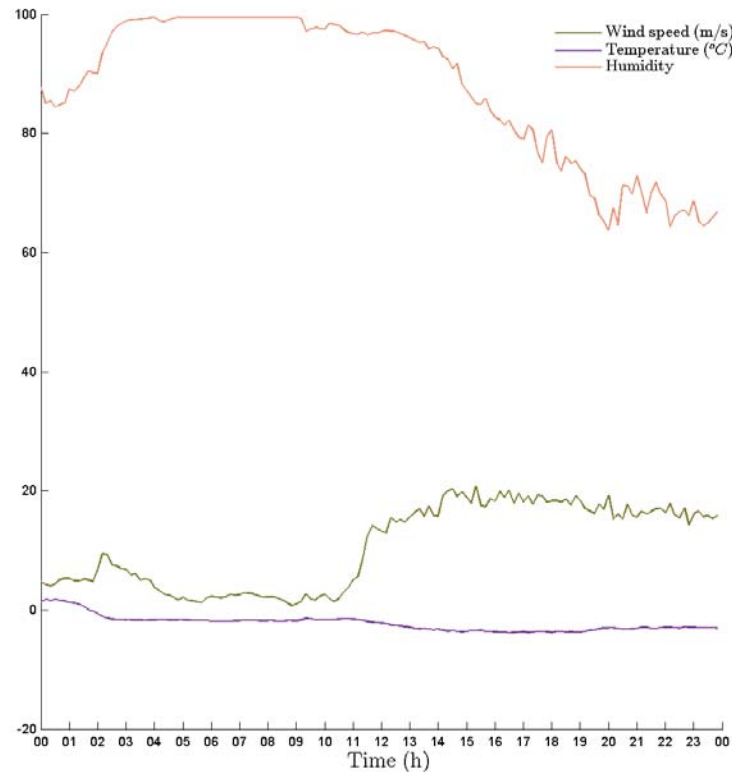
Figure 2.10: *Wind speed, temperature and relative humidity based on 10 minutes measurements in 28. November 2012. When the ice rate sensor indicated icing event, the wind speed and the temperature were low whereas the relative humidity was high.*

2.5   Conclusion drawn from the data analysis

One year of data analysis is not enough to draw a final conclusion on the frequency of icing events in Nanortalik. However, this investigation gave opportunity to study the different techniques. Depending on the used technique, 27, 112, 188 and 446 icing hours were identified during the seven winter months.

It was experienced that none of the above described and used methods is able to precisely capture icing events on its own. However, as it can be seen in the example, a combination of them could give a quite good picture of the process. It was also found that the headed and unheated anemometer method provided the best information about the presence of icing. However with this method, it was not possible to identify the whole length of meteorological icing. In order to do that it was necessary to take a look at the humidity and temperature measurements, which also indicated conditions favourable for icing. According to the recommendation of Baring-Gould et al. [2011], fully heated instruments are needed at sites, which are prone to icing.

Ice sensors could provide a good alternative, but currently none of them works perfectly. There were two HoloOptics ice rate sensors installed in Nanortalik and at the summit on Sermersooq in 2011, but none of them survived the harsh winter conditions. A second

attempt was made in 2012, when a more robust version was installed as a part of the new set-up in Nanortalik. Unfortunately, the connection to that specific instrument was lost after a few of days of icing events, which indicates that it was also destroyed or its cable got loose. However, it was possible to use the indicated icing period as a demonstration case. Quite severe ice accumulation was identified during the night of 28. November. The results could be validated by the high relative humidity, subzero temperature and low wind speed measurements.

Recently a number of recommendations have been published about the proper installation of meteorological test stations in the cold climate areas (e.g. Arbez et al. [2013]). Following these guidances, it is possible to minimize the detrimental effect of icing on the measurements and also more precisely identify the icing events and even the ice rate.

The results and experiences suggest that icing is a threat in South-Greenland during periods with low wind speed and high relative humidity combined with subzero temperature (or close to 0 ^oC). If the decision was made to install a wind turbine in a specific location, it is suggested to include a thorough investigation of risk of ice along with the wind resource analysis.

Chapter 3

Experimental investigation of the effect of ice on wind turbine blades

Experimental investigation of icing of wind turbine blades can give a unique, hands-on experience with phenomenon and issues that are difficult to investigate in full scale. The experiments described in this chapter were carried out in the Collaborative Climatic Wind Tunnel (CWT). Glaze, rime and mixed ice deposits were built up on a NACA 64-618 airfoil profile and the aerodynamic responses were monitored during the accretion process.

This chapter gives an overview of the experimental investigation of the effect of ice build-up on airfoils and describes the ice accretion tests performed in the CWT during the PhD work. A detailed description of the wind tunnel set-up, including e.g. the test facility itself, the spray-system and the force and torque transducers, is also presented here. Since the values measured by the force and torque transducers are in voltage (V), it was necessary to calibrate them to Newton (N), therefore the data calibration is also explained.

3.1 Introduction to wind tunnel testing

Aircraft ice accretion has been a large problem since the very early years of flying (Gent et al. [2000]). It gives a good basis (i.e. Bragg et al. [2005], Blumenthal et al. [2006] or Bragg et al. [2007]) for wind turbine blade icing research. Even though, experimental investigation of effect of ice on airfoil is costly and time consuming, several have been carried out for both airplane and wind turbine airfoils.

Several simulations, both experimental and numerical, have been carried out in order to explore the effects of ice accretion on the aerodynamic forces. During the experiments of Seifert and Richert (Seifert and Richert [1997] and Seifert and Richert [1998]), artificial ice deposits were placed on the leading edge. The molds were made of ice fragments removed from the blades of a small wind turbine. The impact of different ice accretions on lift and drag coefficients were investigated for a range of angles of attack between -10° and 30°. In their study, they showed that the annual energy production loss can be as high as 6-18 % depending on the severity of icing. Jasinski et al. [1997] did similar experiments, but the artificial ice shapes were simulated in NASA's LEWICE ice accretion simulation software.

Both Jasinski et al. [1997] and Bragg et al. [2005] found that the lift coefficient based on the original chord increased by 10 and 16 %, respectively, due to rime ice accretion, which was acting as leading edge flap. Hochart et al. [2008] carried out a two-phase test on a NACA 63-415 profile. In the first phase, ice deposit was built up on a blade profile under in-cloud icing conditions in a wind tunnel, while in the second phase, aerodynamic efficiency tests were performed on the iced profiles. They described how ice affects the power production and pointed out that the outer third part of the blades is the most critical for performance degradation.

It was shown that the artificial materials used for simulating ice on airfoils could produce different performance degradation than the actual ice deposit. The process of selecting these materials and the casting are *"more an art than a science"* (Addy et al. [2003]). It was shown that the surface roughness is a key parameter in proper ice simulation. Even a small amount of ice on the blades can reduce power production due to the changes of surface roughness and therefore changes of aerodynamic forces (Lynch and Khodadoust [2001]).

3.2   Wind tunnel set-up

The aim of the experiments was to explore the impacts of ice accretion on the wind turbine blades. For this purpose, an airfoil was placed into a climatic wind tunnel. The set-up was equipped with a pair of force and torque transducers to monitor the forces that act on the airfoil section.

3.2.1   Test facility

The tests were performed in a closed-circuit climatic wind tunnel (see Figure 3.1) with a test section of 2.0x2.0x5.0 m located at FORCE Technology, in Kgs. Lyngby, Denmark. The wind tunnel was developed and built as a collaboration between the Technical University of Denmark (DTU) and FORCE Technology. The design criteria for the CWT are listed in Table 3.1 (based on Georgakis et al. [2009]). The CWT is equipped with relative humidity and temperature sensors along with a Pitot tube for wind speed measurements, therefore these parameters can be monitored along with the force measurements.

Table 3.1: *Basic specifications of the wind tunnel (based on Georgakis et al. [2009]).*

Temperature	-10 to 40	$[^oC]$
Min. liquid water content	0.2	$[g/m^3]$
Test section cross-sectional area	2.0x2.0	$[\,m\,]$
Test section length	5	$[\,m\,]$
Maximum wind velocity	31	$[m/s]$
Turbulence intensity	0.6 to 20	$[\%]$
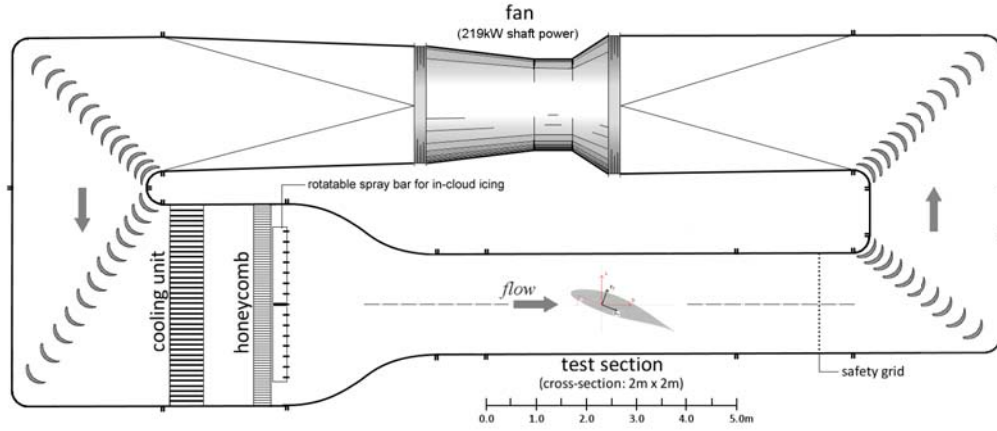
Figure 3.1: *Main features of the CWT (based on Koss and Lund [2013]). The size of the blade section is not scaled.*

3.2.2 Spray-system

Currently, the CWT is capable of operating under rain and icing conditions. To create ice, a spraying system has been mounted in the settling chamber, as it can be seen in Figure 3.1. The system includes 15 evenly spaced (20 cm from one other) nozzles, which mix high-pressure air and water and produce a spray of water droplets that provide uniform cloud in the tunnel (see Figure 3.2).

Figure 3.2: *Spray system produces cloud in the wind tunnel. The system includes 15 evenly spaced nozzles.*

According to the manufacturer (Schick [2008]), the median volume diameter of the water droplets was approximately 25 μm for glaze and mixed ice tests and approximately 20 μm for the rime ice tests. The smaller MVD for the rime ice case was chosen due to the typically smaller droplet size common during these conditions (ISO 12494 [2001]). The target liquid water content was approximately 0.6-65 g/m^3

3.2.3   Airfoil and testing rig

A NACA 64-618 airfoil section with 900 mm chord length and 1350 mm span borrowed from LM Wind Power was used during the experiments. The airfoil was covered with PVC folio to recreate the surface condition of a painted wind turbine wing. In order to place the section into the tunnel and to set different angles of attack, it was necessary to design a suitable rig (see Figure 3.3).
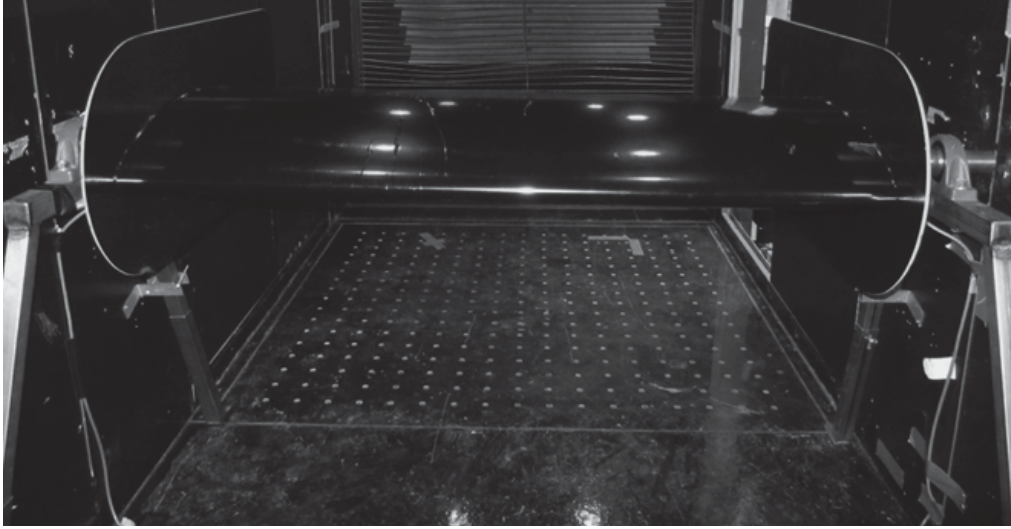

Figure 3.3: *Photo of the test set-up from the tunnel.*

Two wooden end plates were installed on either side of the wing section to avoid distorting influences on the ice accretion and airflow over the wing. The upstream edge of these plates was shaped in a way to minimize their interaction with the flow. The airfoil section was connected in one point, on each side with the supporting structure with moment-free joints. The force transducers were placed on the outer side of the end-plates to separate the measuring system from the airfoil.

The effect of the PVC folio on the ice accretion was investigated before the actual tests. For this purpose, a cylinder was mounted in the tunnel. Half of it was covered with the folio and icing environment was applied. As it can be seen in Figure 3.4, ice could accreted on both coated (right hand side) and uncoated (left hand side) surfaces and no significant differences can be seen. Hence, it was assumed that the PVC folio coating has little or no effect on the ice accretion.

3.2.4   Force and torque transducers

The set-up was equipped with a pair of AMTI MC5 force and torque transducers, which measures the loading simultaneously in all 6 degrees of freedom, i.e. forces Fx, Fy, Fz together with moments Mx, My , Mz in a wing-fixed coordinate system as shown in left hand side of Figure 3.5. The general specifications of the transducers are summarized in Table 3.2 (AMTI [2000]).
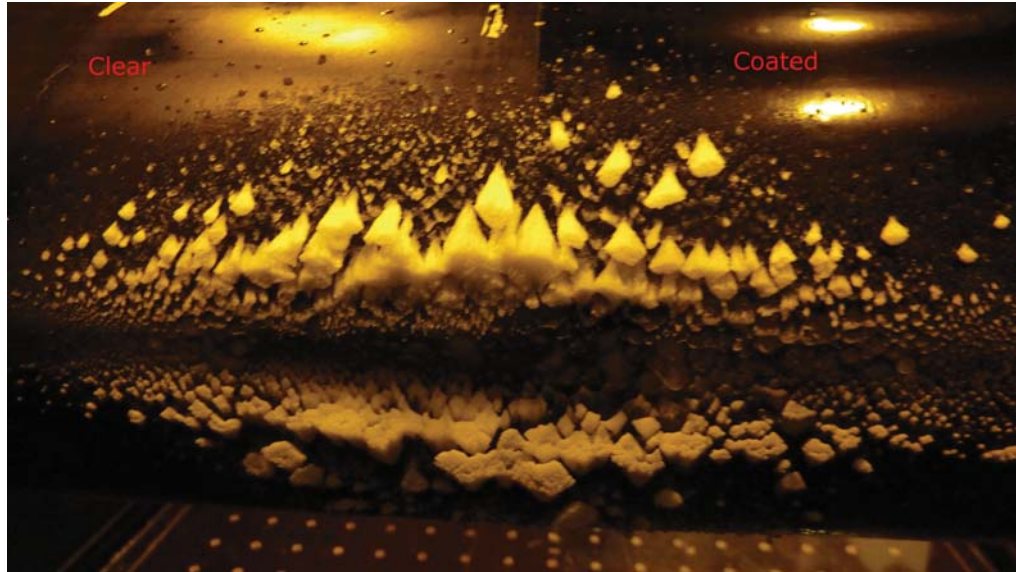
Figure 3.4: *Ice accretion test of the application of PVC folio on a cylinder. The left hand side of the cylinder is uncoated, whereas the right hand side is coated.*
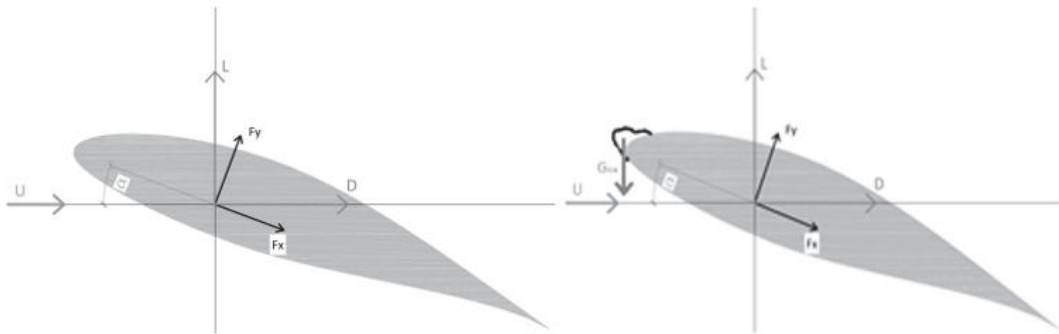
Figure 3.5: *Forces on the airfoil. On the left hand side, the forces on the clean airfoil are shown whereas on the right hand side the forces on the iced airfoil.*

Table 3.2: *General specification of the force transducers (AMTI [2000]).*

Dimension	$D = 12.57$ and $H = 12.70$	$[cm]$
Total weight	3	$[kg]$
Sensor top weight	1.4	$[kg]$
Excitation	10 (or less)	$[V]$
Temperature range	-17 to 52	$[^oC]$
Safety factor	minimum 50% above capacity	
F_x, F_y capacity	11.125	[kN]
F_x, F_y, F_z hysteresis	± 0.2 (full scale output)	[%]
F_x, F_y, F_z non-linearity	± 0.2 (full scale output)	[%]
Cross talks	less than 2 (in all channels)	[%]

Beside the force transducers, it was necessary to use a power amplifier for each transducer with relative power supply, a National Instrument analogue input module and a National Instrument CompactDAQ Chassis for the measurements in order to read the signal from the transducers and the other sensors and transport the data to the computer.

3.2.5   Data calibration

The data registered by the force transducers are in [V] and these values need to be converted to [N] (and [Nm]) using the following equations (eq.3.1 - 3.2):

$$F_x[N] = [\frac{F_x[V]B_{1,1}}{GFx} + \frac{F_y[V]B_{1,2}}{GFy} + ... + \frac{M_z[V]B_{1,6}}{GFz}] * \frac{10^6}{Exc} \tag{3.1}$$

$$F_y[N] = [\frac{F_x[V]B_{2,1}}{GFx} + \frac{F_y[V]B_{2,2}}{GFy} + ... + \frac{M_z[V]B_{2,6}}{GFz}] * \frac{10^6}{Exc} \tag{3.2}$$

where B is the force transducer cross talk-matrix and is dependent on the type of the force transducer. i.e. each transducer has its own cross talk-matrix. Exc is the excitation factor, which is monitored by the force transducer and GFx, GFy, GFz, GMx, GMy and GMz are the power amplifier's gain. Each amplifier has its specific gain values too.

The rotational speed of the fans of the wind tunnel is given in revolutions per minute (rpm) as an input parameter. In Table 3.3, some of the velocities are converted into m/s units. The wind speed (U) in the cross-section can be calculated based on the measurements by

Table 3.3: *Example of rotational speed conversion from rpm to m/s on a specific day.*

U (rpm)	100	300	500	700	800	1000
U (m/s)	1.78	5.71	9.64	13.57	15.56	19.49

the Pitot tube using the following expressions:

$$U = \sqrt{\frac{2 \triangle P}{\rho}} \tag{3.3}$$

Where $\triangle P$ is the pressure difference measured by a Pitot tube and ρ is the air density in kg/m^3 (see eq. 3.4).

$$\rho = \frac{P_{atm} * 100}{287.05 * (T + 273.15)} * (1 - \frac{0.378 p_v}{P_{atm} * 100}) \tag{3.4}$$

Where P_{atm} is the atmospheric pressure of the day [mb], T is the temperature in the tunnel in [^oC] and p_v is the actual vapor pressure from the relative humidity (RH) in [Pa].

$$p_v = E_s * RH \tag{3.5}$$

Where E_s is the vapor pressure [mb], eq.3.6:

$$E_s = c_0 * 10^{\frac{c_1 * T}{c_2 + T}} \tag{3.6}$$

Where $c_0 = 6.1078$, $c_1 = 7.5$ and $c_2 = 273.3$.
As it can be seen from these equations, the wind speed conversion from the Pitot tube is highly dependent on the daily meteorological parameters, which are constantly changing.

3.3 Set-up of wind tunnel tests

Glaze, mixed. and rime ice deposits built up on a NACA 64-618 profile. The aerodynamic forces acting on the blade during ice accretion for different angles of attack (0°, 4°, 7°, 9°, 11°) at various air temperature (approximate, mean value of the set temperature: -3 ^oC, -5 ^oC, and -8 ^oC) were measured along with the mass of ice and the final ice shape. The used temperature range can be described as rather moderate, but due to the limitation of the wind tunnel's cooling unit, colder temperatures could not be used.

Ice was building up on the surface of the airfoil section at different temperatures, ensuring the three investigated icing characteristics for each angle of attack. A list of the wind tunnel tests and the conditions can be found in Table 3.4. The values are approximated. Two different air speeds were targeted: one applied for the ice accretion and the other one for force measurements. The temperature values are mean value of the used temperature during the tests.

Table 3.4: *A summary of the wind tunnel tests and conditions. The two different velocities are target values, one during the ice accretion (Accretion) and the other during the force measurements (Tests). The temperature values are mean value of the used temperature. The LWC parameters are target values. These numbers are approximated.*

Test	AOA (^{o})	T (^oC)	Ice	MVD (μm)	LWC (g/m^3)	U (m/s) Accretion	U (m/s) Tests	t_a (min)
1	0	-3	glaze	25	0.65	15	15	60
2	0	-5	mixed	25	0.65	15	15	60
3	0	-8	rime	20	0.6	10	15	60
4	4	-3	glaze	25	0.65	15	15	60
5	4	-5	mixed	25	0.65	15	15	60
6	4	-8	rime	20	0.6	10	15	60
7	7	-3	glaze	25	0.65	15	15	60
8	7	-5	mixed	25	0.65	15	15	60
9	7	-8	rime	20	0.6	10	15	60
10	9	-3	glaze	25	0.65	15	15	60
11	9	-5	mixed	25	0.65	15	15	60
12	9	-8	rime	20	0.6	10	15	61
13	11	-3	glaze	25	0.65	15	15	62
14	11	-5	mixed	25	0.65	15	15	63
15	11	-8	rime	20	0.6	10	15	64

The tests were performed by first setting the required wind speed and temperature in the test section. Water spray, providing in-cloud environment was then initiated. The air speed was set to 15 m/s (corresponding to Reynolds number, $Re \simeq 1E6$) for glaze and mixed ice and to 10 m/s (corresponding to $Re \simeq 0.6E6$) for rime ice accretion and the

force measurements were taken with 15 m/s for all ice types. Although the effective wind speed is much higher at the tip region of a real wind turbine blade, due to the limitations of the wind tunnel, it was necessary to set a low velocity in order to ensure sufficiently low temperatures. Ice was accumulating on the surface for 60 minutes in 5 minutes intervals. Every 5 minutes the tunnel and the spray system were set to idle to measure the forces and the weight of the already accreted ice mass.

After an hour, the accretion process was stopped and the characteristics of ice deposit were registered and the shape of the changed profile was documented by contour tracing. For this purpose the ice deposit was cut perpendicular to the airfoil axis with a heated blade down to the airfoil surface. Hereafter, a cardboard was placed into the cut and the ice layer contour was drawn onto it, see an example in Figure 3.6. The main feature of the surface could be captured by this method, but the micro structure of the surface roughness could only be registered by a camera. The image was digitalized and the coordinates were saved for further analysis. The accretion process was captured by an action camera, which was installed inside the tunnel upstream from the airfoil profile and was taking photos every 30 seconds.

The main differences between the tests presented in this work from the ones done by Hochart et al. [2008] are that the change of lift coefficient and the mass of accumulated ice were monitored throughout the accretion process and that not only rime and glaze but also mixed ice deposits were studied at different angles of attack.

Figure 3.6: *Example for ice layer contour tracing.*

Ideal condition for mixed ice accretion was ensured with slowly, manually adjusted, decreasing air temperature. Thus, the accreted ice showed both glaze and rime ice characteristics. An example of the temperature drop throughout the accretion is illustrated in Figure 3.7. This temperature curve was registered during the 4 ^{o} angle of attack mixed ice tests in case of $Re \simeq 1E6$, $MVD \simeq 25\mu m$ and $LWC \simeq 0.65g/m^3$.
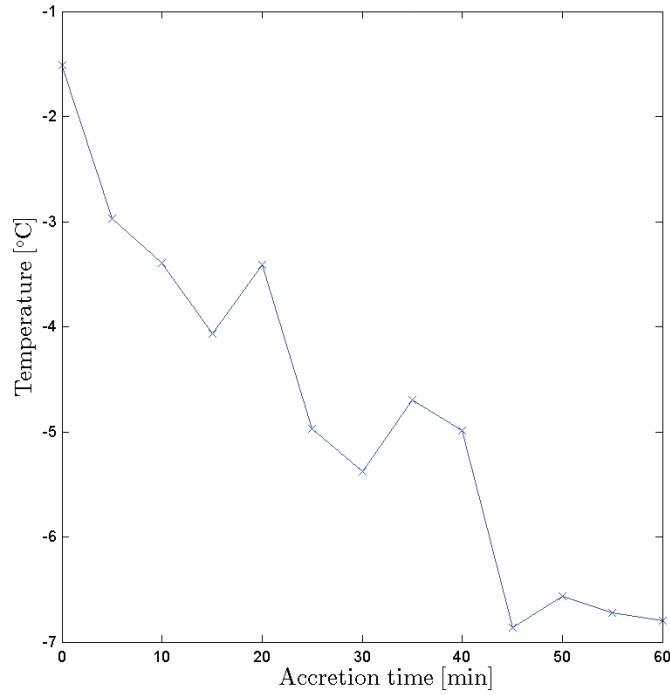
Figure 3.7: *Example for the mean temperature changes during mixed ice accretion for $\alpha = 4^o$. The target temperature was manually adjusted throughout the mixed icetests in order to ensure the necessary condition for mixed ice formation.*

In case of some of the ice tests, flow visualization was also performed. The set-up contained a water based smoke generator and a 5 W laser with the specifications summarized in Table 3.5. Green laser beam was used to light up the smoke around the airfoil. During the flow visualisation, very low wind speed was applied, hence it was possible to capture the flow features caused by the altered airfoil profile.

Table 3.5: *Specification of the laser used for flow visualizations.*

Laser colour	Green
Wave type	continuous-wave
Wave length	532 nm
Diode type	diode-pumped solid-state
Lens type	45 degree Powell lens line generator
Beam diameter	2 mm

Due to the high adhesion of the ice deposit, it was not possible to manually remove it from the airfoil without causing damage on the set-up. Therefore, it was necessary to increase the temperature in the tunnel and melt the ice. In some cases, the aerodynamic forces were monitored during melting.

3.4   Wind tunnel correction

The confined flow in the wind tunnel alters the flow field around the airfoil compared to full-scale and hence affects the measured aerodynamic forces on the wing section. The measured forces were corrected for both, lift interference and blockage interference. Lift interference is caused by the changes of the stream direction and stream curvature, and the blockage interference is the result of the changes in stream velocity and longitudinal pressure gradient. These two interferences are independent of each other (ESDU 76028 [1976]). The tunnel correction was performed by following ESDU 76028 Lift-interference and blockage corrections for two-dimensional subsonic flow in ventilated and closed wind-tunnels methodology.

These equations were derived with the linearised potential flow theory (detailed in ESDU 76028) and are valid for subsonic flows. The incremental correction of lift coefficient ($\triangle C_L$) due to lift interference can be calculated by integrating the residual loading correction along the airfoil chord (c):

$$\triangle C_L = -\frac{\pi}{2}\left(\frac{c}{h}\right)^2 \frac{\delta_1}{\beta^2} C_L \tag{3.7}$$

δ_1 represents the effect of changes in streamline curvature, c is the chord length and h is the height of the wind tunnel. In case of closed wind tunnels, $\delta_1 = \dfrac{\pi}{24}$. β is the Prandtl-Glauert compressibility parameter, which depends on the Mach number (M_∞), $\beta = \left(1 - M_\infty^2\right)^{1/2}$. The drag coefficient correction ($\triangle C_D$) can be done as followed:

$$\triangle C_{DB} = -\frac{-2A_e^2 K}{c\beta^4 h^3} - C_D \Omega_s \epsilon_{sc} \tag{3.8}$$

$$\triangle C_{DR} = -\frac{c}{h}\delta_0 C_L^2 \tag{3.9}$$

However, $K = 0$ and $\delta_0 = 0$ for closed wind tunnels, which makes these equations even simpler. The blockage is a combination of the model and the wake, therefore both has to be added to the blockage factor, ϵ_B.

$$\epsilon_B = \Omega_s \epsilon_{sc} + \Omega_w \epsilon_{wc} \tag{3.10}$$

Ω_s and Ω_w are the blockage factor rations and have unit magnitude for the closed wind tunnels.

$$\epsilon_{sc} = \frac{\phi A_e}{6\beta^3 h^2} \tag{3.11}$$

$$\epsilon_{wc} = \frac{1}{4}\left(\frac{c}{h}\right)\frac{C_D}{\beta^2} \tag{3.12}$$

A_e is an equivalent area for the airfoil section and C_D is the drag coefficient. The aerodynamic coefficients from the wind tunnel measurements need to be corrected to free-air values by the ratio of the corrected to uncorrected kinetic pressure, G.

$$G = \frac{1}{1 + (1 - M_\infty^2)\epsilon_B} \tag{3.13}$$

The free-air values of lift and drag coefficient based on the above explained corrections are:

$$(C_L)_f = (C_L + \triangle C_L)\,G \tag{3.14}$$

$$(C_D)_f = (C_D + \triangle C_{DB} + \triangle C_{DR})\,G \tag{3.15}$$

3.5 Pretests

Prior to the icing wind tunnel tests, it was necessary to perform some pretests in order to have reference data for the further analysis. Basically two different simulations were performed, static tests and dry tests. Static tests were done to study the response of the force transducers. Additional weight was placed in the centreline of the blade up to 20 kg (see Figure 3.8) and the angle of the airfoil was set to 0° and 5°.

Figure 3.8: *Photo of static test. 20 kg additional weight was placed on the airfoil.*

Since the loads were acting as point loads on the airfoil, it was expected that each force transducer monitors the half of the loading. In case of 0° angle of attack:

$$F_y = m * g \tag{3.16}$$

where m is the weight in $[kg]$ and g is the gravitational constant $[m/s^2]$.

Table 3.6 summarizes the results based on eq. 3.16 and the measured values of normal force (F_y) at $\alpha = 0^o$ and at $\alpha = 5^o$. It can be seen that the values measured at $\alpha = 0^o$ are in quite good agreement with the expected values. Some differences can be noticed in case of $\alpha = 5^o$. The reason could be that the in-line component of the gravity force was tiny compared to the normal force and since the transducers' measuring range is wide, so it is possible that they could not accurately capture these small forces.

During the dry tests, different angles of attack were set with different flow velocities. The aim was to get a reference C_L curve, which can be compared to the one from the literature and can be used later as a basic for the ice tests. Based on the information from LM Wind Power, the highest lift coefficient can be found at 11° and the maximum lift/drag ratio is at 4°, therefore these two angles of attack were included in the study. A number of wind speeds, i.e. 300 rpm, 500 rpm, 700 rpm, 800 rpm, 1000 rpm, were tested at different angles of attack, α = -10°, -5°, 0°, 1°, 2°, 3°, 4°, 5°, 7°, 10°, 11° and 12° , in order to produce a base lift curve. The wind speeds are given in revolutions per minutes

(rpm). These values are the input parameters of the wind tunnel and can be found in m/s in *Wind tunnel set-up* section and correspond to $Re \simeq 31000, 56000, 80000, 920000$ and 1150000, respectively.

In Figure 3.9, the corrected wind tunnel measurements are plotted against the ones presented in the work of Abbott and von Doenhoff [1959]. The measurements differ from the reference values, probably due to the different flow speeds and the fact that the wind tunnel data were only corrected against lift and blockage interference.

Table 3.6: *Expected and measured forces (at $\alpha = 0^o$ and at $\alpha = 5^o$) acting on the airfoil during static tests.*

Weight (kg)	eq. 3.16 [N]	F_y measured [N] at $\alpha = 0^o$	F_y measured [N] at $\alpha = 5^o$
1	9.81	9.75	9.63
2	19.62	19.48	19.33
3	29.43	29.21	29.00
4	39.24	38.99	38.73
5	49.05	48.97	48.51
6	58.86	58.7	57.95
7	68.67	68.48	67.65
8	78.48	78.26	77.37
9	88.29	88.07	87.08
10	98.1	97.88	97.33
11	107.91	107.7	106.46
12	117.72	117.49	116.24
13	127.53	127.31	125.92
14	137.34	137.09	135.63
15	147.15	147.01	146.34
16	156.96	156.83	155.07
17	166.77	166.6	164.80
18	176.58	176.41	174.58
19	186.39	186.25	184.27
20	196.2	196.08	195.32

The wing-tip vortices on a wing with free ends (are caused by the pressure difference between the suction and the pressure side) from the finite airfoil induce downwash, which reduces the effective angle of attack and thus the lift (Fox et al. [2009]) and also delays stall to higher AOA (Brandt [2004]). This effect is shown in Figure 3.10 and similar characteristics can be noticed on the curves plotted in Figure 3.9. The geometric angle of attack needs to be increased compared to an infinite airfoil section to get the lift coefficient of the section:

$$\triangle\alpha = \frac{C_L}{\pi ar} \tag{3.17}$$

Where ar is the aspect ratio $ar = \dfrac{b^2}{A_p} = \dfrac{windspan^2}{wingarea}$.
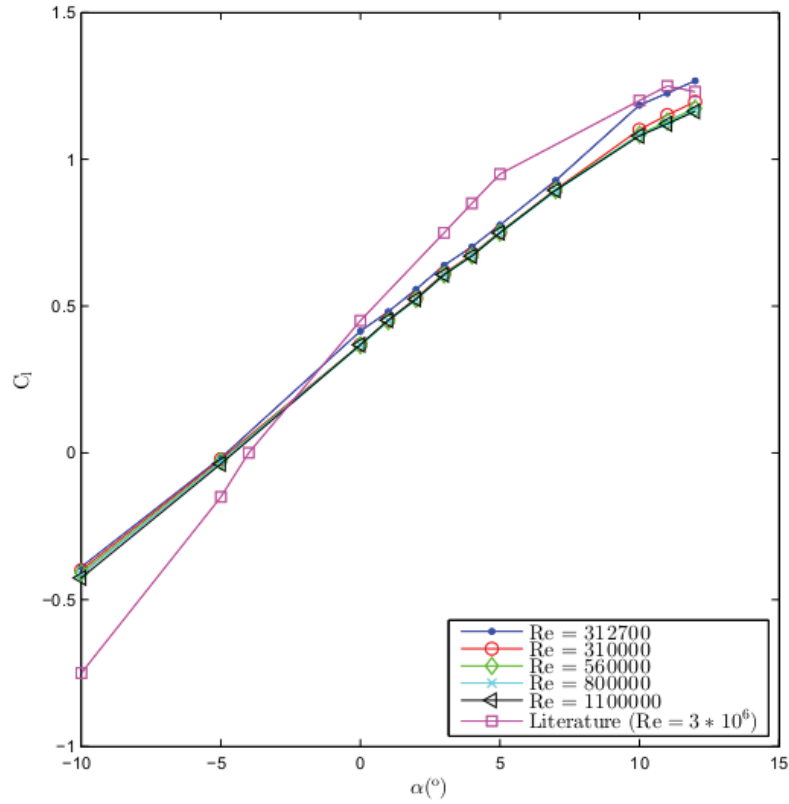
Figure 3.9: *Lift coefficient based on the wind tunnel measurements as a function of the angle of attack plotted against the lift curve from Abbott and von Doenhoff [1959].*

The end-plates were installed on the set-up to reduce these effects, but the results imply that this was not entirely possible and the end-plates did have an influence on the results because of the boundary layer on these reducing the velocity on the airfoil near the end plate. In Figure 3.11 a-d, examples of flow visualization on an airfoil made by LM Wind Power are shown for different angles of attack. It can be seen that even at low AOA, the tunnel walls had impact on the flow (marked with red ellipses in Figure 3.11a) and it increased with increasing angle.

There are different techniques to reduce the effect of the tunnel walls and the end-plates during testing, such as side-wall suction or blowing. In that way, it is possible to minimize the interaction between the wall boundary layer and the airfoil pressure field (Catalano and Caixeta Jr. [2004]).

The results of 300 rpm differs from the others at higher angles of attack in Figure 3.9. The reason could be the very low wind speed, which gives different flow conditions around the airfoil. Also note that the lift curve did not reach its maximum at $\alpha = 11^o$ as would have been expected, but was even higher at $\alpha = 12^o$. Due to the limitation of the set-up, it was not possible to test larger AOA, but it is very likely that the stall is delayed because of the different flow conditions inside the tunnel and of the previously mentioned wing-tip vortices.
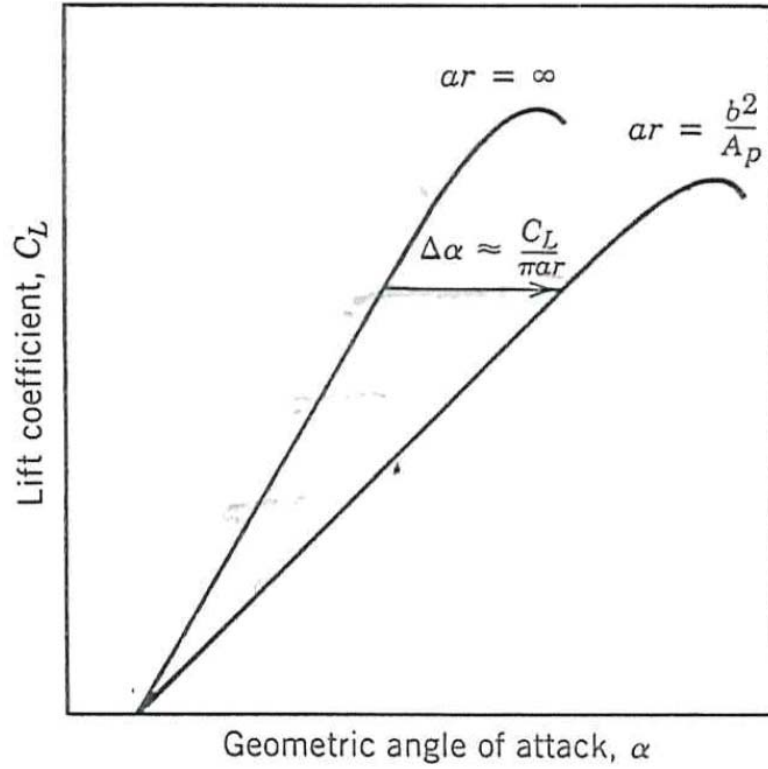
Figure 3.10: *Effect of finite aspect ration on lift coefficient (Fox et al. [2009]).*

(a) $\alpha = 0^o$

(b) $\alpha = 8^o$
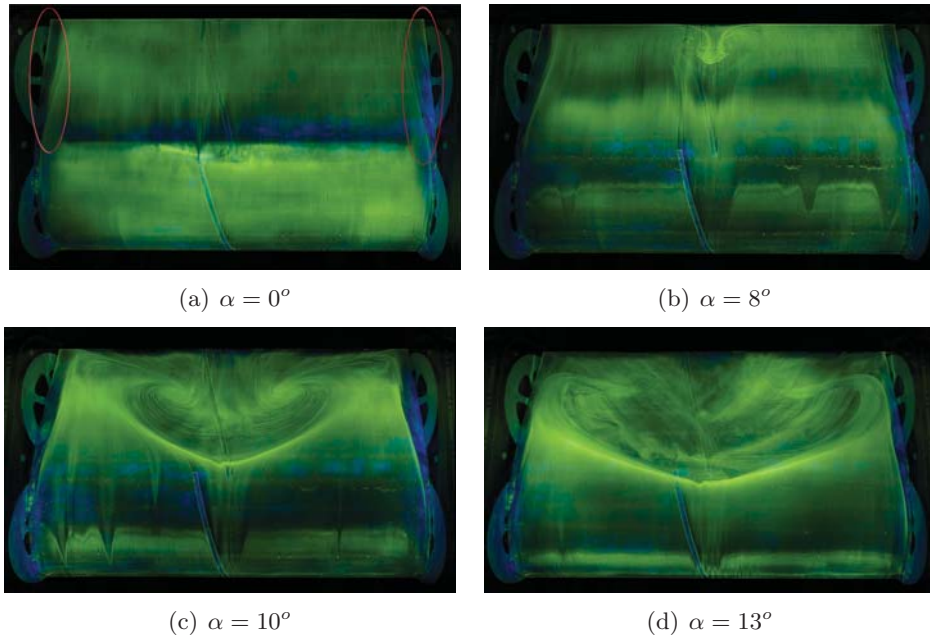

(c) $\alpha = 10^o$

(d) $\alpha = 13^o$

Figure 3.11: *Flow visualization showing the impact of the wind tunnel walls on the flow around a finite airfoil (Photo credit: LM Wind Power). Red ellipses mark the effect of the tunnel walls on the flow above the airfoil.*

3.6 Temperature dependency of the measurements

In other tests performed in the wind tunnel using force and torque transducer from the same manufacturer, it was experienced that the temperature has a major influence on the measurements. Thus, a simple experiment was done to test the performance of the used force transducer at subzero temperatures. During these tests, the wind tunnel was cooled to different temperatures and a testing routine was run with the following steps: (1) zero measurement, (2) point force, (3) $U \cong 500rpm$. First step was performed in order to measure the static noise, which had to be substracted from the other measurements. In step 2, a weight with $1739.6g$ was placed on the airfoil in the same position as it was done during the reference static tests and the response of the transducers was studied. During the last step, wind speed with $U \cong 10m/s$ was applied and the resulted lift coefficient was studied. When the air temperature reached its minimum, the heating was turned on. Measurements were taken at following set of temperatures; $T = 15^{o}C$, -4.5^{o}C, -7°C, -9°C, -6.5^{o}C, -1°C, 3°C.

As the results show in Table 3.7, the temperature does not have significant effect on the performance of the force transducers. The reason for the minor changes in the measured values could be the fact, that the sampling time was set to $60s$ due to the limitation of the used monitoring software. Another reason could be, that the wind speed is a function of the air density, which is a temperature-dependent parameter. The difference between the applied weight and the measured weight would be caused by the wide measuring range, i.e. due to the wide measuring range, the transducers cannot measure accurately the very small forces. The average measured load is 1353.1 g, which means an average relative deviation of 0.78%. The highest relative deviation, 2.36% was measured at -4.5^{o}C whereas the smallest relative reduction, 0.09% at -7°C. This showed that the temperature does not have any significant effect on the performance of the force transducers. Thus, no special actions are required.

Table 3.7: *Results of temperature dependency tests.*

Temperature	Weight (g)	C_l
$15^{o}C$	1763.3	0.3710
$-4.5^{o}C$	1780.6	0.3802
$-7^{o}C$	1738.0	0.3849
$-9^{o}C$	1742.5	0.3877
$-6.5^{o}C$	1737.6	0.4086
$-0^{o}C$	1759.6	0.3915
$3^{o}C$	1750.4	0.3875

3.7   Results of ice accretion tests

The corrected results of all the simulations including the degradation process of lift coefficient, the accretion of ice throughout the tests and the shapes and characteristics of the ice profiles are described in this section. Even though the accretion time was only 60 minutes, significant changes were monitored. A summary of the measurements is shown in Table 3.8, where the final ice mass and final lift coefficients along with the relative degradation are listed for each tests. The growth rate shows how much ice accumulated in average in a minute on the surface of the airfoil. These numbers are only valid for the previously presented experimental set-up. Hence, as any of the parameters (e.g. AOA, MVD, LWC or wind speed) is changed, the outcome of the experiment changes as well. It can be seen that the collected mass of ice of 7 ^{o} are out of the trend, due to a probably slightly different MVD, and therefore they will be discussed separately.

Table 3.8: *Summary of the results. C_{L0} represents the lift coefficient of the clean airfoil and C_{Lf} is the final lift coefficient at the end of the ice build-up process.*

AOA [^{o}]	0	4	7	9	11
			Glaze ice		
Mass of ice [g/m]	2227.1	2603.6	3269.3	2835.8	2903.4
Growth rate [$g/min/m$]	37.1	43.4	54.5	47.3	48.4
C_{L0} (clean airfoil)	0.317	0.563	0.81	0.904	1.04
C_{Lf} (final, iced airfoil)	0.157	0.366	0.599	0.643	0.807
Degradation [%]	50	35	36	29	22
			Mixed ice		
Mass of ice [g/m]	2450.7	2648.1	3723.9	2658.3	3216.6
Growth rate [$g/min/m$]	40.8	44.1	62.1	44.3	53.6
C_{L0} (clean airfoil)	0.32	0.579	0.809	0.911	1.038
C_{Lf} (final, iced airfoil)	0.116	0.309	0.515	0.596	0.855
Degradation [%]	64	47	36	35	21
			Rime ice		
Mass of ice [g/m]	2715.9	1792	3117.9	2071.9	2353.9
Growth rate [$g/min/m$]	45.3	29.9	52.0	34.5	39.2
C_{L0} (clean airfoil)	0.319	0.571	0.814	0.96	1.066
C_{Lf} (final, iced airfoil)	0.185	0.431	0.614	0.744	0.805
Degradation [%]	42	25	25	23	24

It was found in all three ice types tests that the lift coefficient decreased significantly even for a small amount of ice and the build-up process is almost linear during this early phase of accretion. The instantaneous lift degradations, $\triangle C_L = C_{L0} - C_{L5}$ are listed in Table 3.9. It can be seen that the immediate degradation is more significant for higher angles of attack than for lower.

Table 3.9: *Summary of instantaneous lift coefficient degradation. C_{L5} represents the lift coefficient measured after 5 minutes of ice accretion and $\triangle C_L$ is the difference of the clean airfoil lift coefficient and the lift coefficient after 5 min of ice accumulation.*

AOA [^{o}]	0	4	7	9	11
			Glaze ice		
C_{L5}	0.279	0.529	0.723	0.814	0.952
$\triangle C_L$	0.038	0.034	0.087	0.09	0.088
			Mixed ice		
C_{L5}	0.286	0.517	0.754	0.814	0.983
$\triangle C_L$	0.034	0.062	0.055	0.097	0.093
			Rime ice		
C_{L5}	0.287	0.527	0.748	0.888	0.993
$\triangle C_L$	0.032	0.044	0.066	0.073	0.073

Linear behaviour of the ice build-up was seen during the simulation and it is visualized in Figure 3.12 where a fragment from one of the ice profile, which fell off the airfoil during melt-off, is shown. The cross-section of the ice fragment shows the layer structure of the ice body. In this case, the visibility of the layers is enhanced by spay and airspeed-off phases to measure the ice mass growth.

In Figure 3.13 a set of photos, which were taken at the end of each accretion tests, is shown. More photos are presented in Appendix B with some details on the differences between the different ice types. In Appendix C, timelaps photos are shown for a glaze, a mixed and a rime ice accretion. The photos were taken 5, 10, 30 and 60 minutes into the accretion.
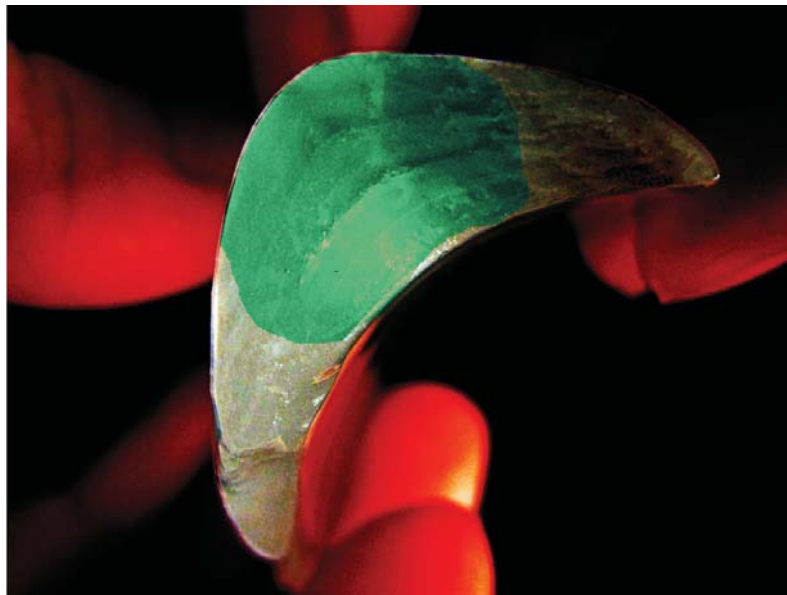

Figure 3.12: *Post-processed photo of a piece of ice fell off the airfoil during melt-off. The equidistant lines in the layer structure of the ice body indicate a linear ice growth over time.*

Figure 3.13: *Iced blade profiles at the end of the accretion tests for the different types of ice at each angles of attack.*

3.7.1 Glaze ice tests

Glaze icing conditions were established for all angles of attack. As ice built up on the surface, the lift force and thus the lift coefficient decreased as it is seen in Figure 3.14. The degradation is already visible after 5 minutes into the accretion. As it is listed in Table 3.8, the lift coefficient decreased the most significant for 0° angle of attack, from 0.317 to 0.157, with approximately 50 % and the least at 11° from 1.04 to 0.807 i.e. by 22 % decrease. The slopes of the fitted polynomials presented in Figure 3.15 are similar, hence the degradation of lift coefficient is alike for all tested AOA, i.e. the lift force degradation is independent of the angle of attack.
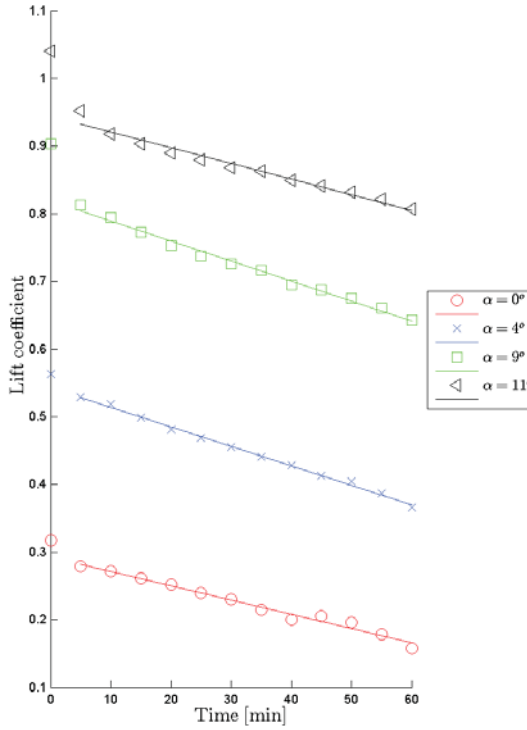

Figure 3.14: *Lift coefficient as a function of ice accretion time for different angles of attack in case of glaze ice, $Re \simeq 1E6$, $MVD \simeq 25m$ and $LWC \simeq 0.65g/m^3$ for a NACA 64-618 profile. A first order polynomial was fitted to the measurement.*
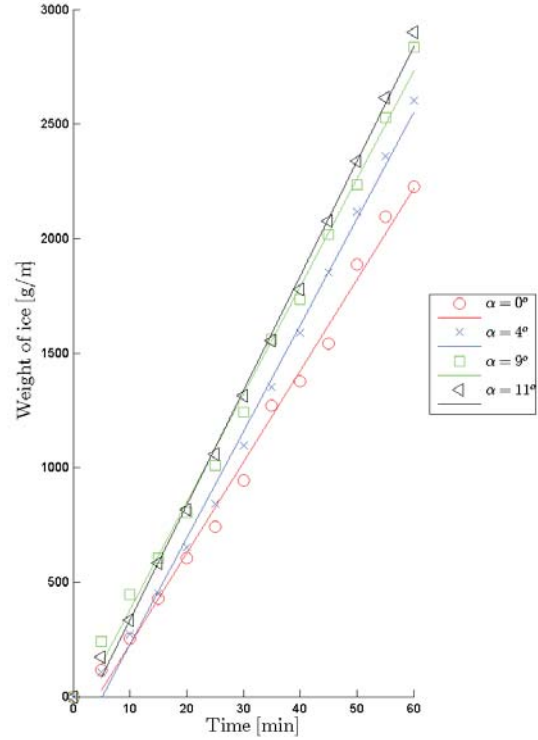
Figure 3.15: *Accreted ice mass as a function of ice accretion time for different angles of attack in case of glaze ice, $Re \simeq 1E6$, $MVD \simeq 25m$ and $LWC \simeq 0.65g/m^3$ for a NACA 64-618 profile. A first order polynomial was fitted to the measurement.*

Parallel to the lift force, the mass of the accreted ice was measured every five minutes. The accumulation of the ice mass over accretion time is shown in Figure 3.15. Here, in contrast to the lift coefficients, the lowest value for ice accretion is observed at 0° and the highest value at 11°. The weight of the accreted ice along with the ice growth rate (g/min/m) for different AOA is summarized in Table 3.8. It can be seen that the ice growth rate is the smallest for lower angle of attack and the largest for the highest angle of attack.

The ice build-up is a nearly linear process in this first stage of the ice accretion exhibiting a linear ice growth behaviour (Figure 3.15). Figure 3.16 shows the different ice shapes collected for all tested AOA.
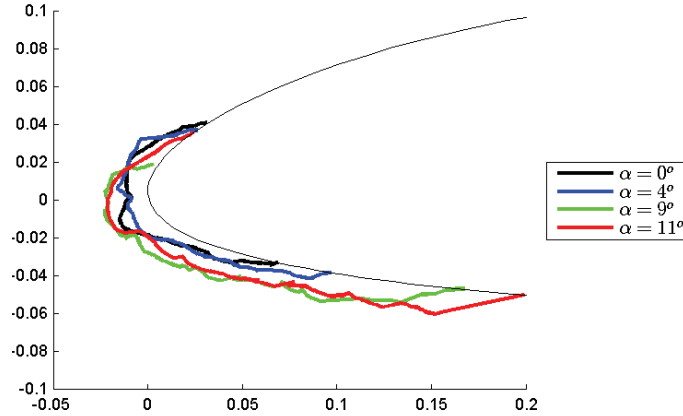

Figure 3.16: *Shapes of ice accretion for the different angles of attack collected after 60 minutes of ice accretion in case of glaze ice tests, $Re \simeq 1E6$, $MVD \simeq 25m$ and $LWC \simeq 0.65g/m^3$ for a NACA 64-618 profile.*

As a typical characteristic of the glaze ice accretion, some of the impinging water droplets froze in impact and some ran off following the streamlines towards the trailing edge. An example of the run off water rivulets on the suction side can be seen in Figure 3.17. The photo was taken during ice accretion. It was experienced that the impinged water droplets attached and formed larger particles and then, as it is also visible in the picture, ran off along both suction and pressure side (see a photo of the pressure side run-back ice in Figure B.2 in Appendix B).
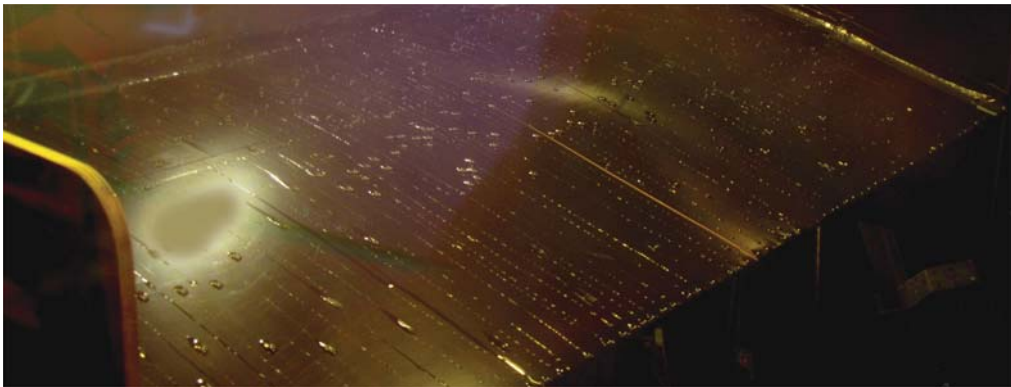

Figure 3.17: *A photo of the trailing edge of the airfoil during glaze ice accretion. Run-off rivulets are clearly visible in this picture.*

With increasing AOA, the length of the ice deposit at the pressure side increased as well and the visible separation line moved along the same side. However the time was not long enough to grow dramatic ice deposit on the surface, the horn shape at the leading edge was visible. An example of an early-stage horn shape is shown in Figure 3.18.
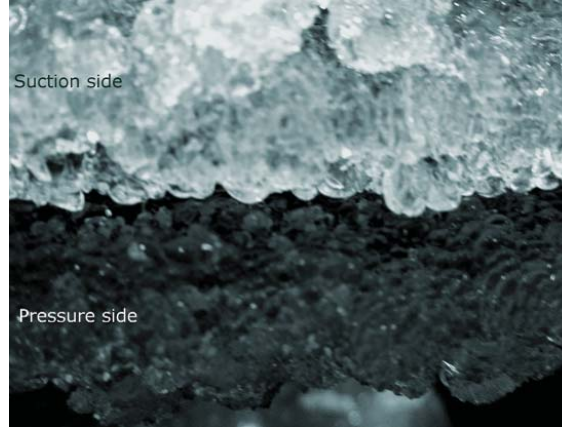
Figure 3.18: *A close-up photo of an early-stage horn ice shape shows a clear separation line between the suction and pressure side. The photo was taken after 60 minutes of glaze ice accretion in case of 0 ^{o} angle of attack and Re $\simeq$ 1E6, MVD $\simeq$ 25m and LWC $\simeq$ 0.65g/m^3 for a NACA 64-618 profile.*

3.7.2   Mixed ice tests

The accreted ice showed both glaze and rime ice characteristics. The lift coefficient as a function of the ice accretion time is shown in Figure 3.19 and the final coefficients are summarized in Table 3.8. As for the glaze ice test results, the process is linear, and a linear curve fitting was applied.

The degradation of the lift coefficient under mixed ice accretion is similar to the changes under glaze ice accretion. The most significant reduction was found at 0° angle of attack, where the lift coefficient decreased with 64 % from 0.320 to 0.116 after 60 minutes of ice accretion and the least significant at the highest angle, 11° from 1.038 to 0.855, which corresponds to a reduction of approximately 21 %. In Figure 3.20, the accreted ice mass is presented as a function of time. The build-up process is practically linear as it was seen also for the glaze ice tests. As it is given in Table 3.8, the smallest growth rate, 40.8 $g/min/m$ was found at 0 ^{o} angle of attack and largest, 53.6 $g/min/m$ at 11°.

 With increasing angle of attack, the amount of ice build-up on the surface was increasing as well. The sampled ice profiles are plotted in Figure 3.21. The stagnation point is quite visual due to the thin nose-like peak appearing at the leading edge. As it can be seen, the peak moved towards the pressure side as the angle of attack increased.

In Figure 3.22, an example of a typical mixed ice profile is shown. The photo was taken following the location of the stagnation point at the leading edge of the iced profile set at 4°. The sample shows characteristics of mixed ice. Close to the center, the ice deposit is more glassy and smooth whereas in the outer areas, the typical milky feathers of rime ice are visible. See a close-up shot of the feathers in Figure B.1 a in Appendix B.
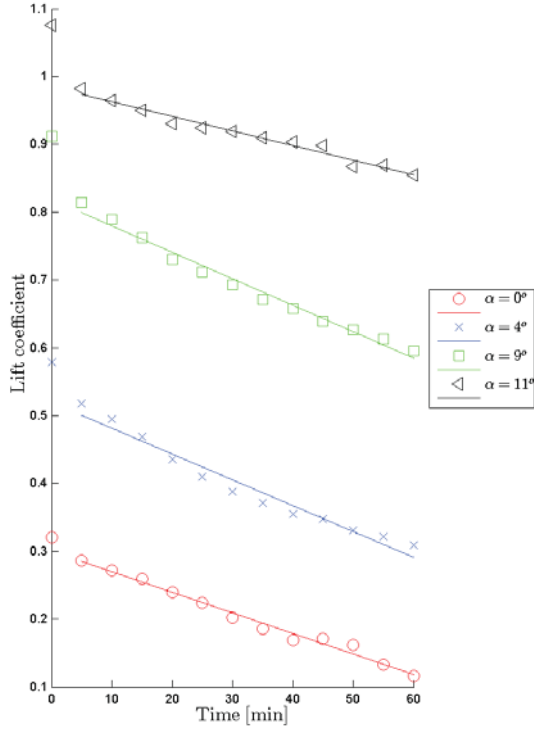
Figure 3.19: *Lift coefficient as a function of ice accretion time for different angles of attack in case of mixed ice, $Re \simeq 1E6$, $MVD \simeq 25m$ and $LWC \simeq 0.65g/m^3$ for a NACA 64-618 profile. A first order polynomial was fitted to the measurement.*

Figure 3.20: *Accreted ice mass as a function of ice accretion time for different angles of attack in case of mixed ice, $Re \simeq 1E6$, $MVD \simeq 25m$ and $LWC \simeq 0.65g/m^3$ for a NACA 64-618 profile. A first order polynomial was fitted to the measurement.*
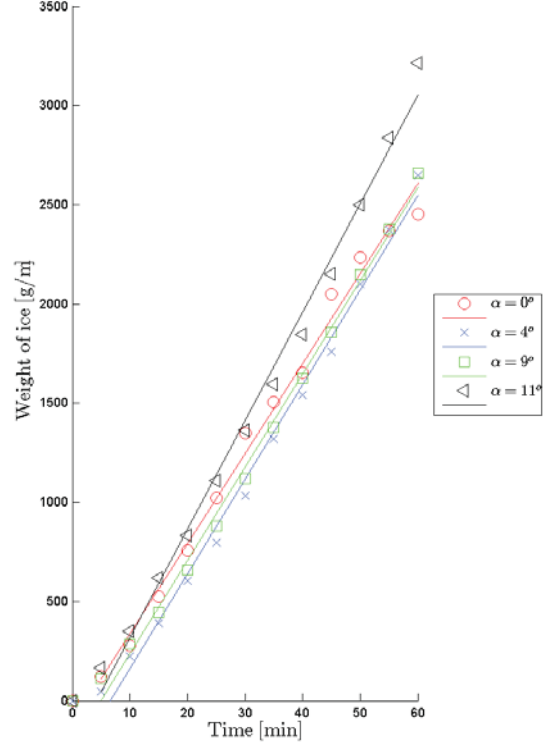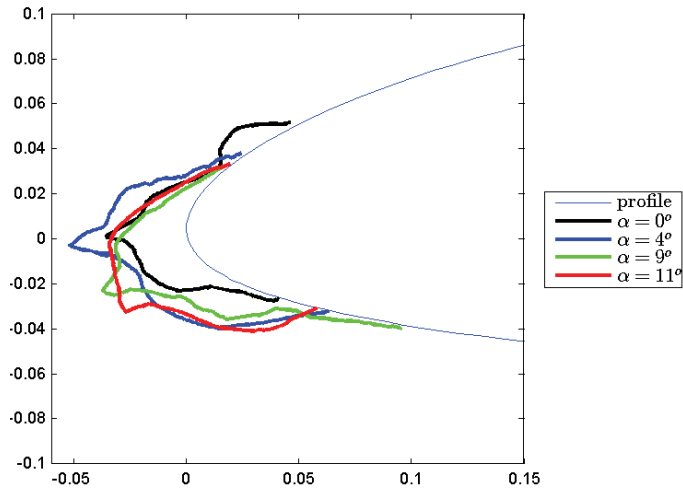

Figure 3.21: *Shapes of ice accretion for the different angles of attack collected after 60 minutes of ice accretion in case of mixed ice tests, $Re \simeq 1E6$, $MVD \simeq 25m$ and $LWC \simeq 0.65g/m^3$ for a NACA 64-618 profile.*

Figure 3.22: *Photo of the 4° angle of attack mix ice test in case of $Re \simeq 1E6$, $MVD \simeq 25m$ and $LWC \simeq 0.65g/m^3$ for a NACA 64-618 profile.*

3.7.3 Rime ice tests

Due to the limitation of the wind tunnel's cooling capacity, it was necessary to reduce the wind speed from 15 m/s to 10 m/s during the build-up process in order to ensure sufficiently low air temperature. The force measurements were conducted with 15 m/s. It is stated in the ISO 12494 [2001] standard that the droplet size in case of rime ice formation is lower than for glaze ice. Hence, the water pressure was reduced to form water droplets with approximately 20 μm median volume diameter (based on the specification of the manufacturer of the spray nozzles). Figure 3.23 and Figure 3.24 show the lift coefficient and the accreted ice mass as a function of the ice accretion time, respectively. It can be seen in Figure 3.24 that the second largest amount ice mass built up in case of $\alpha = 0^o$, which was not expected and probably could happens due to a slightly higher MVD. Similar to the two previous cases of ice accretion, the reduction of lift coefficient and the ice growth are nearly linear. The largest ice accretion was observed at higher angles of attack, 39.2 $g/min/m$ at 11 ^{o} while only 29.9 $g/min/m$ was registered at 4 ^{o}. The lift curves are almost parallel, although the slope of the 11 ^{o} AOA curve slightly differs from the others.

In Figure 3.25, the collected rime ice shapes are plotted for the different angles of attack. All the water droplets freeze on impact, thus there is no run-back ice formation. In case of 0° AOA, the largest amount of the ice built up on the leading edge, whereas as AOA increased, the larger the surface area, which was exposed to the flow, gets therefore more water droplets could stick on the surface.
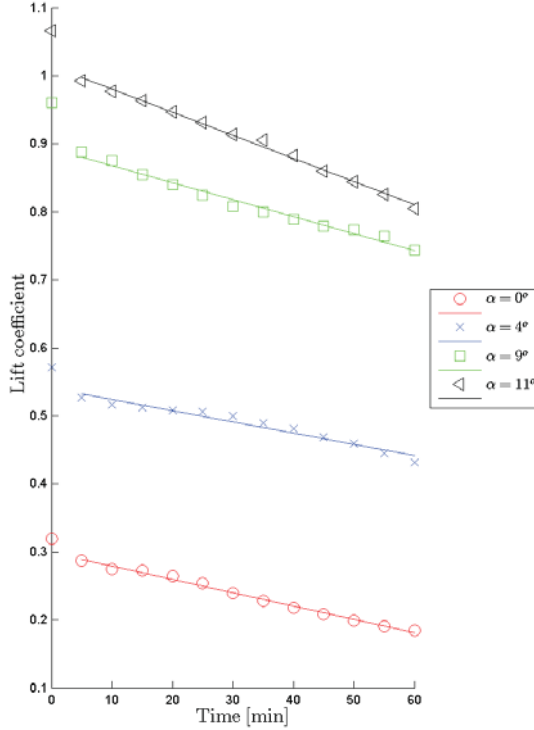
Figure 3.23: *Lift coefficient as a function of ice accretion time for different angles of attack in case of rime ice accreted for $Re \simeq 6E5$ $MVD \simeq 20m$ and $LWC \simeq 0.6g/m^3$ on a NACA 64-618 profile. A first order polynomial was fitted to the measurement.*

Figure 3.24: *Accreted ice mass as a function of ice accretion time for different angles of attack in case of rime ice for $Re \simeq 6E5$ $MVD \simeq 20m$ and $LWC \simeq 0.6g/m^3$ on a NACA 64-618 profile. A first order polynomial was fitted to the measurement.*

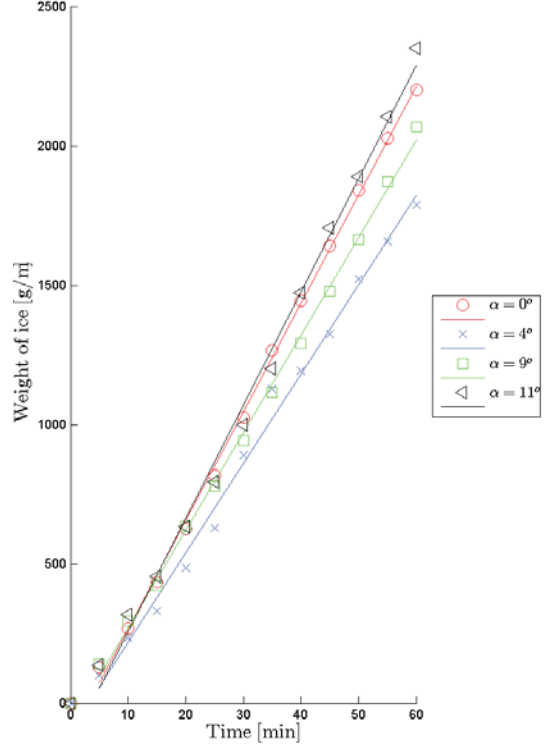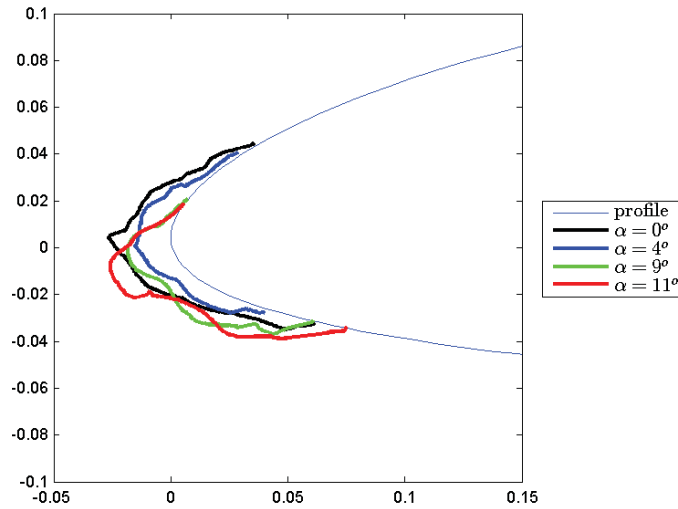**Figure 3.25:** *Shapes of ice accretion for the different angles of attack collected after 60 minutes of ice accretion in case of rime ice tests for $Re \simeq 6E5$ $MVD \simeq 20m$ and $LWC \simeq 0.6g/m^3$ on a NACA 64-618 profile.*
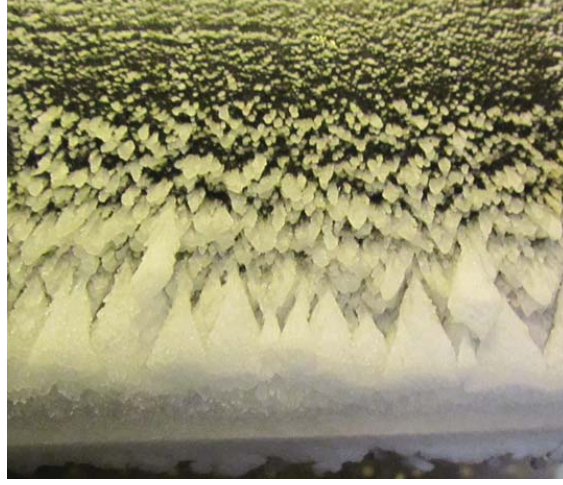
Figure 3.26: *Photo of the 4ᵒ angle of attack rime ice test collected during ice accretion with $Re \simeq 6E5$, $MVD \simeq 20m$ and $LWC \simeq 0.6g/m^3$ for a NACA 64-618 profile.*

A typical rime ice formation is shown in Figure 3.26. The white feathers are sharp and the surface is rough (see another close-up photo of the feathers in Figure B.1 in Appendix B). It was observed that the suction side of the airfoil was covered with tiny, white and dry droplets, which were easily removable. These icing features have a resemblance to dry snow (for a better look see Figure B.3 c in Appendix B). Although the location of the stagnation line is not as obvious for the rime ice deposit in Figure 3.25 as for e.g. glaze ice (Figure 3.16), it is visible in the example shown in Figure 3.26. It can be seen that as the feathers at the leading edge grow to a certain size another row of feathers starts to develop from the outer area growing towards the stagnation point hence covering up the existing feathers. The leading point of the feather only grows to a certain position forming a vertical ice "wall" around the stagnation point.

3.7.4 $\alpha = 7^o$ tests

Since it was quite clear from the amount of the accreted mass given in Table 3.8 that there was a different MVD set for the $\alpha = 7^o$ tests, therefore they are discussed separately from the others.

The reduction of the lift coefficient as a function of accretion time for the three different ice types is shown in Figure 3.27. As it is seen, first order polynomials could be fitted to the points, thus the degradation process is almost linear. The lift coefficient decreased the least, 22 % in case of rime ice tests and most significant for mixed ice tests, 34 %. For the glaze ice test, the degradation was 25 %. Similarly to the previous cases, the degradation is already visible after 5 minutes into the accretion.
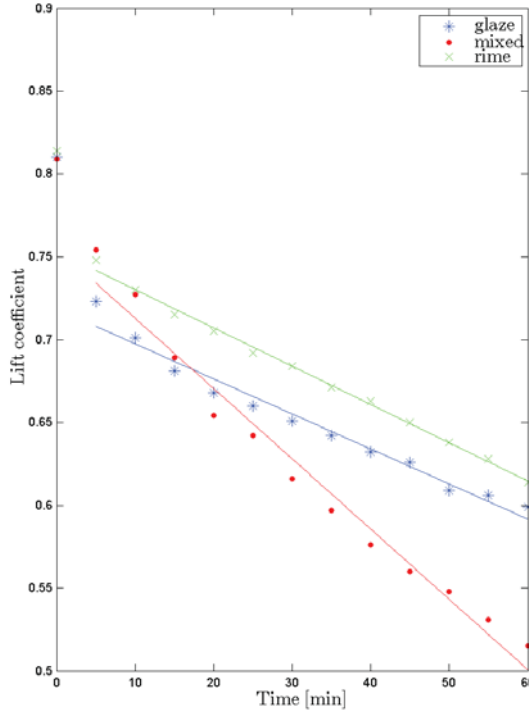
Figure 3.27: *Lift coefficient as a function of ice accretion time for $\alpha = 7^o$ in case of glaze, mixed and rime ice, $Re \simeq 1E6$, $MVD \simeq 25m$ for glaze and mixed ice and $MVD \simeq 20m$ for rime ice and $LWC \simeq 0.6 - 0.65g/m^3$ for a NACA 64-618 profile. A first order polynomial was fitted to the measurement.*

Figure 3.28: *Accreted ice mass as a function of ice accretion time for $\alpha = 7^o$ in case of glaze, mixed and rime ice, $Re \simeq 1e^6$, $MVD \simeq 25m$ for glaze and mixed ice and $MVD \simeq 20m$ for rime ice and $LWC \simeq 0.6 - 0.65g/m^3$ for a NACA 64-618 profile. A first order polynomial was fitted to the measurement.*
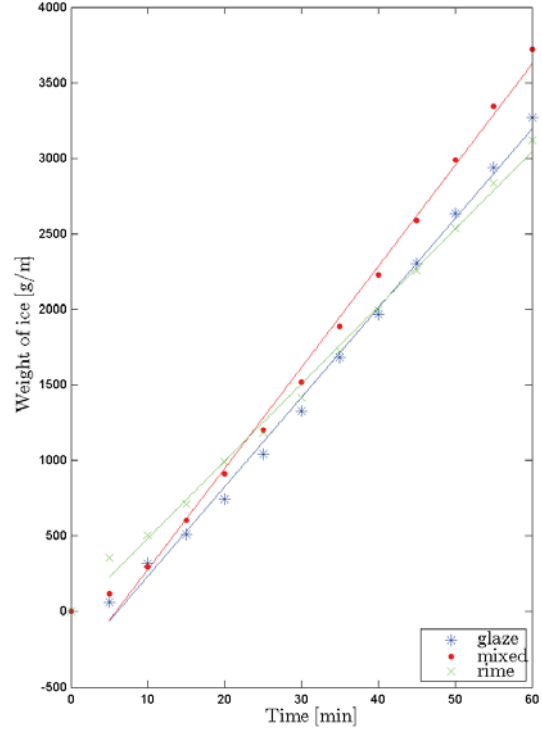
The most ice mass accretion was seen in case of mixed ice and the least for rime ice, see Figure 3.28. In Figure 3.29, the collected ice profiles are shown. It can be seen, that the smallest ice deposit was building up in case of the rime ice test while the largest one in case of the mixed ice test. The rime ice accreted only on the leading edge of the airfoil, whereas the other two types accumulated also on the pressure side of the airfoil.

3.7.5   Flow visualization

Flow visualization was performed in order to see how the flow changes around the airfoil's leading edge due to ice accretion. Because of the placement of the smoke generator and the laser, it was only possible to capture the flow at the suction side. In Figure 3.30 a, Figure 3.30 b and Figure 3.30 c, flow visualization around glaze ice, mixed ice and rime ice accretion, respectively, can be seen. The ice build-up can be found in the right corner. It can be noticed that the ice deposit disturbs the flow significantly in all cases. It was expected that the flow is rather well-attached for the clean airfoil, which was then also experienced during the numerical analysis.

It can be seen in Figure 3.30 that the sharp ice edge causes local, immediate separation
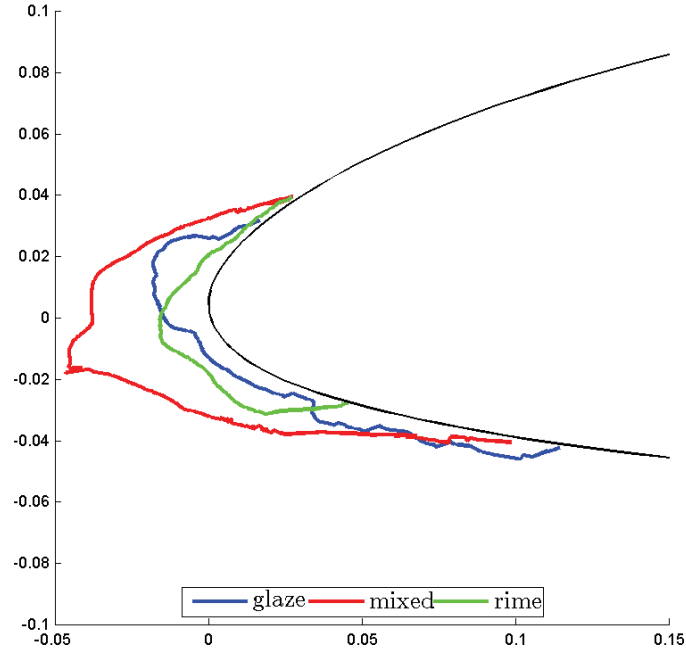
Figure 3.29: *Collected ice profiles from the wind tunnel tests for $\alpha = 7^o$ after 60 minutes of accretion in case of glaze, mixed and rime ice, $Re \simeq 1E6$, $MVD \simeq 25m$ for glaze and mixed ice and $MVD \simeq 20m$ for rime ice and $LWC \simeq 0.6 - 65g/m^3$ for a NACA 64-618 profile.*

and recirculation zone behind the ice peak for rime and mixed ice accretion. In case of glaze ice, the local separation is not as strong, however the flow is highly disturbed by the small ice beads formed in the airfoil.

3.7.6 Drag coefficient measurement

Due to the test set-up, the force transducers turn when the AOA was changed, i.e. a wing fixed coordinate system was used. Therefore, the drag forces had to be calculated from the measured component forces. The in-line forces were very small compared to the measuring range of the transducers causing high uncertainties. An example of the changes of drag coefficient at $\alpha = 7^o$ is shown in Figure 3.31.

As ice accumulated on the surface, the drag coefficient increased. The largest increment was found in case of mixed ice accretion. It can be also noticed that however the initial changes in the first 5 minutes were significant, they were not as significant as it was seen for the lift coefficient.
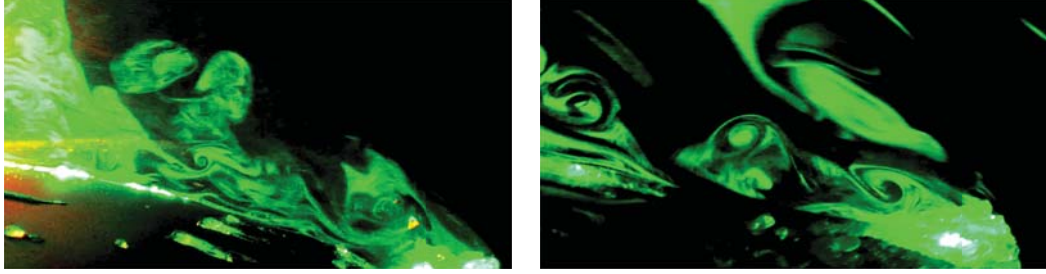
(a) Flow visualization of glaze ice accretion for $\alpha = 11^o$

(b) Flow visualization of mixed ice accretion for $\alpha = 11^o$
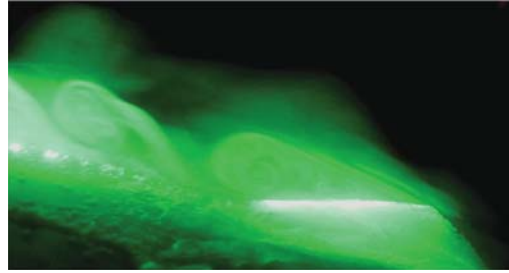
(c) Flow visualization of of rime ice accretion for $\alpha = 7^o$

Figure 3.30: *Flow visualization of ice accretion.*
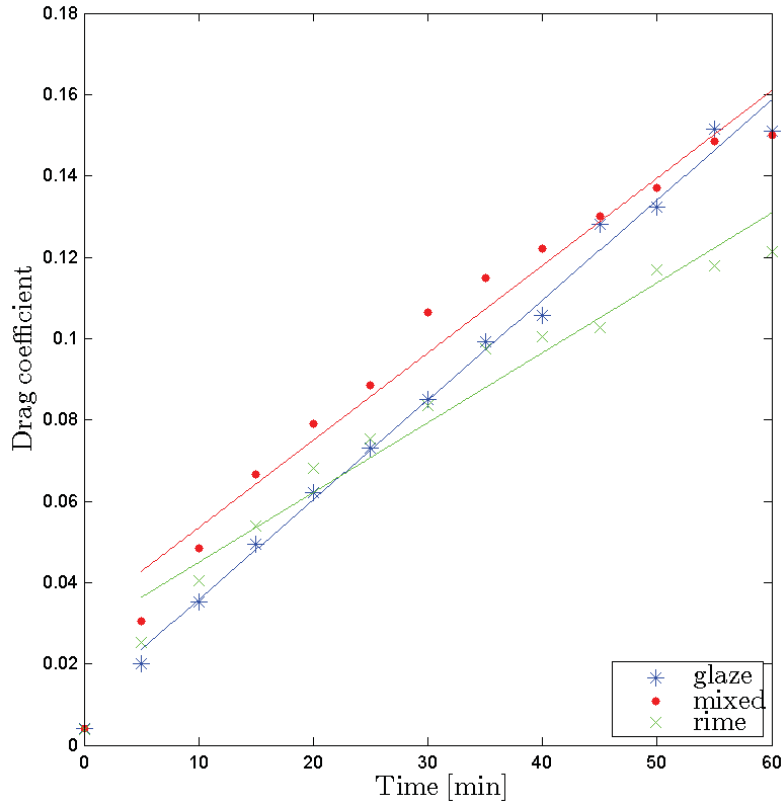
Figure 3.31: *Drag coefficient as a function of ice accretion time for $\alpha = 7^o$ in case of glaze, mixed and rime ice, $Re \simeq 1E6$, $MVD \simeq 25m$ for glaze and mixed ice and $MVD \simeq 20m$ for rime ice and $LWC \simeq 0.6 - 0.65 g/m^3$ for a NACA 64-618 profile. A first order polynomial was fitted to the measurement.*

3.7.7   Melting process

No significant changes were found neither for the weight of the ice mass nor for the aerodynamic forces as long as the air temperature stayed below 0 ^oC. However, as soon as the temperature rose above freezing point, the melting process started. As air temperature increased the ice deposit became smoother and more streamlined. When the temperature of the airfoil was above the freezing point, the warmer environment started to heat the ice from inside and hence it started to melt. A very thin layer of melt water appeared between the ice and the airfoil surface, which is assumed to cause ice shedding in case of a rotating blade. In case of this stationary set-up, it was seen that when the gravity force of the ice deposit was larger than the adhesion force caused by the water layer and the aerodynamic forces, the ice deposit fall off (e.g. in case of mixed ice tests). In case of smaller ice accretion (like rime ice), the ice stayed on the airfoil until it melted completely.

Since the surface temperature of the airfoil was not monitored during the experiments, it was not possible to precisely identify when it rose above zero and thus when the melting from inside began (i.e. the ice deposit would be shed off the rotor). Therefore further investigation of the melting process was not done.

3.8   Discussion of results of wind tunnel tests

The above presented results are analysed and compared in this section. Direct comparison of the rime ice measurements is limited to the other two types due to the lower wind speed applied during the ice accretion. Significant difference between the $\alpha = 7^o$ tests and the other tests was only seen in case of the amount of the accreted ice mass. The more ice accumulated on the airfoil for $\alpha = 7^o$ likely due to a different MVD set-up. Since the weight of ice was subtracted from the lift measurements, it does not have any effect on the lift coefficient.

In all presented cases, it was found that the lift coefficient decreased right after ice started to build up on the airfoil. The immediate change is associated to the aerodynamic properties of an airfoil, which depend strongly on the surface roughness as it was also shown by e.g. Addy [2000] and Lynch and Khodadoust [2001]. The instantaneous reduction of the lift coefficient, as shown in Table 3.8, is more significant for higher angles of attack because the surface roughness is changed over a larger area. This is reflected by the lift coefficient curves (in Figure 3.14, Figure 3.19, Figure 3.23 and Figure 3.27) where the slope of the drop in the first 5 minutes is much steeper than of the polynomials fitted to the points. Consequently, the surface roughness itself has higher influence on the immediate lift degradation than the altered airfoil profile. It can be also noticed in these figures that the difference between the immediate reduction of lift coefficient for the different ice types is not significant, which indicates that the initial degradation is independent of the ice formation type for the same angle of attack.

Nearly linear ice build-up process was seen in all cases and that assumption was also supported by the layered structure seen in Figure 3.12. Even though the least amount of ice built up on the airfoil at 0° AOA, the relative reduction of lift was the most severe here. The reason could be that at low angle of attack, ice was accreted mainly at the leading

edge, changing the geometry of the profile and thus causing higher disturbance in the flow at the suction side than at higher angles. In case of larger incident angles, the ice shape is flatter and follows the streamlines on the pressure side, as shown in Figure 3.16, Figure 3.21 and Figure 3.25, and thus induces less flow disturbance on the important suction side. It appears that the angle of attack has an influence on the mass and also on the shape of the ice deposit. The same conclusion was drawn from the numerical simulations by Homola et al. [2009] and Virk et al. [2010a].

Larger amount of ice built up in case of mixed ice tests compared to glaze ice tests for the same angle of attack (except in case of 9 ^{o}, probably due to a slightly different droplet size). It is due to the nature of the mixed ice, when the temperature reaches lower levels and becomes sufficiently cold for rime ice formation, all the water particles freeze on impact, causing larger ice deposit on the already altered airfoil profile. Since the local collection efficiency of the airfoil's surface is increased in the areas where ice already formed, the ice accretion process speeds up and also increases in complicity (Battisti [2009]). The reduction of lift coefficient was more significant in case of mixed ice deposit than for glaze ice. The reason could be the very irregular mixed ice shapes, which highly disturbed the flow around the airfoil.

Both Jasinski et al. [1997] and Bragg et al. [2005] pointed out that the lift coefficient based on the original chord was sometimes higher in case of rime ice tests compared to the clean airfoil. This behaviour was not seen during the experiments presented in this paper probably because of different icing conditions and accretion time and thus different ice shape and size.

The mass of accreted ice highly depends on the wind speed, the temperature and liquid water content and the droplet size [Makkonen, 1984]. The latter three parameters were set to ensure the environmental conditions necessary for the chosen ice formation type. It was experienced that even a very small change in the droplet size led to significantly different ice mass. Due to the limitations of the wind tunnel's cooling capacity, considerably lower wind speed was applied than what it is acting on the tip region of a wind turbine. Therefore the accumulated ice mass is less than it would have been in case of the outer part of a wind blade.

Although the physical characteristics of the ice deposits were similar to the one published in other studies e.g. Bose [1992] and ISO 12494 [2001] standard, some differences were observed. In case of glaze ice deposits, as it can be seen in Figure 3.18, the ice deposit is the consists of small beads. It was seen during the experiments that the water droplets, which did not freeze on impact, formed small beads before they eventually ran off. Every 5 minutes, the tunnel and the spray system was set to idle for approximately one and a half minutes in order to measure the weight of the accreted ice mass. Even though this period is short, it could provide just enough time to get these large water droplets to freeze. At low air speeds such as 5-10 m/s, the gravity has significant influence on the vertical deflection of the droplet trajectories, causing gravitational sedimentation (Kollár et al. [2005]), which could be the reason for the dry ice sedimentation seen on the suction side in case of rime ice accretion during the experiment (see Figure B.3 c in Appendix B).

In case of the mixed ice tests, the observed peak at the stagnation point in Figure 3.21 and Figure 3.29 could probably be formed also due to the static feature of the tests. These peaks are not experienced or have been reported yet in case of an actual rotating wind turbine blade. It also has to be kept in mind that due to atmospheric turbulence, wind shear, and tower passage, the angle of attack is varying in time around a mean value on a wind turbine blade, which will give a broader ice accretion at the leading edge since the stagnation point is not constant.

In case of the drag coefficients, it has to be noted, that the values are very likely incorrect due to the high uncertainties of the measurement of small forces. However, the trend of the changes of drag coefficient is as it was expected, i.e. as AOA increased, the ice accretion caused increase in the drag because the area exposed to the wind got larger (ISO 12494 [2001]). Although there are other methods of drag force measurements, but due to the nature of the experiments, none of them were suitable. E.g. in case of using a wake rack with pressure devices would have failed because the small pressure tubes would very likely have frozen immediately, making the measurements impossible.

Melting was observed during the test campaign as well. It was noticed that there was almost no mass changes until the air temperature was subzero. When the surface temperature of the airfoil rose above the freezing point, ice started to melt from "inside" producing a thin water layer between the ice and the airfoil. At that point, the ice would have shed off the blade if it was rotating, but due to the static nature of the test it was not.

The flow visualization confirmed that the flow was highly disturbed by the ice accretion. In Figure 3.30 b and Figure 3.30 c, the mixed and rime ice accretion can be seen, respectively. As a typical feature of these types of ice, ice feathers with sharp edges formed. These edges caused immediate flow separation and thus vortices and small recirculation zones at the suction side. In case of the glaze ice formation, smooth surface and therefore less disturbance was expected, but due to small ice beads the flow pattern was disturbed quite significantly, as seen in Figure 3.30 b.

3.9 Conclusion drawn from the experimental study

In this chapter, the results of a series of experiments on a NACA 64-618 profile in a climatic wind tunnel were presented. There were a number of tests performed at different angles of attack and temperatures to monitor the alteration of aerodynamic forces along with the weight of accumulated ice throughout the first 60 minutes of ice accretion under controlled conditions. It was seen that all types of ice had significant negative influence on the flow field around the airfoil. The flow visualization confirmed that the flow was highly disturbed by the ice accretion. Both the ice accretion and the lift coefficient degradation showed a nearly linear trend. The alteration of the surface roughness has a more significant influence on the initial lift coefficient than the shape of the changed airfoil profile. As the angle of attack increased the larger the degradation of the instantaneous lift coefficient got.

It was also found, that not only the temperature, but also the angle of attack has an

influence on the mass and also the shape of ice deposit. Even though the least amount of ice built up on the airfoil at low angles of attack, the relative reduction was the most severe in these cases, i.e. the higher the angle of attack the lower the relative lift coefficient degradation.

The importance of MVD was experienced when a small, accidental change caused out of trend ice mass accretion on the airfoil. More ice built up on the airfoil during the mixed ice tests than during the glaze ice tests and hence caused more significant lift coefficient degradation.

Similarly to previous studies, the shape and mass of ice deposits were found to be highly dependent of LWC, MVD and temperature. Although most of the physical characteristics were in good agreement with the expectations based on other studies and standards, there were some differences observed. During glaze ice accretion, tiny ice beads froze to the surface and in case of mixed ice, a sharp nose-like ice peak formed around the stagnation point. It is suspected that both formation occurred due to the nature of the wind tunnel tests.

The changes of drag coefficient was monitored as well. The increase was found to be also a nearly linear process for all ice types. It is, however, suspected that the measured values are much higher due to the measurement range of the used transducers.

It can be concluded that even one hour of ice accretion has significant influence on the aerodynamics of the airfoil and the angle of attack at which the ice builds up on the surface is highly important.

In order to be able to properly study the impact of ice on drag force, a more suitable measuring system is needed, which is either heated so it could handle the impacts of ice or is a different force transducer, which has a better response to low forces. An infra-red camera would be very useful to study the mechanism of melting. In that way the surface temperature of the ice and the airfoil would be followed.

Chapter 4

Numerical investigation of icing of wind turbine blades

In this chapter a numerical investigation of the impact from ice accumulation on wind turbine blades is presented. As it was mentioned in the previous chapter, ice profiles were collected for further numerical analysis during the wind tunnel tests. They were directly compared to results of the dedicated ice simulation model, TURBICE from VTT, Technical Research Centre of Finland in order to validate the ice shapes and to calibrate the wind tunnel parameters for LWC and MVD. The collected profiles were also used to numerically analyse the impacts of ice accretion on the flow behaviour and the aerodynamic characteristics of the airfoil using Ansys Fluent. This chapter gives a short summary of the most relevant publications in the field and details the set-up and results of the present numerical study.

4.1 Introduction to numerical investigation

In the recent years, especially due to the tremendous increase in computing power, CFD simulations, even in 3D, has become much faster. It is now also possible to some degree estimate the shape and mass of ice deposit on airfoils and thus determine the performance of an iced wind turbine more punctual than earlier. The ice accretion models have been improved and the impacts of ice on wind turbine behaviour are also known better by now (Makkonen et al. [2001]), but there are still several issues and unsolved problems when it comes to the prediction of ice risk and production loss.

There are presently dedicated ice accretion models available on the field. One of the most well-known model is Nasa's LEWICE, which is built up of four modules; potential flow field calculation, particle trajectory and impingement calculation, thermodynamic and ice growth calculation, and finally the geometry modification due to ice growth. The ice accretion itself is a time-stepping procedure (Wright et al. [2008]). Another, comprehensive numerical ice accretion software is TURBICE from VTT Technical Research Centre of Finland, which also uses the panel method to calculate the potential flow (Makkonen et al. [2001]). The results have been verified by icing wind tunnel testing of both aircraft and wind turbine airfoils (Homola et al. [2010b]). Fensap-ICE is an aerodynamics and icing simulation system from Newmerical Technologies International (NTI). This model was developed for solving aeronautic issues, however it has been recently used in wind energy applications (Virk et al. [2010b], Virk et al. [2012] and Reid et al. [2013]).

There are three modules set in a loop; the flow field calculation using the compressible Navier-Stokes equations with FENSAP (or other solvers), the computation of the collection efficiency distribution with DROP3D, and then the prediction of the ice accretion shape by a shallow-water icing model with ICE3D (Habashi et al. [2001]).

Simulations with computational fluid dynamics (CFD) based techniques are used to numerically analyze the impacts of ice accretion on the flow behavior and the aerodynamic characteristics of the airfoil. The analysis can be done using either an individual CFD program, e.g. Ansys Fluent, or aerodynamics and icing simulation program with built-in CFD module such as Fensap-ICE.

In some recent studies, the numerical simulations were carried out in two steps (e.g. Virk et al. [2010a], Etemaddar et al. [2012]). In the first step, the physical characteristics of the accreted ice (e.g. shape and size) were predicted with one of the above described ice accretion models. In the second step, CFD analyses were performed on the iced airfoil to estimate the effect on drag and lift forces. Homola et al. [2010a] combined TURBICE and Ansys Fluent to investigate the effect of ice on a NACA 64-618 profile. The ice profiles were the results of three different droplet sizes and air temperatures and they were analysed at different angles of attack ranging from -10° to $+20^o$. The lift coefficient was found to be reduced in all cases and the smallest change was observed in case of streamlined rime ice, while there was larger reduction experienced with horn shaped glaze ice. During the CFD simulations, it was found that the horn type glaze ice caused the largest separation, and thus significant lift reduction and higher drag coefficient.

Etemaddar et al. [2012] was also using a NACA 64-618 in their numerical analysis, however instead of TURBICE, they used LEWICE. It was found that the ice load increases with liquid water content (LWC), median volume diameter (MVD) and relative wind speed.

Two 2-D studies (Virk et al. [2010b] and Virk et al. [2012]) have been carried out using Fensap-ICE. Virk et al. [2010b] studied only one section with different angles of attack and atmospheric temperatures, whereas Virk et al. [2012] selected five sections along the blade radius, thereby each tests were performed with different angle of attacks and relative wind speeds. The results showed that the angle of attack has influence on the rate and shape of ice growth and for lower angle of attacks the icing is less severe near to the tip (Virk et al. [2010b]).

Recently, a 3D study was done with Fensap-ICE by Reid et al. [2013]. They pointed out that the largest performance degradations were seen at lower wind speed, where the ice deposit caused small separations in places where it was not experienced with the clean profile.

4.2   Numerical set-up

The iced airfoil profiles, which are used for the numerical analysis, were collected with contour tracing method during icing wind tunnel tests, see details in Section 3.3. The collected ice profiles were further analysed in Ansys Fluent at different wind speeds and were verified by TURBICE ice accretion model. The main goal was to validate the wind tunnel measurements by numerical methods.

4.2.1   Ice accretion simulation

In order to verify the collected ice profiles and to calibrate the environmental parameters in the wind tunnel, which are difficult to measure accurately, computations were performed with a numerical ice accretion model, TURBICE from VTT, Technical Research Centre of Finland. Constant air temperature is an input parameter of the program. For mixed ice, it is necessary to have variable air temperature, therefore that ice type could not be tested. MVD, LWC, meteorological wind speed, rotating speed of the wind turbine, pitch angle, air temperature, air pressure and accretion time had to be specified before the analysis. These parameters were chosen to ensure similar environment as it was set during the wind tunnel tests. In Table 4.1, the simulation parameters of the validation tests are listed.

Table 4.1: *Input parameters of validation simulations with TURBICE.*

Parameters	Glaze test					Rime test				
	1.	2.	3.	4.	5.	1.	2.	3.	4.	5.
AOA (^{o})	0	4	7	9	11	0	4	7	9	11
MVD (μm)	27	27	27	27	27	23	23	23	23	23
LWC (g/m^3)	0.65	0.65	0.65	0.65	0.65	0.6	0.6	0.6	0.6	0.6
T (^oC)	-3	-3	-3	-3	-3	-8	-8	-8	-8	-8
U (m/s)	15	15	15	15	15	10	10	10	10	10
Time (min)	60	60	60	60	60	60	60	60	60	60

TURBICE code is described in details by Makkonen et al. [2001] and hence, the following description of the built-in models is brief. The model uses iterative method for finding the upper and lower grazing trajectories. TURBICE models ice build-up on a 2-D airfoil in potential flow field. The flow field is perpendicular to the airfoil axis and calculated by the panel method. Depending on the angle of attack, the number of panels varies between 40 and 120. First, droplet trajectories are integrated by the steady state equations using fifth order Runge-Kutta scheme, beginning at 10 chord length upstream of the section. Both the potential flow solution and the droplet trajectories are recalculated in the model after each simulated ice layer. The local collision efficiency at the impact point is derived from the ratio of the initial perpendicular separation between two closely spaced droplet trajectories to the final separation of their impact points.

The surface roughness of ice has significant effect on both the heat transfer from the airfoil and on the whereabouts of location where the transition from laminar to turbulent flow occurs. The model calculated the sand grain roughness of the ice layer. The icing process

itself is time-dependent. The time dependency in the roughness model is accounted for the multiplication factor, which depends on the freezing point, and the number of simulated ice layers.

In order to calculate the heat and mass transfer, the surface of the airfoil section is divided into finite areas. The mass and energy balance of these areas are used to determine the freezing fraction and the surface temperature. When the freezing fraction is zero, ice does not form, whereas when it is unity, rime ice accretes on the surface. In the energy balance, TURBICE takes into account convection, evaporation, droplet heating, IR radiation, friction and heat contained in the runback water. Based on the local values of ice mass flux and density, the local ice thickness and thus ice layers can be calculated in a small time step.

The growth direction of rime ice is the mean direction of arrival of the droplet trajectories. In case of glaze ice the growth direction depends on the freezing factor, e.g. when it tends to unity the growth direction is the same as in rime icing. In the runback area, the ice grows perpendicular to the local area.

4.2.2 Computational fluid dynamics

Simulations with Ansys Fluent were conducted to quantify the impacts of ice accretion on the flow behavior and the aerodynamic characteristics of the iced airfoil from the wind tunnel tests. First, the aerodynamic forces measured during the experiments were verified. Due to the limitation of the CWT's cooling unit, it was necessary to set relatively low target wind speed (15 m/s which corresponds to approximately $Re \simeq 1E6$) to ensure stable and low enough air temperature. A number of numerical tests were performed with higher wind speeds, i.e. 25 m/s ($Re \simeq 1.5E6$) and 40 m/s ($Re \simeq 2.5E6$) as well. For each simulation, profiles with ice deposit accreted at the same AOA as the investigation of the flow behaviour and the aerodynamic characteristics were done, were used. These tests are referred as "dedicated profile" tests or simulations.

The impact of angle of attack was investigated with one single ice profile. For this investigation, the glaze and rime iced airfoils collected at $\alpha = 0^o$ and 11° were chosen and they were tested in flows with 0°, 4°, 7°, 9° and 11° incident angles and 25 m/s wind speed. These tests are referred as "single profile" tests or simulations.

The ice profiles were collected from specific spanwise locations, and therefore 2-D models were constructed in Ansys Workbench. The control volume around the airfoil was rectangular with edges positioned at 50 chords length away in vertical direction and 20 chords length from the horizontal direction.

An inflation layer was added to the mesh to produce a structured, fine mesh in the vicinity of the airfoil (see Figure 4.1) to achieve the desired wall Y^+ distribution and thus to give a better representation of the flow near the airfoil surface. The first layer height is dependent on the surface roughness, since the roughness height may not exceed it. However, it was experienced that Ansys Fluent cannot properly handle micro surface roughness, therefore it was not included in the analysis, see detailed explanation in the next section.

Table 4.2: *Setup of mesh and inflation layer of each dedicated profile simulations in Ansys Workbench. *In case of the clean airfoil, the number of nods and elements were slightly different for each simulations due to the various angles of attack.*

Profile	AOA	First layer height (m)	Nr. of layers of inflation layer	Growth rate	Nr. of nods	Nr. of elements
Clean	all	$1e^{-5}$	50	1.2	~ 81250	$\sim$ 81000*
Glaze ice	0	$1e^{-5}$	38	1.2	94474	93699
	4	$1e^{-5}$	38	1.2	95045	94275
	7	$1e^{-5}$	30	1.25	93878	93095
	9	$1e^{-5}$	35	1.2	94524	93767
	11	$1e^{-5}$	38	1.2	95181	94403
Mixed ice	0	$1e^{-5}$	38	1.2	96890	96107
	4	$1e^{-5}$	38	1.2	95690	94914
	7	$1e^{-5}$	40	1.2	95803	95025
	9	$1e^{-5}$	38	1.2	95072	94279
	11	$1e^{-5}$	38	1.2	94806	94030
Rime ice	0	$1e^{-5}$	38	1.2	94009	93247
	4	$1e^{-5}$	38	1.2	93315	92576
	7	$1e^{-5}$	35	1.25	94643	93843
	9	$1e^{-5}$	38	1.2	94192	93432
	11	$1e^{-5}$	36	1.2	94811	94041

Only the large scale and resolved surface roughness affected the flow. It was aimed to construct a similar mesh and thus inflation layer for all the different profiles, but sometimes due to the complexity of the ice shapes, minor changes had to be done. In Table 4.2, the setup of mesh and inflation layer of each test is summarized.

For the simulations, fully turbulent flow was assumed considering the roughness of the ice deposit. Spalart-Allmaras and $k - \omega$ SST turbulence models were used. It was found in previous studies (Mortensen [2008]) that the solution converges faster and easier using Spalart-Allmaras model than with the $k - \omega$ SST turbulence model. Therefore for the clean profiles, the first 500 iterations were done by using Spalart-Allmaras model providing an initial guess for the $k - \omega$ SST turbulence model and achieving more stable convergence. It was shown by Chung and Addy [2000] that Spalart-Allmaras model is the best performing model for ice accretion simulations and hence it was used during the iced profiles' analysis. For all cases, 5000 iterations were done to ensure stable solution.
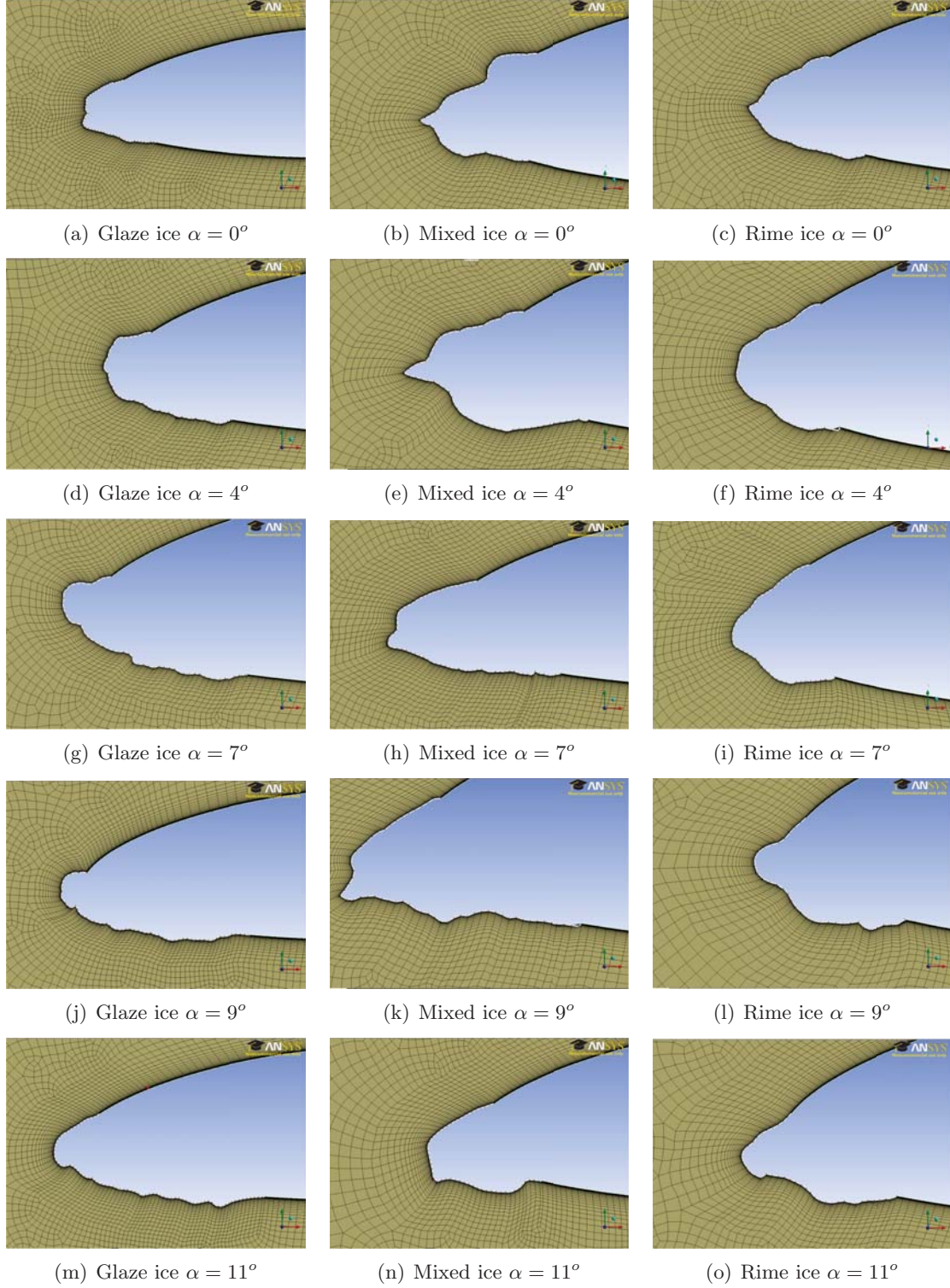
(a) Glaze ice $\alpha = 0^o$

(b) Mixed ice $\alpha = 0^o$

(c) Rime ice $\alpha = 0^o$

(d) Glaze ice $\alpha = 4^o$

(e) Mixed ice $\alpha = 4^o$

(f) Rime ice $\alpha = 4^o$

(g) Glaze ice $\alpha = 7^o$

(h) Mixed ice $\alpha = 7^o$

(i) Rime ice $\alpha = 7^o$

(j) Glaze ice $\alpha = 9^o$

(k) Mixed ice $\alpha = 9^o$

(l) Rime ice $\alpha = 9^o$

(m) Glaze ice $\alpha = 11^o$

(n) Mixed ice $\alpha = 11^o$

(o) Rime ice $\alpha = 11^o$

Figure 4.1: *Mesh around the airfoil profiles for glaze, mixed and rime ice accretion in case of $\alpha = 0^o$, 4°, 7°, 9° and 11°.*

4.3   Surface roughness

During ice accretion, the surface roughness changes as ice builds up. This causes alteration of the boundary layer and affects the convective heat transfer and also the collection efficiency of the object (Fortin et al. [2003]). Therefore proper implementation in to the numerical model would be essential. In order to study the effect of the roughness height on the results, different scenarios were set. The first layer height of the mesh is dependent on the surface roughness height, which may not exceed it, hence for each tested roughness height, a new mesh was constructed.

The iced airfoil was divided into two parts; the ice deposit and the airfoil it self. In that way it was possible to construct different inflation layer for the iced and the clean part of the airfoil and also to set surface roughness only for the ice. A test campaign was carried out with $\alpha = 7^o$ glaze ice profile. Different roughness heights were set for the ice deposit but no roughness was implemented for the airfoil, i.e. the runback ice and the tiny, rough ice formations, which were seen on the suction side in case of rime ice, were neglected. These were neglected because as it was also shown by Sagol et al. [2013], the trailing edge roughness has almost no effect on the performance and never the less it would not have been possible to properly model the runback rivulets of glaze ice accretion in 2-D. Table 4.3 gives an overview of the settings.

Table 4.3: *Set-up of inflation layer to study the effect of roughness height on the results*

Roughness height (m)	First layer height (m)	Growth rate	Nr. of layers.
0	1E-5	1.25	35
9E-6	1E-5	1.25	35
5E-5	6E-5	1.1	35
6E-5	6E-5	1.1	35
9E-5	1E-4	1.1	30
5E-4	5.5E-4	1.1	30

Table 4.4: *Lift coefficients as the results of the different roughness heights.*

Roughness height (m)	0	9E-6	5E-5	6E-5	9E-5	5E-4
C_L	0.8	0.8	0.796	0.795	0.795	0.803

In Table 4.4, the lift coefficients as the results of the different roughness heights are listed. It was found that the changes of roughness height did not have a significant effect on the forces. The largest difference in the lift coefficient was 0.56 % in case $r_h = 9E$-5 m, which is negligible small. Figure 4.2, gives an example of the velocity contours around the glaze iced airfoil at $\alpha = 7^o$ including surface roughness, $r_h = 5.5$E-4 m. Anomalies can be seen in the plot, which are marked with red circles. These anomalies could occur because the first layer height was not small enough to give a good representation of the flow near the airfoil surface.
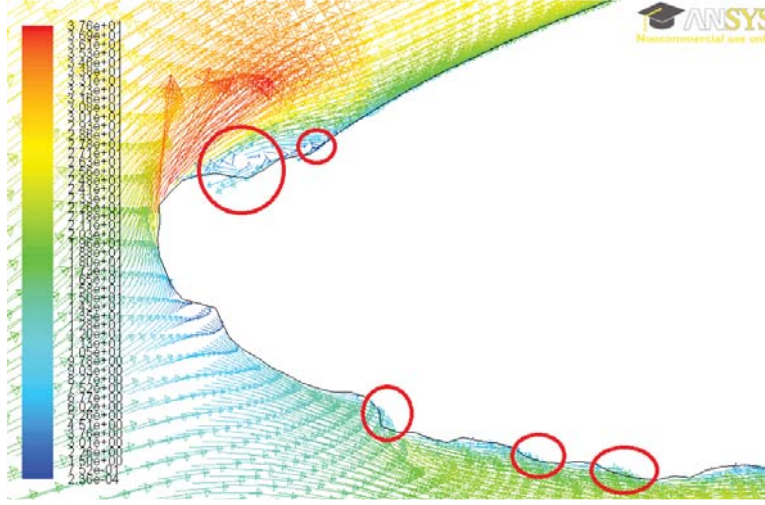
Figure 4.2: *Velocity contours example of including surface roughness into the numerical simulations. In this picture, $r_h = 5e^{-4}$ m and hence a larger first layer height of the inflation layer was chosen, $h_1 = 5.5e^{-4}m$. The red circles highlight the anomalies of the velocity contours around the airfoil.*

It was experienced that either the surface roughness height was set too low to have any significant effect on the results or the first layer height of the inflation layer was set too large to provide a proper interpretation of the flow conditions in the vicinity of the ice deposit.

An attempt was made to write a user defined function (UDF) in C programming language, which can be later used as a wall boundary condition to describe the equivalent sand grain roughness (K_s). In this step, the recommendations of Shin et al. [1991] were followed:

$$K_s = \left(\frac{K_s^*}{K_{sbase}^*}\right)_{LWC} * \left(\frac{K_s^*}{K_{sbase}^*}\right)_T * \left(\frac{K_s^*}{K_{sbase}^*}\right)_U * K_{sbase}^* * c \qquad (4.1)$$

Where c denotes the airfoils chord length and $K_{sbase}^* = 0.001177$. Temperature (T) is given in Kelvin [K] and velocity V is the air speed velocity. Each sand grain roughness parameter can be calculated as:

$$\left(\frac{K_s^*}{K_{sbase}^*}\right)_{LWC} = 0.5714 + 0.2475(LWC) + 1.2571(LWC)^2 \qquad (4.2)$$

$$\left(\frac{K_s^*}{K_{sbase}^*}\right)_T = 0.047T - 11.27 \qquad (4.3)$$

$$\left(\frac{K_s^*}{K_{sbase}^*}\right)_V = 0.4286 + 0.0044139V \qquad (4.4)$$

Although the UDF was written and imported to Fluent, the issue with the first layer height of the inflation layer was not solved. It was also experienced, when the temperature was accidentally given in [^oC] as an input parameter and thus the output of $\left(\frac{K_s^*}{K_{sbase}^*}\right)_T$

became negative and so did K_s. However, there was not any error messages given by Fluent and the simulation could run without any problem, which clearly indicates the issues with the roughness handling of Fluent.

Based on these results and experiences, it was decided not to implement the micro surface roughness in order to be able to properly simulate the flow conditions close to the airfoil and ice surface and to ensure the validity of the log law.

4.4 Results of numerical investigation

4.4.1 Ice accretion simulation

The aim of the TURBICE tests was to validate the collected ice profiles and the setting of the meteorological variables, especially MVD and LWC. Therefore a set of simulations were performed using the same input parameters as the target values of the wind tunnel tests. In Figure 4.3, the TURBICE profiles are plotted against the experimental ones for glaze and rime ice for $\alpha = 0^o$ (the profiles of the other four angles of attack can be found in Appendix D).

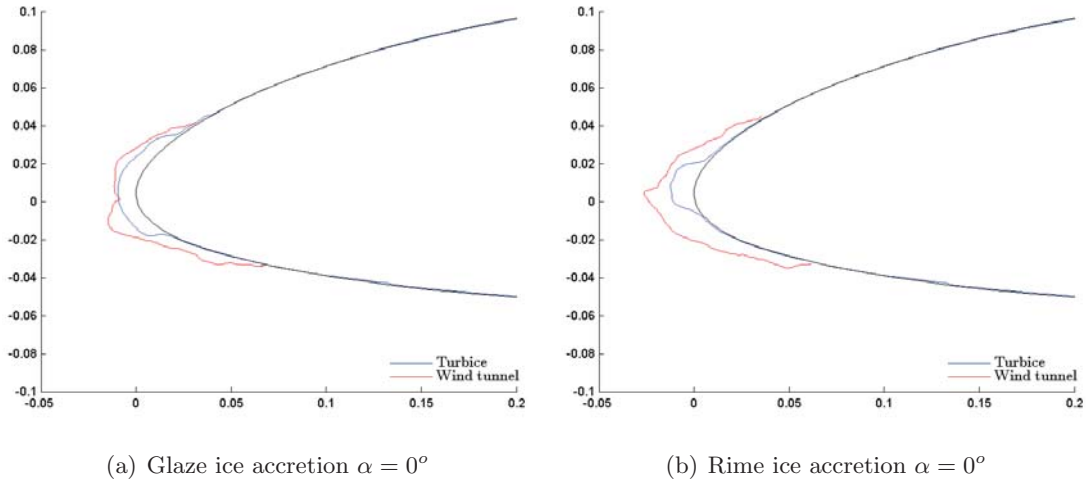(a) Glaze ice accretion $\alpha = 0^o$ (b) Rime ice accretion $\alpha = 0^o$

Figure 4.3: *Results of TURBICE simulation plotted against the profiles from the wind tunnel tests for both glaze and rime ice accretion at $\alpha = 0^o$.*

As it can be seen in these plots, the numerical profiles are significantly smaller than the ones from the wind tunnel, which indicates underestimation of the input parameters, especially the MVD.

Therefore additional simulations were performed in order to find the valid combination of LWC and MVD. The first TURBICE tests run with 90 minutes accretion time, but after the first wind tunnel experiment, it was obvious that 60 minutes accretion time is long enough to produce significant amount of ice on the airfoil and considerably reduce the lift coefficient. Therefore the accretion time in TURBICE had to be also reduced. However the already collected 90 minutes data could provide help in finding the valid

MVD and LWC combination. In Figure 4.4, sets of ice profiles with different MVD and LWC combinations are plotted against the one from the wind tunnel tests. Figure 4.4 a and b show different glaze ice accretion scenarios for $\alpha = 4^o$ and 9°, respectively. In Figure 4.4 c and d, the same angles of attack can be seen for rime ice. (The profiles of the other angles of attack can be found in Appendix D.)
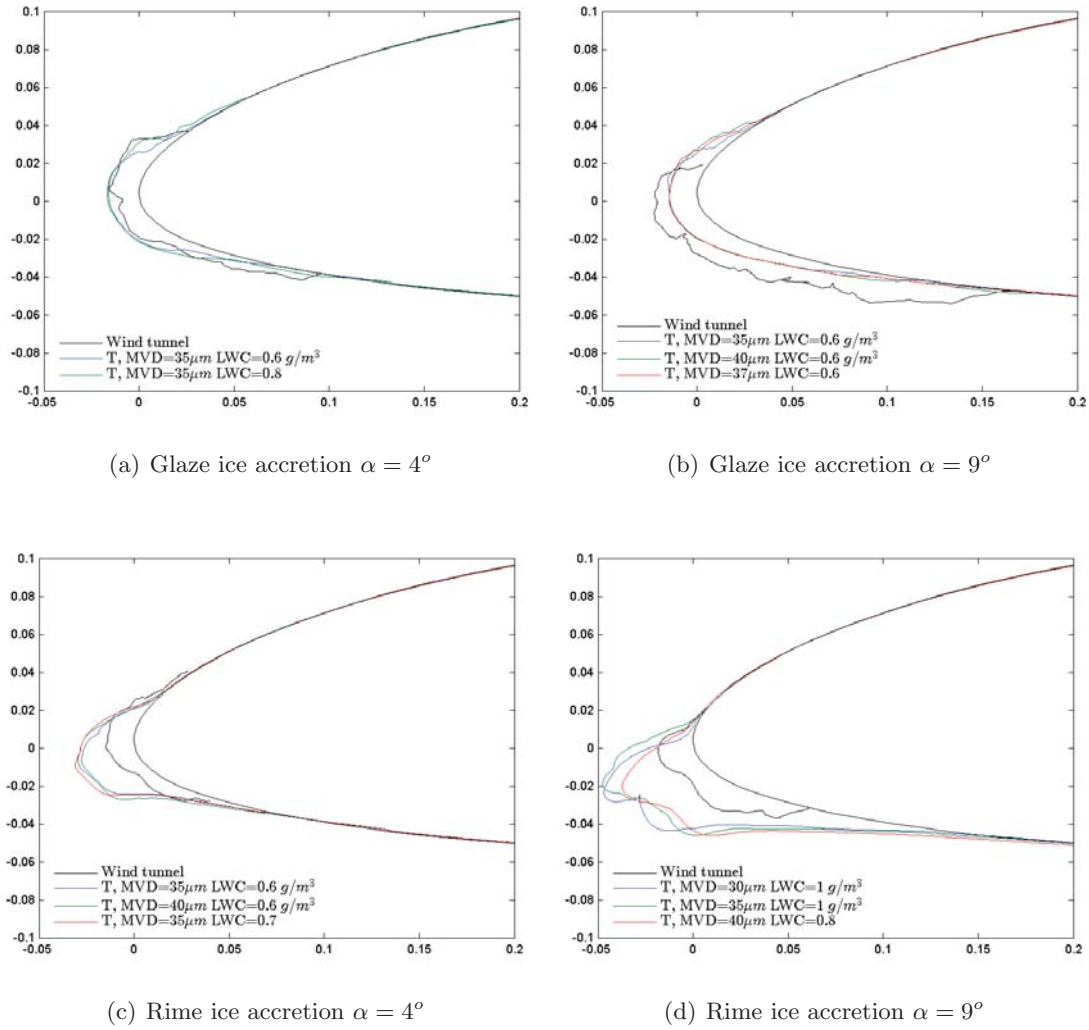

(a) Glaze ice accretion $\alpha = 4^o$

(b) Glaze ice accretion $\alpha = 9^o$

(c) Rime ice accretion $\alpha = 4^o$

(d) Rime ice accretion $\alpha = 9^o$

Figure 4.4: *Results of different settings of TURBICE simulation plotted against the profiles from the wind tunnel tests for glaze and rime ice accretion. In the first row, profiles collected at $\alpha = 4^o$ and 9° can be seen for glaze ice and in the second row for rime ice.*

For glaze ice profile from the wind tunnel tests (see red curves in the plots above), a large amount of ice deposit can be noticed at the pressure side of the airfoil for higher AOA compared to the results of the numerical simulations. When MVD was even higher the run back ice at the pressure side did not got thicker but it spread in a much larger area. In Figure 4.4 a and b, it can be seen that the computational ice profiles, which were accumulated for 90 minutes, are smaller than the ones from the wind tunnel therefore it

was decided to continue the investigation only with rime ice profile.

The results gave the best fits for all angles of attack for rime ice accretion with $LWC \simeq$ $1g/m^3$ and $MVD \simeq 40\mu m$ and rather than 0.6 g/m^3 and $23\mu m$, as specified by the manufacturer of the spray nozzles based on the setted water and air pressure. It is assumed that for glaze ice, MVD and LWC are higher than these values because of the slightly different settings.

4.4.2 Computational fluid dynamics

There have been in all 60 dedicated profile simulations performed with Ansys Fluent, including clean, glaze iced, mixed iced and rime iced airfoils with different wind speeds (15 m/s, 25 m/s and 40 m/s). 15 m/s wind speed was chosen to simulate similar flow conditions as in the wind tunnel to compare the results directly. Higher wind speeds were investigated to see the influence of ice on the lift coefficient for more realistic situations.

Table 4.5 summarises the lift coefficients for the clean profiles for different wind speeds. Comparing these results to the wind tunnel measurements, it is indicated that the vertical walls had significant influence on the measurement. It can be seen that the numerical analysis gave 20 % higher lift coefficients. This suggests that the effective airfoil span is 20 % shorter than the geometric span, i.e. it is approximately 1.08 m instead of 1.35 m. Based on this information, the measured lift coefficients are corrected in Table 4.6. The uncorrected results are presented in the previous chapter, see Table 3.8.

Table 4.5: *Lift coefficient of the clean airfoils for different wind speeds from Ansys Fluent simulations.*

	U			α		
	m/s	0°	4°	7°	9°	11°
	15	0.38	0.76	1.01	1.15	1.28
C_L	25	0.39	0.78	1.07	1.16	1.27
	40	0.39	0.79	1.1	1.18	1.29

The lift coefficients and the relative changes caused by the iced airfoil are listed in Table 4.7. Comparing the different ice types, the most significant lift degradation was found for mixed ice tests and the smallest for rime ice for most cases. The lowest lift reduction was found at lower angles of attack. For glaze and rime ice tests, the largest relative change was seen at $\alpha = 9^o$ and for mixed ice tests, at $\alpha = 7^o$. Comparing the relative lift coefficient reduction to the ones in Table 4.6, it can be seen that much higher reduction was found during the experiments.

In Figure 4.5, the results achieved at 15 m/s wind speed, are plotted against the ones from the wind tunnel tests for the dedicated profile tests. It can be seen, that however the values collected during the wind tunnel tests are much lower than the ones from the numerical analysis, the trend of these curves is similar to the numerical one. The streamlines and the velocity distribution around the clean airfoil for different angles of attack are plotted in Figure 4.6 and Figure 4.7, respectively. The results for ice cases

Table 4.6: *Corrected wind tunnel lift measurements. The presence of the vertical walls and end plates reduced the effective chord width with 20 %.*

	Glaze ice				
AOA	0°	4°	7°	9°	11°
C_{L0} (clean airfoil)	0.40	0.70	1.01	1.13	1.30
C_{Lf} (final, iced airfoil)	0.20	0.46	0.64	0.80	1.01
Degradation [%]	50	35	36	29	22
	Mixed ice				
AOA	0°	4°	7°	9°	11°
C_{L0} (clean airfoil)	0.40	0.72	1.01	1.14	1.30
C_{Lf} (final, iced airfoil)	0.15	0.39	0.64	0.75	1.07
Degradation [%]	64	47	36	35	18
	Rime ice				
AOA	0°	4°	7°	9°	11°
C_{L0} (clean airfoil)	0.40	0.71	1.02	1.20	1.33
CLf (final, iced airfoil)	0.23	0.54	0.77	0.93	1.01
Degradation [%]	42	25	25	23	24

Table 4.7: *Lift coefficients and relative changes for the iced airfoils for the dedicated profile tests from Ansys Fluent simulations.*

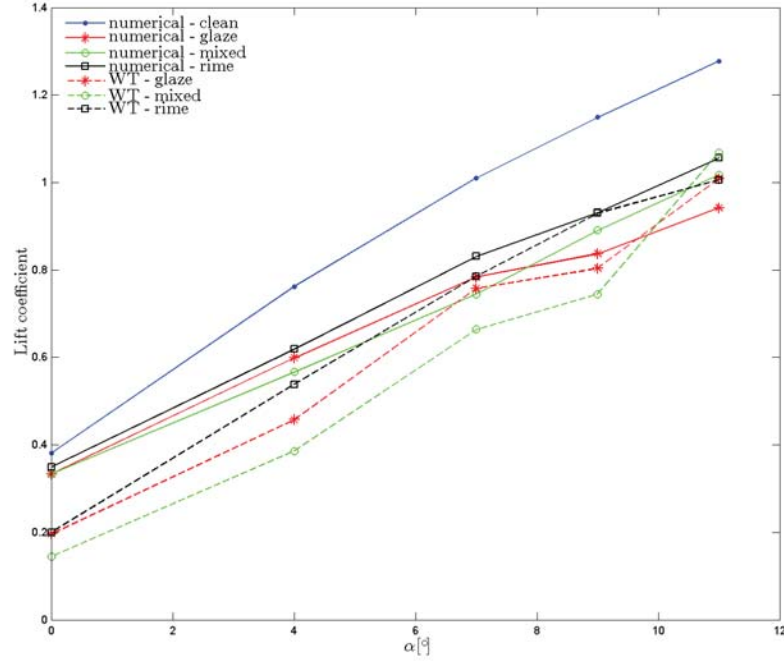|	U	Glaze iced profile				
	(m/s)	0°	4°	7°	9°	11°
	15	0.35	0.6	0.78	0.84	0.92
C_L	25	0.33	0.6	0.8	0.85	0.94
	40	0.35	0.61	0.81	0.85	0.92
	15	11	21	22	27	25
C_L change (%)	25	11	23	25	28	28
	40	9	23	24	28	28
	U	Mixed iced profile				
	(m/s)	0°	4°	7°	9°	11°
	15	0.33	0.57	0.75	0.89	1.02
C_L	25	0.34	0.57	0.75	0.9	0.99
	40	0.34	0.58	0.76	0.9	1
	15	12	26	26	22	20
C_L change (%)	25	15	27	29	23	22
	40	13	27	28	24	22
	U	Rime iced profile				
	(m/s)	0°	4°	7°	9°	11°
	15	0.35	0.62	0.83	0.93	1.06
C_L	25	0.35	0.62	0.84	0.94	1.02
	40	0.35	0.63	0.84	0.95	1.03
	15	8	19	18	19	17
C_L change (%)	25	10	20	22	19	19
	40	9	21	20	19	20

Figure 4.5: *Dedicated profile tests - Lift coefficient as a function of the angle of attack for clean (●), glaze (∗), mixed (○) and rime (□) ice profiles' results from the numerical analysis (with solid line) and the wind tunnel measurements (dashed lines).*

can be seen in Figure 4.8. In Figure 4.9, Figure 4.10 and Figure 4.11, the same for iced profiles can be seen. The results are discussed using these six figures.

As it is seen in Figure 4.6, the flow around the clean airfoil is rather smooth and well attached. In Figure 4.7, the color-range represents the flow speed around the airfoil (blue to red). It can be seen that the incoming velocity decreases to 0 m/s at the stagnation point (also represented by the blue arrows in Figure 4.11) and speeds up at the outer side of this zone. As AOA increases, the magnitude of the velocity decreases at the pressure side.   Comparing Figure 4.6 and Figure 4.9, it can be seen that the ice accretion has influence on the flow field around the airfoil, especially on the location of the leading edge separation and the trailing edge separation.

It can be seen in Figure 4.11 that the flow slows in the vicinity of the iced leading edge and the caused disturbance is highly dependent on the shape of the ice deposit. Small ice peaks, protrusions formed and behind these, areas with very low velocity and even recirculation zones can be observed (see e.g. glaze ice profile at 7° in Figure 4.11 g). These peaks form mainly on the suction side, where they also cause localized speed up and separation due to their sharp edge. For rime ice accretion, especially for the lower AOA, $\alpha = 0^o, 4^o$ and 7°, multiple local separation points can be found on the suction side, which cause slightly lower velocity zones compared to the clean profile.

It is suspected that the separation happened earlier in case of iced airfoils and due to the shape of the ice, a relatively thick zone around the airfoil with lower velocity (compared
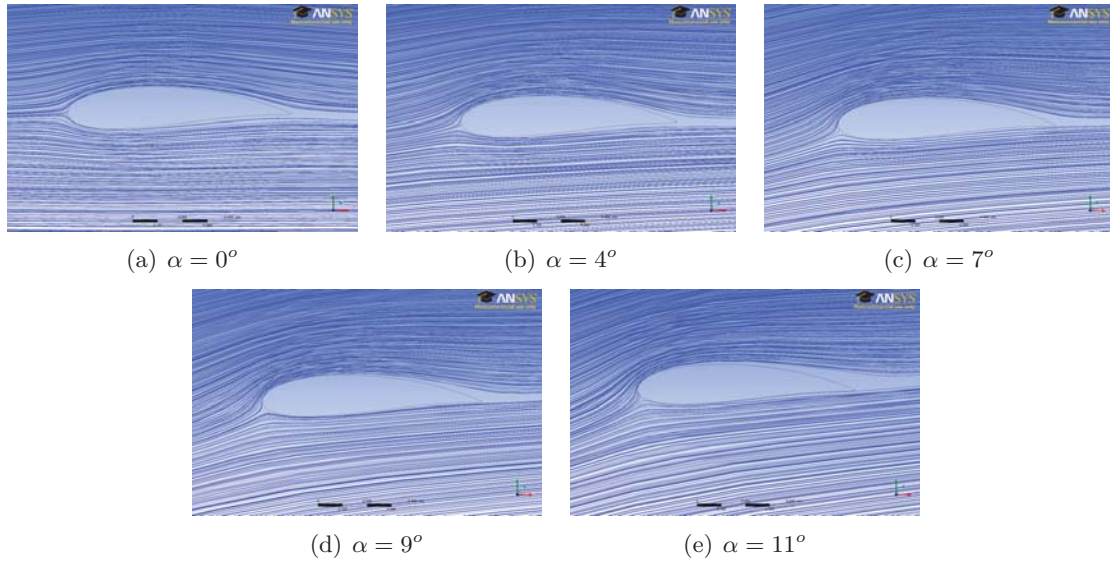
(a) $\alpha = 0^o$ (b) $\alpha = 4^o$ (c) $\alpha = 7^o$

(d) $\alpha = 9^o$ (e) $\alpha = 11^o$

Figure 4.6: *Streamlines around the clean airfoil at different angle of attack. First row, from left $\alpha = 0^o$, 4° and 7°, second row from the left $\alpha = 9^o$ and 11°.*
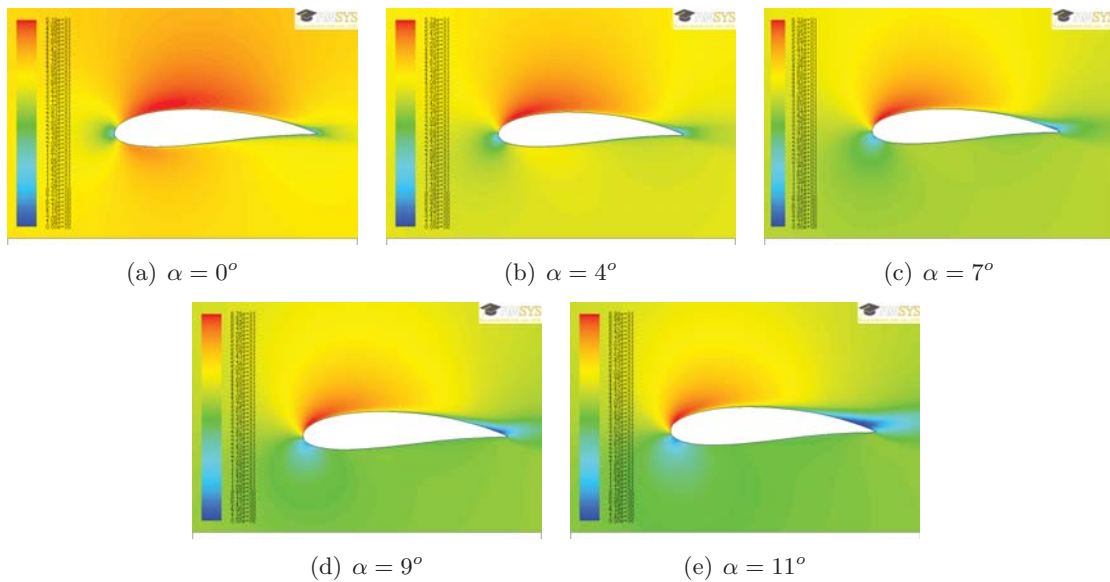

(a) $\alpha = 0^o$ (b) $\alpha = 4^o$ (c) $\alpha = 7^o$

(d) $\alpha = 9^o$ (e) $\alpha = 11^o$

Figure 4.7: *Contours of velocity magnitude around the clean airfoil at the tested angles of attack. First row, from left $\alpha = 0^o$, 4° and 7°, second row from the left $\alpha = 9^o$ and 11°. In the color bar, red represents the highest where blue the lowest wind speed.*

(a) $\alpha = 0^o$ (b) $\alpha = 4^o$ (c) $\alpha = 7^o$

(d) $\alpha = 9^o$ (e) $\alpha = 11^o$
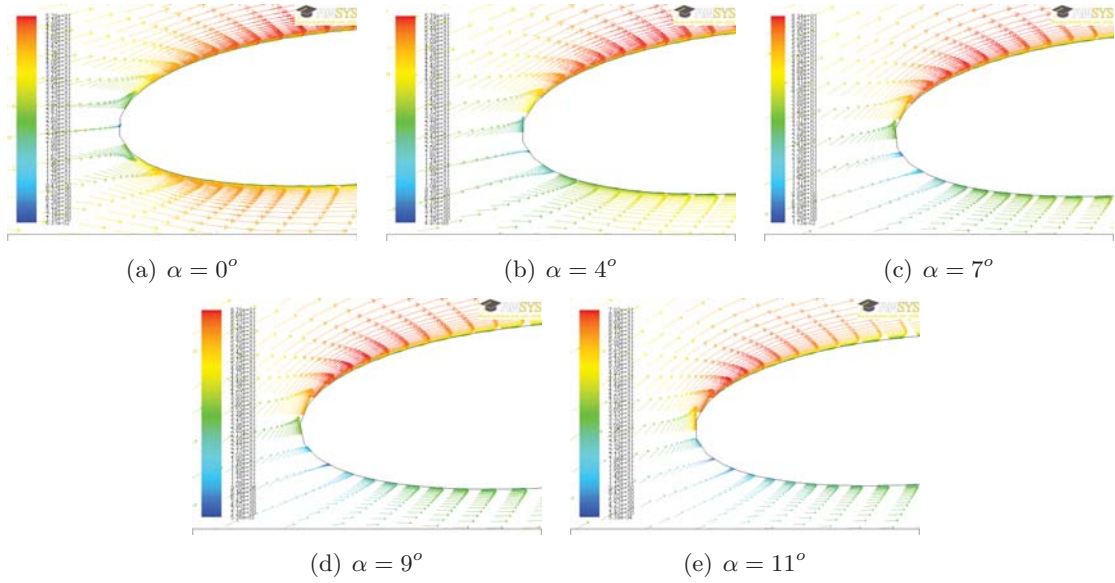
Figure 4.8: *Velocity vectors around the leading edge of the clean airfoil at the tested angles of attack. First row, from left $\alpha = 0^o$, 4° and 7°, second row from the left $\alpha = 9^o$ and 11 ^{o}. In the color bar, red represents the highest where blue the lowest wind speed.*

to the clean profile) could develop close to the airfoil. Another separation zone can be seen at the trailing edge, which increased as AOA increased in case of the clean profile, see Figure 4.6. In case of mixed ice deposits, a "nose" shaped ice formation can be also spotted around the stagnation point, which was not seen in case of the other two types of ice simulations. The highest flow disturbance and recirculation zones happen clearly in case of glaze and mixed ice accretion.

(a) Glaze ice $\alpha = 0^o$ (b) Mixed ice $\alpha = 0^o$ (c) Rime ice $\alpha = 0^o$

(d) Glaze ice $\alpha = 4^o$ (e) Mixed ice $\alpha = 4^o$ (f) Rime ice $\alpha = 4^o$

(g) Glaze ice $\alpha = 7^o$ (h) Mixed ice $\alpha = 7^o$ (i) Rime ice $\alpha = 7^o$

(j) Glaze ice $\alpha = 9^o$ (k) Mixed ice $\alpha = 9^o$ (l) Rime ice $\alpha = 9^o$

(m) Glaze ice $\alpha = 11^o$ (n) Mixed ice $\alpha = 11^o$ (o) Rime ice $\alpha = 11^o$
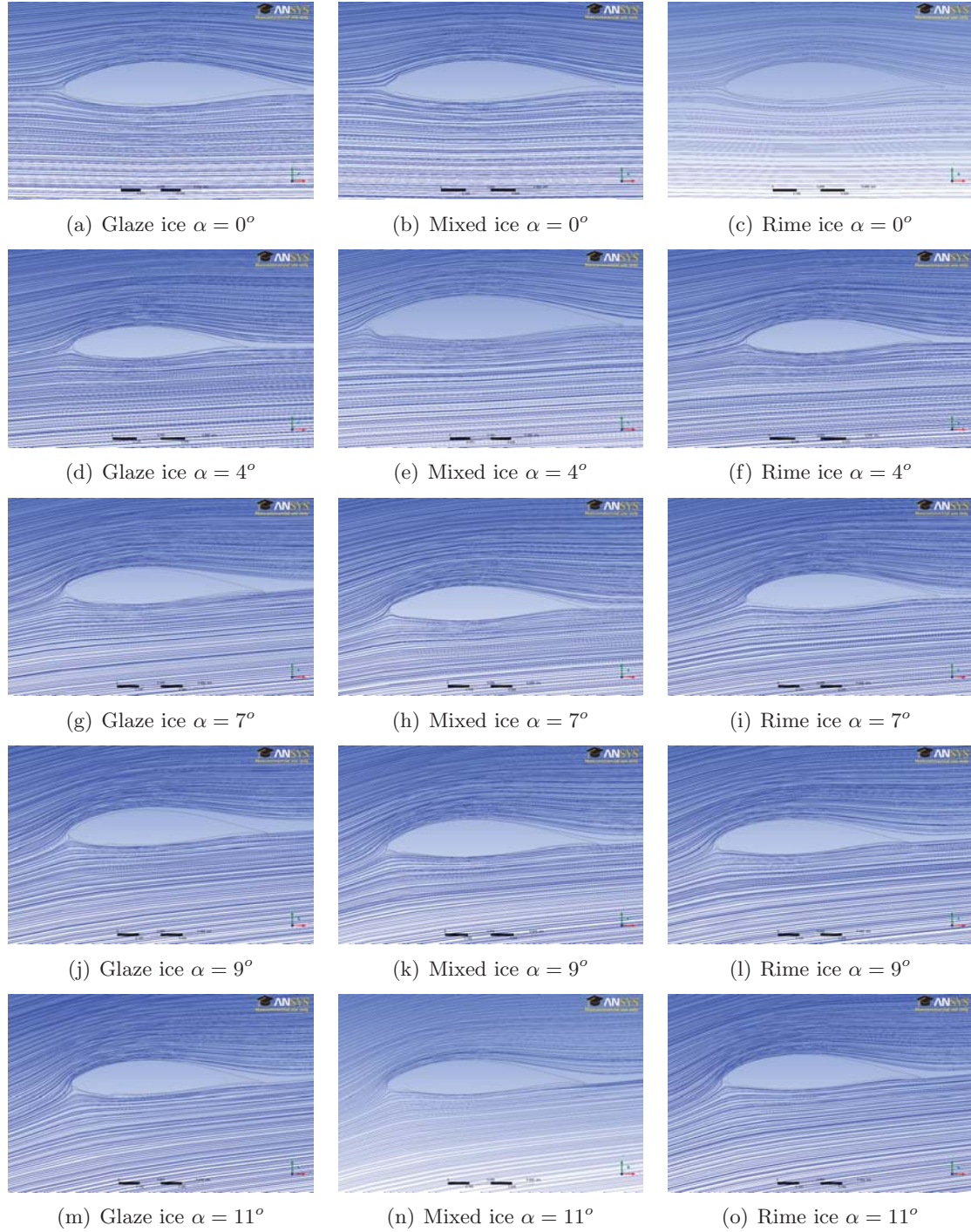
Figure 4.9: *Streamlines around the iced airfoil for increasing angle of attack for all studied ice types. In the columns, the results are grouped by the ice types and in the rows by the angles of attack from $\alpha = 0^o$ (top) to $\alpha = 11^o$ (bottom).*

(a) Glaze ice $\alpha = 0^o$ (b) Mixed ice $\alpha = 0^o$ (c) Rime ice $\alpha = 0^o$

(d) Glaze ice $\alpha = 4^o$ (e) Mixed ice $\alpha = 4^o$ (f) Rime ice $\alpha = 4^o$

(g) Glaze ice $\alpha = 7^o$ (h) Mixed ice $\alpha = 7^o$ (i) Rime ice $\alpha = 7^o$

(j) Glaze ice $\alpha = 9^o$ (k) Mixed ice $\alpha = 9^o$ (l) Rime ice $\alpha = 9^o$

(m) Glaze ice $\alpha = 11^o$ (n) Mixed ice $\alpha = 11^o$ (o) Rime ice $\alpha = 11^o$
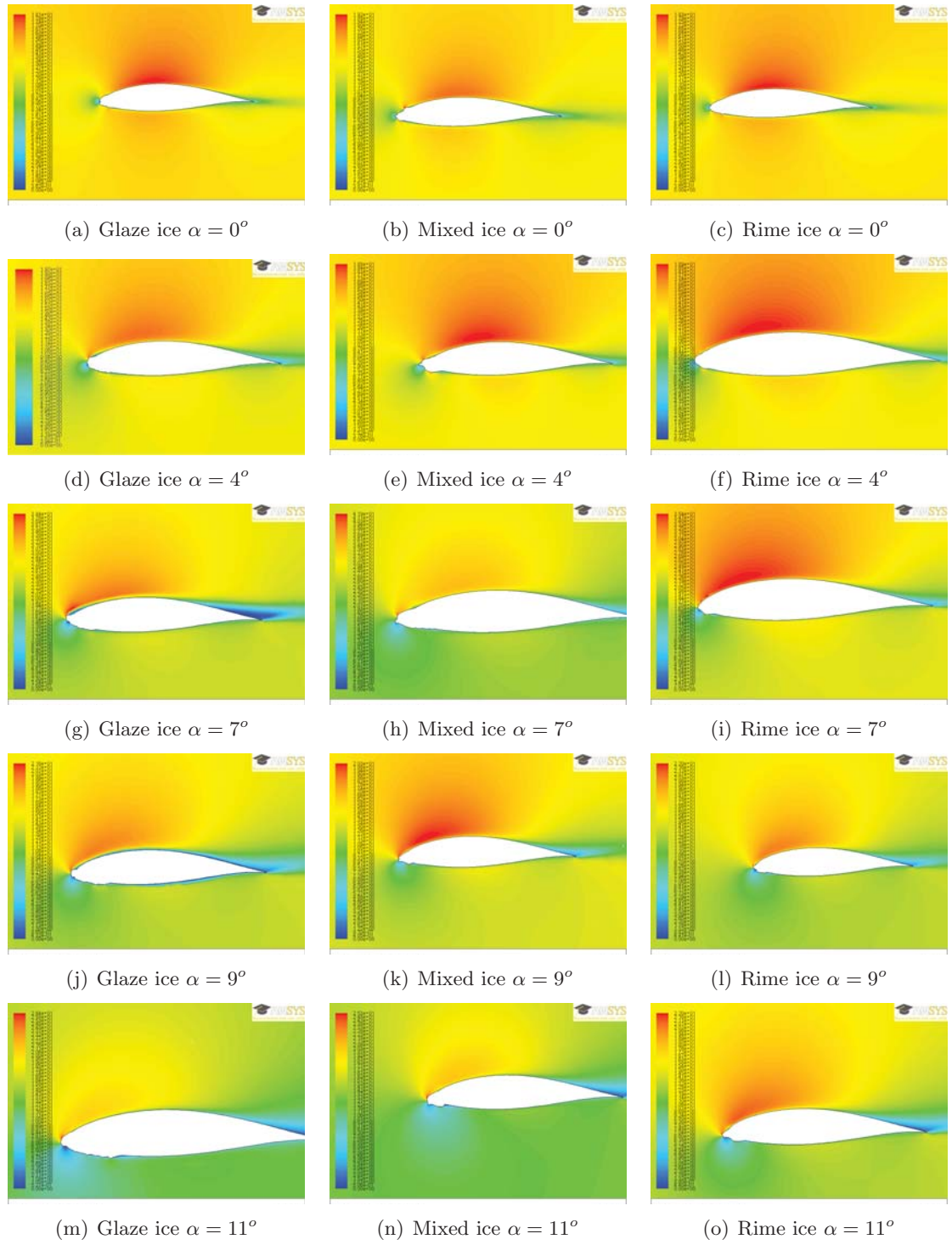
Figure 4.10: *Contours of velocity magnitude (m/s) around the iced airfoil for all studied ice types. In the columns, the results are grouped by the ice types and in the rows by the angles of attack from $\alpha = 0^o$ (top) to $\alpha = 11^o$ (bottom).*

(a) Glaze ice $\alpha = 0^o$ (b) Mixed ice $\alpha = 0^o$ (c) Rime ice $\alpha = 0^o$

(d) Glaze ice $\alpha = 4^o$ (e) Mixed ice $\alpha = 4^o$ (f) Rime ice $\alpha = 4^o$

(g) Glaze ice $\alpha = 7^o$ (h) Mixed ice $\alpha = 7^o$ (i) Rime ice $\alpha = 7^o$

(j) Glaze ice $\alpha = 9^o$ (k) Mixed ice $\alpha = 9^o$ (l) Rime ice $\alpha = 9^o$

(m) Glaze ice $\alpha = 11^o$ (n) Mixed ice $\alpha = 11^o$ (o) Rime ice $\alpha = 11^o$

Figure 4.11: *Velocity vectors colored by velocity magnitude (m/s) around the iced airfoil for all studied ice types. In the columns, the results are grouped by the ice types and in the rows by the angles of attack from $\alpha = 0^o$ (top) to $\alpha = 11^o$ (bottom).*
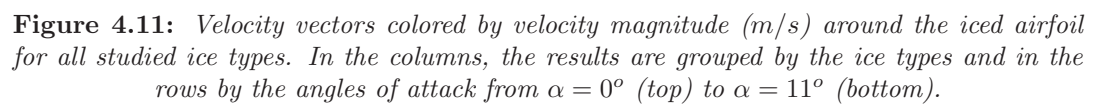
In Figure 4.12, lift coefficient - angle of attack curves are plotted for glaze and rime accretion in case of single profile tests. In the top figures, the profiles were collected at $\alpha = 0^o$ whereas in the lower figures at $\alpha = 11^o$. It can be seen that in case of $\alpha = 0^o$ profiles, there is quite significant difference between the lift coefficients from the dedicated profile tests and from single profile tests at higher angle of attack. The curves fit much better for the profiles collected at $\alpha = 11^o$, however at $\alpha = 0^o$, it was found that the single glaze profile caused 19% larger lift coefficient than the dedicated one and even larger than it was seen for the clean profile. The results are summarized in Table 4.8.
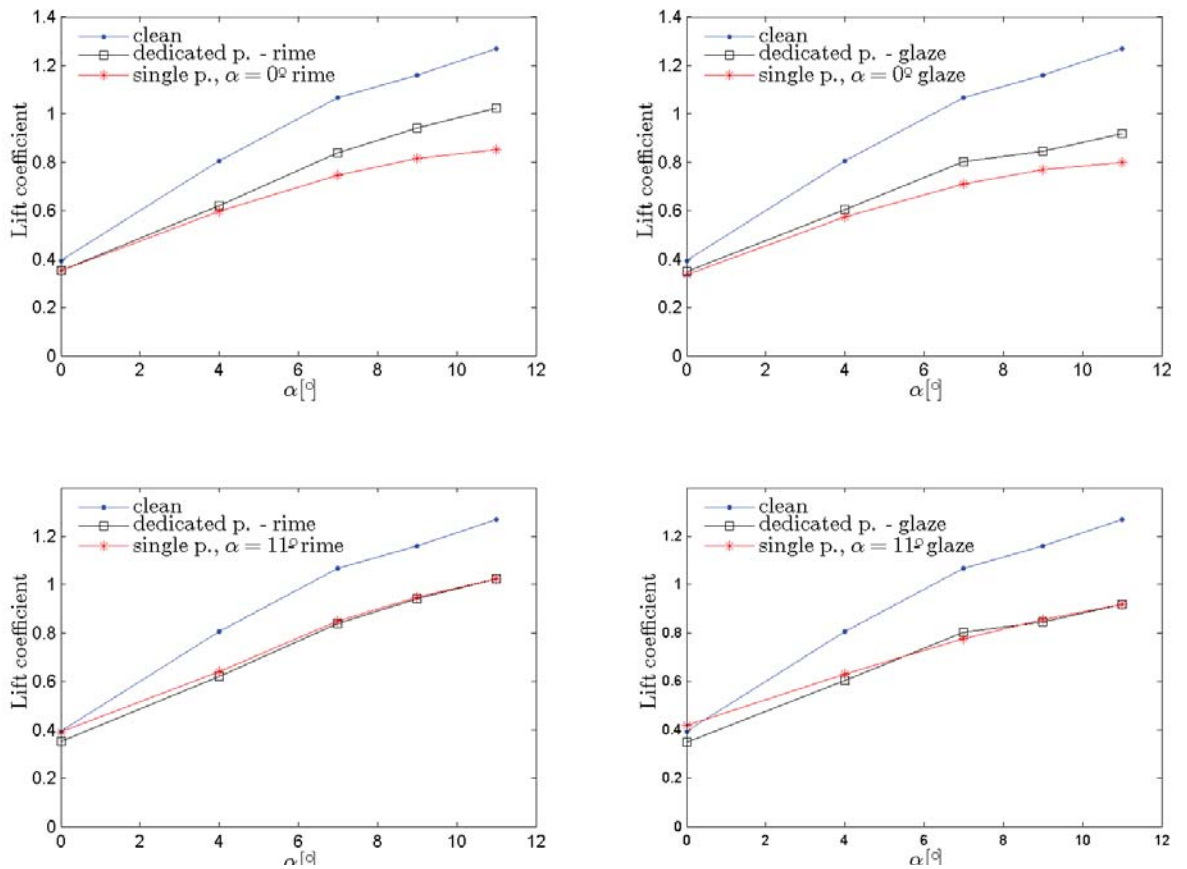
Figure 4.12: *Comparison of lift coefficient - angle of attack curves for glaze and rime ice accretion for clean ($\bullet$), single ($*$) and dedicated ($\square$) ice profiles. In the top row, the results of $\alpha = 0^o$ profile are compared to the clean and dedicated profiles whereas in the second row $\alpha = 11^o$.*

Drag coefficient was also studied during the numerical analysis, however, it was not possible to directly compare the results to the measured drag coefficient from the experimental study because the quality of the drag measurements was very likely influenced by the measuring range of the force transducers. Drag curves of the dedicated ice profile tests are plotted against the clean airfoil data in Figure 4.13. As it can be seen, the iced drag coefficient increased significantly compared to the clean one for all angle of attack and ice types. The largest drag increase was found for mixed ice accretion at $\alpha = 11^o$.

Table 4.8: *Comparison of the results of dedicated profile and single profile simulations and the relative difference between them.*

		Rime ice profile				
	AOA (^{o})	0	4	7	9	11
C_L	Dedicated profile	0.35	0.62	0.84	0.94	1.02
	Single p., $\alpha = 0^o$	0.35	0.6	0.75	0.82	0.85
	Difference (%)	0	4	11	13	17
C_L	Dedicated profile	0.35	0.62	0.84	0.94	1.02
	Single p., $\alpha = 11^o$	0.39	0.64	0.85	0.95	1.02
	Difference (%)	10	3	1	1	0
		Glaze ice profile				
	AOA (^{o})	0	4	7	9	11
C_L	Dedicated profile	0.35	0.6	0.8	0.85	0.92
	Single p., $\alpha = 0^o$	0.34	0.57	0.71	0.77	0.8
	Difference (%)	4	5	12	9	13
C_L	Dedicated profile	0.35	0.6	0.8	0.85	0.92
	Single p., $\alpha = 11^o$	0.42	0.63	0.78	0.86	0.92
	Difference (%)	19	5	3	1	0

Figure 4.13: *Drag coefficient as a function of the angle of attack for the clean NACA 64-618 and the* **dedicated ice profile** *tests, glaze, mixed and rime ice accretion.*

In order to demonstrate the influence of ice on the characteristics of the airfoil in another way, the local pressure coefficient along the chord length are plotted for the clean airfoil and the ice airfoils for $\alpha = 0^o$ in Figure 4.14 and Figure 4.15, respectively.
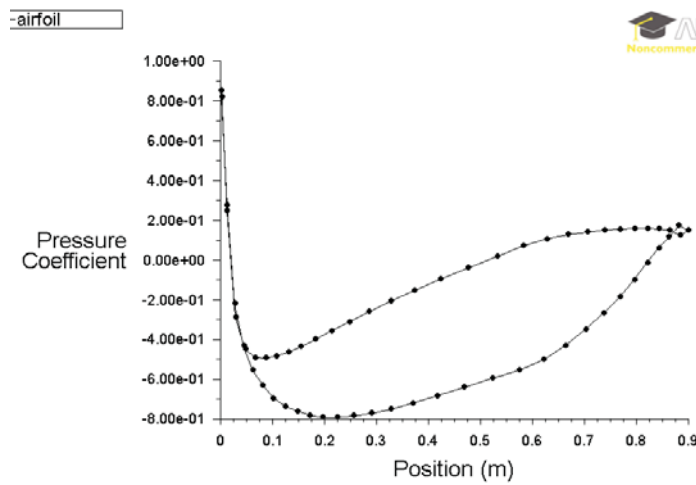
Figure 4.14: *Pressure coefficient of the clean airfoil.*

It is clearly visible that ice accumulation causes pressure fluctuation. The local pressure coefficient around the ice deposit increases for each ice type compared to the clean airfoil's pressure coefficients at the same location. Downstream from the ice deposit, the pressure recovers, however the values are higher. The smallest differences between the suction and the pressure side are seen for mixed ice accretion and this difference is also smaller than for the clean airfoil.

4.5 Discussion of numerical investigation

4.5.1 Ice accretion modelling

It was shown by e.g. Etemaddar et al. [2012] that LWC and MVD are two of the most important parameters, which define the size of the ice load on airfoils. Therefore it is crucial to know them precisely. The results shown in Figure 4.3 indicate that the MVD and LWC are larger than the target parameters. It is known that the size and the dynamics of the droplets are dependent on the aerodynamic drag, gravity, droplet collision, evaporation and the turbulence of the flow (Kollár et al. [2005]). Kollár et al. [2005] concluded that the MVD may increase by 20 % due to coalescence, which could be the reason for the underestimation of the size of the droplets which impinged on the surface of the airfoil.

At low air speeds such as 5-10 m/s, the gravity has significant influence on the vertical deflection of the droplet trajectories causing gravitational sedimentation. The vertical deflection of the droplet trajectories has influence on the vertical LWC distribution, which means the maximum LWC occurs at lower height. It could cause thick ice deposit in case of the experimental glaze ice accretion at higher angles of attack since as the AOA increases the larger the surface area gets, which faces the flow (see Figure 4.4).

Another reason for the different ice profiles and the thicker runback ice at the pressure side could be the way of how ice was accreted on the airfoil during the wind tunnel tests. When the tunnel was set idle for the measurements, that short period could provide just
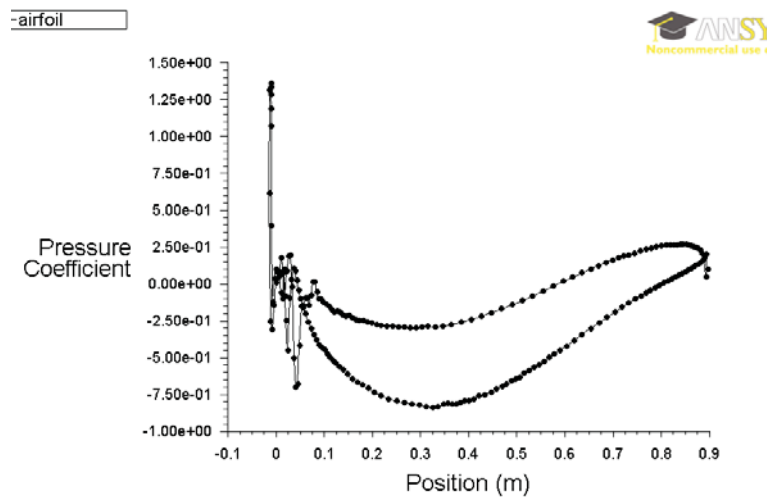
(a) Glaze iced airfoil
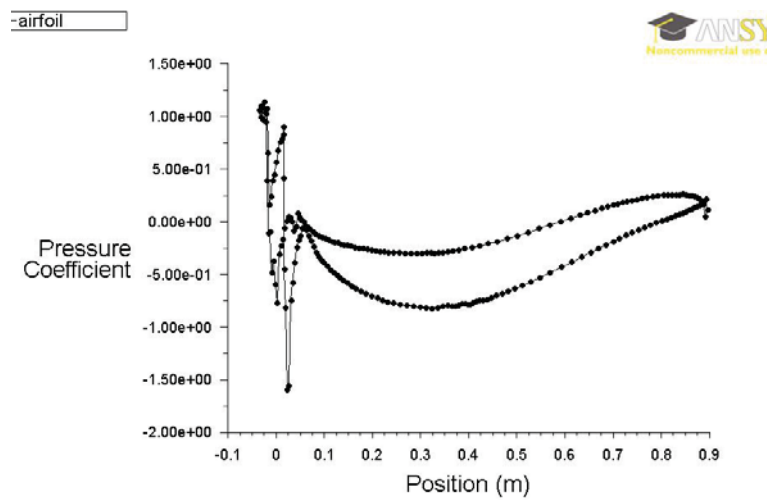
(b) Mixed iced airfoil
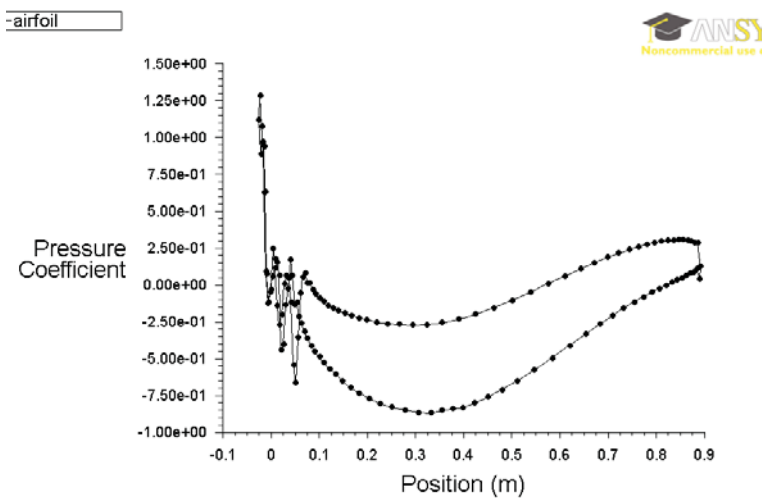
(c) Rime iced airfoil

Figure 4.15: *Pressure coefficient of the glaze, mixed and rime iced airfoil.*

enough time for the water layer to freeze and hence the collided water droplets could not completely ran back or bounce off the airfoil.

This indicates that the development of the ice profiles was influenced by the combination of the applied low wind seed, and thus coalescence and vertical deflection of the droplet trajectories, and the characteristics of the wind tunnel tests.

Additional simulations suggest that in case of rime ice profiles, the numerical profiles agree well with the experimental ones, if LWC is increased to $1g/m^3$ and the MVD to $40\mu m$.

4.5.2 Computational fluid dynamics

The roughness sensitivity tests showed that changing the roughness height and thus the first layer height of the mesh does not have a significant influence on the aerodynamics but has detrimental effect on the flow simulation in the vicinity of the iced airfoil profile. Therefore micro surface roughness was neglected during the simulations.

The trend of the lift coefficient - angle of attack curves from the numerical analyses are in good agreement with the ones from the wind tunnel tests, as shown in Figure 4.5. However, the values from the wind tunnel are much lower than the ones from the numerical simulations due to the fact that the measurements were only corrected for lift interference and blockage interference but not for the presence of the vertical walls. Based on the numerical results of the clean airfoil studies, it was found that the vertical walls had strong impact on the measurements and the effective chord width was reduced by 20 %. The immediate effect of the vertical wall on the flow behaviour is also visible on the flow visualisation photos from LM Wind Power presented in Figure 3.11 in the previous chapter.

After correcting the experimental results, still quite large differences were found. A reason for these differences could be that with the contour tracing method, the small changes of surface roughness could not be documented therefore they were not implemented in the numerical analysis. It was shown in many studies (e.g. Bragg et al. [2005]) that the roughness highly affects the aerodynamics of the airfoil. Based on the differences in the aerodynamic effect between 2 D and 3D ice shapes, Addy [2000] concluded that the surface roughness and the irregularities present in natural aircraft ice are important characteristics. The CFD models were 2-D, and thus it was impossible to properly implement the highly 3-D structure of the ice deposit, which was seen for example in Figure 3.18 or in Figure 3.26. It can be seen that the beads and feathers are very complex and rough, and probably it would be quite challenging to properly model them even in 3-D. These could also cause the differences between the results of the wind tunnel tests and the numerical simulations.

The measured relative reduction of lift coefficient (listed in Table 4.6) shows also quite large difference from the ones listed in Table 4.7, which implies that the combination of the presence of the wind tunnel's vertical walls and the changed surface roughness had significant influence on the measurements. For lower angles of attack, especially $\alpha = 0^o$,

the difference between the measured and simulated relative reduction is significantly large, which indicates that the altered surface roughness had the highest influence on the lift reduction.

Similarly to e.g. Homola et al. [2010a], lift was found to decrease in all cases. E.g. Virk et al. [2010b] found higher lift coefficients for rime iced profiles than for the clean profiles due to the increased effective chord length and camber of the blade profile. This was not experienced in the presented cases of dedicated profile simulations. However, as it can be seen in Figure 4.11, the curvature of the ice shapes follows well the curve of the airfoil at the suction side, i.e. acts as an extended leading edge, and thus could cause less significant lift degradation than e.g. the glaze ice accretion.

A tendency of increased lift reduction was seen for glaze ice accretion as the AOA increased. This is due to the characteristics of glaze ice. During glaze ice accretion, because of the relatively higher air temperature $(0 -^- 4^oC)$, not all water droplets freeze to the surface on impact and hence some run along the airfoil and freeze later (Bose [1992]). As AOA increases, the area exposed to the water droplets increases as well, therefore it causes more flow disturbance and thus more lift reduction.

In most cases, mixed ice accretion caused more significant lift degradation than glaze ice accretion due to the large ice deposit, which accumulated on the leading edge and hence caused higher flow disturbance (see Figure 4.11).

A significant change in the flow pattern was observed, when a comparison was made between flow around the clean and the iced blade profiles due to the changes of the aerodynamically shaped leading edge curve. As AOA was increased, the surface area, which faced the incoming flow and thus the water droplets, increased as well causing major changes in the local flow pattern.

In Figure 4.11, small local separations are seen, which were also reported in the study of Reid et al. [2013]. In these set of figures, it can be noticed that the suction effect was reduced at the suction side (which was also reported by Villalpando et al. [2012]) and led to lift reduction.

The impact of single ice profiles collected at $\alpha = 0^o$ and $\alpha = 11^o$ were studied at different angles of attack. The lift coefficients of $\alpha = 0^o$ for both glaze and rime ice accretion are lower than the ones found in case of dedicated profile tests. The reason for this difference could be that ice was accumulated only on the leading edge in case of $\alpha = 0^o$ and when the incident angle of incoming flow is increased, the stagnation point moves downstream of the ice deposit disturbing the flow on the suction side, which has higher influence on the lift coefficient than the pressure side. The profiles collected at $\alpha = 11^o$ did not cause significantly different lift curves from the multiple profiles because for $\alpha < 11^o$ values, the ice deposit is downstream of the stagnation point.

Drag coefficient was also studied during the numerical analysis for $U = 25m/s$. As it was expected the drag coefficient increased compared to the clean airfoil for each AOA and ice type. The curves in Figure 4.13 are not smooth and it is not possible to fit any poly-

nomial to the point either. The reason is the differently iced profiles, which have different influence on the flow field and thus on the aerodynamics. The largest drag increase was found for mixed ice tests, since the large ice deposit accreted for mixed ice condition and the flow was disturbed the most significantly. It was seen that for lower AOA, the drag coefficient of the iced airfoils was smaller than of the clean profile.

Around the ice deposit, the local pressure coefficient increased and is fluctuating due to the rather rough and complex surface. Downstream of the ice, the pressured coefficient curves became smooth again.

4.6   Conclusion drawn from the numerical investigation

In this chapter, the collected ice profiles were numerically studied in order to validate the settings of the wind tunnel and the profiles and also to analyse the impacts of ice accretion on the flow conditions around the iced airfoil and the lift coefficient.

The TURBICE simulations showed that the values of the median volume diameter and liquid water content were underestimated. The resulted MVD and LWC were larger than the target values for rime ice accretion. The results of TURBICE simulation also indicate that the development of the ice profiles was influenced by the combination of the applied low wind seed, and thus coalescence and vertical deflection of the droplet trajectories, and the characteristics of the wind tunnel tests.

The results of the Ansys Fluent analyses imply that the combination of the presence of the vertical wall of the wind tunnel and the changed surface roughness had significant influence on the measurements. However, the trend of the lift coefficient - angle of attack curves from the numerical analyses are in good agreement with the ones from the wind tunnel tests. Comparing the measured lift coefficient to the computational ones, it was found that the effective span was approximately 80% of the geometric span due to the presence of the end plates. Based on this information, the measured lift coefficients were corrected.

Quite large differences between the measured relative lift reductions and the numerical ones were observed, because the surface roughness was not possible to be implemented in the CFD simulation. A significant change in the flow pattern was observed, when a comparison was made between clean and iced blade profiles due to the changes of the aerodynamically shaped leading edge curve. The sharp edges at the suction side of glaze and mixed ice profiles led to a speed up, which caused a large separation bubble. In case of rime iced profile, the flow followed a similar pattern as it was observed for the clean airfoil and the magnitude of the velocity did not differ significantly from the clean profile. For all three cases, there were some vortex formations noticed behind the ice peaks at the pressure side causing tiny recirculation zones, which led to some flow disturbance and retardation. However, they did not have a large influence on the change of the overall leading edge aerodynamics. The experiments also showed a clear 3-D ice pattern that requires 3-D computations.

As it was expected, the drag coefficient increased due to the ice accretion for all ice types.

The largest increase was experienced in case of mixed ice for $\alpha = 11^o$. It was also seen that the ice deposit caused pressure fluctuation, and the pressure coefficient increased for each ice type for the shown $\alpha = 0^o$ cases.

The importance of the angle of attack, on which the profiles were collected, on the lift coefficient was shown. The results of the single profile tests in case of $\alpha = 0^o$ for both glaze and rime ice accretion gave lower lift coefficients than the ones for dedicated profile tests. The reason for this difference could be that ice was accumulated only on the leading edge in case of $\alpha = 0^o$ and when the incident angle of incoming flow increased, the stagnation point moved downstream from the ice deposit on the suction side.

Chapter 5

Transformation of lift coefficients

Seifert and Richert [1997] introduced a transformation method with which they claimed it was possible to transform measured aerodynamic coefficients from an iced airfoil to any other airfoils. In that work, the measured iced NACA 4415 profile was used to transform e.g. the lift coefficient to a NACA 63-415 airfoil. In Figure 5.1, the method of how to interpolate the iced coefficients of an airfoil is shown. NACA denotes the measured airfoil whereas NP refers to the "new profile".
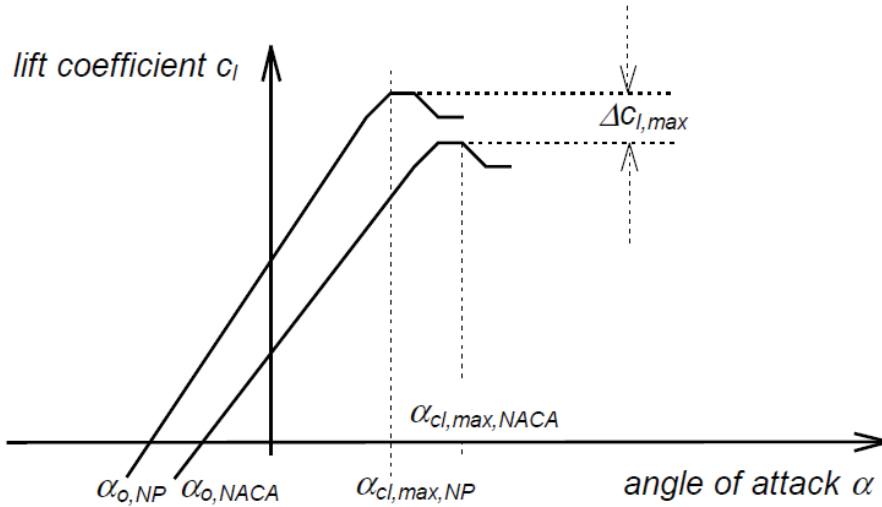
Figure 5.1: *Method to interpolate the iced coefficients of the airfoil (Seifert and Richert [1997]). NACA denotes the measured airfoil whereas NP the "new profile".*

The aim of this study was to see whether it had been possible to transform the lift coefficients of the measured iced NACA 4415 to the NACA 64-618, which was used in this PhD work. The results were then compared to the results of the wind tunnel tests and also of the numerical simulations. Only the rime iced airfoil's results are used because that type of ice was studied by Seifert and Richert [1997] as well.

The method is rather poorly explained in the reference, therefore first, it was necessary to reproduce the published results for the NACA 63-415. The following routine was followed:

$$\triangle C_L^{clean} = C_{L,NACA}^{clean} - C_{L,NP}^{clean} \tag{5.1}$$

$$C_{L,NP}^{iced} = C_{L,NACA}^{iced} - \triangle C_L^{clean} * K_a \tag{5.2}$$

Where *clean* refers to the clean airfoil and *iced* to the iced airfoil. K_a is a multiplication factor gained from the difference between the maximum (clean) lift coefficients:

$$K_a = \frac{C_{L,NP}^{max}}{C_{L,NACA}^{max}} \tag{5.3}$$

Using these equations, it was possible to transport the lift coefficients of the 2% iced NACA 4415 to the new, NACA 63-415 profile. The lift curve of the 2% iced airfoil was chosen because that amount of ice was close to the mass accreted on the NACA 64-618 during the wind tunnel tests. In Figure 5.2, the transformed lift curve can be seen along with the lift curve of the transformed by Seifert and Richert [1997] and the clean one as well.
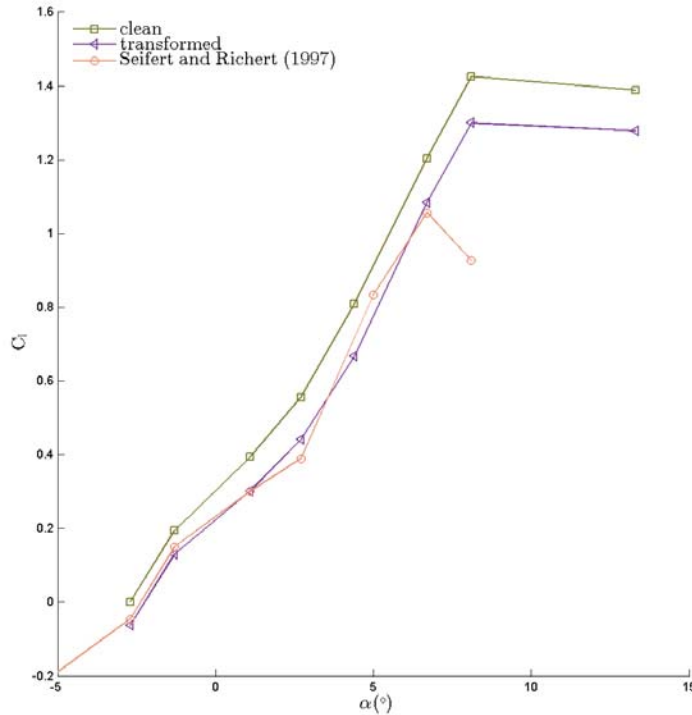
Figure 5.2: *Transformed lift curve of the iced NACA 63-415 airfoil along with the lift curve of the clean section and the one transformed by Seifert and Richert [1997].*

As it can be seen in the figure, the transformed (purple) curve follows quite well the one published in the paper (orange), it only differs significantly at $\alpha = 8^o$, where it suddenly stalls. After carefully studying all the curves in the paper, it was not possible to find physical explanation for this behaviour, therefore it was assumed that the routine explained above is acceptable.

In Figure 5.3, the transported lift curves of the NACA 64-618 based on the corrected wind tunnel measurement and the corrected iced lift coefficients (labelled as *wind tunnel* in the figure) are plotted. Whereas in Figure 5.4, the transported lift curve of the NACA 64-618 based on the results of the numerical simulations and one from the CFD simulation (denoted as *numerical*) are shown.
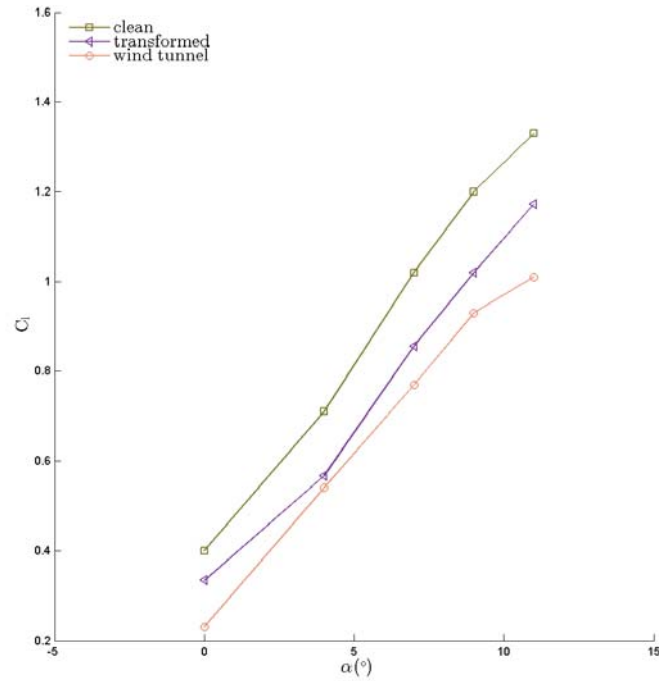
Figure 5.3: *Transformed lift curve of the NACA 64-618 based on the corrected* **wind tunnel measurements** *compared to the corrected iced lift coefficients (labelled as wind tunnel).*
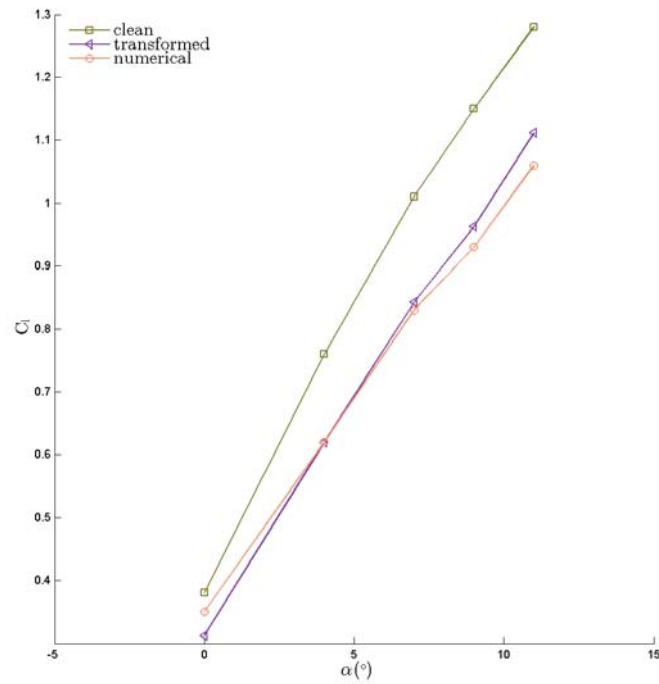
Figure 5.4: *Transformed lift curve of the NACA 64-618 based on the results of the* **numerical simulations** *compared to the iced, numerical lift coefficients (labelled as numerical).*

Comparing Figure 5.3 and Figure 5.4, it can be seen that the transformed lift curve fits much better to the one from the CFD analysis. A reason could be that the 2 % ice mass was different from the one collected during the wind tunnel tests or that the method does not include the change of the surface roughness as it was not included in the numerical analysis either. Another reason for the difference between the lift curve from the wind tunnel tests and the transformed one could be that it is unknown at which AOA the tested ice fragment was collected. The importance of this information was shown in Section 4.4.2.

Although only one independent scenario was demonstrated for the usability of the method of Seifert and Richert [1997], the results are promising. It is suspected that it could be a strong basis of a very useful aerodynamic coefficient transformation model.

Chapter 6
Conclusion drawn from the PhD work

The PhD study was carried out at the Department of Wind Energy, Technical University of Denmark. The work can be divided into two larger parts. In the first part, the influence of environmental and meteorological parameters on the occurrence of icing events was studied on a specific case in South-Greenland. In the larger, second part, experimental and numerical investigations of the impact of ice accretion on wind turbine blades were carried out.

During the risk analysis of icing in South-Greenland, different direct and indirect techniques, which can identify probable icing periods, were studied. Similarly to other studies, it was experienced that none of the methods can identify icing events certainly on its own. However, combining the different techniques, a quite good picture of these events can be obtained. The best performing technique was found to be the comparison of the output of heated and unheated anemometers.

Dedicated ice rate sensor from HoloOptics was also tested in two locations in South-Greenland. Despite of the expectations, the instrument could not provide data for the whole length of the measurement campaign because due to unknown reasons (might be voltage outage or lightening), all three, independently installed instruments broke during winter. However when they were functional, they could provide useful information not only about the extent of the icing event but also about its severity.

The data analysis indicates that icing events usually occur during periods with low wind speed, high relative humidity and subzero (or close to $0\,^o$) temperature especially during night or cloudy/foggy periods. The same observation was reported by the research group at Summit Station. It can be concluded that icing might be a significant issue in South Greenland, but a more thorough and dedicated, location dependent investigation is necessary when the decision is made to install wind turbines in a specific location.

Wind tunnel tests were performed on a NACA 64-618 airfoil at the Collaborative Climatic Wind Tunnel. During the experimental work, glaze, rime, and mixed ice accretions were studied and the changes of aerodynamic forces and the accreted mass were monitored as ice was building up on the blade. Both processes were found to be nearly linear. The immediate alteration of the surface roughness was experienced to have more significant detrimental effect on the lift coefficient than the shape of the changed airfoil in that very

early stage of ice accretion. With increasing angle of attack the degradation of the instantaneous lift coefficient increases as well. The most significant lift coefficient degradation was seen in case of mixed ice accretion. The largest ice mass also accumulated for that ice type and caused high flow disturbance, which could then lead to the high lift reduction.

The results of the experimental investigation showed that the type of the ice accretion has significant impact on the degree of the reduction of the lift coefficient and thus on the power production loss. Independently of the ice type, ice accumulation has strong negative influence on the flow field around the airfoil, which was also confirmed by both the flow visualization and the numerical analysis. It was also observed that the ice accretion is highly 3-D. In case of glaze ice accretion, small ice bead formation was observed whereas in case of mixed ice accretion, a sharp nose-like ice peak formed around the stagnation point. These could occur, because the airfoil was static during the tests and also because the wind tunnel was set to idle every 5 minutes for measurement for couple of minutes, which was long enough time to freeze all the already impinged liquid water droplets.

The mass and the shape of the ice deposit are highly dependent on LWC, MVD and temperature. It also has to be underlined that the accreted mass was smaller than it would have accumulated on the blade of an operating wind turbine due to the relatively low wind speed that was applied in the wind tunnel in order to ensure low enough air temperature.

The increase of the drag coefficient was also nearly linear process, however due to the wide measuring range of the force transducers, the presented values are probably too high. A brief analysis of the melting process was also done. It was observed that as long as the air temperature remained subzero inside the tunnel, no ice melting happened, which implies the sun is probably the most important element of the melting process at low temperature. As air temperature increased above freezing point, a thin melt water layer appeared between the ice and the airfoil, which most likely helps the ice deposit to shed off from a rotating wind turbine blade.

At the end of each wind tunnel test, the shape of the ice deposit was recorded by contour tracing method. These profiles were then used during the numerical investigation. Dedicated computational ice accretion model, TURBICE from VTT, Technical Research Centre of Finland was used to calibrate the environmental parameters for MVD and LWC. The simulations showed that these values were underestimated in the wind tunnel. MVD was larger due to coalescence of the incoming droplets, which then impinged on the surface of the airfoil. The vertical deflection of the droplet trajectories had influence on the vertical LWC distribution, i.e. the maximum LWC occurred at lower height. The combined effect of these two phenomena could also lead to formation of a larger ice deposit at the pressure side of the airfoil. Additional simulations suggested that the best fits are for all angles of attack for rime ice accretion with $LWC \simeq 1g/m^3$ and $MVD \simeq 40\mu m$ and rather than 0.6 g/m^3 and $23\mu m$, as specified by the manufacturer of the spray nozzles based on the setted water and air pressure.

Simulations with Ansys Fluent were then performed to quantify the impacts of ice accretion on the flow behaviour and the aerodynamic characteristics of the iced airfoil from the

wind tunnel tests. Comparison was made between the lift coefficients of the clean profile from the numerical analysis and the ones from the wind tunnel tests, which implied that the presence of the vertical walls had significant influence on the measurements. It was found that the effective span was 20% shorter than the geometric one. After correcting the wind tunnel measurements, there were still quite significant differences found. The reason could be the micro surface roughness of the ice deposit, which was not implemented in the numerical model due to the experience that Fluent cannot properly handle it. The other explanation could be the strong 3-D characteristics of the ice deposit (beads and feathers), which cannot be properly modelled in 2-D, but have significant influence on the flow.

Although the drag coefficients could not be directly compared to the results of the wind tunnel tests, the drag curves were studied. It was seen that the drag increases significantly for all ice types. The largest increase was found at $\alpha = 11^o$ for mixed ice.

A significant change in the flow pattern was observed for all cases and the most significant flow disturbance was caused by mixed ice accretion. For all three ice types, there were some vortex formations noticed behind the ice peaks at the pressure side, which caused tiny recirculation zones and led to minor flow disturbance. However, they did not have a large influence on the change of the overall leading edge aerodynamics. At the suction side, especially for glaze ice, small ice peaks formed, which caused local speed-up at their sharp edges. Behind these peaks recirculation zones could develop. The most significant flow disturbance and also the largest number of recirculation zones formed in case of glaze and mixed ice, which led to the highest lift coefficient reductions as well.

It was shown that the lift coefficients are highly dependent on the angle of attack on which the profiles were collected. The impact of single ice profiles collected at $\alpha = 0^o$ and $\alpha = 11^o$ were studied in flows with different incident angles. The lift coefficients of $\alpha = 0^o$ for both glaze and rime ice accretion were lower than the ones found in case of dedicated profile tests.

Furthermore, it can be concluded that even one hour of ice accretion can significantly reduce the lift coefficient of an airfoil and that the angle of attack at which the ice builds up on the surface is highly important.

The final lift curves of rime ice accretion from both experimental and numerical investigation were used in a demonstration of the transformation model of Seifert and Richert [1997]. It was found that the transformed lift curve fits much better to the one from the CFD analysis. The reason could be either that the method does not include the change of the surface roughness therefore the transformed lift curve could fit to the numerical one or because it is unknown at which AOA the tested ice fragment was collected and the importance of this information was clearly shown during the numerical investigation. However, it can be concluded that the usability of the method of Seifert and Richert [1997] is promising and it could probably provide a strong basis for a very useful aerodynamic coefficient transformation model.

Chapter 7

Future work

Although during the three years of PhD study, several topics related to icing of wind turbine blades were investigated, the findings have raised a number of questions and have given ideas for further improvements, studies and researches. In this chapter some of these suggestions are listed.

Experimental investigation

- There is a desperate need for standardize MVD and LWC techniques especially since it was shown several times that these two are of the most important parameters.

- Drag force measurements with heated measurement system or a more suitable force balance (with smaller measurement range to be able to capture the very small changes as well) could give similar information on the changes as it was seen in case of the list measurements.

- More wind tunnel tests with different LWC, MVD and AOA and different airfoil sections

- Employment of infra-red camera to study the surface temperature prior and also during ice accretion could give useful information on the accretion process ans also would be essential for the melting investigation.

- Thorough surface roughness tests including ageing of airfoil surface. It was shown that sand and insects are changing the surface roughness of the blades. So a study of their impacts of ice accretion might be interesting.

- More detailed melting investigation would be interesting.

- Measurement of adhesion force of ice could be an additional feature.

Numerical investigation

- Proper surface roughness implementation is crucial for correct representation of the changes of flow conditions due to ice accretion.

- Since in this study, only 2-D cases were modelled and it was seen that there might be significant differences in the aerodynamic effect between 2-D and 3-D ice shapes, therefore a detailed 3-D study is suggested.

- During the present work RANS turbulence models were used therefore it is suggested to to test LES and DES models as well.

Appendix A
Risk of ice in South-Greenland for wind energy

In this Appendix chapter, the plots of the different ice detection methods, which were detailed in Chapter 2, are shown.

A.1 Relative humidity and temperature

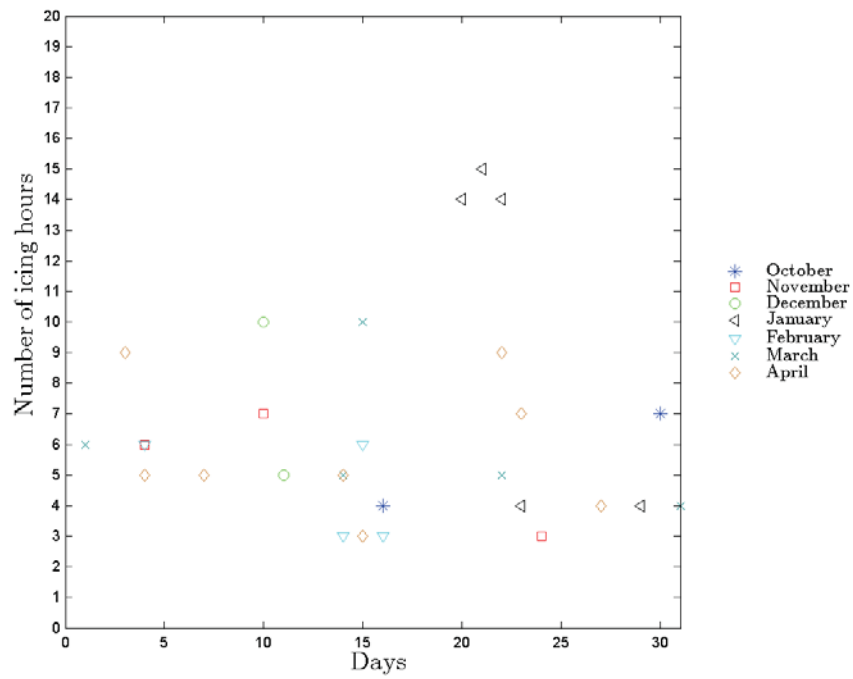In total 112 hours of icing event in 16 days were identified with this method during the studied 7 winter months.
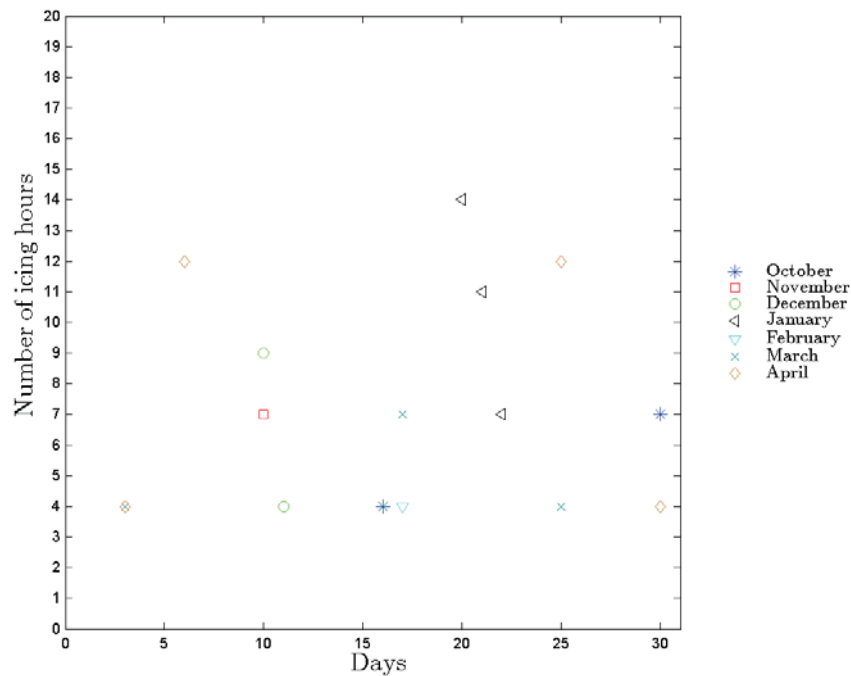
Figure A.1: *Number of daily icing hours based on RH and temperature measurements during winter months 2007-2008.*

A.2 Cloud base height and temperature

In total 188 hours of icing event in 29 days were identified with this method during the studied 7 winter months.

Figure A.2: *Number of daily icing hours based on CBH and temperature measurements during winter months 2007-2008.*

A.3   Heated and unheated anemometers

In total 446 hours icing hours in 56 days were identified with this method during the studied 7 winter months.
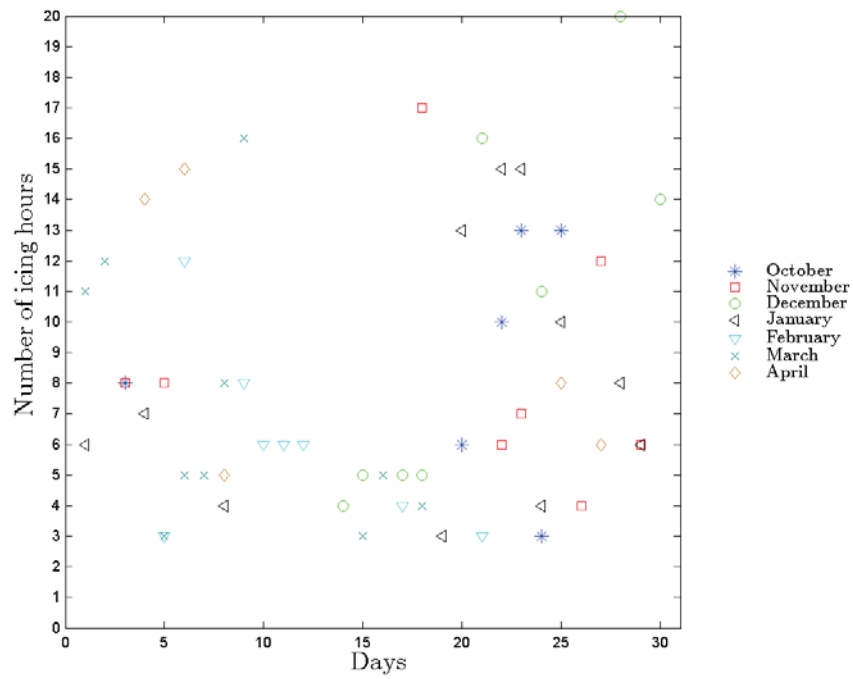
Figure A.3: *Number of daily icing hours based on the differences between heated and unheated anemometers during winter months 2007-2008.*

A.4   Frozen anemometer

In total 27 hours with frozen up unheated anemometers in 5 days were identified with this method during the studied 7 winter months.
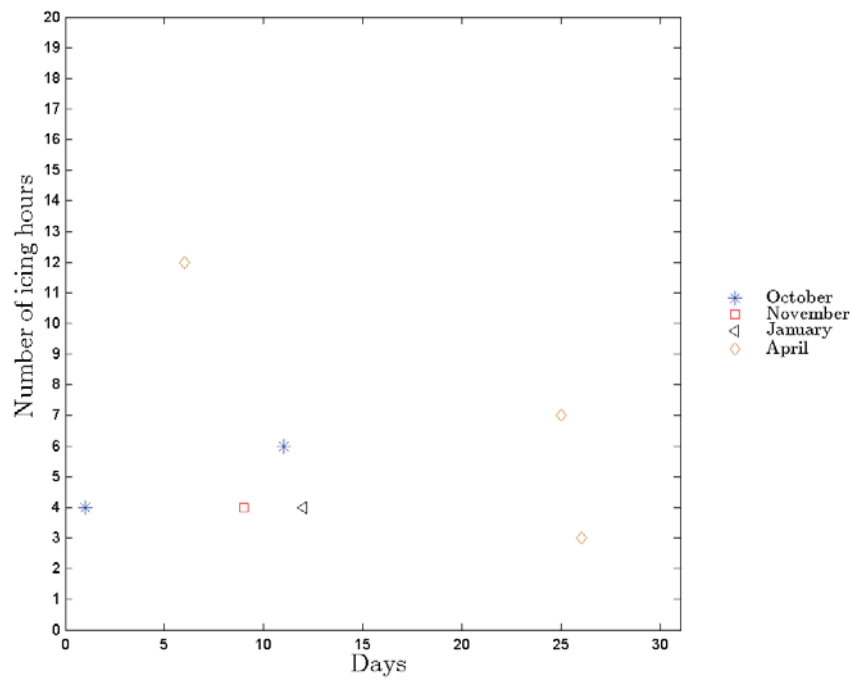
Figure A.4: *Number of daily icing hours based on frozen up anemometers during winter months 2007-2008.*

A.5   Wind vane and temperature

In total 108 days where more than 30 minutes of 10 minutes measurements of zero STD of the unheated wind vane (A.5) and only 17 days of the heated one (A.6) were identified with this method during the studied 7 winter months.
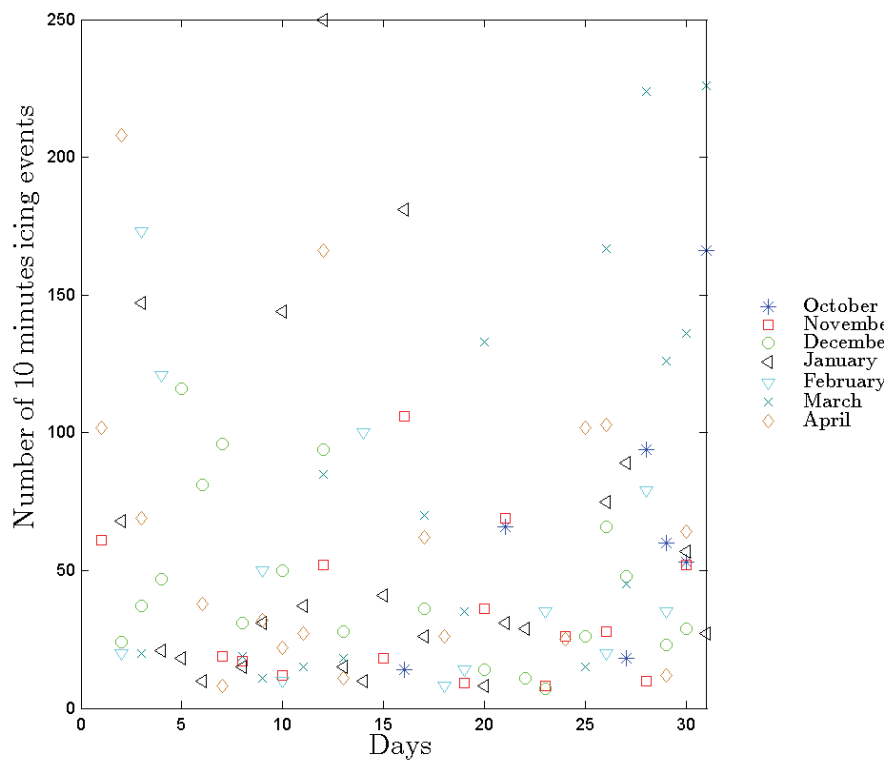
Figure A.5: *Number of daily icing hours based on the standard deviation of unheated wind vane data and temperature measurements during winter months 2007-2008.*
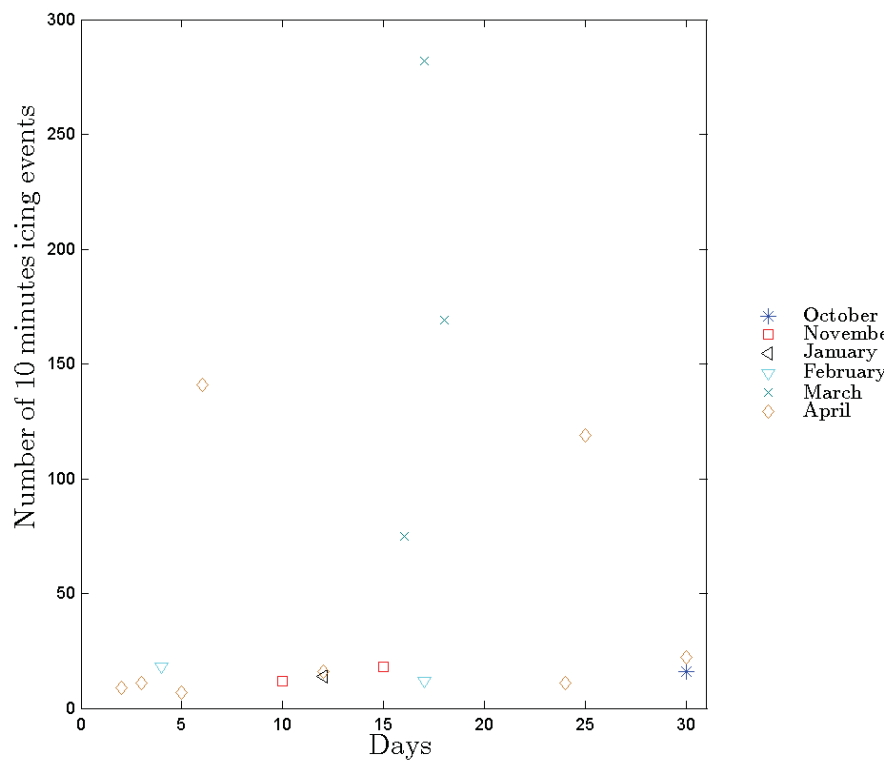
Figure A.6: *Number of daily icing hours based on the standard deviation of heated wind vane data and temperature measurements during winter months 2007-2008.*

Appendix B

Ice accretion on a NACA 64-618 section

In this Appendix chapter, some extra photos from the experiments performed in the CWT are shown focusing on details. First, the two different kinds of feathers can be seen in Figure B.1, on the left hand side, the feathers formed during mixed ice accretion whereas on the right hand side, during rime ice accretion are shown. It can be noticed, that the feathers of the mixed ice are more opaque whereas of the rime ice are white. The reason is probably the different temperature and environmental parameters, i.e. MVD and LWC.
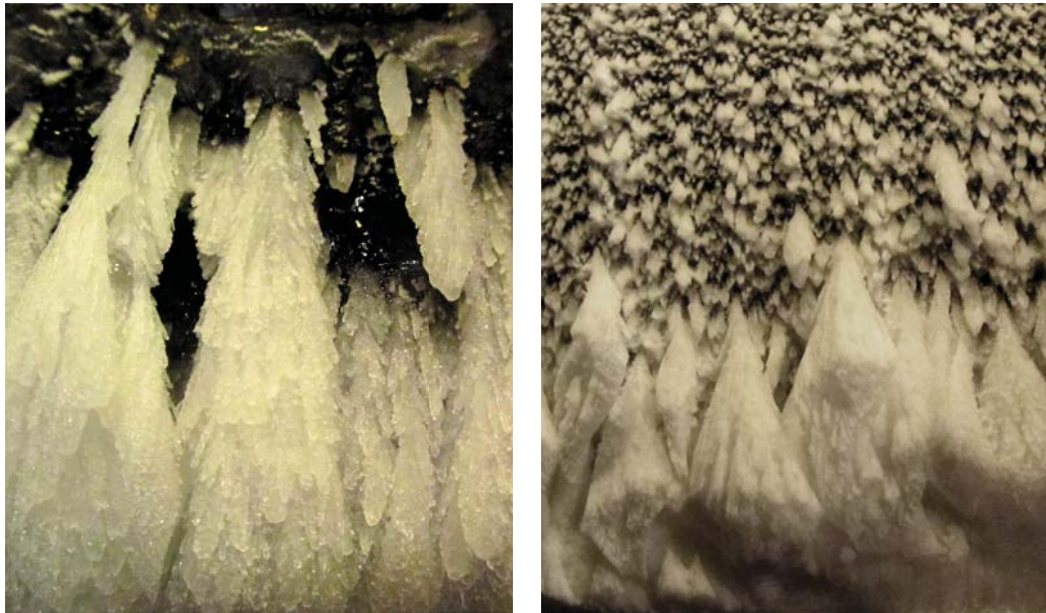
(a) Mixed ice accretion

(b) Rime ice accretion

Figure B.1: *Two different kinds of feather formation seen during the wind tunnel tests.*

In Figure B.2, the pressure side of the airfoil is captured after glaze ice accretion for $\alpha = 7^o$. It can be seen that a great area was exposed to the flow and thus the spraying. The small icicles could form due to the nature of the test campaign, i.e. the tunnel was set to idle for measurements and this time was enough to get some of the water droplets to freeze.

Figure B.2: *Glaze iced pressure side of the airfoil for $\alpha = 7^o$.*

Depending on the type of the accreted ice, different amount of ice can accumulate on the suction side, with different characteristics and roughness. Three example for the three tested ice types can be seen in Figure B.3. In Figure B.3 a, some run-back rivulets can be seen in case of glaze ice accretion. These could form because not all the impinged water droplets freeze on impact to the surface. Small dry ice accretion can be observed in Figure B.3 b and c. These small ice formation could form due to gravity. They altered the originally smooth airfoil surface into rough and had very low adhesion, therefore they could be easily removed. It is assumed that they could form due to the stationary airfoil section.

(a) Glaze ice accretion
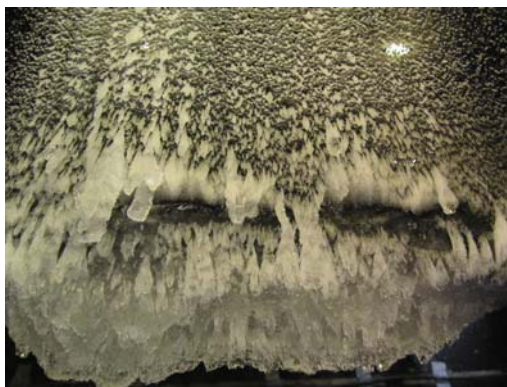
(b) Mixed ice accretion

(c) Rime ice accretion

Figure B.3: *The different ice formation seen on the suction side for glaze, mixed and rime accretion.*

Appendix C

Timelaps of ice accretion

As it was mentioned in Section 3.3, an action camera was installed inside the wind tunnel upstream from the airfoil and was taking photos every 30 s throughout the ice accretion. Some of these photos are presented in this Appendix chapter to see how the accretion process happened. In Figure C.1, Figure C.2 and Figure C.3, the time-laps photos of 5, 10, 30 and 60 minutes accretion time can be seen for glaze, mixed and rime ice accretion, respectively. It can be observed that regardless of the type of the ice, quite significant amount of ice accreted on the airfoil only after 5 minutes.

(a) $t = 5min$

(b) $t = 10min$

(c) $t = 30min$

(d) $t = 60min$
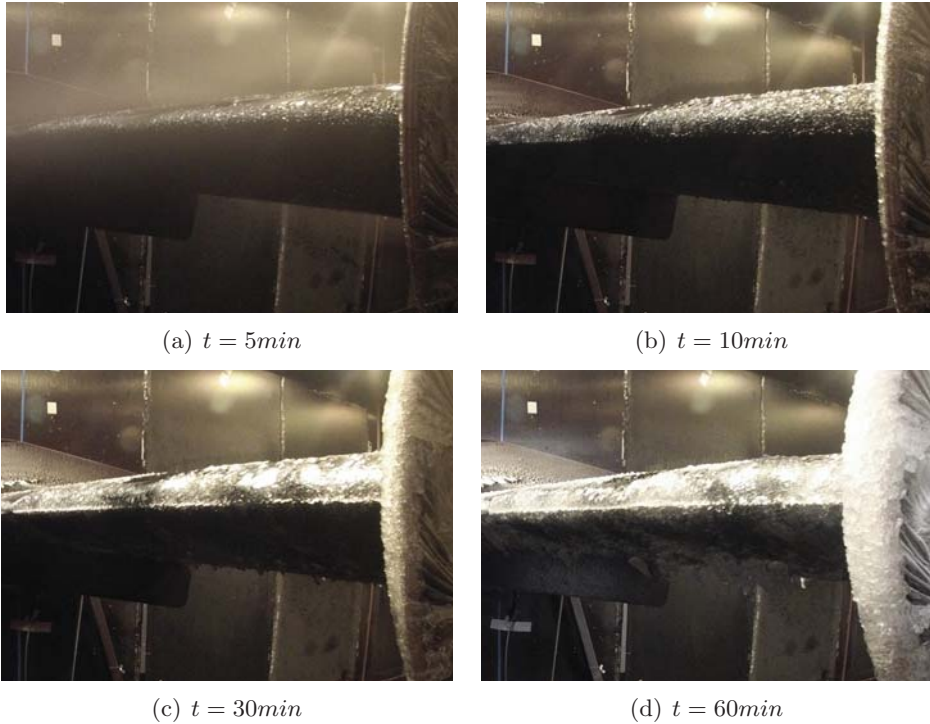
Figure C.1: *Time-laps of **glaze ice** accretion, $\alpha = 9^o$.*

(a) $t = 5min$ (b) $t = 10min$

(c) $t = 30min$ (d) $t = 60min$
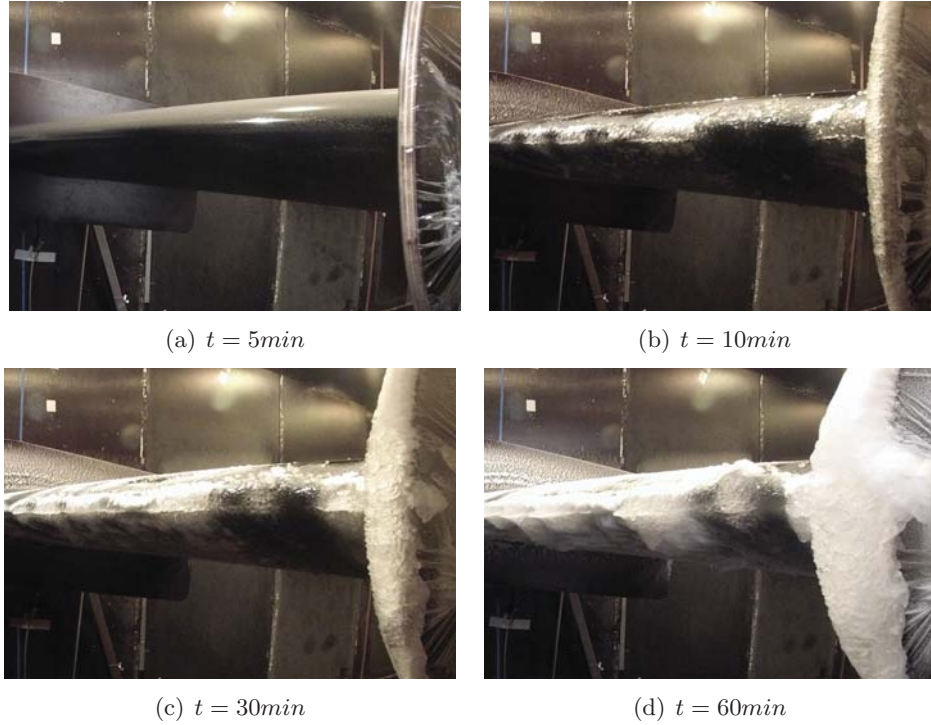
Figure C.2: *Time-laps of **mixed ice** accretion, $\alpha = 7^o$.*

(a) $t = 5min$ (b) $t = 10min$

(c) $t = 30min$ (d) $t = 60min$
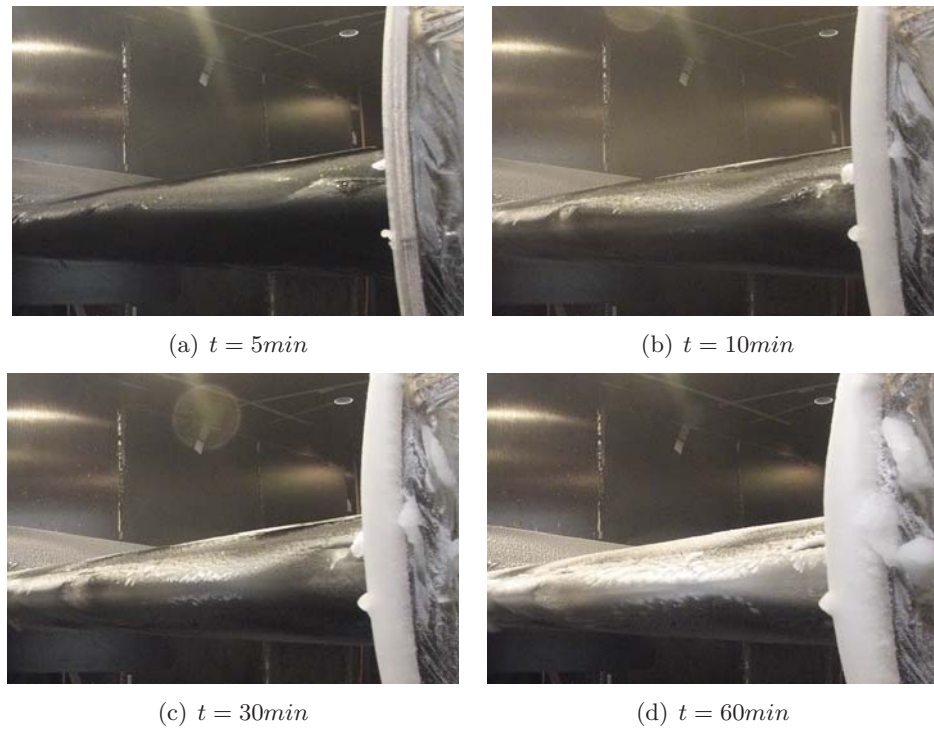
Figure C.3: *Time-laps of **rime ice** accretion, $\alpha = 4^o$.*

Appendix D

TURBICE ice accretion model, results

In Section 4.4.1, the results of the computational ice accretion model, TURBICE are detailed and some samples of the results are also shown there. In this Appendix chapter, the rest of the results are presented.

A direct comparison of the profiles from the wind tunnel to the ones from TURBICE are shown in Figure D.1 and Figure D.2. As it can be seen, setting the same environmental parameters for LWC and MVD in TURBICE as the aimed ones from the wind tunnel tests resulted in significantly smaller numerical ice profiles, which indicates that these two parameters were highly underestimated.

Since the TURBICE simulations were done prior the final wind tunnel tests, it was necessary to produce as many scenarios as it was possible in order to have a catalogue to be able to properly verify the environmental parameters for LWC and MVD. Using the plots in Figure D.3 and D.4, it gave valuable help for the range necessary for the additional numerical simulations. It could be concluded that LWC can be found in a range between $0.8 - 1g/m^3$ where as MVD is around $35 - 40\mu m$.
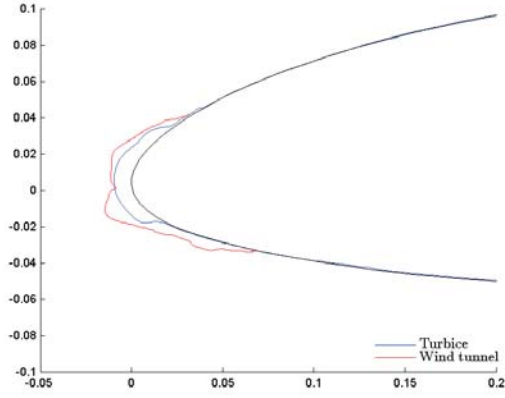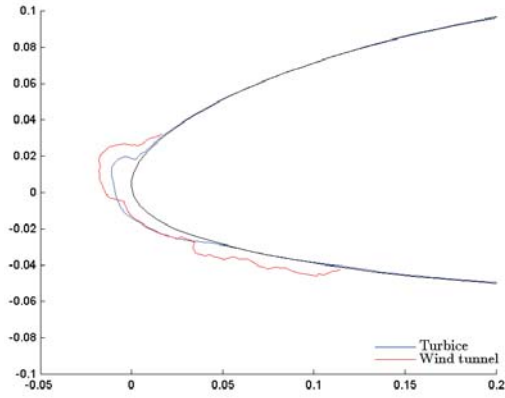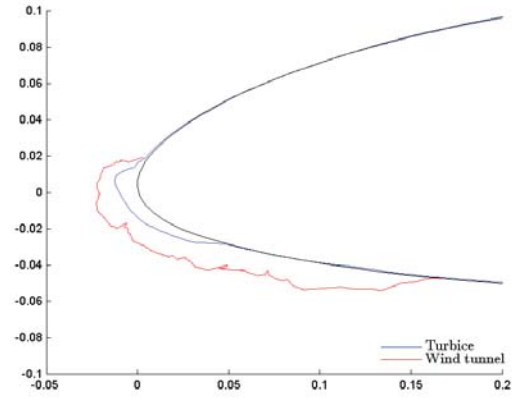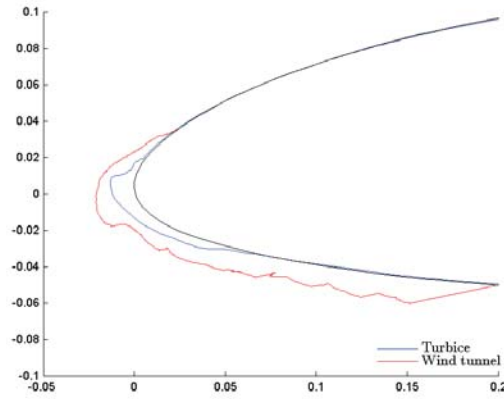
(a) Glaze ice accretion $\alpha = 0^o$
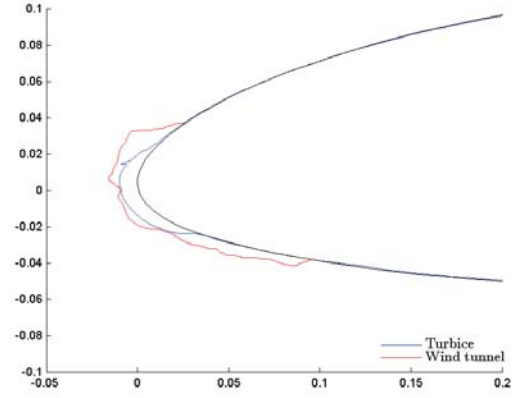
(b) Glaze ice accretion $\alpha = 4^o$

(c) Glaze ice accretion $\alpha = 7^o$

(d) Glaze ice accretion $\alpha = 9^o$

(e) Glaze ice accretion $\alpha = 11^o$

Figure D.1: *Results of TURBICE simulation plotted against the profiles from the wind tunnel tests for **glaze ice** accretion with $LWC = 0.65 g/m3$ and $MVD = 27\mu m$.*
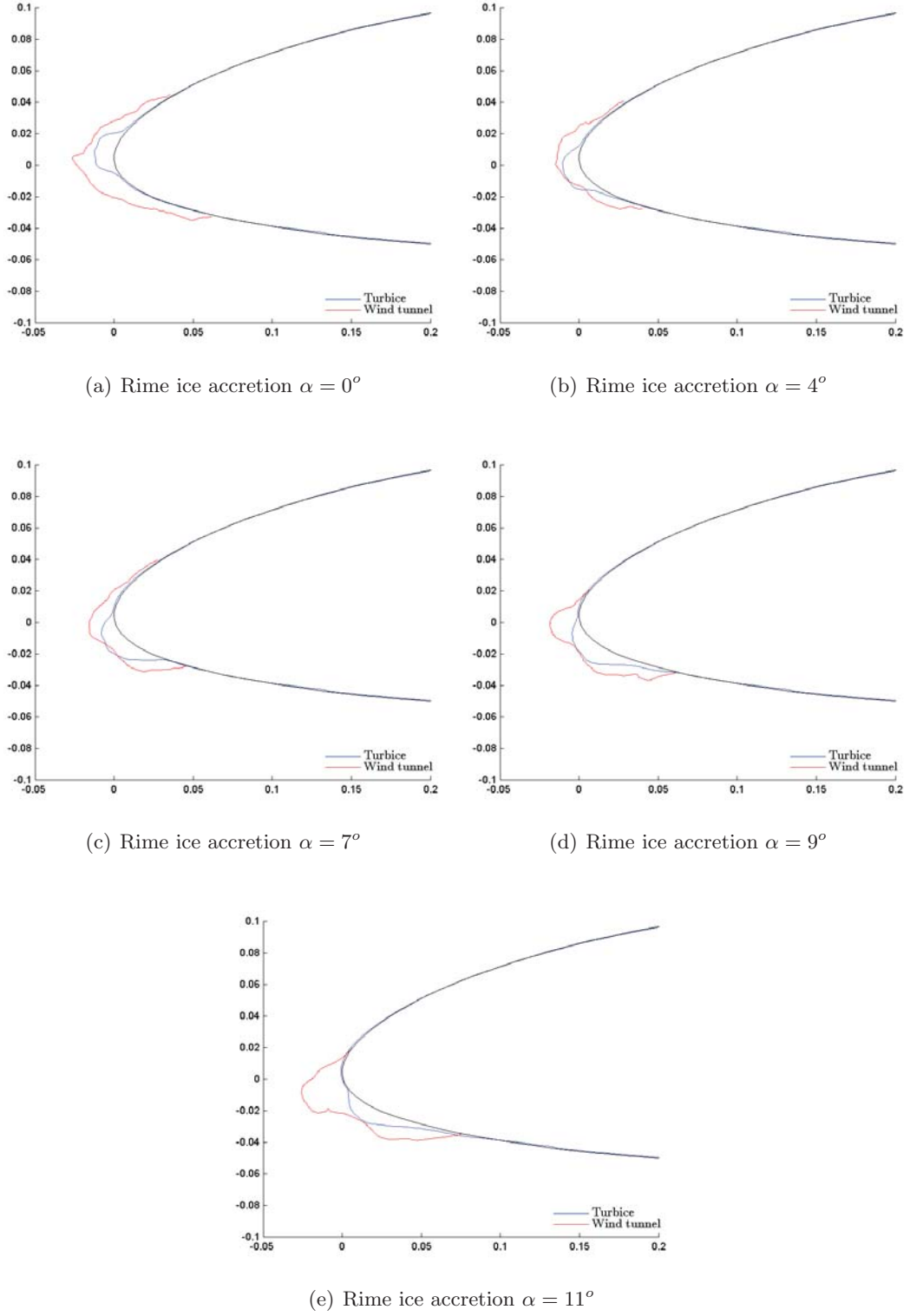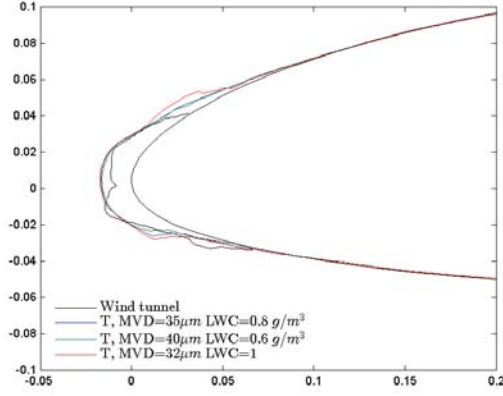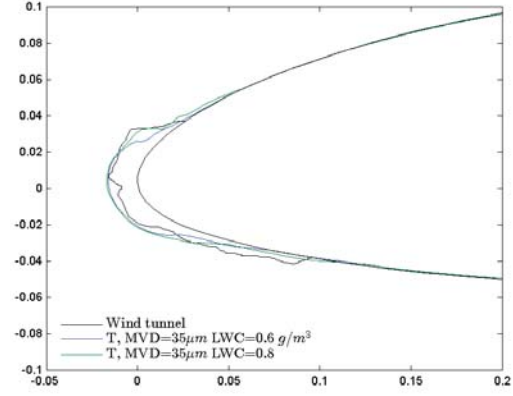
(a) Rime ice accretion $\alpha = 0^o$

(b) Rime ice accretion $\alpha = 4^o$

(c) Rime ice accretion $\alpha = 7^o$

(d) Rime ice accretion $\alpha = 9^o$

(e) Rime ice accretion $\alpha = 11^o$

Figure D.2: *Results of TURBICE simulation plotted against the profiles from the wind tunnel tests for* **rime ice** *accretion with $LWC = 0.60g/m3$ and $MVD = 23\mu m$.*
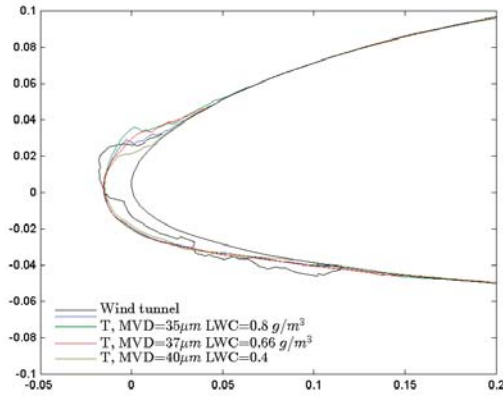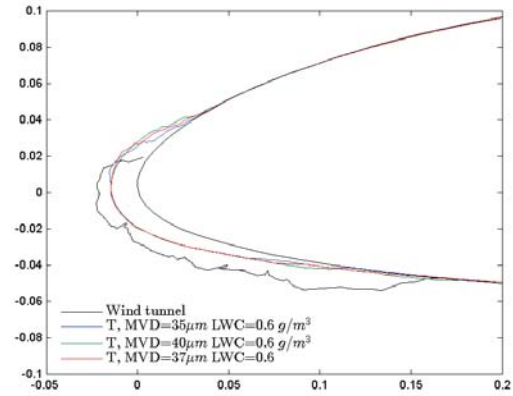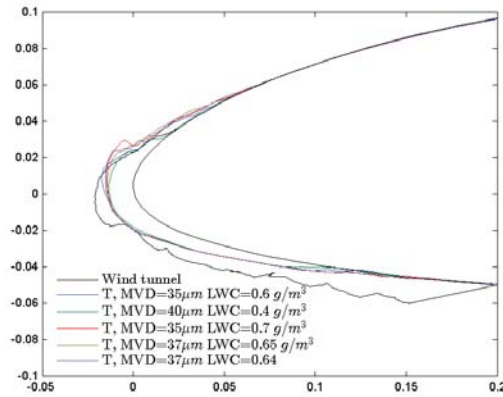
(a) Glaze ice accretion $\alpha = 0^o$

(b) Glaze ice accretion $\alpha = 4^o$

(c) Glaze ice accretion $\alpha = 7^o$

(d) Glaze ice accretion $\alpha = 9^o$

(e) Glaze ice accretion $\alpha = 11^o$

Figure D.3: *Results of different settings of TURBICE simulation plotted against the profiles from the wind tunnel tests for **glaze ice** accretion.*
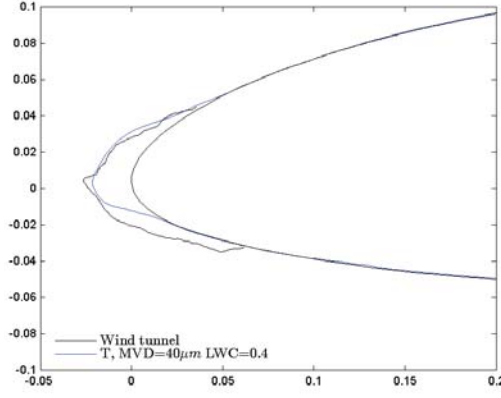
(a) Rime ice accretion $\alpha = 0^o$

(b) Rime ice accretion $\alpha = 4^o$

(c) Rime ice accretion $\alpha = 7^o$

(d) Rime ice accretion $\alpha = 9^o$

(e) Rime ice accretion $\alpha = 11^o$

Figure D.4: *Results of different settings of TURBICE simulation plotted against the profiles from the wind tunnel tests for* **rime ice** *accretion.*
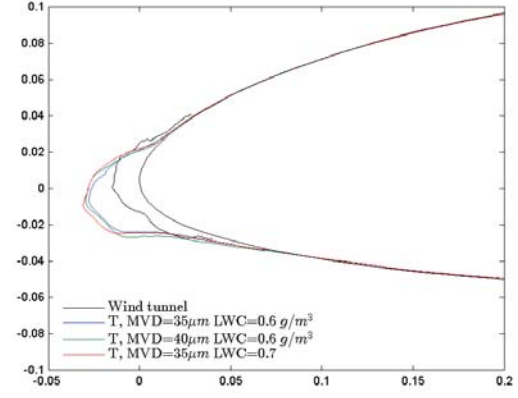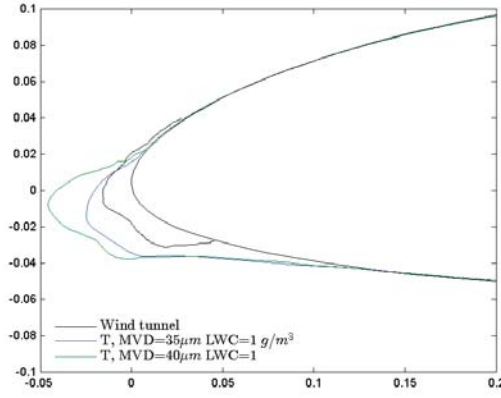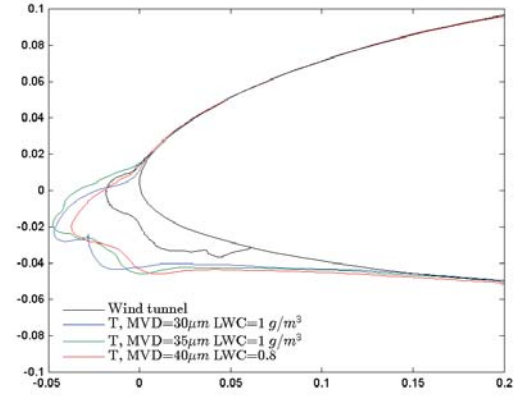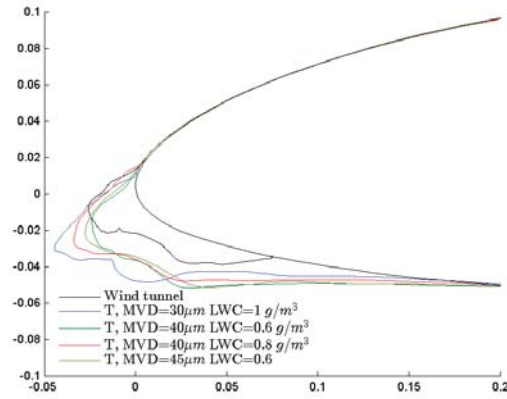
Appendix E

Submitted and published papers

In this Appendix chapter, the submitted journal papers and published conference proceeding are enclosed:

- Hudecz, A., Hansen, M. O. L., Dillingh, J. and Turkia, V., (2013). *Numerical Investigation of the Effects of Ice Accretion on a Wind Turbine Blade.* Wind Energy. (Submitted)

- Hudecz, A., Koss, H. H. and Hansen, M. O. L., (2013). *Icing Wind Tunnel Tests of a Wind Turbine Blade.* Wind Energy. (Submitted)

- Hudecz, A., Koss, H. H. and Hansen, M. O. L., (2013). *Ice Accretion on Wind Turbine Blades.* In XV. International Workshop on Atmospheric Icing on Structures, St-Johns, Newfoundland, September 8 to 11, 2013. (Oral presentation)

RESEARCH ARTICLE

Numerical investigation of the effects of ice accretion on a wind turbine blade

A. Hudecz[1], M. O. L. Hansen[1 2], J. Dillingh[3] and V. Turkia[3]

[1]Department of Wind Energy, Technical University of Denmark, Kgs. Lyngby, Denmark
[2]Centre for Ships and Ocean Structures, Department of Marine Technology, Norwegian University of Science and Technology, Trondheim, Norway
[3]VTT, Technical Research Centre of Finland

ABSTRACT

This paper presents the results of a numerical investigation of iced wind turbine blades. The iced sections were collected during climatic wind tunnel testing. Different angles of attack, wind speeds and ice formations (glaze, mixed and rime ice) were analysed. The collected profiles and the settings of the wind tunnel were validated by results of a numerical ice accretion model, TURBICE. The wind tunnel parameter value of the median volumetric diameter was found to be underestimated. However, after correcting the wind tunnel parameters for LWC and MVD, the rime ice profiles were in good agreement with the results of the numerical modelling. CFD simulations with Ansys Fluent were carried out to numerically analyse the impacts of ice accretion on the flow behaviour and on the aerodynamic characteristics of the airfoil. The trend of the reduction of lift coefficients agrees quite well with the wind tunnel test results. However, the relative degradation was found to be lower than it was for the experiments. Also the importance of the angle of attack, on which the profiles were collected, on the aerodynamics was shown.

Correspondence
Adriana Hudecz, DTU Wind Energy, Kemitorvet 204/230, 2800 Kgs. Lyngby, Denmark
email: ahud@dtu.dk or adrianahudecz@gmail.com

ABBREVIATIONS

AOA angle of attack
CWT climatic wind tunnel
LWC liquid water content
MVD median volumetric diameter

NOMENCLATURE

C_L lift coefficient
T (C^o) mean air temperature
U (m/s) mean wind speed
α $(^o)$ angle of attack

1. INTRODUCTION

As fewer temperate sites become available, cold climate and hence severe icing problems have to be faced when erecting wind turbines in areas like e.g. Finland, Sweden or Canada or at mountainous or hilly onshore sites at regions such as northern Spain, Alps, mountainous areas in Germany or Scotland. Wind turbines in these sites may be exposed to icing

conditions or temperatures outside their standard design limits.

There are presently dedicated ice accretion models available on the field. One of the most well-known model is Nasa's LEWICE, which is built up of four modules; potential flow field calculation, particle trajectory and impingement calculation, thermodynamic and ice growth calculation, and finally the geometry modification due to ice growth. The ice accretion itself is a time-stepping procedure ([2]). Another, comprehensive numerical ice accretion software is TURBICE from VTT Technical Research Centre of Finland, which also uses the panel method to calculate the potential flow ([1]). The results have been verified by icing wind tunnel testing of both aircraft and wind turbine airfoils [3]. Fensap-ICE is an aerodynamic and icing simulation system from Newmerical Technologies International (NTI). This model was developed for solving aeronautic issues, however it has been recently used in wind energy applications ([4], [5] and [6]). There are three modules set in a loop; the flow field calculation using the solution of the compressible Navier-Stokes equations with FENSAP (or other solvers), the computation of the collection efficiency distribution with DROP3D, and then the prediction of the ice accretion shape by a shallow-water icing model with ICE3D [7].

Simulations with computational fluid dynamics (CFD) based techniques are used to numerically analyze the impacts of ice accretion on the flow behavior and the aerodynamic characteristics of the airfoil. The analysis can be done by either an individual CFD program, e.g. Ansys Fluent, or aerodynamics and icing simulation program with built-in CFD module such as the above mentioned Fensap-ICE.

In some recent studies, the numerical simulations were carried out in two steps (e.g. [8], [9]). In the first step, the physical characteristics of the accreted ice (e.g. shape and size) were predicted with one of the above described ice accretion models. In the second step, CFD analyses were performed on the iced airfoil to estimate the effect on drag and lift forces. Homola et al. (2010) [10] combined TURBICE and Ansys Fluent to investigate the effect of ice on a NACA 64-618 profile. The ice profiles were the results of three different droplet sizes and air temperatures and they were analysed at different angles of attack ranging from -10° to $+20^o$. The lift coefficient was found to be reduced in all cases and the least change was observed in case of streamlined rime ice, while there was larger reduction experienced with horn shaped glaze ice. During the CFD simulations, it was found that the horn type glaze ice caused the largest separation, and thus significant lift reduction and higher drag coefficient.

Etermaddar et al. (2012) [9] was also using a NACA 64-618 in their numerical analysis, however instead of TURBICE, they used LEWICE. It was found that the ice load increases with liquid water content (LWC), median volumetric diameter (MVD) and relative wind speed.

Two 2-D studies ([4] and [5]) have been carried out using Fensap-ICE. Homola et al. (2009) [4] studied only one section with different angles of attack and atmospheric temperatures, whereas Virk et al. (2012) [5] selected five sections along the blade radius, thereby each tests were performed with different angle of attacks and relative wind speeds. The results showed that the angle of attack has influence on the rate and shape of ice growth and for lower angle of attacks the icing is less severe near to the tip [4].

This paper presents the results of a series of numerical analysis of an iced NACA 64-618 profile with 0.9 m chord length. The iced airfoil profiles were collected with contour tracing method during icing wind tunnel tests (presented in Hudecz et al. 2013 [14]). The tests were carried out at Collaborative Climatic Wind Tunnel (CWT) at Force Technology in Denmark. Each simulation was carried out at different angle of attack, i.e. $\alpha = 0^o, 4^o, 7^o, 9^o$ and 11° at moderately low wind speed, $\sim 10 - 15 m/s$ for glaze, rime and mixed ice. The collected ice profiles were further analyzed in Ansys Fluent at different wind speed and compared to results of TURBICE model. The main goal is to validate the wind tunnel force measurements and to calibrate the wind tunnel parameters for LWC and MVD using numerical methods.

2. NUMERICAL SIMULATION

2.1. Ice accretion simulation

In order to verify the collected ice profiles and calibrate the environmental parameters in the tunnel, which are difficult to measure accurately, computations were made with a numerical ice accretion model, TURBICE from VTT, Technical Research Centre of Finland. Since constant air temperature is an input parameter of the program, mixed ice formation cannot be modeled. MVD, LWC, meteorological wind speed, rotating speed of the wind turbine, pitch angle, air temperature, air pressure and accretion time had to be specified before the analysis. These parameters were chosen carefully in order to ensure similar environment as it was during the wind tunnel tests. In Table I, the simulation parameters of the

validation tests in TURBICE are listed. MVD and LWC are target values, which were set in the tunnel and the listed temperatures and wind speeds are mean temperature and velocity, which were achieved during the ice accretion.

Table I. Input parameters of validation tests done with TURBICE

Parameters	Glaze ice					Rime ice				
	I.	II.	III.	IV.	V.	I.	II.	III.	IV.	V.
AOA (^{o})	0	4	7	9	11	0	4	7	9	11
MVD (μm)	27	27	27	27	27	23	23	23	23	23
LWC (g/m^3)	0.65	0.65	0.65	0.65	0.65	0.6	0.6	0.6	0.6	0.6
T (^oC)	-3	-3	-3	-3	-3	-8	-8	-8	-8	-8
U (m/s)	15	15	15	15	15	10	10	10	10	10
Time (min)	60	60	60	60	60	60	60	60	60	60

2.2. Computational fluid dynamics

Simulations with Ansys Fluent were afterwards conducted to quantify the impacts of ice accretion on the flow behavior and the aerodynamic characteristics of the iced airfoil from the wind tunnel tests. First, the aerodynamic forces measured during the experiments were verified. Due to the limitation of the CWT's cooling unit, it was necessary to set relatively low target wind speed (15 m/s which corresponds to appr. $Re = 1E6$) to ensure stable and low enough air temperature. A number of numerical tests were done with higher wind speed, 25 m/s ($Re = 1.5E6$). For each simulation, each of the ice deposit accreted at the same AOA as the investigation of the flow behaviour and the aerodynamic characteristics was done. These tests are refereed as "dedicated profile" tests or simulations.

The impact of angle of attack was investigated with one single profile. For this investigation, the glaze and rime iced airfoils collected at $\alpha = 0^o$ and 11° were chosen and they were tested in flows with 0°, 4°, 7°, 9° and 11° incident angles and 25 m/s wind speed. These tests are refereed as "single profile" tests or simulations.

The ice profiles were collected from specific spanwise locations, and therefore a 2-D model was done in Ansys Workbench. The control volume around the airfoil was rectangular with edges positioned at 50 chords length away in vertical direction and 20 chords length from the horizontal direction.

An inflation layer was added to the mesh to produce a structured, fine mesh in the vicinity of the airfoil to achieve the desired wall Y^+ distribution and thus give a better representation of the flow near the airfoil surface, see examples for $\alpha = 0^o$ in Figure 1. The first layer height is dependent on the surface roughness, since the roughness height may not exceed it. However, it was found that Ansys Fluent cannot properly handle micro surface roughness, therefore it was not included in the analysis and only the large scale roughness resolved in the grid is felt by the flow. It was aimed to construct similar mesh and also inflation layer for all the different profiles, but sometimes due to the complexity of the curve of the ice shapes, minor changes had to be done. In Table II, the set-up of mesh and inflation layer of each test is summarized.

For the simulations, fully turbulent flow was assumed considering the roughness of the ice deposit. Spalart-Allmaras and $k - \omega$ SST turbulence models were used. It was found in previous studies [11] that the solution converges faster and easier using Spalart-Allmaras model than with the $k - \omega$ SST turbulence model. Therefore for the clean profiles, the first 500 iterations were done by using Spalart-Allmaras model providing an initial guess for the $k - \omega$ SST turbulence model and achieving more stable convergence. However, it was shown by Chung and Addy (2000) [12] that Spalart-Allmaras model is the best performing model when simulating ice accretions and hence it was used during the iced profiles' analysis. In all 5000 iteration were done to ensure stable solution.
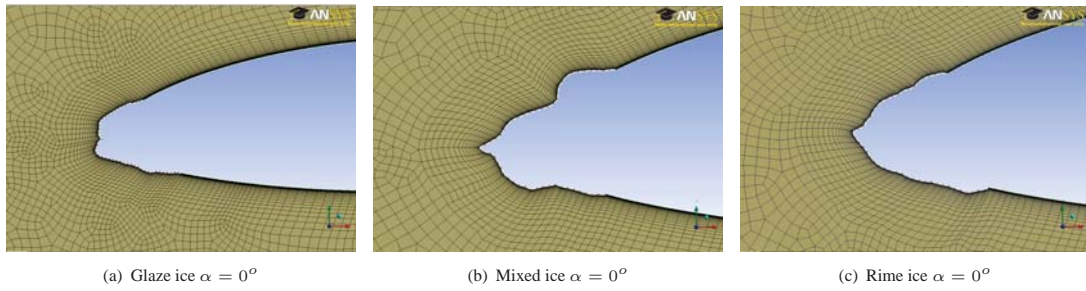
3. RESULTS
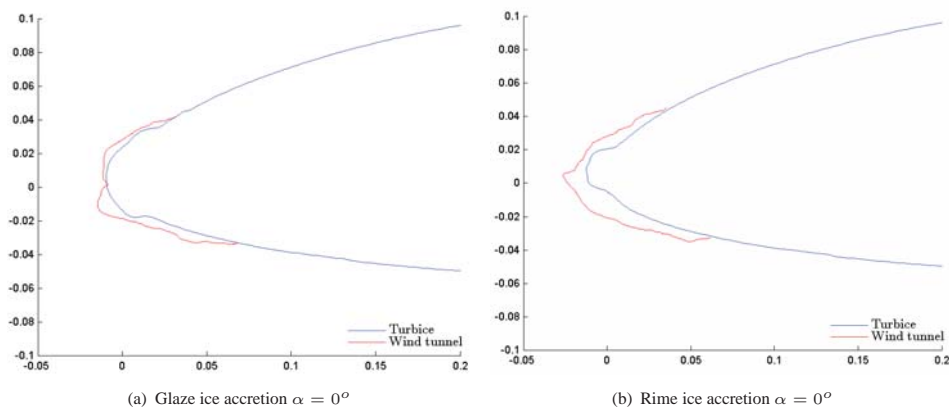
3.1. Ice accretion simulation

The aim of the TURBICE tests was to validate the collected ice profiles and the setting of the meteorological variables, especially MVD and LWC. Therefore a set of simulations were performed using the same input parameters as the target

Table II. Set-up of mesh and inflation layer of each "multiple profile" simulations in Ansys Workbench. ∗ In case of the clean airfoil, the number of nods and elements were slightly different for each simulations due to the various angles of attack.

Profile	AOA	First layer height (m)	Nr. of layers of inflation layer	Growth rate	Nr. of nods	Nr. of elements
Clean	all	$1E-5$	50	1.2	~ 81250	$\sim 81000*$
Glaze ice	0	$1E-5$	38	1.2	94474	93699
	4	$1E-5$	38	1.2	95045	94275
	7	$1E-5$	30	1.25	93878	93095
	9	$1E-5$	35	1.2	94524	93767
	11	$1E-5$	38	1.2	95181	94403
Mixed ice	0	$1E-5$	38	1.2	96890	96107
	4	$1E-5$	38	1.2	95690	94914
	7	$1E-5$	40	1.2	95803	95025
	9	$1E-5$	38	1.2	95072	94279
	11	$1E-5$	38	1.2	94806	94030
Rime ice	0	$1E-5$	38	1.2	94009	93247
	4	$1E-5$	38	1.2	93315	92576
	7	$1E-5$	35	1.25	94643	93843
	9	$1E-5$	38	1.2	94192	93432
	11	$1E-5$	36	1.2	94811	94041

(a) Glaze ice $\alpha = 0^o$ (b) Mixed ice $\alpha = 0^o$ (c) Rime ice $\alpha = 0^o$

Figure 1. Mesh around the airfoil profiles for glaze, mixed and rime ice accretion in case of $\alpha = 0^{\,o}$

values of the wind tunnel tests. In Figure 2, two of the TURBICE profiles are plotted against the experimental ones for glaze and rime ice at $\alpha = 0^o$. As it can be seen in these plots, the numerical profiles are significantly smaller than the

(a) Glaze ice accretion $\alpha = 0^o$ (b) Rime ice accretion $\alpha = 0^o$

Figure 2. Results of TURBICE simulation plotted against the profiles from the wind tunnel tests for both glaze and rime ice accretion at $\alpha = 0^o$.

the ones from the wind tunnel, which indicates underestimation of the input parameters, especially the MVD. Therefore additional TURBICE simulations were performed in order to find the the best fits. The results gave the best fits for all angles of attack for rime ice accretion with $LWC \simeq 1 g/m^3$ and $MVD \simeq 40 \mu m$, rather than 0.6 g/m^3 and $23 \mu m$, as specified by the manufacturer of the spray nozzles based on the setted water and air pressure.

3.2. Computational fluid dynamics

There have been in all 40 dedicated profile simulations performed with Ansys Fluent, including clean, glaze iced, mixed iced and rime iced airfoils with different wind speeds (15 m/s and 25 m/s). 15 m/s wind speed was chosen to simulate similar flow conditions as in the wind tunnel and thus compare the results directly. Higher wind speed was investigated to see the influence of ice on the lift coefficient for a more realistic situation.

Table III summarises the lift coefficients for the clean profiles for different wind speeds for the Fluent simulations along with the ones from the wind tunnel tests (presented in [13] and [14]) and from Abbot and Doenhoff (1959) [15]. It can be noticed that at higher AOA, the numerical C_L agrees well to the data from Abbot and Doenhoff (1959) [15]. However, they differs from the ones from the wind tunnel. The lower values in the experiments are caused by the fact that the total forces are measured using force transducers and that end effect lowers the loads compared to full 2-D. It can be concluded that the end effect reduces the effective chord width by, based on these results, 20 %. In Table IV, the measured lift coefficients of the iced airfoils from the wind tunnel experiments are listed for comparison. In Table V, the lift coefficients and the

Table III. Lift coefficient of the clean airfoils for different wind speeds from Ansys Fluent simulations (first three rows), wind tunnel tests (4th row) and measured by Abbott and Doenhoff (1959) [15] (5th row)

	U	AOA (^{o})				
	(m/s)	0°	4°	7°	9°	11°
C_L	15	0.38	0.76	1.01	1.15	1.28
	25	0.39	0.78	1.07	1.16	1.27
C_L from [13], [14]	15	0.319	0.571	0.814	0.96	1.066
C_L from [15]		0.45	0.85	1.05	1.15	1.25

Table IV. Wind tunnel lift measurements (from Hudecz et al. (2013 a) [13] and Hudecz et al. (2013 b) [14]). C_{Lf} is the final lift coefficient at the end of the ice build-up process.

| Ice type	Glaze ice				
C_{Lf} (final, iced airfoil)	0.157	0.366	0.515	0.643	0.807
Degradation [%]	50	35	36	29	22
Ice type	Mixed ice				
C_{Lf} (final, iced airfoil)	0.116	0.309	0.515	0.596	0.855
Degradation [%]	64	47	36	35	21
Ice type	Rime ice				
C_{Lf} (final, iced airfoil)	0.185	0.431	0.614	0.744	0.805
Degradation [%]	42	25	25	23	24

relative changes from ice-free data are listed. It can be seen that the most significant lift degradation was found for mixed ice tests and the smallest for rime ice for most cases. The lowest lift reduction was found at lower angles of attack. For glaze and rime ice tests, the largest relative change was seen at $\alpha = 9^o$ and for mixed ice tests, at $\alpha = 7^o$. Comparing the relative lift coefficient reduction to the ones in Table IV, it can be seen that much higher reduction was found during the experiments.

In Figure 3, the results achieved at 15 m/s wind speed are plotted against the ones from the wind tunnel tests. It can be seen that however the values collected during the wind tunnel tests are much lower than the ones from the numerical analysis, the trend of these curves is similar to the numerical ones and they are nearly parallel.

The streamlines and the velocity distribution around the clean airfoil at different angles of attack are plotted in Figure 4 and Figure 5, respectively. Then in Figure 6, and Figure 7, the results for iced cases can be seen.

Table V. Lift coefficient and relative changes for the iced airfoils from Ansys Fluent simulations

	U	Glaze iced profile				
	(m/s)	0°	4°	7°	9°	11°
C_L	15	0.35	0.6	0.78	0.84	0.92
	25	0.33	0.6	0.8	0.85	0.94
C_L change (%)	15	11	21	22	27	25
	25	11	23	25	28	28
	U	Mixed iced profile				
	(m/s)	0°	4°	7°	9°	11°
C_L	15	0.33	0.57	0.75	0.89	1.02
	25	0.34	0.57	0.75	0.9	0.99
C_L change (%)	15	12	26	26	22	20
	25	15	27	29	23	22
	U	Rime iced profile				
	(m/s)	0°	4°	7°	9°	11°
C_L	15	0.35	0.62	0.83	0.93	1.06
	25	0.35	0.62	0.84	0.94	1.02
C_L change (%)	15	8	19	18	19	17
	25	10	20	22	19	19
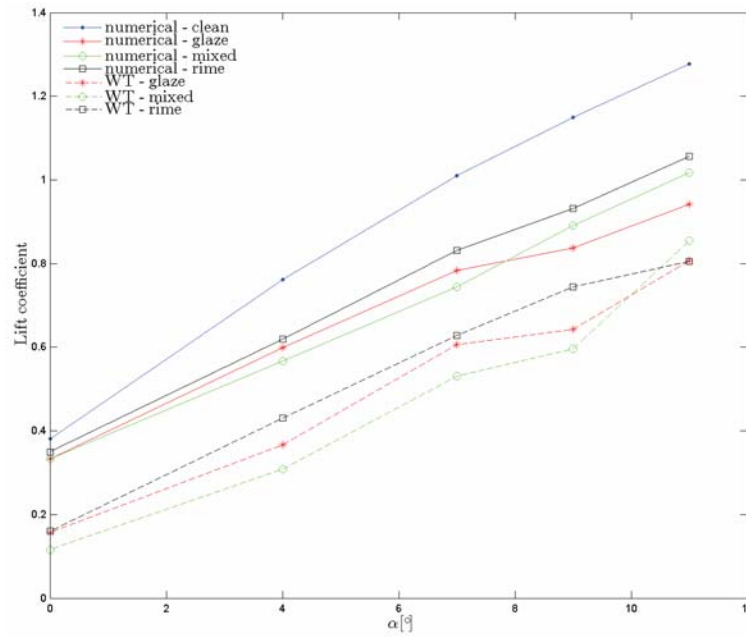
Figure 3. Lift coefficient as a function of the angle of attack for clean (•), glaze (∗), mixed (○) and rime (□) ice profiles' results from the numerical analysis (with solid line) and the wind tunnel measurements (dashed lines)

In Figure 5, it can be seen that the incoming velocity decreases to $0\ m/s$ at the stagnation point (represented by blue arrows) and speeds up at the outer side of this zone. As AOA increases, the magnitude of the velocity decreases at the pressure side. The flow around the airfoil is rather smooth and well attached. Comparing Figure 4 and Figure 6, it can be noticed that the ice accretion has influence on the flow around the airfoil, especially on the location of the leading edge and the trailing edge separation.

It is seen in Figure 7 that the flow slows in the vicinity of the iced leading edge and the caused disturbance is highly dependent on the shape of the ice deposit. Small ice peaks, protrusions formed and behind these, areas with very low velocity and even recirculation zones can be observed (see e.g. glaze ice profile at 7° in Figure 7g). These peaks form especially on the suction side, where they also cause localized speed up due to their sharp edge. For rime ice accretion at
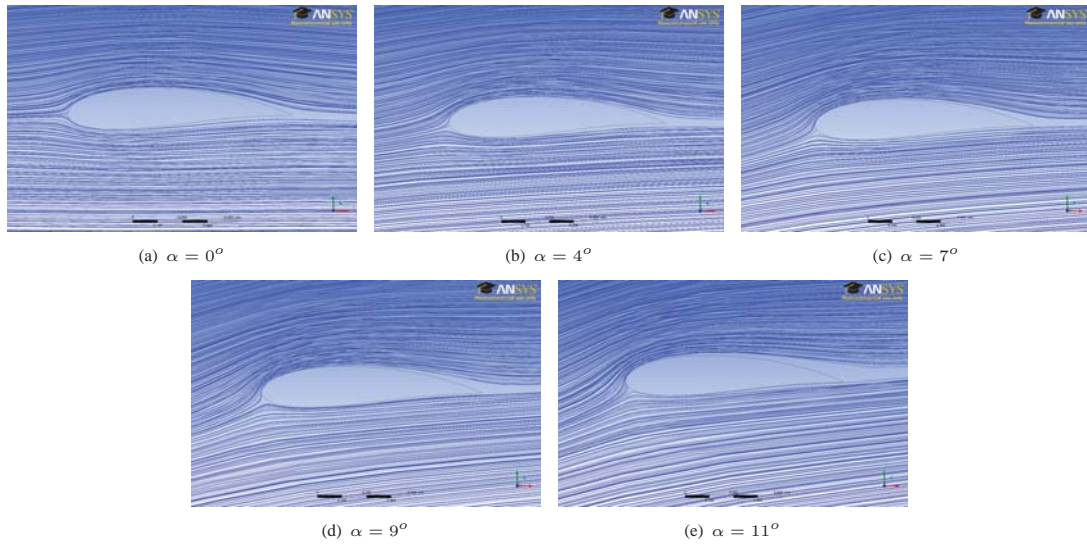
Figure 4. Streamlines around the clean airfoil at different angle of attack. First row, from left $\alpha =0^o$, 4° and 7°, second row from the left $\alpha = 9^o$ and 11 ^{o}.
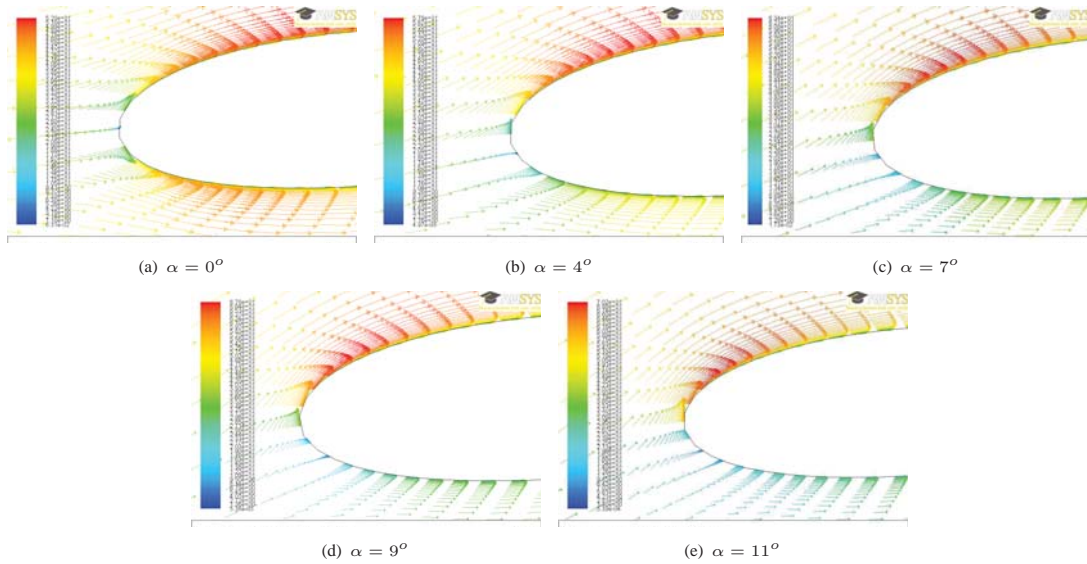

Figure 5. Velocity vectors around the leading edge of the clean airfoil at the tested angles of attack. First row, from left $\alpha =0^o$, 4° and 7°, second row from the left $\alpha =9^o$ and 11°. In the color bar, red represents the highest where blue the lowest wind speed.

lower AOA, $\alpha = 0^o$, 4° and 7°, multiple local separation points can be spotted on the suction side, which cause slightly lower velocity zones compared to the clean profile.

It is suspected that the separation happened earlier in case of iced airfoils and due to the shape of the ice, a relatively thick area around the airfoil with lower velocity (compared to the clean profile) could develop close to the airfoil. Another separation zone can be seen at the trailing edge, which increased as AOA increased in case of the clean profile. In case of mixed ice deposits, a "nose" shaped ice formation can be also seen around the stagnation point, which was not seen in case of the other two types of ice simulations. The most flow disturbance and recirculation zones happen clearly in case of glaze and mixed ice accretion.

In Figure 3, the points represent dedicated ice profiles, i.e. each profile was collected and tested at a specific angle of
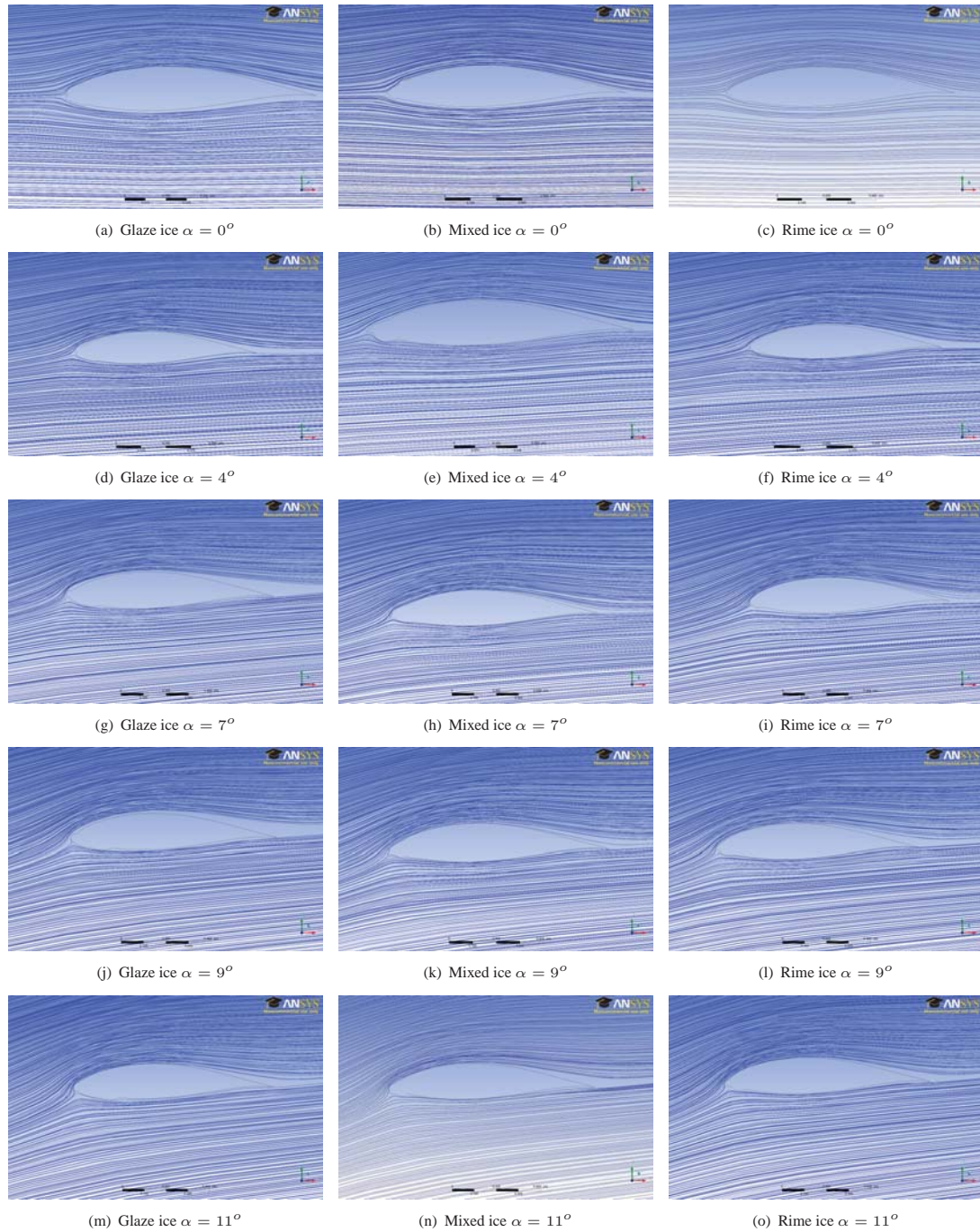
Figure 6. Streamlines around the iced airfoil for increasing angle of attack for all studied ice types. In the columns, the results are grouped by the ice types and in the rows by the angles of attack from $\alpha = 0^o$ (top) to $\alpha = 11^o$ (bottom).

attack. In Figure 8, lift coefficient - angel of attack curves are plotted for glaze and rime accretion in case of single profile tests. The "single profile" curves represent the results of one specific profile on the aerodynamic characteristics at the other angles of attacks. In the top figures, the profiles were collected at $\alpha = 0^o$ whereas in the lower figures at $\alpha = 11^o$. It can be seen that in case of $\alpha = 0^o$ profiles, there is a quite significant difference between the lift coefficients simulated with dedicated profiles and single profile at higher angle of attack. The curves fits much better for the profiles collected at $\alpha = 11^o$, however at $\alpha = 0^o$, it was found that the single glaze profile caused 19% larger lift coefficient than the dedicated

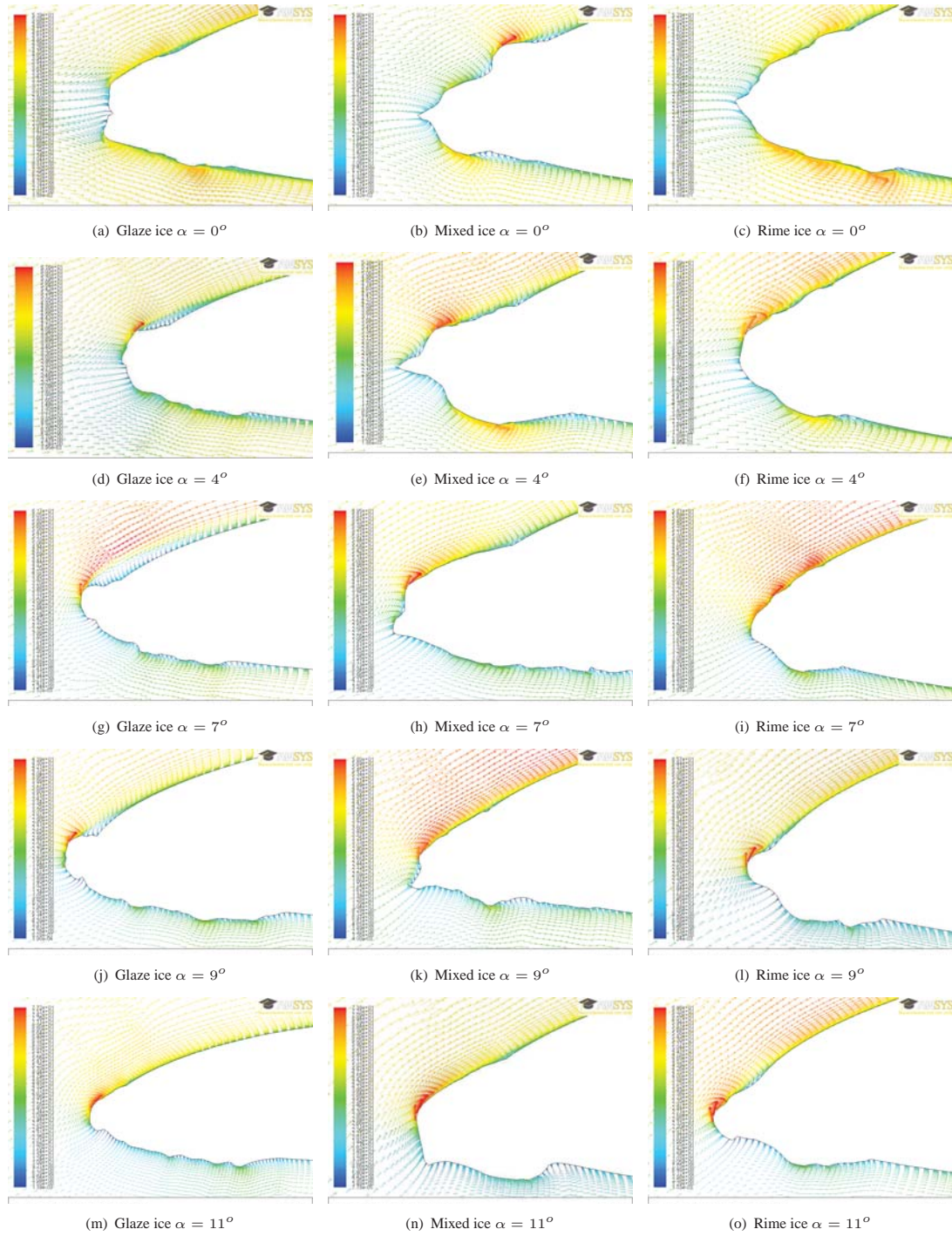(a) Glaze ice $\alpha = 0^o$ (b) Mixed ice $\alpha = 0^o$ (c) Rime ice $\alpha = 0^o$

(d) Glaze ice $\alpha = 4^o$ (e) Mixed ice $\alpha = 4^o$ (f) Rime ice $\alpha = 4^o$

(g) Glaze ice $\alpha = 7^o$ (h) Mixed ice $\alpha = 7^o$ (i) Rime ice $\alpha = 7^o$

(j) Glaze ice $\alpha = 9^o$ (k) Mixed ice $\alpha = 9^o$ (l) Rime ice $\alpha = 9^o$

(m) Glaze ice $\alpha = 11^o$ (n) Mixed ice $\alpha = 11^o$ (o) Rime ice $\alpha = 11^o$

Figure 7. Velocity vectors colored by velocity magnitude (m/s) around the iced airfoil for all studied ice types. In the columns, the results are grouped by the ice types and in the rows by the angles of attack from $\alpha = 0^o$ (top) to $\alpha = 11^o$ (bottom).

one and even larger than it was seen for the clean profile. The results are summarized in Table VI. It has to be kept in mind that these values are only valid for the set-up used in these particular tests.
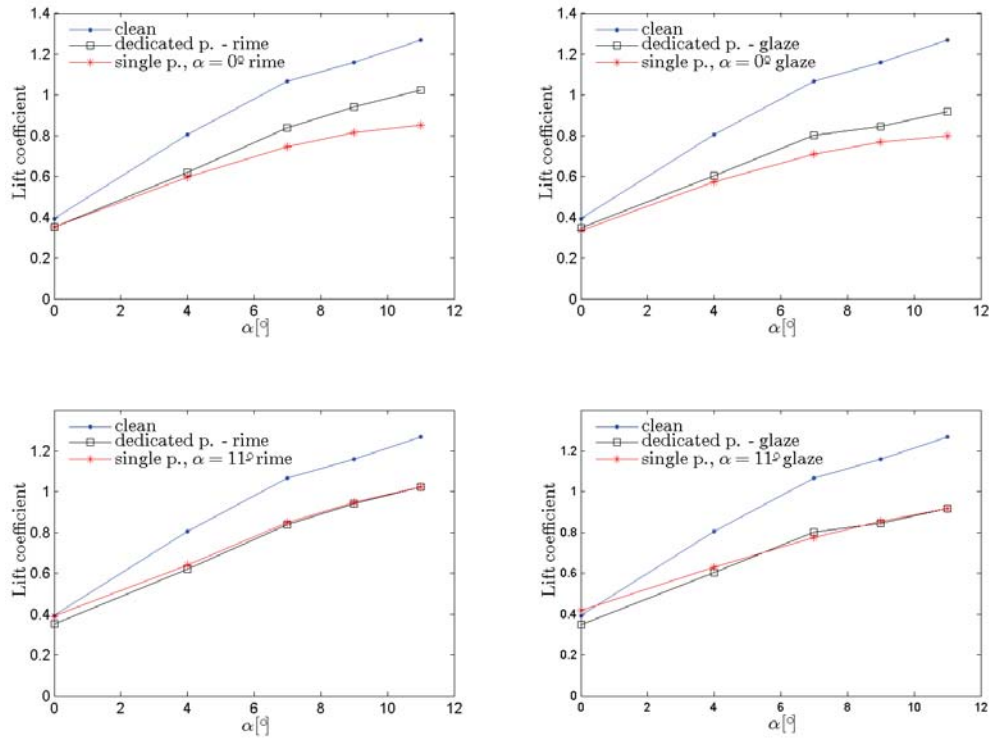
Figure 8. Comparison of lift coefficient (based on the numerical simulations) - angle of attack curves for glaze and rime ice accretion for clean (•), single (∗) and dedicated (□) ice profiles. In the top row, the results of $\alpha = 0^o$ profile are compared to the clean and dedicated profiles whereas in the second row $\alpha = 11^o$.

Table VI. Results of dedicated profiles and single profile simulations and the relative difference between them.

		Rime ice profile				
	AOA (^{o})	0	4	7	9	11
C_L	Dedicated profiles	0.35	0.62	0.84	0.94	1.02
	Single p., $\alpha = 0^o$	0.35	0.6	0.75	0.82	0.85
	Difference (%)	0	4	11	13	17
C_L	Dedicated profiles	0.35	0.62	0.84	0.94	1.02
	Single p., $\alpha = 11^o$	0.39	0.64	0.85	0.95	1.02
	Difference (%)	10	3	1	1	0
		Glaze ice profile				
	AOA (^{o})	0	4	7	9	11
C_L	Dedicated profiles	0.35	0.6	0.8	0.85	0.92
	Single p., $\alpha = 0^o$	0.34	0.57	0.71	0.77	0.8
	Difference (%)	4	5	12	9	13
C_L	Dedicated profiles	0.35	0.6	0.8	0.85	0.92
	Single p., $\alpha = 11^o$	0.42	0.63	0.78	0.86	0.92
	Difference (%)	19	5	3	1	0

4. DISCUSSION

4.1. Ice accretion simulation

The results shown in Figure 2 indicates that the MVD and LWC are larger than the target parameters claimed by the manufacturer of the spray nozzles. It is known that the size and the dynamics of the droplets are dependent on the aerodynamic drag, gravity, droplet collision, evaporation and the turbulence of the flow [17]. Kollar et al. [2005] concluded that the MVD may increase by 20 % due to coalescence, which could be the reason for the underestimation of the size of

the droplets which impinged on the surface of the airfoil. At low air speeds such as 5-10 m/s, the gravity has significant influence on the vertical deflection of the droplet trajectories, causing gravitational sedimentation. The vertical deflection of the droplet trajectories has influence on the vertical LWC distribution, i.e. the maximum LWC occurs at lower height. It could cause the thick ice deposit in case of the experimental glaze ice accretion at higher angles of attack since as the AOA is increased the larger the surface area, which faces the flow.

Additional simulations suggest that in case of rime ice profiles, the numerical profiles agree well with the experimental ones, if LWC is increased to $1g/m^3$ and the MVD to $40\mu m$.

4.2. Computational fluid dynamics

The results of the dedicated and single profile tests are discussed separately in this section.

4.2.1. Simulations with dedicated profiles

The lift coefficient - angle of attack curves from the numerical analyses are qualitatively in good agreement with the ones from the wind tunnel tests, as shown in Figure 3. However, the values from the wind tunnel are much lower than the ones from the numerical simulations due to the fact that these data were only corrected for lift interference and blockage interference but not for the presence of end effect from the vertical walls. In case of the iced airfoils, another reason for these differences could be that with the contour tracing method, the small changes of surface roughness could not be documented therefore they were not implemented in the numerical analysis, and it was shown in many studies (e.g. [16]) that it has significant effect on the aerodynamics of the airfoil. Based on the differences in the aerodynamic effect between 2-D and 3-D ice shapes, Addy (2000) [18] concluded that the surface roughness and the irregularities present in natural aircraft ice are important characteristics. These could also cause the differences between the results of the wind tunnel tests and the numerical simulations.

A comparison was made between the clean airfoil lift coefficients of the wind tunnel tests and the numerical simulations along with the C_L values presented by Abbott and Doenhoff (1959) [15], which implies that it is likely that the end effect caused by the vertical walls led to an approximately 20 % reduction in the effective width of the airfoil section.

The measured relative reduction of lift coefficient (listed in Table IV) shows also quite large difference from the ones listed in Table V, which implies that the combination of the presence of the wind tunnel's vertical walls and the changed surface roughness had significant influence on the measurements. For lower angles of attack, especially $\alpha = 0^o$, the difference between the measured and simulated relative reduction is significantly large, which indicates that the altered surface roughness had the highest influence on the lift reduction.

Similarly to e.g. Homola et al. (2010) [10], lift was found to decrease in all cases. E.g. Virk et al. (2010) [19] found a higher value of lift coefficient for rime iced profiles than for the clean profiles due to the increased effective chord length and camber of the blade profile. This was not experienced in the presented cases of dedicated profile simulations. However, as it can be seen in Figure 7, the curvature of the ice shapes follows well with the curve of the airfoil at the suction side, i.e. acts as an extended leading edge, and thus could cause less significant lift degradation than e.g. the glaze ice accretion.

A tendency of increased lift reduction was seen for glaze ice accretion as the AOA increased. This is due to the characteristics of glaze ice. During glaze ice accretion, because of the relatively higher air temperature ($0 - -4^oC$), not all water droplets freeze to the surface on impact and hence some run along the airfoil and freeze later [20]. As AOA increases, the area exposed to the water droplets increases as well, therefore it causes more flow disturbance and thus more lift reduction.

In most of the cases, mixed ice accretion caused more significant lift degradation than glaze ice accretion due to the large ice deposit, which accumulated on the leading edge and hence higher flow disturbance (see Figure 7).

A significant change in the flow pattern was observed, when a comparison was made between clean and iced blade profiles due to the changes of the aerodynamically shaped leading edge curve. As ice built up on the leading edge, the surface area, which faced the incoming flow and thus the water droplets, increased, causing major flow disturbance.

4.2.2. Simulations with single profiles

The impact of single ice profiles collected at $\alpha = 0^o$ and $\alpha = 11^o$ were studied at different angles of attack. The lift coefficients of $\alpha = 0^o$ for both glaze and rime ice accretion are lower than the ones found in case of dedicated profile tests. The reason for this difference could be that ice was accumulated only on the leading edge in case of $\alpha = 0^o$ and when

the incident angle of incoming flow is increased, the stagnation point moves downstream of the ice deposit disturbing the flow on the suction side, which has higher influence on the lift coefficient than the pressure side. The profiles collected at $\alpha = 11^o$ did not cause significantly different lift curves from the multiple profiles because for $\alpha < 11^o$ values, the ice deposit is downstream of the stagnation point. However at $\alpha = 0^o$, the lift coefficient got larger for the single profile.

5. CONCLUSION

A two phases numerical analysis has been performed to study the effect of glaze, rime and mixed ice accretion on the aerodynamics of an iced NACA 64-618 airfoil. The profiles were collected from icing wind tunnel tests. In the first phase, validation of the collected profiles and the environmental conditions were done by numerical ice accretion model, TURBICE from VTT, Research Centre of Finland. CFD simulations with Ansys Fluent were carried out to numerically analyse the impacts of ice accretion on the flow behaviour and on the aerodynamic characteristics of the airfoil with different wind velocities.

The TURBICE simulations showed that the values of the median volumetric diameter and liquid water content in the wind tunnel were underestimated. The resulted MVD was significantly larger than the target value due to the applied low wind speed and thus coalescence of the water droplets. Vertical deflection of the droplet trajectories had influence on the vertical LWC distribution, which lead to more ice accumulation on the pressure side than it was found during the numerical simulation.

Comparison between the measured and the numerical lift coefficient of the clean airfoil suggests that presence of the vertical walls reduced the effective width of airfoil by approximately 20 %. The results of the CFD analyses of the iced airfoils imply that the combination of the presence of the vertical wall of the wind tunnel and the changed surface roughness had significant influence on the measurements. However, the trend of the lift coefficient - angle of attack curves from the numerical analyses are in good agreement with the ones from the wind tunnel tests. A significant change in the flow pattern was observed, when a comparison was made between clean and iced blade profiles due to the changes of the aerodynamically shaped leading edge curve.

The importance of the angle of attack, on which the profiles were collected, on the lift coefficient was shown. The results of the single profile tests in case of $\alpha = 0^o$ for both glaze and rime ice accretion gave lower lift coefficients than the ones for dedicated profile tests.

In future work, a proper implementation of the surface roughness and also the runback ice rivulets is suggested in order to eliminate the errors caused by the lack of surface roughness.

ACKNOWLEDGMENT

REFERENCES

1. Makkonen L., Laakso T., Marjaniemi M., and Finstad K. J. *Modeling and prevention of ice accretion on wind turbines.* Wind Energy, 25(1):3-21, 2001.
2. Wright W. B., Potapczuk M. G., and Levinson L. H. *Comparison of LEWICE and Glenn ICE in the SLD Regime.* In 46th Aerospace Sciences Meeting and Exhibit, Reno, Nevada, January 7-10, 2008.
3. Homola M. C., Wallenius T., Makkonen L., Nicklasson P. J., and Sundsb P. A. *Turbine Size and Temperature Dependence of Icing on Wind Turbine Blades.* Wind Engineering, 34(6):615-628, 2010.
4. Homola M. C., Wallenius T., Makkonen L., and Nicklasson P. J. *The relationship between chord length and rime icing on wind turbines.* Wind Energy, 13(7):627-632, 2009.
5. Virk M. S., Homola M. C., and Nicklasson P. J. *Atmospheric icing on large wind turbine blades.* International Journal of Energy and Environment, 3(1):1-8, 2012.
6. Reid T., Baruzz G., Switchenko D. and Habashi W. G. *FENSAP-ICE Simulation of Icing on Wind Turbine Blades, Part 1: Performance Degradation.* 51st AIAA Aerospace Sciences Meeting including the New Horizons Forum and Aerospace Exposition 07 - 10 January 2013, Grapevine (Dallas/Ft. Worth Region), Texas

7. Habashi W. G., Morency F., and Beaugendre H. *FENSAP-ICE: a comprehensive 3D Simulation Tool for Inflight Icing.* In 7th International Congress of Fluid Dynamics and Propulsion, Sharm-El-Sheikh, Egypt, December, 2001.

8. Virk M. S., Homola M. C., and Nicklasson P. J. *Effect of Rime Ice Accretion on Aerodynamic Characteristics of Wind Turbine Blade Profiles.* Wind Engineering, 34(2):207-218, Mar. 2010.

9. Etemaddar M., Hansen M. O. L., and Moan T. *Wind turbine aerodynamic response under atmospheric icing conditions.* Wind Energy, 2012.

10. Homola M. C., Virk M. S., Wallenius T., Nicklasson P. J., and Sundsb P. A. *Effect of atmospheric temperature and droplet size variation on ice accretion of wind turbine blades.* Journal of Wind Engineering and Industrial Aerodynamics, 98(12):724-729, 2010b.

11. *Mortensen K. CFD Simulation of an airfoil with leading edge ice accretion.* Master thesis. Department of Mechanical Engineering, Technical University of Denmark, 2008.

12. Chung J. J.and Addy, H. E. *A Numerical Evaluation of Icing effects on a Natural Laminar Flow Airfoil.* NASA TM-2000-209775, January 2000.

13. Hudecz A., Koss, H. and Hansen, M. O. L. *Ice Accretion on Wind Turbine Blades.* IWAIS XV, St-Johns, Newfoundland, September 8-11, 2013

14. Hudecz A., Koss, H. and Hansen, M. O. L.*Icing Wind Tunnel Tests of a Wind Turbine Blade.* Submitted paper

15. Abbott I. and von Doenhoff A. *Theory of Wing Sections. Including a Summary of AirfoilData.* Courier Dover Publications, 1959.

16. Bragg M, Broeren A. P, and Blumenthal L. *Iced-airfoil aerodynamics.* Progress in Aerospace Sciences 2005, 41(5):323-362.

17. Kollar L. E., Farzaneh M., and Karev A. R. *Modeling droplet collision and coalescence in an icing wind tunnel and the influence of these processes on droplet size distribution.* International Journal of Multiphase Flow, 31(1):69-92, 2005.

18. Addy, H. E. Jr, *Ice Accretions and Icing Effects for Modern Airfoils.* Technical report. NASA TM-2000-209775, April 2000.

19. Virk M. S., Homola M. C., and Nicklasson P. J. *Relation Between Angle of Attack and Atmospheric Ice Accretion on Large Wind Turbine's Blade.* Wind Engineering, 34(6):607-614, 2010.

20. Bose N. *Icing on a small horizontal-axis wind turbine - Part 1: Glaze ice profiles.* Journal of Wind Engineering and Industrial Aerodynamics 1992, 45:7585.

RESEARCH ARTICLE

Icing wind tunnel tests of a wind turbine blade

A. Hudecz[1], H. Koss[2] and M. O. L. Hansen[13]

[1]Department of Wind Energy, Technical University of Denmark, Kgs. Lyngby, Denmark
[2]Department of Civil Engineering, Technical University of Denmark, Kgs. Lyngby, Denmark
[3]Centre for Ships and Ocean Structures, Department of Marine

ABSTRACT

Wind tunnel tests were performed to investigate how ice accumulates for moderate low temperatures on an airfoil and how the aerodynamic forces are changing during the process of ice build-up. The tests were performed on a NACA 64-618 airfoil profile at the Collaborative Climatic Wind Tunnel located at FORCE Technology, in Kgs. Lyngby, Denmark. The aerodynamic forces acting on the blade during ice accretion for different angles of attack at various air temperatures were measured along with the mass of ice and the final ice shape. For all three types of ice accretion, glaze, mixed and rime ice, it was found that the lift coefficient decreased dramatically right after ice started to build up on the airfoil due to the immediate change of the surface roughness. This degradation is more significant for higher angles of attack than for lower. An almost linear degradation of the lift coefficient and linear ice build-up were seen. Even though the least amount of ice was building up on the airfoil at low angles of attack, the reduction was percentage-wise the most sever among the investigated cases. The most ice accretion and thus the largest lift degradation were seen for mixed ice tests.

ABBREVIATIONS

AOA   angle of attack
CWT   climatic wind tunnel
LWC   liquid water content
MVD   median volumetric diameter

NOMENCLATURE

C_L lift coefficient
C_{L0} lift coefficient of the clean airfoil
C_{L5} lift coefficient of airfoil after 5 minutes of ice accretion
C_{Lf} lift coefficient
D drag force
G_{ice} gravity force of ice deposit
L lift force
Re Reynolds number
T (C^o) mean air temperature
U (m/s) mean wind speed
α $(^o)$ angle of attack

1. INTRODUCTION

In cold climate areas, wind turbines are exposed to severe conditions. As conditions can differ significantly from site to site it is quite difficult to describe a typical cold climate site. These could be regions where icing events and / or periods occur with temperatures below the operational limits of standard wind turbines. At sites with temperatures below 0° and a humid environment for larger periods of the year, icing represents an important threat to the durability and performance. These conditions can be found in sub-arctic or arctic regions, like in the Nordic countries in Europe or in Canada and in high altitude mountains, e.g. in the Alps (Tammelin et al. (1998) [1], Tallhaug et al. (2009) [2] and Baring-Gould et al. (2011)) [3]. Even a small amount of ice on the blades can reduce power production due to the changes of surface roughness and therefore changes of the aerodynamic forces (Lynch and Khodadoust (2001) [4]).

Several simulations, both experimental and numerical, have been carried out in order to explore the effect of ice accretion on the aerodynamic forces. During the experiments of Seifert and Richert (1997) [5], artificial ice deposits were placed on the leading edge. These molds were made of ice fragment removed from the blades of a small wind turbine. Effects of different amount of ice accretions on lift and drag coefficients were investigated for an angle of attack range between -10° and 30°. In their study, they showed that the annual energy production loss can be 6-18 % depending on the severity of icing. Jasinski et al. (1997) [6] made the same experiment, but the artificial ice shapes were simulated in NASA's LEWICE ice accretion simulation software. Both Jasinski et al. (1997) [6] and Bragg et al. (2005) [7] found that the lift coefficient based on the original chord increased by 10 and 16 %, respectively, due to the rime ice accretion, which was acting as leading edge flap. Hochart et al. (2008) [8] carried out a two-phase test on a NACA 63-415 profile. In the first phase, ice deposit was built up on a blade profile under in-cloud icing conditions in a wind tunnel, while in the second phase, aerodynamic efficiency tests were carried out on the iced profiles. They described how ice affects the power production and pointed out that the outer third part of the blades is the most critical in case of performance degradation.

It was shown that the artificial materials used for simulating ice on the airfoil could produce different performance degradation than the actual ice deposit. The process of selection of these materials and the casting are *"more an art than a science"* (Addy et al. (2003)) [9].

The experiments described in this paper were carried out in the Collaborative Climatic Wind Tunnel (CWT). Glaze, rime and mixed ice deposits were built up on a NACA profile. The aerodynamic forces acting on the blade during ice accretion for different angles of attack (0°, 4°, 7°, 9°, 11°) at various air temperature (approximate, mean value of the established temperature: -3 ^{o}C, -5 ^{o}C, and -8 ^{o}C) were measured along with the mass of ice and the final ice shape. The tested temperature range can be described as rather moderate, but due to the limitation of the wind tunnel's cooling unit, these temperatures could be reached. The experiments were run for 60 minutes in order to study the early phase of icing. Measurements were taken every five minutes. The main differences between the tests presented in this paper from the ones done by Hochart et al. (2008) [8] are that the change of lift coefficient and the mass of accumulated ice are monitored throughout the accretion process and that not only rime and glaze but also mixed ice deposits were studied at different angles of attack.

2. EXPERIMENTAL METHOD AND WIND TUNNEL CORRECTION

The aim of the experiment was to explore the effect of ice on the wind turbine blades. For this purpose, an airfoil was placed into a climatic wind tunnel. The set-up was equipped with a pair of force and torque transducers in order to monitor the forces that act on the airfoil section.

Test facility. The tests were performed in a closed-circuit climatic wind tunnel (see Figure 1) with a test section of 2.0x2.0x5.0 m located at FORCE Technology, in Kgs. Lyngby, Denmark. The wind tunnel was developed and built as a collaboration project between the Technical University of Denmark (DTU) and FORCE Technology.

The airfoil was placed in the middle of the test section. The design criteria for the CWT are listed in Table I (Georgakis et al. (2009) [10]). The CWT is equipped with relative humidity and temperature sensors along with a Pitot tube, therefore these parameters can be monitored along with the force measurements.

Spray-system. Presently, the CWT is capable to allow tests under rain and icing conditions. To create ice, a spraying system has been mounted in the settling chamber, as it can be seen in Figure 1. The system includes 15 evenly spaced (20 cm from one other) nozzles. The nozzles mix high-pressure air and water and produce spray of water droplets, which provides uniform cloud in the tunnel (see Figure 2).
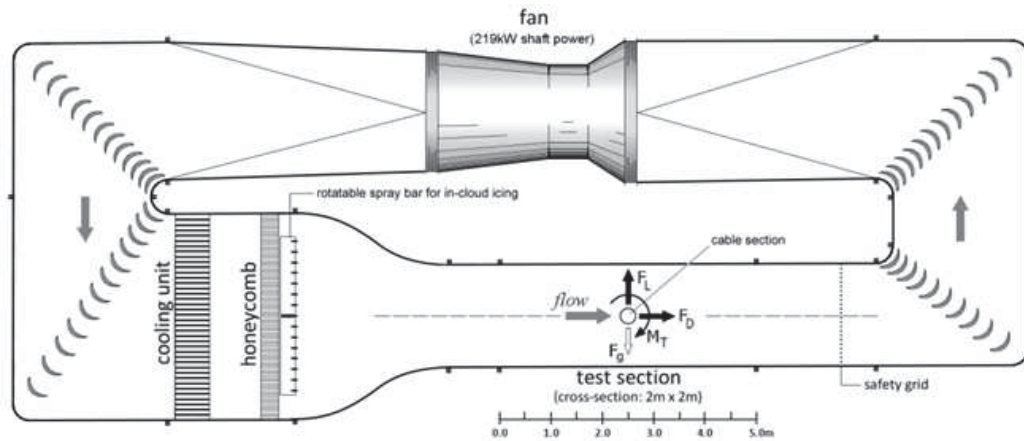
Figure 1. Main features of the CWT. The test section is 2.0x2.0x5.0 m (Koss and Lund (2013) [11])

Table I. Basic specifications of the wind tunnel (based on Georgakis et al. (2009) [10])

Temperature	-10 to 40	$[^{o}C]$
Min. liquid water content	0.2	$[g/m^3]$
Test section cross-sectional area	2.0x2.0	$[\, m\,]$
Test section length	5	$[\, m\,]$
Maximum wind velocity	31	$[m/s]$
Turbulence intensity	0.6 to 20	$[\%]$

According to the manufacturer (Schick (2009) [12]), the median volumetric diameter of the water droplets was

Figure 2. Spray system produces cloud in the wind tunnel.

approximately 25 μm for glaze and mixed ice tests and approximately 20 μm for the rime ice tests. Rime ice is typically forming of smaller droplet size (ISO 62494 standard [13]), therefore 20 μm MVD was chosen for these tests. The target liquid water content was approximately $0.7g/m^3$.

Airfoil and testing rig. NACA 64-618 airfoil section with 900 mm chord length and 1350 mm width from LM Wind Power was used during the experiments. The airfoil was covered with PVC folio to recreate the surface condition of a painted wind turbine wing. In order to place the section into the tunnel and to set different angles of attack, it was necessary to design a suitable rig (see Figure 3). Two wooden end plates were installed on either side of the wing section to avoid distorting influences on the ice accretion and airflow over the wing. The upstream edge of these plates was shaped in a way to minimize their interaction with the flow. The airfoil section was connected in one point, on each side with the supporting structure with moment-free joints. The force transducers were placed on the outer side of the end-plates to separate the

Figure 3. Photo of the test set-up from the tunnel.

measuring system from the airfoil.

Force and torque transducers. The set-up was equipped with a pair of AMTI MC5 force and torque transducers, which measures the loading simultaneously 6 degrees of freedom, i.e. forces Fx, Fy, Fz together with moments Mx, My , Mz in a wing-fixed coordinate system as shown in left hand side of Figure 4. On the iced airfoil, not only the lift force but also
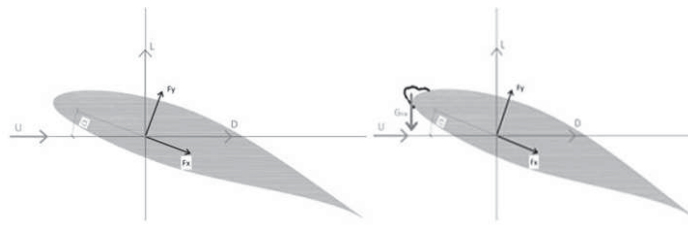

Figure 4. Forces on the airfoil. On the left hand side, the forces on the clean airfoil are shown while on the right hand side the forces on the iced airfoil.

the gravity force of the ice deposit was acting (G_{ice}, see right hand side of Figure 4) and the combined effect of these two forces was measured by the force transducers. In order to study the pure effect of the altered airfoil profile and surface roughness, this force due to added ice mass was subtracted from the lift measurements.

Simulations. Ice was building up on the surface of the airfoil section at different temperatures, ensuring the three investigated icing characteristics for each angle of attack. A list of the wind tunnel tests and the conditions can be found in Table 2. The values are approximated. The two different air speeds are target velocities: one applied for the ice accretion and the other for force measurements. The temperature values are mean value of the established temperature during the tests. The tests were performed by first setting the required wind speed and temperature in the test section. Water spray, providing in-cloud environment was then initiated. The air speed was set to 15 m/s for glaze and mixed ice and to 10 m/s for rime ice accretion and the force measurements were taken with 15 m/s for all ice types. Although the effective wind speed is much higher at the tip region of wind turbine blades, it was necessary due to limitations of the wind tunnel to set low velocity in order to ensure sufficiently low temperatures. The ice accreted on the surface for 60 minutes in 5 minutes intervals. Every 5 minutes the tunnel and the spray system were set to idle to measure the forces and the weight of the already accreted ice mass.

After an hour, the accretion process was stopped and the characteristics of ice were registered and the shape of the ice profile was documented by contour tracing. For this purpose the ice layer was cut perpendicular to the airfoil axis with a heated blade down to the airfoil surface. Hereafter, a cardboard was placed into the cut and the ice layer contour was drawn onto the cardboard, see an example in Figure 5. The main feature of the surface could be captured by this method, but the micro structure of the surface roughness could only be registered by a camera. The image was digitalized and the coordinates were saved for further analysis. The accretion process was captured by an action camera, which was installed inside the tunnel upstream from the airfoil profile and was taking photos every 30 seconds.

Wind tunnel corrections. The confined flow in the wind tunnel alters the flow field around the airfoil compared to full-

Table II. A summary of the wind tunnel tests and the conditions. The two different velocities are target velocities, one during the ice accretion (Accretion) and the other during the force measurements (Tests). The temperature values are mean value of the established temperature. The LWC parameters are target values. The here listed values are approximated.

Test	AOA (^{o})	T (^oC)	Ice	MVD (μm)	LWC (g/m^3)	U (m/s) Accretion	U (m/s) Tests	t (min)
1	0	-3	glaze	25	0.7	15	15	60
2	0	-5	mixed	25	0.7	15	15	60
3	4	-3	glaze	25	0.7	15	15	60
4	4	-5	mixed	25	0.7	15	15	60
5	4	-8	rime	20	0.7	10	15	60
6	9	-3	glaze	25	0.7	15	15	60
7	9	-5	mixed	25	0.7	15	15	60
8	9	-8	rime	20	0.7	10	15	61
9	11	-3	glaze	25	0.7	15	15	62
10	11	-5	mixed	25	0.7	15	15	63
11	11	-8	rime	20	0.7	10	15	64

Figure 5. Example for ice layer contour tracing.

scale and affects hence the measured aerodynamic forces on the wing section. The measured forces were corrected for both, lift interference and blockage interference. Lift interference is caused by the changes of the stream direction and stream curvature, and the blockage interference is the result of the changes in stream velocity and longitudinal pressure gradient. These two interferences are independent of each other (ESDU 76028 [14]). The tunnel correction was performed by following ESDU 76028, Lift-interference and blockage corrections for two-dimensional subsonic flow in ventilated and closed wind-tunnels methodology.

3. RESULTS

The corrected results of all the simulations including the degradation process of lift coefficient, the accretion of ice throughout the tests and the shapes and characteristics of the ice profiles are described in this section. The results are summarized in Table III, where the final ice mass and final lift coefficients along with the relative degradation are listed for each tests. The growth rate shows how much ice accumulated in average in a minute on the surface of the airfoil. These numbers are only valid for the previously presented experimental set-up. Hence, as any of the parameters (e.g. AOA, MVD, LWC or wind speed) is changed, the outcome of the experiment changes as well.

It was found in all three icing conditions that the lift coefficient was decreasing significantly even for a small amount of ice and the ice build-up process is almost linear during this early phase of accretion. The instantaneous lift degradations, $\triangle C_L = C_{L0} - C_{L5}$ are listed in Table 4. It can be concluded that the immediate degradation is more significant for higher

Table III. Summary of the results. C_{L0} represents the lift coefficient of the clean airfoil and C_{Lf} is the final lift coefficient at the end of the ice build-up process

	Glaze ice				Mixed ice				Rime ice		
AOA [^{o}]	0	4	9	11	0	4	9	11	4	9	11
Mass of ice[g/m]	2227.1	2603.6	2835.8	2903.4	2450.7	2648.1	2658.3	3216.6	1792	2071.9	2353.9
Growth rate [$g/min/m$]	37.1	43.4	47.3	48.4	40.8	44.1	44.3	53.6	29.9	34.5	39.2
C_{L0} (clean airfoil)	0.317	0.563	0.904	1.04	0.32	0.579	0.911	1.038	0.571	0.96	1.066
C_{Lf} (final, iced airfoil)	0.157	0.366	0.643	0.807	0.116	0.309	0.596	0.855	0.431	0.744	0.805
Degradation [%]	50	35	29	22	64	47	36	21	25	23	24

angles of attack than for lower.

The liner behaviour of the ice build-up is visualized in Figure 6 where a fragment from one of the ice profile, which was

Table IV. Summary of instantaneous lift coefficient degradation. C_{L5} represents the lift coefficient measured after 5 minutes of ice accretion and $\triangle C_L$ is the difference of the clean airfoil lift coefficient and the lift coefficient after 5 min of ice accumulation.

	Glaze ice				Mixed ice				Rime ice		
AOA [^{o}]	0	4	9	11	0	4	9	11	4	9	11
C_{L5}	0.279	0.529	0.814	0.952	0.286	0.517	0.814	0.983	0.527	0.888	0.993
C_{L0} (clean airfoil)	0.317	0.563	0.904	1.04	0.32	0.579	0.911	1.038	0.571	0.96	1.066
$\triangle C_L$	0.038	0.034 0.09	0.088	0.034	0.062	0.097	0.093	0.044	0.073	0.073	

falling off the airfoil during melt-off, is shown. The cross-section of the ice fragment shows the layer structure of the ice body. In this case, the visibility of the layers is enhanced by spay and airspeed-off phases to measure the ice mass growth.

3.1. Glaze ice tests

Glaze icing conditions were established for all angles of attack. The changes in the lift coefficient leading to the degradation trend of the lift force are shown in Figure 7. The degradation is already visible after 5 minutes into the accretion. As it is listed in Table 3, the lift coefficient decreases the most for 0o angle of attack, from 0.317 to 0.157, with approximately 50 % and the least at 11o from 1.04 to 0.807 i.e. by 22 % decrease. The slopes of the fitted polynomials presented in Figure 7 are similar, hence the degradation of lift coefficient is alike for all tested AOA or in other words the lift force degradation is independent of the angle of attack. Parallel to the lift force the mass of the accreted ice was measured every five minutes. The development of the ice mass over accretion time is shown in Figure 8. Here, in contrast to the lift coefficients, the lowest value for ice accretion is observed at 0° and the highest value at 11°. The weight of the accreted ice along with the ice growth rate (g/min/m) for different AOA is summarized in Table III. It can be seen that the ice growth rate is the lowest for lower angle of attack and the highest for the highest angle of attack.

As pointed out above, the ice build-up is a linear process in this first stage of the ice accretion exhibiting a linear ice growth behaviour (Figure 8). Figure 9 shows the different ice shapes for all tested AOA. As a typical characteristic of the glaze ice accretion, some of the impinging water droplets froze in impact and some ran off following the streamlines towards the trailing edge where they froze almost completely. With increasing AOA, the length of the ice deposit at the pressure side increased as well and the visible separation line moved along the same side. However the time was not long enough to grow dramatic ice deposit on the surface, the horn shape at the leading edge was visible. An example of an early-stage horn shape is shown in Figure 10.
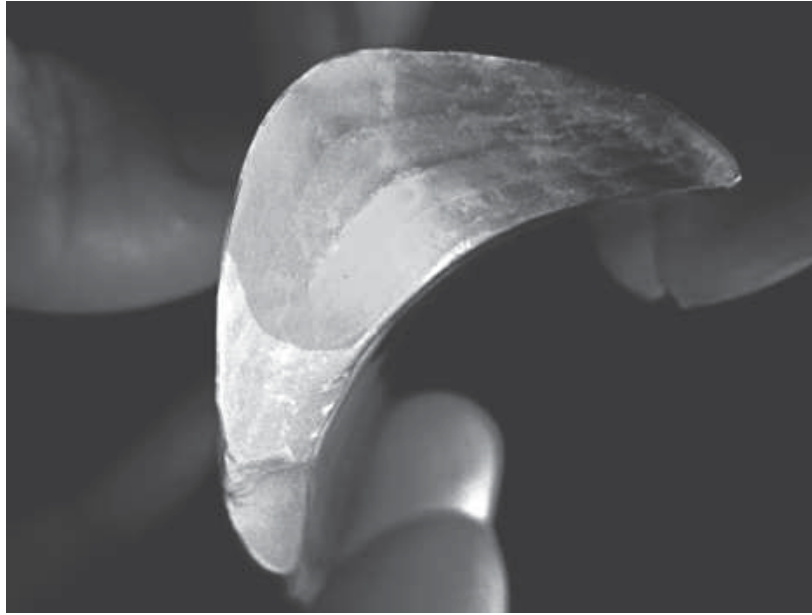
Figure 6. Post-processed photo of a piece of ice felt off the airfoil during melt-off. The equidistant lines in the layer structure of the ice body indicate a linear ice growth over time.
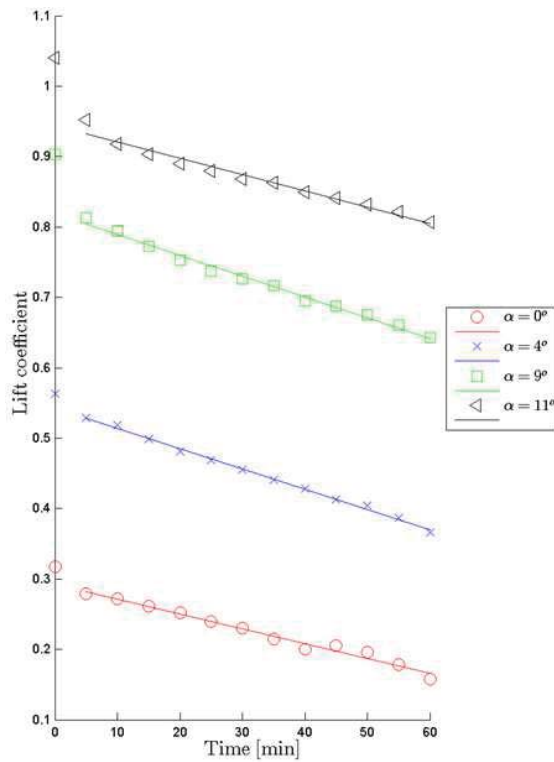

Figure 7. Lift coefficient as a function of ice accretion time for different angles of attack in case of glaze ice, $Re \simeq 1E6$, $MVD \simeq 25m$ and $LWC \simeq 0.65g/m^3$ for a NACA 64-618 profile. A first order polynomial was fitted to the measurement.
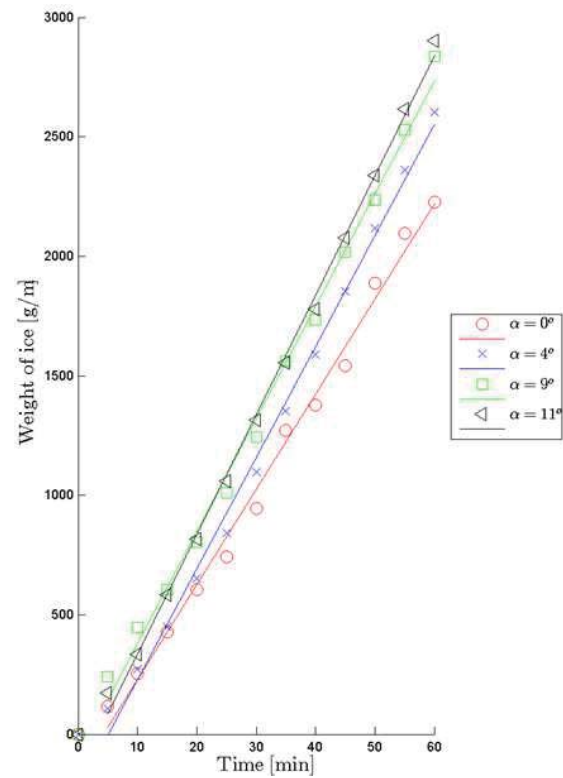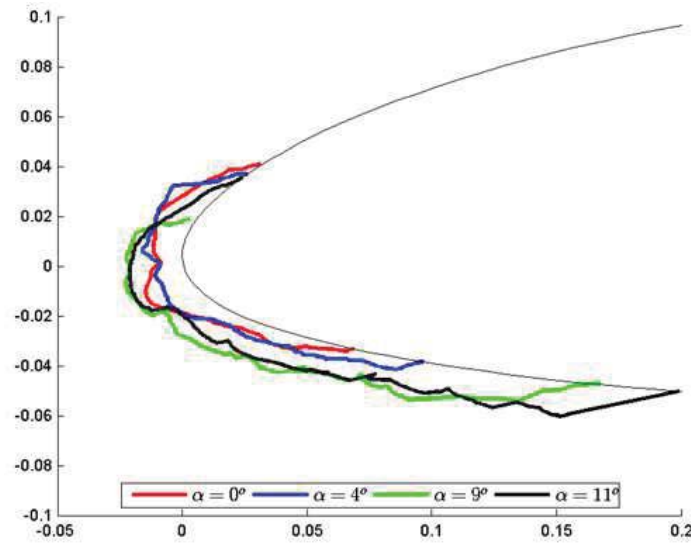

Figure 8. Accreted ice mass as a function of ice accretion time for different angles of attack in case of glaze ice, $Re \simeq 1E6$, $MVD \simeq 25m$ and $LWC \simeq 0.65g/m^3$ for a NACA 64-618 profile. A first order polynomial was fitted to the measurement.

Figure 9. Shapes of ice accretion for the different angles of attack collected after 60 minutes of ice accretion in case of glaze ice tests, $Re \simeq 1E6$, $MVD \simeq 25m$ and $LWC \simeq 0.65g/m^3$ for a NACA 64-618 profile.
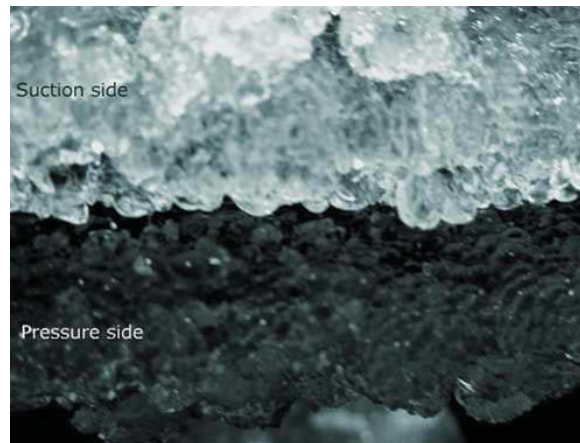
Figure 10. A close-up of an early-stage horn ice shape shows a clear separation line between the suction and pressure side. The photo was taken after 60 minutes of glaze ice accretion in case of 0° angle of attack and $Re \simeq 1E6$, $MVD \simeq 25m$ and $LWC \simeq 0.65g/m^3$ for a NACA 64-618 profile.

3.2. Mixed ice tests

The accreted ice showed both glaze and rime ice characteristics. The lift coefficient as a function of the ice accretion time is shown in Figure 11 and the final coefficients are summarized in Table III. As for the glaze ice test results, the process is linear, and a linear curve fitting was applied. The degradation of the lift coefficient under mixed ice accretion is similar to the development under glaze ice accretion. The most significant degradation was found at 0° angle of attack, where the lift coefficient decreased with 64 % from 0.320 to 0.116 after 60 minutes of ice accretion and the least significant at the highest angle, 11° from 1.038 to 0.855, which corresponds to an approximately to a reduction of 21 %. In Figure 12, the accreted ice mass is presented as a function of time. The build-up process is practically linear as in case of the glazes ice tests. As it is given in Table 3, the smallest growth rate, 40.8 g/min/m was found at 0° angle of attack and largest, 53.6 g/min/m at 11°.

With increasing angle of attack, the amount of ice build-up on the surface was increasing as well. The sampled ice profiles are plotted in Figure 13. The stagnation point is quite visual due to the thin peak appearing at the leading edge. As it can be seen, the peak is moving towards the pressure side as the angle of attack is increasing.
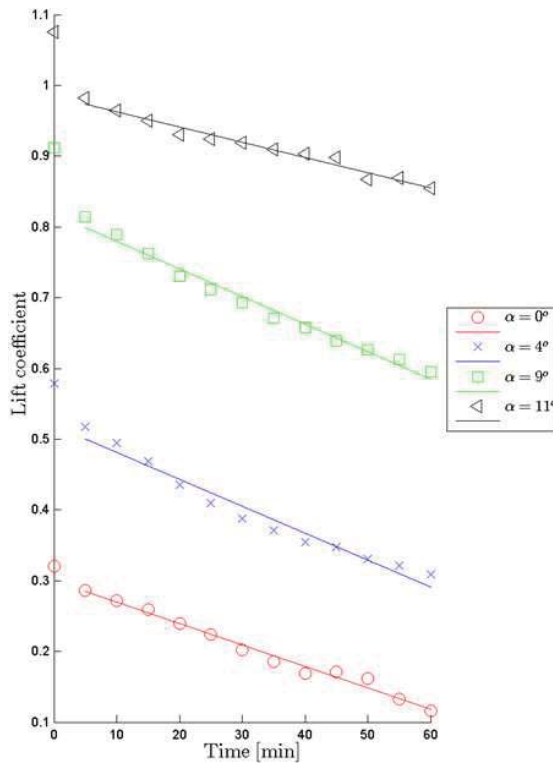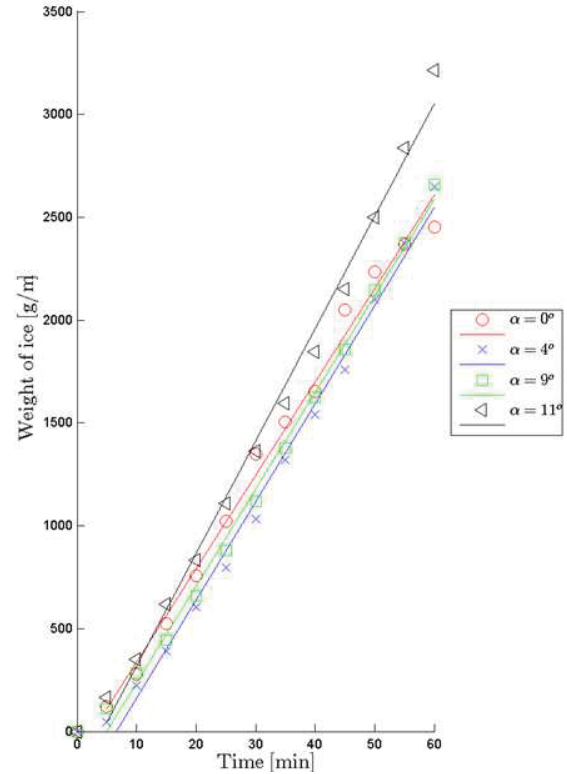
Figure 11. Lift coefficient as a function of ice accretion time for different angles of attack in case of mixed ice, $Re \simeq 1E6$, $MVD \simeq 25m$ and $LWC \simeq 0.65g/m^3$ for a NACA 64-618 profile. A first order polynomial was fitted to the measurement.

Figure 12. Accreted ice mass as a function of ice accretion time for different angles of attack in case of mixed ice, $Re \simeq 1E6$, $MVD \simeq 25m$ and $LWC \simeq 0.65g/m^3$ for a NACA 64-618 profile. A first order polynomial was fitted to the measurement.

In Figure 14, an example of a typical mixed ice profile is shown. The photo was taken following the location of the stagnation point at the leading edge of the iced profile set at 4°. The sample shows characteristics of mixed ice. Close to the center the ice deposit is more glassy and smooth whereas in the outer areas, the typical milky feathers of rime ice are visible.

3.3. Rime ice tests

Due to the limitation of the wind tunnel's cooling capacity, it was necessary to reduce the wind speed from 15 m/s to 10 m/s during the build-up process in order to ensure sufficiently low air temperature. The force measurements were conducted with 15 m/s. It is stated in the ISO 12494 standard that the droplet size in case of rime ice formation is lower than for glaze ice. Hence, the water pressure was reduced to form water droplets with approximately 20 μm mean volumetric diameter (based on the specification of the manufacturer). Similar to the two other ice types, Figure 15 and Figure 16 show the lift coefficient and the accreted ice mass as a function of the ice accretion time. Similar to the two previous case of ice accretion the reduction of lift coefficient and the ice growth are linear. The largest ice accretion was observed at higher angles of attack, 39.2 g/min/m at 11° while only 29.9 g/min/m at 4°. The lift curves are also similar to glaze and mixed ice accretion, although the slope of the 11° AOA curve slightly differs from the other two. In Figure 17, the collected rime ice shapes are plotted for the different angles of attack. All the water droplets freeze on the surface on impact, thus there is no run-back ice formation. In case of 0° AOA most of the ice built up on the leading edge.

A typical rime ice formation is shown in Figure 18. The white feathers are sharp and the surface is rough. It was observed that the suction side of the airfoil was covered with tiny, white and dry droplets, which were easily removable. These icing features have a resemblance to dry snow. Although the location of the stagnation line is not as obvious for the rime ice
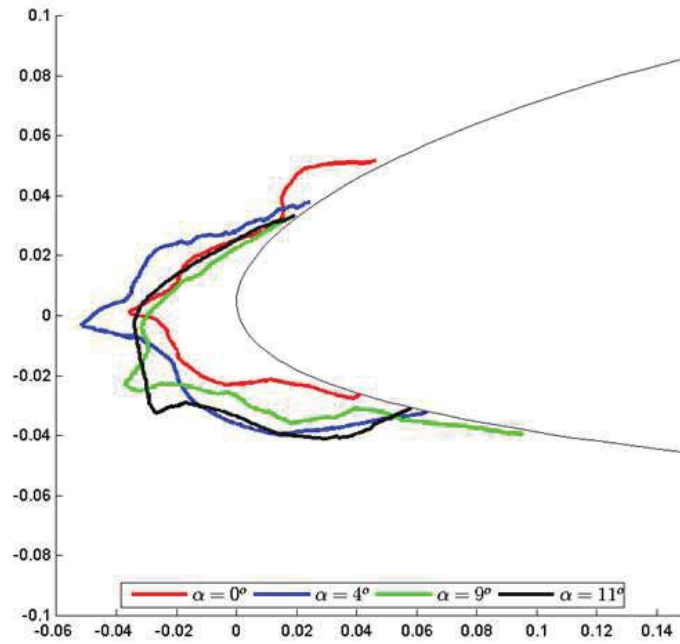
Figure 13. Shapes of ice accretion for the different angles of attack collected after 60 minutes of ice accretion in case of mixed ice tests, $Re \simeq 1E6$, $MVD \simeq 25m$ and $LWC \simeq 0.65g/m^3$ for a NACA 64-618 profile.
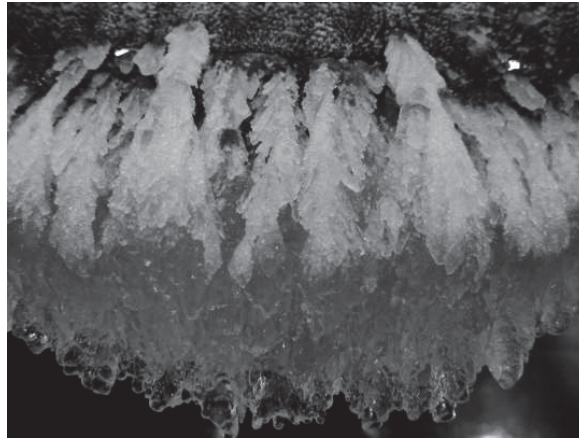

Figure 14. Photo of the 4° angle of attack mix ice test in case of $Re \simeq 1E6$, $MVD \simeq 25m$ and $LWC \simeq 0.65g/m^3$ for a NACA 64-618 profile.

deposit as for e.g. glaze ice (Figure 10), it is visible in the example shown in Figure 18. It can be seen that as the feathers at the leading edge grow to a certain size another row of feathers starts to develop from the outer area growing towards the stagnation point hence covering up the existing feathers. The leading point of the feather only grows to a certain position forming the "wall" in the ice layer around the stagnation point.

4. DISCUSSION

The above presented results are analysed and compared in this section, however a direct comparison of the rime ice measurements is limited to the other two types due to the lower wind speed applied during the ice accretion.

In all three ice accretion tests, it was found that the lift coefficient decreased right after ice started to build up on the airfoil. The immediate change is associated to the aerodynamic properties of an airfoil, which are highly dependent of the surface
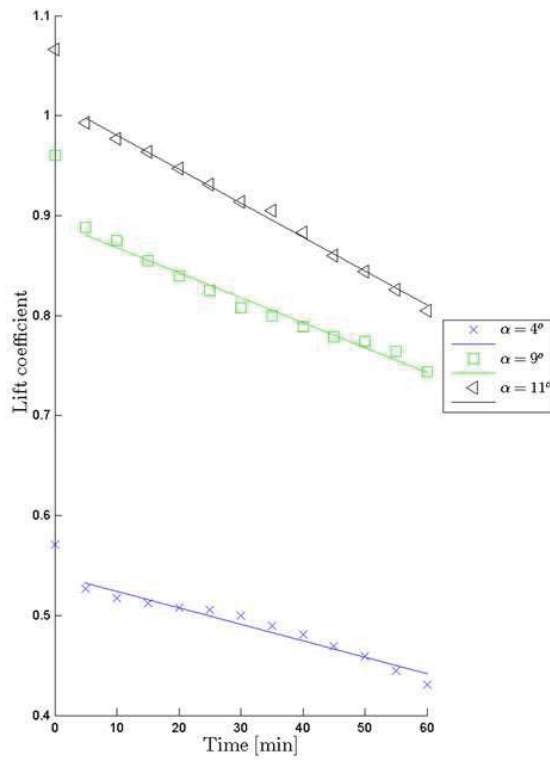
Figure 15. Lift coefficient as a function of ice accretion time for different angles of attack in case of rime ice accreted for $Re \simeq 6E5$ $MVD \simeq 20m$ and $LWC \simeq 0.6g/m^3$ on a NACA 64-618 profile. A first order polynomial was fitted to the measurement.
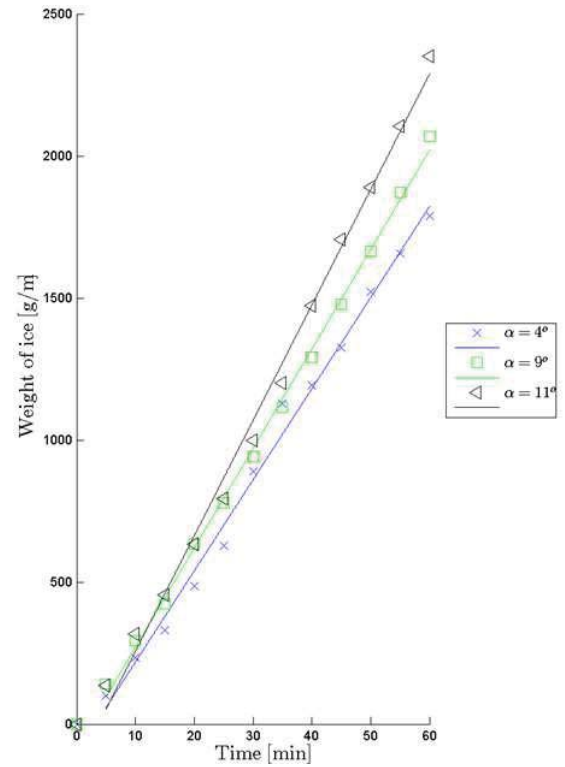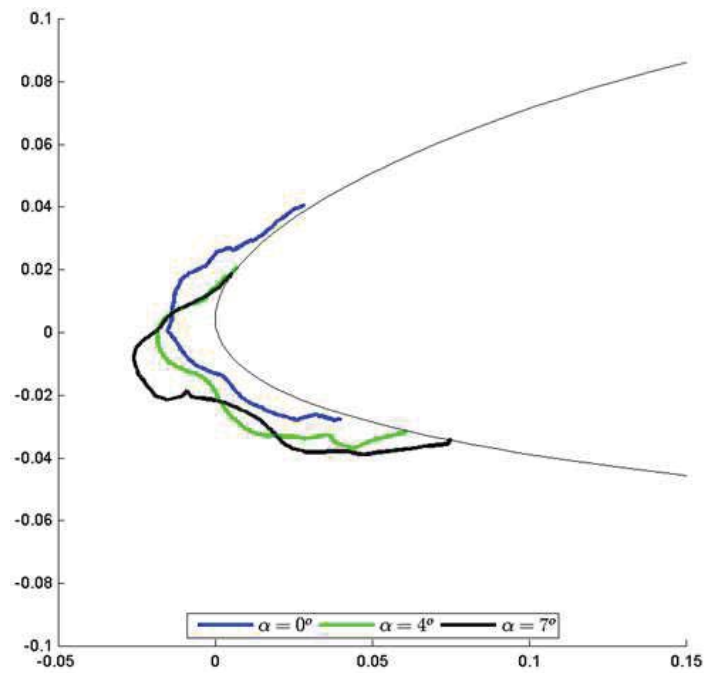
Figure 16. Accreted ice mass as a function of ice accretion time for different angles of attack in case of rime ice for $Re \simeq 6E5$ $MVD \simeq 20m$ and $LWC \simeq 0.6g/m^3$ on a NACA 64-618 profile. A first order polynomial was fitted to the measurement.

Figure 17. Shapes of ice accretion for the different angles of attack collected after 60 minutes of ice accretion in case of rime ice tests for $Re \simeq 6E5$ $MVD \simeq 20m$ and $LWC \simeq 0.6g/m^3$ on a NACA 64-618 profile.
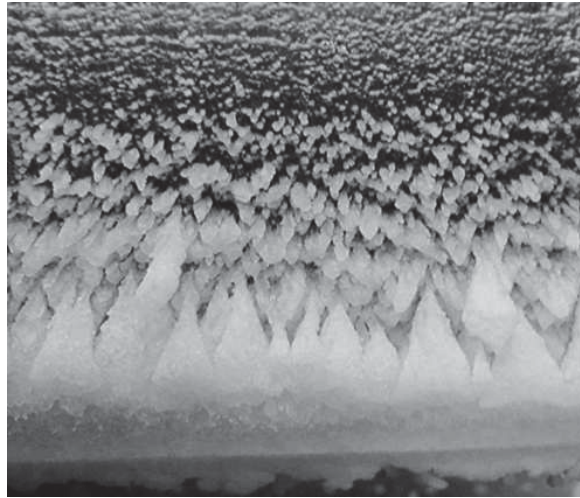
Figure 18. Photo of the 4° angle of attack rime ice test collected during ice accretion with $Re \simeq 6E5$, $MVD \simeq 20m$ and $LWC \simeq 0.6g/m^3$ for a NACA 64-618 profile.

roughness. The instantaneous decrease of the lift coefficient, as shown in Table III, is more significant for higher angles of attack because the surface roughness is changed over a larger area. This is reflected by the lift coefficient curves (Figure 7, Figure 11 and Figure 15) where the slope of the drop in the first 5 minutes is much steeper than of the polynomials fitted to the points. Consequently, the surface roughness itself has higher influence on the immediate lift degradation than the altered airfoil profile.

Even though the least amount of ice was building up on the airfoil at 0° AOA, the relative reduction of lift was the most severe. The reason could be that at low angle of attack, ice was accreted mainly at the leading edge, changing the geometry of the profile and thus causing higher disturbance in the flow than at higher angles. In case of larger incident angles, the ice shape is flatter and follows the streamlines on the pressure side, as shown in Figure 9, Figure 13 and Figure 17, thus inducing less flow disturbance. It appears that the angle of attack has an influence on the mass and also the shape of ice. The same conclusion was drawn from the numerical simulations by Homola et al. [15] 2009 and Virk et al. 2010 [16].

The similar instantaneous reduction of lift coefficient in case of the glaze and mixed ice tests, see Table IV, is possible because the mixed ice is the result of decreasing air temperature during ice accretion, hence, it starts of as glaze ice.

Larger amount of ice was building up in case of mixed ice tests compared to glaze ice tests for the same angle of attack (except in case of 9°, probably due to a slightly different droplet size). It is due to the nature of the mixed ice, when the temperature reaches lower levels and becomes sufficiently cold for rime ice formation, all the water particles freeze on impact, causing larger ice deposit on the already altered airfoil profile.

The reduction of lift coefficient was more significant in case of mixed ice deposit compared to glaze ice. The reason could be the very irregular ice shapes, which were formed on the leading edge of the profile. This happens because the rime-like part of the mixed ice formation started on and the particles stuck on an already non-streamlined, altered profile.

Both Jasinski et al. (1997) [6] and Bragg et al. (2005) [7] pointed out that the lift coefficient based on the original chord was sometimes increasing in case of rime ice tests compared to the clean airfoil. This behaviour was not seen during the experiments presented in this paper probably because of different icing conditions and accretion time and therefore different ice shape and size.

The mass of accreted ice highly depends on the wind speed, the temperature and liquid water content and the droplet size (Makkonen (1984) [17]). The latter three parameters were set to ensure the environmental conditions necessary for the chosen ice formation type. It was, however, experienced, but not presented in this paper, that even a very small change in the droplet size led to significantly different ice mass. As it was explained earlier, due to the limitations of the wind tunnel's cooling capacity, considerably lower wind speed was applied than what it is acting on the tip region of a wind turbine. Therefore the accumulated ice mass is less than it would have been in case of the outer part of a wind blade.

Although the physical characteristics of the ice deposits were similar to the one published in other studies e.g. Bose (1992) [18] and ISO 12494 [13] standard, some differences were observed. In case of glaze ice deposits, as it can be seen in Figure 10, the ice deposit consists of small beads. It was seen during the experiments that the water droplets, which did not freeze on the surface on impact, formed small beads before they eventually ran off. Every 5 minutes, the tunnel and the spray system was set to idle for approximately one and a half minutes in order to measure the weight of the accreted ice mass. Even though this period is short, it could provide just enough time to get these water beads to freeze.

In case of the mixed ice tests, the observed peak at the stagnation point in Figure 13 could probably be formed due to the static feature of the tests. These peaks are not experienced or have been reported yet in case of an actual rotating wind turbine blade. Due to atmospheric turbulence, wind shear and tower passage, the angle of attack is varying in time around a mean value on a wind turbine blade which will give a broader ice accretion at the leading edge since the stagnation point is not constant.

5. CONCLUSION

In this paper, the results of a series of experiments on a NACA 64-618 profile in a climatic wind tunnel were presented. There were a number of tests performed at different angles of attack and temperature in order to monitor the alteration of the lift coefficient and thus the lift force along with the weight of accumulated ice throughout the first 60 minutes of ice accretion under controlled conditions. It was seen that both the ice accretion and the degradation shows a linear trend. The alteration of the surface roughness has a more significant effect on the initial lift coefficient than the shape of the changed airfoil profile. As the angle of attack increased the larger the degradation of the instantaneous lift coefficient got.

It was also found, that not only the temperature, but the angle of attack has an influence on the mass and also the shape of ice deposit. Even though the least amount of ice was building up on the airfoil at low angles of attack, the relative reduction was the most severe in these cases, thus the higher the angle of attack the lower the lift coefficient degradation.

More ice built up on the airfoil during the mixed ice tests than the glaze ice tests and hence causing more significant lift coefficient degradation.

ACKNOWLEDGMENT

REFERENCES

1. Tammelin B, Cavaliere M, Holttinen H, Morgan C, Seifert H. and Santti K. *Wind energy production in cold climate (WECO)*. Technical report, Finnish Meteorological Institute, 1998.
2. Tallhaug L, Ronsten G, Horbaty R, Cattin R, Laakso T, Durstewitz M, Lacroix A, Peltola E, and Wallenius T. *Wind energy projects in cold climate*. Technical report, Executive Committee of the International Energy Agency Programme for Research and Development on Wind Energy Conversion Systems, 2009.
3. Baring-Gould I, Cattin R, Durstewitz M, Hulkkonen M, Krenn A, Laakso T, Lacroix A, Peltola E, Ronsten G, Tallhaug L, and Wallenius T. *13. Wind Energy Projects in Cold Climates*. Technical report, 2011.
4. Lynch F. T. and Khodadoust A. *Effects of ice accretions on aircraft aerodynamics*. Progress in Aerospace Sciences 2001, 37(8):669-767.
5. Seifert H. and Richert F. *Aerodynamics of iced airfoils and their influence on loads and power production*. European Wind Energy Conference, 1997.
6. Jasinski W. J, Noe S. C, Selig M. S, and Bragg M. B. *Wind turbine performance under icing conditions*. Journal of Solar Energy Engineering 1997, ASME, 120(1):60-65.
7. Bragg M, Broeren A. P, and Blumenthal L. *Iced-airfoil aerodynamics*. Progress in Aerospace Sciences 2005, 41(5):323-362.
8. Hochart C, Fortin G, and Perron J. *Wind turbine performance under icing conditions*. Wind Energy 2008, 11:319333.
9. Addy H. E, Broeren A. P, Zoeckler J. G, and Lee S. *A Wind Tunnel Study of Icing Effects on a Business Jet Airfoil*. In: American Institute of Aeronautics and Astronautics, 41. Aerospace Sciences Meeting and Exhibit, 2003.

10. Georgakis C, Koss H, and Ricciardelli F. *Design specifications for a novel climatic wind tunnel for the testing of structural cables.* International Symposium on Cable Dynamics (ISCD) - 8, 2009, Paris, France.

11. Koss H. H. and Lund M. S. M. *Experimental Investigation of Aerodynamic Instability of Iced Bridge Cable Sections.* In: 6th European and African Conference on Wind Engineering, Cambridge, UK, 2013

12. Schick R. J. *Spray technology reference guide: Understanding drop size, bulletin 459c.* Technical report, Spraying Systems Co.

13. ISO 12494. *Atmospheric icing of structures.* Technical report, ISO Copyright Office, Geneva, Switzerland, 2001.

14. ESDU 76028, *Lift-Interference and Blockage Corrections for Two-Dimensional Subsonic Flow in Ventilated and Closed Wind Tunnel, ESDU 1976.*

15. Homola M. C, Wallenius T, Makkonen L, and Nicklasson P. J. *The relationship between chord length and rime icing on wind turbines.* Wind Energy 2009, 13(7):627-632.

16. Virk M. S, Homola M. C, Nicklasson P. J. *Effect of Rime Ice Accretion on Aerodynamic Characteristics of Wind Turbine Blade Profiles.* Wind Engineering 2010, 34 (2):207-218.

17. Makkonen L. *Atmospheric Icing on Sea Structure.* U.S. Army Cold Regions Research and Engineering Laboratory, Hanover, New Hampshire, 1984.

18. Bose N. *Icing on a small horizontal-axis wind turbine - Part 1: Glaze ice profiles.* Journal of Wind Engineering and Industrial Aerodynamics 1992, 45:7585.

Ice Accretion on Wind Turbine Blades

Adriána Hudecz[#1], Holger Koss [*2], Martin O. L. Hansen [#†3]

[#]*Department of Wind Energy, Technical University of Denmark*
[1] `ahud@dtu.dk`
[3] `molh@dtu.dk`

[*]*Department of Civil Engineering, Technical University of Denmark*
[2] `hko@byg.dtu.dk`

[†]*Centre for Ships and Ocean Structures, Department of Marine Technology, Norwegian University of Science and Technology*

Abstract — **In this paper, both experimental and numerical simulations of the effects of ice accretion on a NACA 64-618 airfoil section with 7º angle of attack are presented. The wind tunnel tests were conducted in a closed-circuit climatic wind tunnel at Force Technology in Denmark. The changes of aerodynamic forces were monitored as ice was building up on the airfoil for glaze, rime and mixed ice. In the first part of the numerical analysis, the resulted ice profiles of the wind tunnel tests were compared to profiles estimated by using the 2D ice accretion code TURBICE. In the second part, Ansys Fluent was used to estimate the aerodynamic coefficients of the iced profiles. It was found that both reduction of lift coefficient and increase of drag coefficient is a nearly linear process. Mixed ice formation causes the largest flow disturbance and thus the most lift degradation. Whereas, the suction side of the rime iced ice profile follows the streamlines quite well, disturbing the flow the least. The TURBICE analysis agrees fairly with the profiles produced during the wind tunnel testing.**

I. INTRODUCTION

In cold climate areas with temperatures below 0ºC and humid environment for larger periods of the year icing represents an significant threat to the performance and durability of wind turbines (Tammelin et al. [1], Tallhaug et al. [2] and Baring-Gould et al. [3]). In this paper, both experimental and numerical simulations of the effects of ice accretion on a NACA 64-618 airfoil section are presented. The experiments were performed in a closed-circuit climatic wind tunnel at FORCE Technology in Denmark. Aerodynamic forces were monitored throughout the icing process for 7º angle of attack at different temperatures, which were used to ensure adequate environment for the typical ice types, rime, glaze and mixed ice, which threaten the operation of wind turbine.

There were already a number of wind tunnel tests conducted on iced airfoils in the past. Seifert and Richert [4] and Jasinski et al. [5] used artificial ice deposits during their experiments. In case of Seifert and Richert's tests [4], the molds were made of actual ice fragments from a wind turbine, whereas Jasinski et al. [5] simulated the ice profiles with Nasa's ice accretion code, LEWICE. Hochart et al. [6] performed two-phase experiments. In the first phase, the ice deposit was grown and then in the second phase, efficiency tests were performed. The main difference from these tests and the ones presented in this paper is the fact that the aerodynamic forces were monitored as ice was accumulating. At the end of the tests, the ice profiles were documented by contour tracing for further, numerical analysis.

In the recent years, especially due to the increased computer power, it became possible to determine the performance of iced wind turbine much faster and more accurately with computational fluid dynamics (CFD) and panel method based models. Homola et al. [7] have used a two-steps method, combining TURBICE and Ansys Fluent to investigate the effect of ice similarly on a NACA 64-618 profile. TURBICE is comprehensive numerical ice accretion software from VTT, Technical Research Centre of Finland, which uses panel method to calculate the potential flow. It was verified by icing wind tunnel testing of both aircraft and wind turbine airfoils. The accuracy of the solution is dependent on the number of the panels and their distribution around the section (Makkonen et al., [8]). Homola et al. [7] found that the lift coefficient was reduced in all cases and the smallest change was observed in case of rime ice. During the CFD simulations, it was found that the horn type glaze ice shape causes the largest separation, which leads to a significantly reduced lift and higher drag coefficient.

Etemaddar et al. [9] has also used the same profile in their numerical analysis. In their study, they combined Nasa's LEWICE code with Ansys Fluent and pointed out that the ice load increases with liquid water content (LWC), median volumetric diameter (MVD) and relative wind speed.

The numerical simulations presented in this paper were carried out in two parts. First, the collected ice profiles were compared to profiles generated in TURBICE. In the second part, numerical analyses were done on the iced profiles from the wind tunnel tests in Ansys Fluent.

The aim of the wind tunnel tests was to investigate the changes of aerodynamics as ice built up on the airfoil for glaze, rime and mixed ice tests. The relative changes of lift and drag coefficients along with the shape of the ice deposits could be compared to results of the numerical analysis.

II. ABBREVIATIONS AND NOMENCLATURE

AOA, α – angle of attack
C_L – lift coefficient
C_D – drag coefficient
D – drag force
G_{ice} – gravity force of ice deposit
L – lift force
LWC – liquid water content
MVD – median volumetric diameter
SP – separation point
U – mean wind speed

III. METHODS

In this section, both experimental and numerical set-up of the analyses is detailed.

A. Wind Tunnel Tests – Experimental Setup

The tests were performed in the Collaborative Climatic Wind Tunnel (CWT) at FORCE Technology. The wind tunnel was developed and built as a collaboration project between Technical University of Denmark and FORCE Technology. The main specifications are listed in TABLE I.

TABLE I BASIC SPECIFICATIONS OF THE WIND TUNNEL (based on Georgakis et al. [10])

Temperature	-5 to 40 ^oC
Minimum liquid water content (LWC)	0.2 g/m^3
Test section cross-sectional area	2.0x2.0 m
Test section length	5 m
Maximum wind speed velocity	31 m/s
Turbulence intensity	0.6 to 20 %

NACA 64-618 airfoil section (900 mm chord length and 1350 mm width) provided by LM Wind Power was used during the experiments. A pair of AMTI MC5 force and torque transducers was used to measure the loading simultaneously around 6 degrees of freedom. Based on the measured forces (F_x and F_y), which are visualized in Fig. 1, and the known angle of attack (α) and wind speed (U), the lift (L) and drag (D) forces along with the weight of ice (G_{ice}) can be calculated.
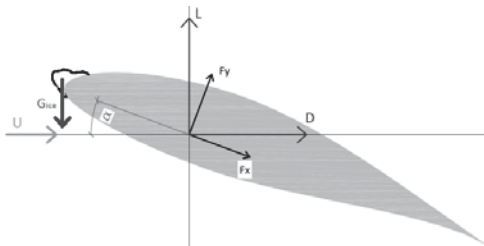

Fig. 1. Forces acting on the iced airfoil. F_y and F_x are directly measured by the force transducers and based on these and the known angle of attack and wind speed (U), the lift (L) and drag (D) forces along with the weight of ice (G_{ice}) can be calculated.

The tests were performed by first setting the target wind speed and temperature in the test section. A constant angle of attack, 7° was used in these experiments. As soon as the target temperature was reached, the water spray, and thus in-cloud environment, was set. For glaze and mixed ice tests, 15 m/s wind speed was applied during ice build-up while for the rime ice test due to the limitation of the wind tunnel's cooling unit, it was necessary to reduce the wind speed to 10 m/s in order to ensure cold enough temperature. The ice accretion process was running for 60 minutes and every five minutes the forces were measured. Based on the force measurements, not only the aerodynamic forces but also the gravity force of the accumulated ice was calculated. In order to study the pure effect of the altered airfoil profile, this force was subtracted from the lift measurements. At the end of the tests, the ice profiles were documented by contour tracing and were used in the numerical simulation part.

The flow in a wind tunnel is different from that, which occurs in the free-air due to the presence of the tunnel walls, therefore the measurements were corrected by following ESDU 76028, *Lift-interference and blockage corrections for two-dimensional subsonic flow in ventilated and closed wind-tunnels methodology* [11].

The specifications of the presented tests are summarized in TABLE II. The temperatures listed here are the mean values of the established temperature during the tests. The MVD and LWC values are target values based on the specification of the manufacturer of the spray nozzles (Schick [12]).

TABLE II THE SPECIFICATION OF THE PRESENTED TESTS.

	Glaze ice test	Mixed ice test	Rime ice test
AOA (^{o})	7	7	7
T (^oC)	-3	-5	-8
MVD (μm)	25	25	20
LWC (g/m^3)	0.7	0.7	0.7
U_{accr} (m/s)	15	15	10
U_{test} (m/s)	15	15	15

B. Numerical Simulation Setup – TURBICE.

TURBICE simulations were performed at VTT, Technical Research Centre of Finland in order to compare the results of the wind tunnel tests to a numerical ice accretion model. For the air temperature only a constant value can be defined in the simulation program. Hence, mixed ice simulation could not be modeled. There are a number of other input parameters, such as MVD, LWC, meteorological wind speed, rotating speed of the wind turbine, pitch angle, air temperature, air pressure and accretion time. These parameters were set to ensure similar conditions as it was in the wind tunnel.

Since the MVD and LWC were only target values in the wind tunnel tests, several scenarios were analyzed in TURBICE and only the best fits are presented here. The input parameters of the different tests are listed in TABLE III.

TABLE III INPUT PARAMETERS FOR THE PRESENTED TURBICE TESTS

Parameters	Glaze test 1.	Glaze test 2.	Rime test 1.	Rime test 2.
AOA (^{o})	7	7	7	7
MVD (μm)	25	30	25	25
LWC (g/m^3)	0.65	0.65	0.4	0.6
Temp (^oC)	-3	-3	-8	-8
Time (min)	60	90	60	90

C. Numerical Simulation Setup – Ansys Fluent.

CFD simulations are used to analyze numerically the impacts of ice accretion on the flow behavior and on the aerodynamic characteristics of the airfoil. As it was mentioned before, the ice profiles were collected at the end of the wind tunnel tests and were further analyzed by Ansys Fluent. Since the ice profiles were collected from specific locations, 2D models were done. The construction and meshing of each model was done using Ansys Workbench. The control volume around the blade was rectangular with edges positioned at 50 chords length away in vertical direction and 20 chords length from the horizontal direction (cross flow). It was necessary to set the horizontal boundaries further away to avoid any effect caused by these boundaries on the flow around the airfoil.

An inflation layer was added to the mesh in order to produce a structured, fine mesh in the vicinity of the airfoil to achieve a better representation of the flow near the airfoil surface. The first layer height is dependent on the surface roughness, since the roughness height may not exceed it. However, it was found that Ansys Fluent cannot properly handle surface roughness; therefore it was not included in the analysis. In TABLE IV, the setup of the inflation layer is listed. The height of the first layer was set small enough to ensure the validity of the log law.

TABLE IV Setup of Inflation in Ansys Model

	Clean profile	Glaze ice test	Mixed ice test	Rime ice test
First layer height (m)	1e-5	1e-5	1e-5	1e-5
Nr. of layers of inflation layer	40	40	40	35
Growth rate	1.2	1.2	1.2	1.2

In Fig. 2, an example of the mesh around the leading edge is shown. An appropriate size was chosen for the quadrilaterals so they can follow the complex curve of the ice deposit.
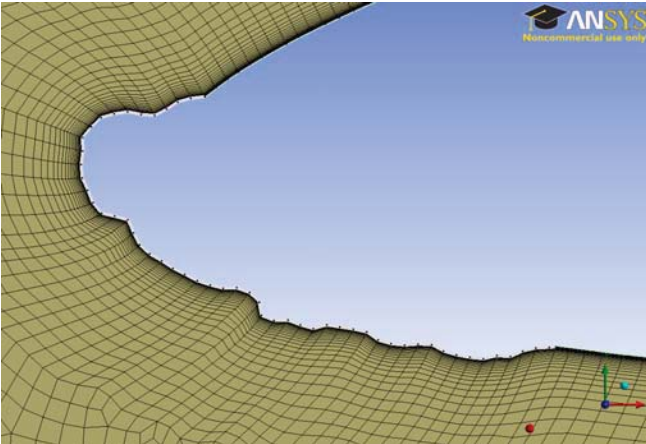

Fig. 2 Mesh around the iced leading edge in case of glaze iced airfoil. The height of the first layer is 1e-5 m and there are 40 layers in the inflation layer.

During the simulation Spalart-Allmaras and k-Ω SST turbulence models were used. It was found in previous studies (e.g. Mortensen [13]) that the solution using Spalart-Allmaras

model converges faster and easier than with the k-Ω SST turbulence model. Therefore the first 500 iterations were done by using Spalart-Allmaras model providing an initial guess for the k- Ω SST turbulence model and achieving more stable convergence. However, Chung and Addy [14] pointed out that Spalart-Allmaras model is the best performing model when simulating ice accretions; therefore that model was used for the iced profiles.

IV. RESULTS

The above discussed simulations' results are presented in this section. It should be kept in mind that these values are only valid for the set-up used in these particular tests.

A. Wind tunnel tests

The forces caused by the wind acting on the iced airfoil along with the gravity force of ice were measured throughout the accretion process. Based on these force measurements, it was possible to calculate the lift and drag coefficient of the continuously altered airfoil. The reduction of the lift coefficient as a function of accretion time for the three different ice types is shown in Fig. 3. As it is seen, first order polynomials could be fitted to the points, thus the degradation process is almost linear. Even though the accretion time was only 60 minutes, significant changes were monitored. The lift coefficient decreased the least, 22 % in case of rime ice tests and most significant for mixed ice tests, 34 %. For the glaze ice test, the degradation was 25 %.

The degradation is already visible after 5 minutes into the accretion. This sudden drop seems to be more severe than the one happened between 5 and 10 min. The slope of the drop in the first 5 minutes is much steeper than of the polynomials fitted to the points.
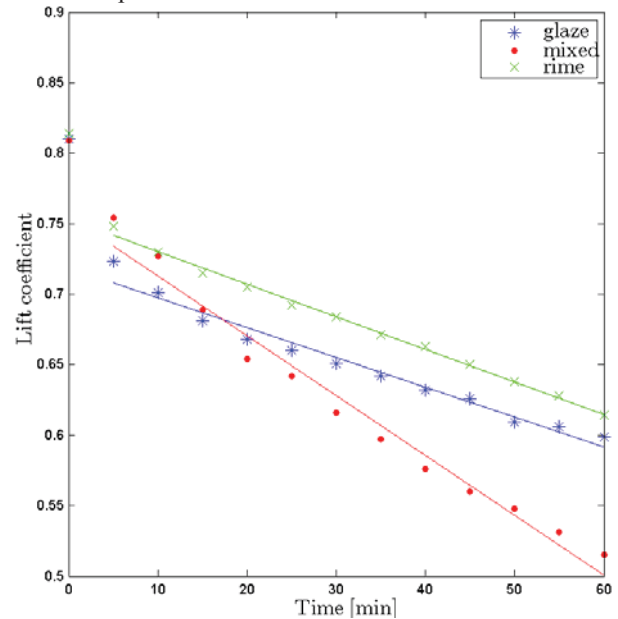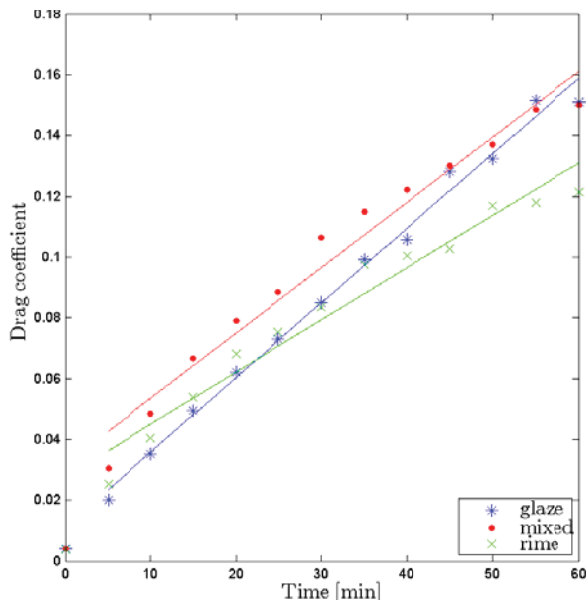

Fig. 3 Alteration of lift coefficient as a function of ice accretion time for 7° AOA in case of glaze (*), mixed (.) and rime ice (x). The environmental

conditions were the following: LWC~0.7 g/m^3, MVD~25 for glaze and mixed ice and MVD~20 for rime ice and Re~1e6.

An increase of drag force and hence an increase of drag coefficient was experienced during the tests. This tendency is illustrated in Fig. 4. Similarly to the initial lift coefficient degradation, rapid increase of drag coefficient can be observed in the first five minutes. However, contrary to the lift curves, the process does not seem to slow down, i.e. the slope of the initial increase does not differ significantly from the slope of the fitted polynomials. It is clearly visible in Fig. 4 that the smallest increase of the drag coefficient occurs under rime ice conditions.

Fig. 4 Alteration of drag coefficient as a function of ice accretion time for 7° AOA in case of glaze (*), mixed (.) and rime ice (x). The environmental conditions were the following: LWC~0.7 g/m^3, MVD~25 μm for glaze and mixed ice and MVD~20 for rime ice and Re~1e6.

In Fig. 5, the collected ice profiles are shown. It can be seen, that the smallest ice deposit was building up in case of the rime ice test while the largest one in case of the mixed ice test. The rime ice accreted only on the leading edge of the airfoil, whereas the other two types accumulated also on the pressure side of the airfoil. The stagnation point is quite clear in all three cases (marked with orange circles in Fig. 5).
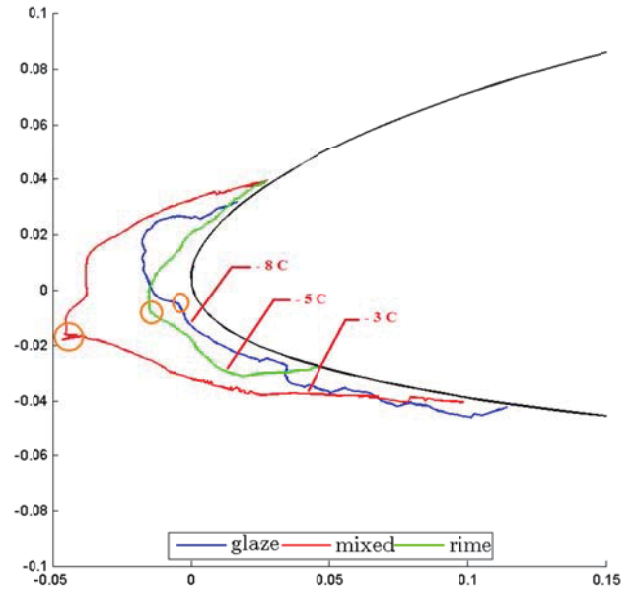

Fig. 5 Collected ice profiles from the wind tunnel tests for α=7° after 60 minutes of accretion. The environmental conditions were the following: U~15 m/s, LWC~0.7 g/m^3, MVD~25 for glaze and mixed ice and U~10m/s, MVD~20 for rime ice. The orange circles illustrates the stagnation points.

B. Numerical Simulation – TURBICE

As it was mentioned above, it was only possible to simulate conditions resulting in glaze and rime ice accretion on the airfoil. The results are plotted against the shapes collected from the climatic wind tunnel tests. Fig. 6 shows the results from the glaze simulations. The red curve represents the profile collected from the wind tunnel for LWC~0.7 g/m^3, MVD~25 μm, the blue line illustrates the result from TURBICE with LWC~0.65 g/m^3, MVD~25 μm during 60 minutes of accretion time, whereas the TURBICE results of LWC~0.65 g/m^3, MVD~30 μm and 90 minutes of accretion time are plotted in green.
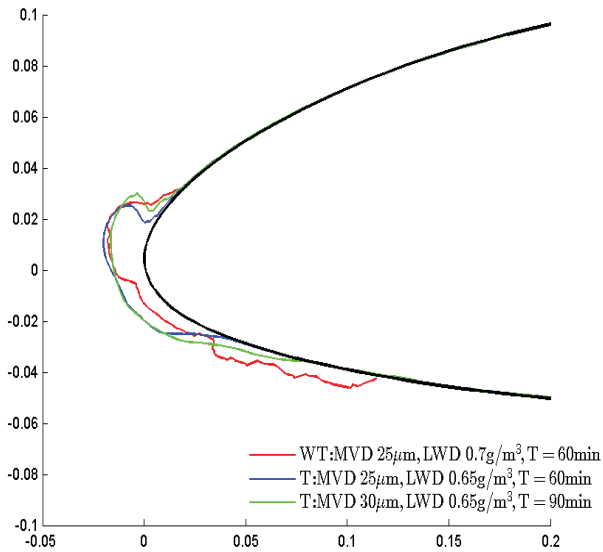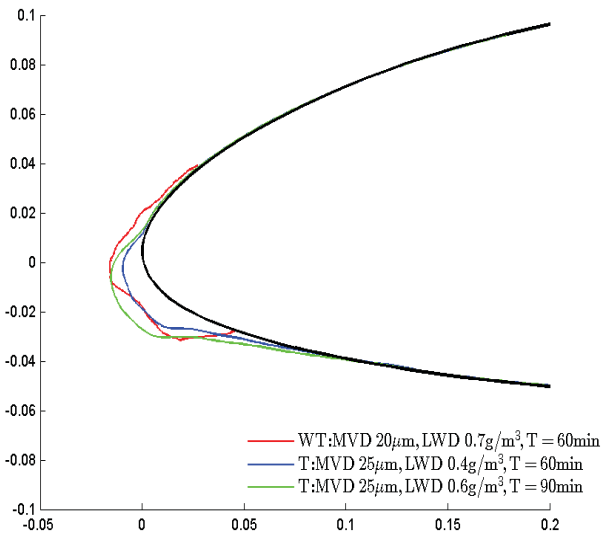
Fig. 6 Ice profiles from both the wind tunnel (WT) test and TURBICE (T) simulations for glaze ice. The red curve represents the profile collected from the wind tunnel for LWC~0.7 g/m³, MVD~25 µm, the blue line illustrates the result of LWC~0.65 g/m³, MVD~25 µm during 60 minutes of accretion time, whereas the results of LWC~0.65 g/m³, MVD~30 µm and 90 minutes of accretion time plotted in green.

In Fig. 7, the results of the rime ice test are shown. The red curve represents the profile collected from the wind tunnel for LWC~0.7 g/m³, MVD~20 µm, the blue line illustrates the result from TURBICE of LWC~0.4 g/m³, MVD~25 µm during 60 minutes of accretion time, whereas the results of LWC~0.6 g/m³, MVD~25 µm and 90 minutes of accretion time from TURBICE are plotted in green.

Fig. 7 Ice profiles from both the wind tunnel (WT) test and TURBICE (T) simulations for rime ice. The red curve represents the profile collected from the wind tunnel for LWC~0.7 g/m³, MVD~20 µm, the blue line illustrates the result of LWC~0.4 g/m³, MVD~25 µm during 60 minutes of accretion time, whereas the results of LWC~0.6 g/m³, MVD~25 µm and 90 minutes of accretion time plotted in green.

C. Numerical Simulation – Ansys Fluent

The results of the numerical simulation with Ansys Fluent are summarized in TABLE V. The relative change refers to the reduction of lift coefficient of iced airfoil related to the lift coefficient of the clean profile. As it can be read from the table, mixed ice accretion caused the most significant reduction of lift coefficient whereas the least was found for rime ice.

TABLE V RESULTS OF NUMERICAL SIMULATIONS BY ANSYS FLUENT

Test	C_L	Relative change [%]
Clean profile	1.01	-
Glaze iced profile	0.784	22
Mixed iced profile	0.762	25
Rime iced profile	0.831	18

In Fig. 8, the velocity vectors colored by the velocity magnitude around the leading edge of the clean airfoil are shown. The color-range represents the flow speed around the airfoil ranging from 0 to 22m/s (blue to red). It can be seen that the incoming velocity decreases to 0 m/s at the stagnation point (represented by blue arrows) and speeds up at the suction side. The flow around the airfoil is rather smooth and well attached.
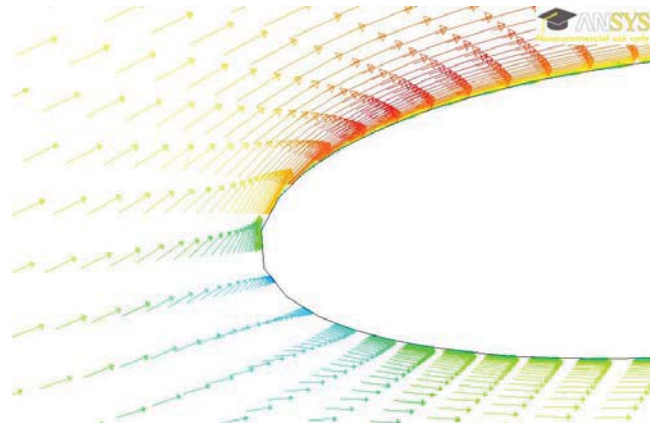

Fig. 8 Velocity vectors colored by the velocity magnitude (m/s) around the clean airfoil for inlet velocity 14 m/s and α=7º. The color-range from 0 to 22 m/s.

In Fig. 9, Fig. 10 and Fig. 11 the velocity vectors colored by the velocity magnitude around the leading edge of the iced airfoil is shown for glaze, mixed and rime ice, respectively. It can be seen that the ice deposit in each case disturbs the flow quite significantly. SP1 and SP2 illustrated the flow separation points at the suction and pressure side, respectively.
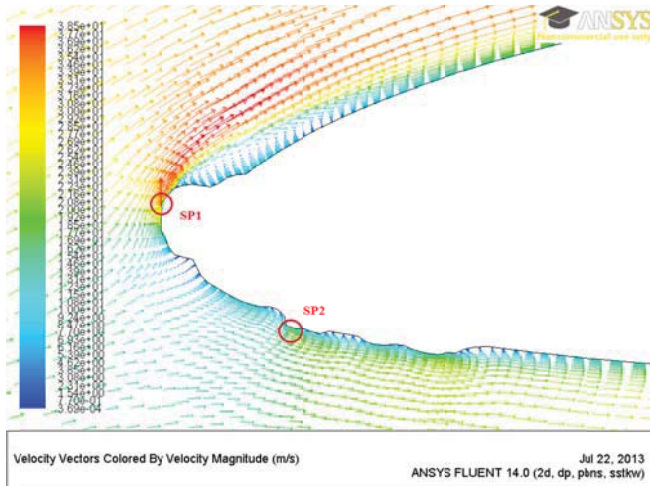
Fig. 9 Velocity vectors colored by the velocity magnitude (m/s) around the glaze iced airfoil for inlet velocity 14 m/s and α=7°. The color-range from 0 to 22 m/s. SP1 and SP2 illustrated the flow separation points at the suction and pressure side, respectively.

A large separation bubble is formed behind the leading edge separation point 1 (SL1) on the suction side of the airfoil, see Fig. 9.

In case of mixed ice deposit, a peak (SP1) was formed around the stagnation point, which reduces the flow speed at the suction side (see Fig. 10). A "nose" shaped ice formation can be also seen around the stagnation point, which was not seen in case of the other two types of ice simulations.
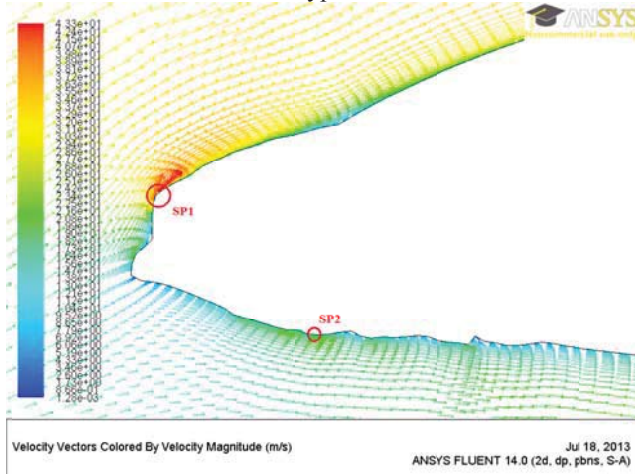

Fig. 10 Velocity vectors colored by the velocity magnitude (m/s) around the mixed iced airfoil for inlet velocity 14 m/s. The color-range from 0 to 22 m/s. SP1 and SP2 illustrated the flow separation points at the suction and pressure side, respectively.

At the suction side in Fig. 11, the accreted rime ice caused small disturbance on the flow pattern, compared to the clean airfoil. However, multiple local separation points can be found on the suction side (marked with red circles), which are causing lower slightly lower velocity zones compared to the clean profile.
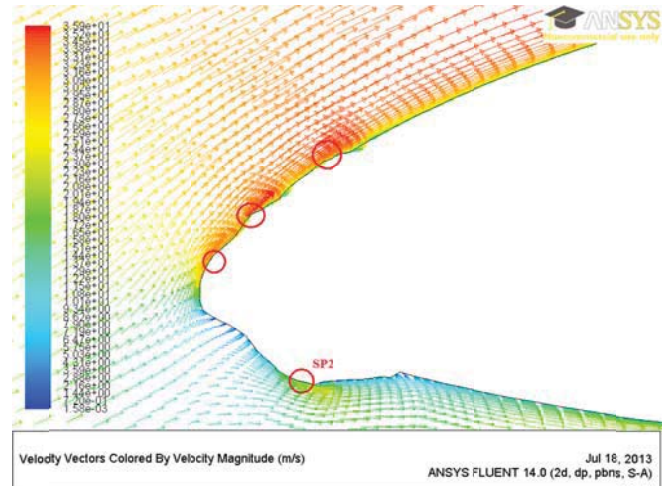

Fig. 11 Velocity vectors colored by the velocity magnitude (m/s) around the rime iced airfoil for inlet velocity 14 m/s and α=7°. The color-range from 0 to 22 m/s. SP2 illustrated the flow separation points at the pressure side, whereas there are multiple separation points marked by red circles at the suction side.

At the pressure side, small recirculation zones can be spotted behind the ice peaks (SL2) for each ice tests.

V. DISCUSSION

A. Wind Tunnel Tests

The results of the wind tunnel tests shows that the lift coefficient decreased whereas the drag coefficient increased for all three ice types (see Fig. 3 and Fig. 4). The same conclusion was drawn in the studies mentioned in the *Introduction*. However, Jasinski et al. [5] showed that in some cases of rime ice accretion, the lift coefficient increased. This behavior was not experienced during the tests presented in this paper.

It can be observed from Fig. 3 that the initial degradation in the first 5 minutes is highly significant in each test, and hence if the reduction would follow this trend, the lift degradation would be much more severe. The immediate reduction of lift coefficient was caused by the changed surface roughness, as it was also shown by e.g. Lynch and Khodadoust [15].

It can be also noticed in Fig. 3, that the difference between the immediate reduction of lift coefficient for the different ice types is not significant, which indicates that the initial degradation is independent of the ice formation type for the same angle of attack.

It was also found that the least lift decrease and drag increase were caused by rime ice accretion. It is because in case of rime ice, the water droplets freeze on impact at the leading edge and this deposit acts as an extended leading edge causing less flow disturbance. For glaze and mixed ice, some of the droplets did not freeze on the surface but ran off along the airfoil and freeze aft, which resulted in larger iced surface area (see Fig. 5), and thus more disturbed flow field. The mixed ice profile had the highest negative influence on the flow and therefore it caused the highest lift degradation.

B. Numerical Simulation – TURBICE

Fig. 6 and Fig. 7 shows the results of TURBICE analyses for both rime and glaze ice together with the wind tunnel results for comparison. The TURBICE profiles and the profiles from the wind tunnel tests were not identical; however, they were in good agreement considering the circumstance that LWC and MVD are not known in the wind tunnel experiment. This leads to that these parameters could not be set accurately for the TURBICE simulation. Since it was not possible to measure LWC and MVD accurately in the wind tunnel, it was not possible to set the correct values in TURBICE. This could be a reason for the differences.

Some of the TURBICE tests used 90 minutes accretion time, which is longer than the duration of the wind tunnel tests. However, this should not be a major issue, because it was seen that the ice build-up is a nearly linear process. Therefore it can be assumed that the shape of an ice profile accreted in 60 minutes is similar to the one presented here.

C. Numerical Simulation – Ansys Fluent.

The trend of the reduction of lift coefficients agrees quite well with the wind tunnel test results. However, the relative degradation was found to be lower than it was for the experiments. The reason could be that with the contour tracing method, the small changes of surface roughness could not be documented therefore they were not implemented in the numerical analysis.

It was seen that the glaze and mixed ice formations caused the most flow disturbance. The sharp edges at the suction side seen in both Fig. 9 and Fig. 10 led to a speed up, which caused a large separation bubble especially in case of glaze ice. In case of rime iced profile, the flow followed a similar pattern as it was observed for the clean airfoil and comparing Fig. 11 and Fig. 8, the magnitude of the velocity did not differ significantly from the clean profile. For all three cases, there were some vortex formations noticed behind the ice peaks at the pressure side causing recirculation zones, which lead to some flow disturbance and retardation. However, it seems that they do not have a large influence on the change of the overall leading edge aerodynamics.

VI. CONCLUSION

Both experimental and numerical analyses have been performed to study the effect of glaze, rime and mixed ice accretion on the aerodynamics of an iced NACA 64-618 profile for 7° angle of attack. The experiments were carried out in a climatic wind tunnel, and for the numerical analyses, TURBICE ice accretion model and Ansys Fluent were used to verify the findings from the wind tunnel tests.

During the wind tunnel tests, the aerodynamic forces were monitored as ice was building up on the surface. Similarly to other studies and also to the numerical investigation, lift coefficient was found to decrease and drag coefficient increased as ice accreted. These processes were found to be nearly linear.

Mixed ice formation caused the most severe lift coefficient reduction, whereas the least was found for rime ice. The largest ice deposit accreted on the profile in case of mixed ice and thus the largest disturbance was seen here. The flow around the rime iced ice profile followed a pattern similar to the streamlines around the clean profile, hence causing low disturbance.

The ice accretion model TURBICE was used to estimate ice profiles for similar conditions as it was set in the wind tunnel. These profiles agree, considering the limitations of known experimental boundary conditions, fairly with the profiles produced during the wind tunnel testing.

It can be concluded that significant lift reduction and thus power production loss can be achieved even in the first hour of ice accretion.

REFERENCES

[1] B. Tammelin, M. Cavaliere, H. Holttinen, C. Morgan, H. Seifert, and K. Santti, Wind energy production in cold climate (WECO). Technical report, Finnish Meteorological Institute, 1998.

[2] L. Tallhaug, G. Ronsten, R. Horbaty, R. Cattin, T. Laakso, M. Durstewitz, A. Lacroix, E. Peltola, and T. Wallnius, "Wind energy projects in cold climate. Technical report, Executive Committee of the International Energy Agency Programme for Research and Development on Wind Energy Conversion Systems, 2009.

[3] I. Baring-Gould, R. Cattin, M. Durstewitz, M. Hulkkonen, A. Krenn, T. Laakso, A. Lacroix, E. Peltola, G. Ronsten, L. Tallhaug, and T. Wallenius. 13. Wind Energy Projects in Cold Climates. Technical report, 2011.

[4] H. Seifert and F. Richert. Aerodynamics of iced airfoils and their influence on loads and power production. European Wind Energy Conference, 1997.

[5] W. J. Jasinski, S. C. Noe, M. S. Selig, and M. B. Bragg. Wind turbine performance under icing conditions. Journal of Solar Energy Engineering, ASME, 120(1):60-65, 1997.

[6] C. Hochart, G. Fortin, and J. Perron. Wind turbine performance under icing conditions. Wind Energy, 11:319333, 2008.

[7] M. C. Homola, M. S. Virk, T. Wallenius, P. J. Nicklasson, and P. a. Sundsbø. Effect of atmospheric temperature and droplet size variation on ice accretion of wind turbine blades. Journal of Wind Engineering and Industrial Aerodynamics, 98(12):724–729, 2010.

[8] L. Makkonen, T. Laakso, M. Marjaniemi, and K. J. Finstad. Modelling and prevention of ice accretion on wind turbines. Wind Energy, 25(1):3–21, 2001.

[9] M. Etemaddar, M. O. L. Hansen and T. Moan. Wind turbine aerodynamic response under atmospheric icing conditions. Wind Energy, DOI: 10.1002/we.1573, 2012.

[10] C. Georgakis, H. Koss, and F. Ricciardelli. Design specifications for a novel climatic wind tunnel for the testing of structural cables. International Symposium on Cable Dynamics (ISCD) - 8, 2009, Paris, France.

[11] ESDU 76028, Lift-Interference and Blockage Corrections for Two-Dimensional Subsonic Flow in Ventilated and Closed Wind Tunnel, ESDU 1976.

[12] R. J. Schick. Spray technology reference guide: Understanding drop size, bulletin 459c. Technical report, Spraying Systems Co.

[13] K. Mortensen, CFD Simulation of an airfoil with leading edge ice accretion, Department of Mechanical Engineering, Technical University of Denmark, 2008

[14] J.J. Chung and H.E. Addy, Jr. A Numerical Evaluation of Icing effects on a Natural Laminar Flow Airfoil. NASA TM-2000-209775, January 2000.

[15] F. T. Lynch and A. Khodadoust. Effects of ice accretions on aircraft aerodynamics. Progress in Aerospace Sciences, 37(8):669-767, 2001.

References

E. Aakervik. Nanortalik, Nanortalik municipality, Greenland - Analysis of Wind Measurements. Technical report, Kjeller Vindteknikk, KVT/EAA/2011/R075, 2011.

I. Abbott and A. von Doenhoff. *Theory of Wing Sections. Including a Summary of Airfoil Data.* Courier Dover Publications, 1959.

H. E. Addy. Ice Accretions and Icing Effects for Modern Airfoils. Technical Report April, NASA's Glenn Research Center, Cleveland, Ohio, 2000.

H. E. Addy, A. P. Broeren, J. G. Zoeckler, and S. Lee. A Wind Tunnel Study of Icing Effects on a Business Jet Airfoil. In *American Institute of Aeronautics and Astronautics, Aerospace Sciences Meeting and Exhibit*, number February, 2003. ISBN 2003212124.

Advisory Circular. Effect of Icing on Aircraft Control and Airplane Deice and Anti-ice Systems. 1996.

AMTI. MC5 Force and Torque Transducer, 2000. URL `http://www.summitmedsci.co.uk/documents/MC5.pdf`.

C. Arbez, A. Amosse, and M. Wadham-Gagnon. Met Mast Configuration Guidelines in Cold Climate. In *IWAIS XV, St. John's, Newfoundland and Labrador, Canada, September*, 2013.

I. Baring-Gould, R. Cattin, M. Durstewitz, M. Hulkkonen, A. Krenn, T. Laakso, A. Lacroix, E. Peltola, G. Ronsten, L. Tallhaug, and T. Wallenius. 13. Wind Energy Projects in Cold Climates. Technical report, 2011.

L. Battisti. Relevance of Icing. Technical report, DTU Wind turbine ice prevention systems selection and design (41326) lecture notes, Technical University of Denmark, 2008.

L. Battisti. Relevance of icing. Technical report, DTU Wind turbine ice prevention systems selection and design (41326) lecture notes, 2009.

L. Battisti, R. Fedrizzi, and A. Brighenti. Sea Ice and Icing Risk for Offshore Wind Turbines. In *Owemes 2006, 20-22 April. Citavecchia, Italy*, pages 20–22, 2006.

L. Blumenthal, G. Busch, A. Broeren, and M. Bragg. Issues in Ice Accretion Aerodynamic Simulation on a Subscale Model. *44th AIAA Aerospace Sciences Meeting and Exhibit*, pages 1–20, Jan. 2006.

N. Bose. Icing on a Small Horizontal-Axis Wind Turbine - Part 1 : Glaze Ice Profiles. *Journal of Wind Engineering and Industrial Aerodynamics*, 45, 1992.

M. Bragg, A. Broeren, and L. Blumenthal. Iced-Airfoil Aerodynamics. *Progress in Aerospace Sciences*, 41(5):323–362, July 2005. ISSN 03760421.

M. B. Bragg, A. P. Broeren, H. E. Addy, and M. G. Potapczuk. Airfoil Ice-Accretion Aerodynamics Simulation. *Collection of Technical Papers - 45th AIAA Aerospace Sciences Meeting*, (January), 2007.

S. A. Brandt. Chapter 4: Wings and Airplanes. In *Introduction to Aeronautics: A Design Perspective*, page 509. American Institute of Aeronautics and Astronautics, 2004.

V. Carlsson. Measuring Routines of Ice Accretion for Wind Turbine Applications. Master Thesis, Umeaa Univesitet, 2009.

F. M. Catalano and P. R. Caixeta Jr. Wind Tunnel Wall Boundary Layer Control for 2D High Lift Wing Testing. In *24th International Congress of the Aeronautical SCIENCES*, 2004.

R. Cattin. Icing of Wind Turbines. Elforsk report 12:13. Technical Report January, 2012.

J. J. Chung and H. E. J. Addy. A Numerical Evaluation of Icing Effects on a Natural Laminar Flow Airfoil. In *38th Aerospace Sciences Meeting & Exhibit, January 10-13*, 2000.

T. Dahl. Summit Station Wind Power Pilot Project. Technical report, CH2M Hill Polar Services, 2009.

ESDU 76028. Lift-Interference and Blockage Corrections for Two-Dimensional Subsonic Flow in Ventilated and Closed Wind Tunnel. Technical report, 1976.

M. Etemaddar, M. O. L. Hansen, and T. Moan. Wind Turbine Aerodynamic Response Under Atmospheric Icing Conditions. *Wind Energy*, 2012.

S. Fikke, G. Ronsten, A. Heimo, S. Kunz, M. Ostrozlik, J. Sabata, B. Wareing, B. Wichura, J. Chum, T. Laakso, and L. Makkonen. COST 727 : Atmospheric Icing on Structures Measurements and data collection on icing : State of the Art. Technical Report 75, Publication of MeteoSwiss, 2006.

G. Fortin and J. Perron. Spinning Rotor Blade Tests in Icing Wind Tunnel. In *AIAA 2009-4260, 1st AIAA Atmospheric and Space Environments Conference, San Antonio, TX*, number June, pages 1–16, 2009.

G. Fortin, J.-L. Laforte, and A. Beisswenger. Prediction of Ice Shapes on NACA0012 2D Airfoil. *SAE Technical Papers 2003-01-2154.*, June 2003.

G. Fortin, P. J. Perron, and P. A. Ilinca. Behaviour and Modeling of Cup Anemometers under Icing Conditions. In *XI. International Workshop on Atmospheric Icing on Structures, Montreal, Canada*, number June, 2005.

R. W. Fox, A. T. McDonald, and P. J. Pritchard. *Introduction to Fluid Mechanics*. John Wiley & Sons Inc., 2009.

REFERENCES

R. W. Gent, N. P. Dart, and J. T. Cansdale. Aircraft Icing. *Philosophical Transactions of the Royal Society A: Mathematical, Physical and Engineering Sciences*, 358(1776): 2873–2911, Nov. 2000. ISSN 1364-503X.

C. T. Georgakis, H. Koss, and F. Ricciardelli. Design Specifications for a Novel Climatic Wind Tunnel for the Testing of Structural Cables. In *International Symposium on Cable Dynamics (ISCD), Paris, France*, number 1, 2009.

Germanischer Lloyd Wind Energy GmbH. GL Wind Technical Note 067 Certification of Wind Turbines for Extreme Temperatures , Scope of Assessment, Revision 3. Technical report, 2009.

W. G. Habashi, F. Morency, and H. Beaugendre. FENSAP-ICE : a comprehensive 3D Simulation Tool for In-flight Icing. In *7th International Congress of Fluid Dynamics and Propulsion, Sharm-El-Sheikh, Egypt, December*, number December, pages 1–7, 2001.

C. Hochart, G. Fortin, and J. Perron. Wind Turbine Performance Under Icing Conditions. *Wind Energy*, 11:319–333, 2008.

HoloOptics. User Guide. T 40 series of Icing Rate Sensors. Technical report. URL `http://holooptics.net/`.

M. C. Homola, P. J. Nicklasson, and P. a. Sundsbø. Ice Sensors for Wind Turbines. *Cold Regions Science and Technology*, 46(2):125–131, Nov. 2006. ISSN 0165232X.

M. C. Homola, T. Wallenius, L. Makkonen, and P. J. Nicklasson. The relationship between chord length and rime icing on wind turbines. *Wind Energy*, 13(7):627–632, 2009.

M. C. Homola, M. S. Virk, T. Wallenius, P. J. Nicklasson, and P. a. Sundsbø. Effect of Atmospheric Temperature and Droplet Size Variation on Ice Accretion of Wind Turbine Blades. *Journal of Wind Engineering and Industrial Aerodynamics*, 98(12): 724–729, Dec. 2010a. ISSN 01676105.

M. C. Homola, T. Wallenius, L. Makkonen, P. J. Nicklasson, and P. A. Sundsbø. Turbine Size and Temperature Dependence of Icing on Wind Turbine Blades. *Wind Engineering*, 34(6):615–628, 2010b.

IEA-RETD. Renewable Energies for Remore Areas and Islands (REMOTE). Technical report, IEA Renewable Energy Technology Deployment, 2012.

A. Ilinca. Analysis and Mitigation of Icing Effects on Wind Turbines. In I. Al-Bahadly, editor, *Wind Turbines*, chapter 8., pages 177–214. InTech, 2011.

ISO 12494. Atmospheric icing of Structures. Technical report, ISO Copyright Office, Geneva, Switzerland, 2001.

W. J. Jasinski, S. C. Noe, M. S. Selig, and M. B. Bragg. Wind Turbine Performance Under Icing Conditions. *Transactions of the ASME. Journal of Solar Energy Engineering*, 120 (1):60–65, 1997.

L. E. Kollár, M. Farzaneh, and A. R. Karev. Modeling Droplet Collision and Coalescence in an Icing Wind Tunnel and the Influence of These Processes on Droplet Size Distribution. *International Journal of Multiphase Flow*, 31(1):69–92, Jan. 2005. ISSN 03019322.

H. Koss and M. S. M. Lund. Experimental Investigation of Aerodynamic Instability of Iced Bridge Cable Sections. In *6th European and African Conference on Wind Engineering, Cambridge, UK*, 2013.

A. G. Kraj and E. L. Bibeau. Icing Characteristics and Mitigation Strategies for Wind Turbines in Cold Climates. 2006.

T. Laakso, M. Durstewitz, R. Horbaty, A. Lacroix, E. Peltola, G. Ronsten, L. Tallhaug, and T. Wallenius. State-of-the-art of Wind Energy in Cold Climates. Technical report, IEA Task 19 - Wind Energy in Cold Climates, 2009.

F. T. Lynch and A. Khodadoust. Effects of Ice Accretions on Aircraft Aerodynamics. *Progress in Aerospace Sciences*, 37(2001):669–767, 2001.

L. Makkonen. Atmospheric Icing on Sea Structures. *U.S. Army Cold Regions Research and Engineering Laboratory, Hanover, New Hampshire*, 1984.

L. Makkonen. Models for the Growth of Rime, Glaze, Icicles and Wet Snow on Structures. *Philosophical Transactions of the Royal Society A: Mathematical, Physical and Engineering Sciences*, 358(1776):2913–2939, Nov. 2000. ISSN 1364-503X.

L. Makkonen, T. Laakso, M. Marjaniemi, and K. J. Finstad. Modeling and prevention of ice accretion on wind turbines. *Wind Energy*, 25(1):3–21, 2001.

K. Mortensen. CFD Simulation of an Airfoil with Leading Edge Ice Accretion. Master thesis. Department of Mechanical Engineering, Technical University of Denmark, 2008.

Navigant Research. *BTM Wind Report: World Market Update 2012. International Wind Energy Development Forecast 2013-2017*. 2012.

O. Parent and A. Ilinca. Anti-icing and De-icing Techniques for Wind Turbines : Critical Review. *Cold Regions Science and Technology*, pages 1–9, 2010. ISSN 0165-232X.

T. Reid, G. Baruzzi, and I. Ozcer. FENSAP - ICE Simulation of Icing on Wind Turbine Blades , Part 1 : Performance Degradation. In *51st AIAA Aerospace Sciences Meeting including the New Horizons Forum and Aerospace Exposition 07 - 10 January 2013, Grapevine (Dallas/Ft. Worth Region), Texas*, number January, 2013.

E. Sagol, M. Reggio, and A. Ilinca. Issues Concerning Roughness on Wind Turbine Blades. *Renewable and Sustainable Energy Reviews*, 23:514–525, July 2013. ISSN 13640321.

R. J. Schick. Spray technology reference guide: Understanding drop size, bulletin 459c. Technical report, Spraying Systems Co., 2008.

H. Seifert and F. Richert. Aerodynamics of iced Airfoils and Their Influence on Loads and Power Production. In *European Wind Energy Conference, Dublin Castle, Ireland*, number October, pages 458–463, 1997.

REFERENCES

H. Seifert and F. Richert. A Recipe to Estimate Aerodynamics and Loads on Iced Rotor Blades. In *Paper presented at BOREAS IV, Enontekiö, Hetta, Finland*, number March 1998, pages 1–11, 1998.

J. Shin, B. Berkowitz, H. Chen, and T. Cebeci. Prediction of Ice Shapes and Their Effect on Airfoil Performance. In *29th Aerospace Sciences Meeting. AIAA-91-0264*, 1991.

B. Tammelin, M. Cavaliere, H. Holttinen, C. Morgan, and H. Seifert. Wind Energy Production in Cold Climate. Technical Report January 1996, 1998.

B. Tammelin, H. Dobesch, M. Durstewich, H. Ganander, G. Kury, T. Laakso, and E. Peltola. *Wind Turbines in Icing Environment : Improvement of Tools for Siting , Certification and Operation - NEW ICETOOLS*. Finnish Meteorological Institute, 2005. ISBN 9516976182.

O. Ulleberg and A. Moerkved. Renewable Energy and Hydrogen System Concepts for Remote communities in the West Nordic Region - The Nolsoy Case Study. Technical report, 2008.

F. Villalpando, M. Reggio, and A. Ilinca. Numerical Study of Flow Around Iced Wind Turbine Airfoil. *Engineering Applications of Computational Fluid Mechnanics*, 6(1): 39–45, 2012.

A. Villumsen, K. Jakobsen, M. Holtergaard Nielsen, J. Dragsted, E. Larsen, and K. Schaldemose Hansen. Fyrtaarnsprojekt III - afsluttende rapport 2009. Technical report, Arctic Technology Center, Deparment of Civil Engineering, Technical University of Denmark, 2009.

M. S. Virk, M. C. Homola, and P. J. Nicklasson. Effect of Rime Ice Accretion on Aerodynamic Characteristics of Wind Turbine Blade Profiles. *Wind Engineering*, 34(2): 207–218, Mar. 2010a. ISSN 0309-524X.

M. S. Virk, M. C. Homola, and P. J. Nicklasson. Relation Between Angle of Attack and Atmospheric Ice Accretion on Large Wind Turbine' s Blade. *Wind Engineering*, 34(6): 607–614, 2010b.

M. S. Virk, M. C. Homola, and P. J. Nicklasson. Atmospheric Icing on Large Wind Turbine Blades. *International Journal of Energy and Environment*, 3(1):1–8, 2012.

W. B. Wright, M. G. Potapczuk, and L. H. Levinson. Comparison of LEWICE and GlennICE in the SLD Regime. In *46th Aerospace Sciences Meeting and Exhibit, Reno, Nevada*, number September, 2008.

DTU Vindenergi er et institut under Danmarks Tekniske Universitet med en unik integration af forskning, uddannelse, innovation og offentlige/private konsulentopgaver inden for vindenergi. Vores aktiviteter bidrager til nye muligheder og teknologier inden for udnyttelse af vindenergi, både globalt og nationalt. Forskningen har fokus på specifikke tekniske og videnskabelige områder, der er centrale for udvikling, innovation og brug af vindenergi, og som danner grundlaget for højt kvalificerede uddannelser på universitetet.

Vi har mere end 240 ansatte og heraf er ca. 60 ph.d. studerende. Forskningen tager udgangspunkt i ni forskningsprogrammer, der er organiseret i tre hovedgrupper: vindenergisystemer, vindmølleteknologi og grundlagsskabende forskning.